Towards Sustainable Environment, Novel Designs In Vibration Energy Harvesting Technology: Modelling and Experiment

TOLUWALOJU TUNDE ISAIAH

20383891

Thesis submitted for consideration of the award of the degree of Doctor of Philosophy by University of Nottingham

May 2024

Abstract

The thesis titled "Towards Sustainable Environment: Novel Designs in Vibration Energy Harvesting Technology: Modelling and Experiment," by presenting a novel method in enhancing the power harvested in electromagnetic vibration energy harvester through different mechanical and electrical circuit design. The research focuses on the integration of analytical modelling techniques and experimental validation to optimize the performances of different electromagnetic vibration energy harvester designs. Various considerations to enhance the overall energy conversion efficiency by leveraging the specific inherent characteristics of various proposed designs through material/transducer selection, geometric configurations, and energy conversion mechanisms are explored. Generally, the work emphasizes and aims to contribute to the development of sustainable energy harvesting technologies with the potential to address environmental challenges and promote a greener future. Preliminary analysis and simulation by designing and simulating different transducer coil-magnet geometries indicate that 10.00% increase in magnet size with flux converging material, resulted in 18.55% improvement in flux and harvested power while a new approach of predicting the electromagnetic damping ratio equation to an accuracy of 99.21% was presented.

Firstly, an approach to maximize the power output on a 2DOF harvester design by using different coils connection was presented. Analysis shows that by selecting the appropriate connection mode can enable achieving impedance matching between different sensors/micro devices since the coils could be connected either in individual, series, and parallel modes to match varying load requirements. This approach allows for continuous power to onsite and remote sensors. In addition, while the analytical formulations of the 2DOF designs achieved over 99.20 % fit with the experiment, the designs likewise maximized the harvested power/power densities by over 400 % relative to worse case scenarios of conventional SDOF designs in literatures.

Secondly, an improved damping-stress equation for predicting the linear and nonlinear damping ratio for any fatigue stress level (σ_f) is presented. The nonlinear stress (σ_{nL}) formulation is based on the Osborne Goodman's approach shows that nonlinear behavior onsets in the cantilever beam in the interval $0.64\sigma_f < \sigma_{nL} < 0.8\sigma_f$. Below this interval, the stress is purely linear and it is modelled based on the Lazan hysteresis models while $\sigma_{nL} > 0.8\sigma_f$ initiate a pure nonlinear characteristic in the system. A general comparison of the linear critical stress-damping profiles for material mechanical properties ranging from plastic to non-plastic shows that plastic material attained a larger damping at equivalent stress. The implication of the above is that while the non-plastic material maintains the linear response profile at larger critical stress, the plastic material

onset material/geometric nonlinearity due to larger response associated with it damping. Further studies on the energy harvesting capabilities shows that high-performance thermoplastic polymer are desirable for improved power densities while compromising the bandwidth while using a more rigid steel cantilever configuration compromised the power densities while increasing the bandwidth at equivalent excitations. Fitting the linear and nonlinear analytical equations resulted to an accuracy of 95.00 % with the experimental data thus showing that these methods undertaken for the linear and nonlinear performances provide good approximation for engineering design when the stress-damping relation deviates from linear into nonlinear domain.

Lastly, a novel design which attains a near resonant simultaneous harvester-isolation capabilities through levered configurations was undertaken. The levered design used either a vertical and/or a horizontal guiderail to respectively constrain the responses in desired DOF and to dispel the buckling energy in the spring. Two different designs namely with and without the guiderails are compared. Different from conventional isolators which isolation onsets after $\sqrt{2}$ of the resonant frequency ratio, this design characteristically activate double banded isolation about resonance at resonance frequency ratio ∓ 0.099. The lower and upper bands of the isolation onset occurred on the left- and right- hand sides of the lever while simultaneously harvesting power for efficient and autonomous sensor operations. The shifting of the point of isolation to lower near resonant frequency band considerably reduce the risk of resonant amplification without compromising the stiffness matrix of the design. The analytical solution of the system attained approximately 93.52 % fit with the experimental across all levels of excitations. While the Coulomb damping introduced from the guiderails was found to enhance the bandwidth and degree of isolation. Results showed that using larger energy harvesting coil is beneficial for improved harvestable power while improving the isolation by about 2.90 %. Lastly, while the Coulomb damping from guiderail was also identified beneficial for simultaneous harvester-isolation at optimum resistance at lower spring stiffness, standalone vibration energy harvesting and standalone vibration isolation are enhanced at zero Coulomb force (no guiderails) at larger stiffness and maximum Coulomb force respectively.

Dedication

To my God, my wife, Parents and Every Christian

Acknowledgement

First and foremost, I am grateful to the Almighty God the cradle of life and from whom all wisdom comes. Secondly, my special thanks goes to my advisors; Dr. ChungKet Thein and Dr. Dunant Halim for their guidance, support and expertise as well as to other members of the research team for their valuable feedback and insights.

Without taking an oversight, my profound appreciation goes to the University of Nottingham Ningbo China for the rare privileged support during my years of studies. In addition, I must appreciate my home University where I currently hold an appointment as a Lecturer; Adekunle Ajasin University for allowing to me proceed on study in China on an unpaid leave.

I would like to express my sincere gratitude to my wife for her dexterity especially for over a year when I left her in Nigeria before joining me in China.

Finally, my appreciation goes to all those who have directly or indelicately supported me throughout the completion of my doctoral research studies at the University of Nottingham, Ningbo China; my parent, my family, Church, friends and well-wishers for their unwavering support and encouragement.

This academic feat would not have been possible without the contributions of all those mentioned, and for that, I am truly thankful.

Table of Contents

List of Tables

List of Figures

List of Abbreviation

m_e	Harvester model effective mass
η	Perturbation scaling parameter
β	Nonlinear stiffness parameter
k	Linear stiffness
m_{Tip}	Tip mass
L	Cantilever beam length
T	Cantilever beam thickness
W	Cantilever beam width
ω	Driving frequency
ω_n	Resonance frequency
ζ_{eq}	Total damping in the system
F	Excitation amplitude
F_r	Coulomb frictions in the system
$Y(t)$	Response amplitude in the temporal coordinates
$Y_{Backbone}$	Backbone response
ζ_m	Mechanical damping ration
ζ_{coil}	Redefined electromagnetic damping ratio
c_m	Mechanical damping coefficients
N	Coil turn number
K	Coupling coefficient of coil-magnet configuration
R_l	External load resistance

R_c	Internal resistance of the coil
l_c	Effective coil length.
K	The coupling coefficient
b	The flux densities in the magnet-coil transducer
B	The normalized flux densities in the magnet-coil transducer
c_f	The coil fill factor.
δ	The phase difference
K_s	The critical coupling strength
c_w	Coil width,
l_m	Magnet length
t_m	Magnet width
h_m	Magnet thickness,
D_m	Separation distance between the symmetric magnets
c_d	Clearance distance,
t_s	Width of the flux guiding steel.
B_r	Remanence field
β_{eq}	The magnetic flux density per unit volume
$\overline{\beta_{eq}}$	The normalized magnetic flux density per unit volume
$L_T,$	The length of the model
$w_T,$	The width/thickness of the model
h_c	The height of the model

c_l	The dynamic clearance between the symmetric half magnet and central transducer coil.
J	Current field density
H	Magnetic field density
μ_p	The permeability of the magnetic material
d_m	Maximum coil wire diameter including insulation
A_{eff}	Effective area occupied by the coil
A_T	The total area of coil slot and liner
A_I	The cross-section area of the slot insulation with the slot liner
w_s	Thicknesses of the flux convergent steel
w_{s-con}	Thicknesses of flux feedback/leakage guide steel
w_c	Thickness of the coupled coil
w_m	Thickness of transduction magnet.
w_a	Thickness of air spaces between the symmetric transduction magnets.
F	Damping force
$\dot{z}$	The velocity of oscillation
c_{loss}	The loss constant
W	The electromagnetic energy loss
P_{coil}	The total electromagnetic power loss
W_h	Hysteresis energy losses
W_{cl}	Classical energy losses

W_{ex}	Excess energy losses
P_{Fe}	Ferromagnetic power loss
P_h	Hysteresis power losses
P_{cl}	Classical power losses
P_{ex}	Excess power losses
ζ_{cop}	Coil winding damping ratio,
ζ_h	Hysteresis damping ratio
ζ_{ex}	Excess damping ratio
v_{out}	Harvested Voltage
P_{out}	Harvested Power
ϱ	Energy Harvesting Efficiency
W_0	Total strain energy
D_0	The total damping energy
ϵ	The loss factor
V_T	The total volume of the magnet transducer
σ_f	Fatigue stress level
σ_c	Linear critical stresses
σ_{nl}	Nonlinear critical stresses
σ_{max}	Maximum linear stress
N_s	The number of cycles
z	The Basquin stress exponent
Δt	Operational lifetime

x_1	Responses of masses in the first degree of freedom
x_2	Responses of masses in the second degree of freedom
m_1	Masses of the first DOF
m_2	Masses of the second DOF
F_{r_1}	Coulomb friction of the first DOF
F_{r_2}	Coulomb friction of the second DOF
ω_1	Natural frequencies if the first DOF mass
ω_2	Natural frequencies if the second DOF mass
$[\mathrm{M}_i]$	Mass matrices of 2DOF system
$[\mathrm{c}_i]$	Viscous damping of 2DOF system
$[k_i]$	Stiffness of 2DOF system
$[F_i]$	External force matrices of 2DOF system in the ith DOF
c_{dyn}	Dynamic load capacity
μ	The coefficient of friction
V_{coil_i}	Voltage harvested in the i^{th} DOF.
P_{coil_i}	Power harvested in the i^{th} DOF.
R_{c_i}	Internal resistance of the i^{th} DOF
R_i	Load resistance of the i^{th} DOF
ζ_{e_i}	Electromagnetic damping ratio the i^{th} DOF
i_i	Current induced in the circuit.
V_A	Actual practical volume of the harvester during operation

L_A	Actual practical length of the harvester during operation
T_A	Actual practical thickness of the harvester during operation
W_A	Actual practical width of the harvester during operation
R_l^{opt}	Optimum load resistance
NP_D	Normalized Power density
X_T	The length of the beam on the LHS of the pivot lying between the central pivot and the smaller pivots
X_R	The total length of the lever to the right side of the central pivots
X_L	The total length of the lever to the left sides of the central pivots
m	The mass of the beam portion of length from the LHS end to the the smaller bearing on spring
m_2	mass of the beam portion of length X_T
M_2	mass of the clamp supported on the smaller bearing on the spring
M_{2G}	the effective lumped mass from the bearing holder, guiderail block, and bearing pin
m_1	effective mass of the beam of length X_R
M_{Tip}	the mass of the coupled tip mass
M_{coil}	the mass of the transduction coil
$X_{cog-Coil}$	the center of mass of the coil along x-axis

V	potential energy of lever design
T	kinetic energy of lever design
F_s	damping force of lever design
ϵ	Lever ratio X_R to X_L
ν	Lever ratio X_T to X_L
ζ_T	Total damping ratio of lever design

Abbreviation

VEH	Vibration Energy Harvester
3D	Three dimensional
2DOF	Two-degree-of-freedom
AV	Alternating voltage
DAQ	Data acquisition
FEMM	Finite element magnetic
IoT	Internet of things
MDOF	Multi-degree-of-freedom
NdFeB	Neodymium Iron Boron
PVC	Polyvinyl chloride
SDOF	Single-degree-of-freedom
SHM	Structural health monitoring
PEEK	Polyether ether ketone
LHS	Left Hand Side
RHS	Right Hand Side

List of Publications

Some of the research related to this thesis have been published in or submitted to peer reviewed journals and conferences. A total of ten (10) publications in both peer reviewed journals and conference proceedings as enumerated below are published.

The nomenclatures and style of presentation in this thesis may differ slightly from the publications but the results are however, the same.

Journals.

1) T. I. Toluwaloju, C. K. Thein, D. Halim, and J. Yang, “Dynamic responses of the 2DOF electromagnetic vibration energy harvester through different electrical coil connections,” Mech. Syst. Signal Process. vol. 184, no. March 2022, p. 109709, 2023.
2) Toluwaloju, T.I., Thein, C.K. & Halim, D. (2024). Near resonance vibration isolation on a levered-dual response (LEDAR) Coulomb-damped system by differential preloads/offsets in linear springs. Appl. Math. Mech.-Engl. Ed. 45, 1033–1050..

Conference.

1) T. I. Toluwaloju, C. Thein, and D. Halim, “A novel redefined electromagnetic damping equation for vibration energy harvester,” in International Conference on Electrical, Computer, Communications and Mechatronics Engineering, ICECCME 2021, 2021, no. October, pp. 7–8.

2) T. I. Toluwaloju, C. K. Thein, and D. Halim, “An Effect of Coupling Factor on the Power Output for Electromagnetic Vibration Energy Harvester,” in Engineering Proceedings, 2021, vol. 10, no. 1, p. 5.

3) T. Toluwaloju, C. K. Thein, and D. Halim, “Finite Element Simulation for Predicting the Magnetic Flux Density for Electromagnetic Vibration Energy Harvester †,” Eng. Proc., vol. 27, no. 1, 2022.

4) T. I. Toluwaloju, C. K. Thein, and D. Halim, “A Parametric Analysis on Performance Dependence of Electromagnetic Vibration Harvester on the Coil Position, Coil

Connection, and Magnetic Flux Density," in International Conference on Electrical, Computer, Communications and Mechatronics Engineering, ICECCME 2022, 2022.

5) T. I. Toluwaloju, D. Yadav, C. K. Thein, and D. Halim, "Investigation on the Effect of Magnetic Coupling and Power Harvested in an Electromagnetic Vibration Energy Harvester," Proc. IEEE Int. Conf. Ind. Technol., vol. 2022-August, 2022.

6) T. I. Toluwaloju, C. K. Thein and D. Halim, "Flux feedback mechanism for realizing enhanced flux density in an electromagnetic vibration energy harvester," 2023 3rd International Conference on Electrical, Computer, Communications and Mechatronics Engineering (ICECCME), Tenerife, Canary Islands, Spain, 2023, pp. 1-6, doi: 10.1109/ICECCME57830.2023.10252958.

7) T.I. Toluwaloju, Thein. C, & Halim, D. "On the Resonance/Bandwidth-Coupling Relationship of Electromagnetic Vibration Energy Harvester with a Non-Varying Magnetic Flux Density." Proceedings of the ASME 2023 Conference on Smart Materials, Adaptive Structures and Intelligent Systems. ASME 2023 Conference on Smart Materials, Adaptive Structures and Intelligent Systems. Austin, Texas, USA. September 11–13, 2023. V001T07A009. ASME. https://doi.org/10.1115/SMASIS2023-111515.

8) T.I. Toluwaloju and Thein. C, "Assessing the Efficiency of a Non-Linear Anti-Phase Motion Energy Harvester under Non-Harmonic Excitation". Submitted to 5th International conference on Vibration and Energy harvesting Application. Accepted May, 2024

CHAPTER 1: Introduction and literature review

1.0 Overview of Vibration Energy Harvesting (VEH)

Vibration energy harvesting (VEH) is a technique of harvesting power from ambient source. Energy harvesting from mechanical vibrations has gained significant attention in recent years, particularly in the development of microelectromechanical systems and self-powered sensors. These devices offer the advantage of eliminating the need for external energy storages and sources, such as batteries. Applications of energy harvesting designs can range in usage, including structural health monitoring, wearable devices, and Internet of Things (IoT) applications etc. Vibration energy harvesting has emerged as a promising technology for sustainable development, offering the potential to harness ambient mechanical energy and convert it into usable electrical power to operate sensor nodes, wearable electronics, and micro-gadgets

Energy harvesting technology has been identified to play a pivotal role in the sustainable development of our world by aligning perfectly with our collective efforts towards achieving the Sustainable Development Goals (SDG's). By harnessing ambient energy sources such as solar, wind, and kinetic (e.g., vibration motion) energy, a more sustainable environment could be attained. Most IoT devices powered by energy harvesting technologies are revolutionizing the way we interact with our surroundings. These innovative harvester designs not only provide clean energy solutions but also contribute to reducing carbon footprint and promoting eco-friendly practices. Embracing energy harvesting in sustainable development is not just a choice, it should become a shared responsibility that must be push to the boundaries of innovation and technology to create a greener, more sustainable world for all.

1.1 Towards sustainable development goals

Energy harvesting technologies is focused to attain a sustainable power generation by adopting the renewable energy innovation using variety of energy harvesting systems. Some compelling advantages or impact of such approach toward energy are sustainability initiatives, energy efficiency, clean energy solutions, environmental conservation, smart grid technology, IoT devices powered by energy harvesting, self-

sustaining systems. The driving force behind this evolving technology is to attain revolutionizing sustainability efforts worldwide toward the sustainable development goals, climate action, reducing carbon footprint and eco-friendly energy solutions.

In general, there are a total of 17 Sustainable Development Goals (SDGs) established by the United Nations as part of the 2030 Agenda for Sustainable Development. These goals were formulated to address a wide range of social, economic, and environmental challenges with the aim of promoting millennial sustainable development and improving the well-being of people and the planet. To handle the menace of environmental pollution mainly introduced in the process of energy generation for cities, vehicles and industrial application, vibration energy harvesting designs is identified to be handy to address several of the United Nations Sustainable Development Goals (SDGs). Overall, vibration energy harvesting designs contribute to multiple Sustainable Development Goals by promoting clean and affordable energy, fostering innovation in energy technology, supporting sustainable infrastructure development, and mitigating climate change as follows:

i. **Goal 7 and 9:** Affordable and Clean Energy, Industry, Innovation, and Infrastructure - By harnessing mechanical energy from vibrations, vibration energy harvesting designs can contribute to increasing access to clean and affordable energy. This can help improve the efficiency and sustainability of industrial processes and infrastructure.
ii. **Goal 11:** Sustainable Cities and Communities - Vibration energy harvesting designs can be implemented in urban environments to capture energy from sources such as traffic, machinery, or building vibrations. This can help cities reduce their reliance on fossil fuels and move towards more sustainable energy solutions.
iii. **Goal 13:** Climate Action - By reducing the need for fossil fuels and capturing ambient mechanical energy, vibration energy harvesting designs can help mitigate climate change by reducing greenhouse gas emissions and promoting the use of clean energy sources.

In the recent time, one of the fast evolving energy harvesting approaches is the vibration energy harvester. The beauty of vibration energy harvesting lies in its ability to convert ambient vibrations into usable electricity, offering a renewable and sustainable source of power. This not only contributes towards achieving sustainable development goals it also promotes a cleaner and healthier environment for all, this approach will reduce our reliance on traditional energy sources and paving the way for smarter and more efficient technologies. As different strategies continue to explore the potential of vibration energy harvesting, one of the deliberate attempts to ensuring that energy harvesting technology is embraced as a key player in shaping our sustainable future is achieved in this research through different innovative designs. This works aims to introduce different designs that could harness the power of vibrations to create a more resilient and environmentally sustainable world for generations to come. The innovative design of vibration energy harvesters opens up a world of possibilities for their implementation in various applications from powering wireless sensors in smart buildings to monitoring structural health in infrastructure projects, autonomous power generation for system and sensors in hard to reach environments, and in more subtle applications. In recent applications, different VEH has been incorporated into power management module of systems as an auxiliary power backup in case of failure in main sources thus paving the way towards a more sustainable future since vibration are always present in nature and machines.

However, despite their potential benefits, there are certain challenges that come with the implementation of vibration energy harvesting technology. First challenge is associated with limited availability and variability of vibration sources in different regions. Secondly, current vibration energy harvesting technologies still have limitations in terms of efficiency and power output, which hinder their widespread adoption. Thirdly, there is a need for standardized and scalable approaches in the design and implementation of vibration energy harvesting systems to ensure reliability and compatibility with existing infrastructure. Fourth, vibration energy harvesting faces the challenge of narrow frequency bandwidths, meaning that the harvester operates efficiently only when the excitation frequency closely matches its fundamental frequency. These challenges

highlight the need for continued research and innovation in vibration energy harvesting to overcome these limitations and fully harness its potential for sustainable development.

Recent design endeavor to mitigate the above challenge are currently undertaken such as designs of non-resonant harvester by using quasi zero stiffness (QZS) dynamics in bi-stable or tri-stable configurations, pre-buckled beams and metamaterials. These approaches has been identified as most suitable for application in real life stochastic environments. Another contrasting challenge with the use of VEH designs is those arising from integrating these harvesters into existing infrastructure without disrupting operations poses another hurdle for widespread adoption, however, recent innovation and determination have shown that these challenges can be overcome by continually refining harvester designs, optimizing implementation processes, and raising awareness about the benefits of vibration energy harvesting, especially towards a greener and sustainable world.

Most of the commercialized portably wearable devices and sensor nodes are powered using an external power source such as batteries [1]. Usage of such a conventional battery power module has some form of limitations to the continuously uninterrupted but cheap operations of the body-computer interface gadgets, wearable device, microelectronics, IoT's and sensors [2, 3]. For example, a micro-sized, and cheap power handling systems operated on battery and battery less regimes were reported in [4]. While an on-vibration kinetic harvester was reported as a device that converts normal body movements into electrical power [5], Rodriguez et al. [6] proposes a battery less power handling system as an alternative to overcoming the challenges associated with the usage of batteries to power sensor nodes. Such limitations mentioned earlier include limited lifespan of batteries, retrofitting costs when the system is domiciled in not easy to access environments thus limiting remote/virtual operations, environmental hazards associated with disposing damaged batteries etc. To overcome these challenges, energy harvesting technologies and in particular electromagnetic vibration energy harvesting which is the focus in this thesis become significant. The requirement for quick, accurate, reliable, and efficient and data communication in the last few decades has necessitated the need for a continuous and more reliable power source for sensor nodes. This defined

approach to data exchange is generally referred to as IoT such that the harvested energy can virtually/remotely power low voltage- low power systems autonomously. The concept of IoT is to enable short-ranged data exchange between machines over a common network with minimum human interaction. Asides electromagnetic vibration transduction from ambient sources, a hydro converter flow based electromagnetic based energy harvesting method using a miniature planar coil were studied [7]. The design approach for electromagnetic transduction uses a coupled permanent magnets and induction coils fixed to the tip end of the cantilever beam or mounted to a fixed free spring to form the electromagnetic vibration energy harvester considered here. When the system is set in a vibration, the induction magnets and the coils move out of phase and electric potential is induced in the coil. This induced voltage can be computed using the Faraday's law of induction. This induced voltage can be used as an alternate power supply to wireless sensor nodes and low power consumption devices. The efficient transduction of mechanical to electrical energy is only possible when the mechanical and the electric circuit of the harvester is adequately coupled [8] noting that most commercial vibration energy harvesters are designed for resonant applications [9, 10] although recent endeavor projects to achieve non-resonant applications.

Different from powering wearable electronics, some specific applications of vibration energy harvester design also include structural health monitoring (SHM). Adequate study of structural dynamic characteristic is very important as a robust method for assuring the satisfactory integrity and health monitoring because an unpredicted failure may cause devastating consequences on economic, social, and human life. To ensure and enforce safety in structural design such as bridges and rail track, availability data which characterize the in service attributes of the design are necessary. Therefore, structural health monitoring sensors are incorporated into those dynamic structure to allow for real time monitoring of their structural integrity as demonstrated by [11] using a cost-effective space division multiplexed hybrid vibration sensor used for vibration monitoring while powering a SHM device with battery power module has major limitations of continuous interruption for remote and autonomous operations [13]

Although most conventional sensors have shown limitations with their usage because they are mostly affected by electromagnetic interference and noise inclusion during analog/digital conversion [12]. A miniature and cost-effective power management system (PMS) for low-voltage electromagnetic based energy harvesters (EMEHs) operated as both battery-powered and battery less applications was reported in [14] [15]. To achieve an autonomous monitoring, an internet of things (IoT) based structural health monitoring using a customized data-logger with sensing nodes was a focus in [16].

To attain the practical usage of VEH, most dedicated usage have focused on harvesting vibration energy in trains and rail tracks to light the LED lamps for illumination in rail stations and for onboard sensor monitoring and SHM of rail tracks. In the recent time, the importance of railway in the transportation industry is steadily increasing although above 35% of the total 300,000 railway bridges across Europe are as old as 100 years. SHM of railway bridges to evaluate their structural integrity directly impacts on the reliability of the railway networks [17] as well as strategies employed to monitor bridge health against seismic and severe climatic actions [18] has been discussed. In a separate work, an analytical approach for quantifying the cost-benefit optimization using a stochastic methodology to optimally design structural health monitoring systems is proposed [19]. In general, the above endeavor in the application of VEH designs only initiated linear responses. However, recent endeavor has focused on vibration harvester designs that have a nonlinear characteristic by employing different strategies. One of such endeavor was attained using a simple pendulum to achieve a nonlinear parametric excitation. Parametric excitation is distinct from normal resonant excitation because at least one of its system parameters is modulated to be time dependent [20-21]. To initiate parametric excitations in a cantilever, the excitation is induced by the periodic modulation of certain system parameters such as the attachment of a pendulum to the tip end or usage of a tunable stopper during external vibration. In the absence of the pendulum, this design reduces to a fixed-free SDOF cantilever type harvester.

Other energy harvesting approach such as harvesting energy from ambient sources such as solar, wind, vibration and heat/temperature gradient etc., has shown prospect for continuity and effectiveness because of the high-power density in terms of electrical

conversion [13]. Different regimes of vibration harvester have been undertaken over different methods of transduction. Some notable transduction approach is piezoelectric [14], electromagnetic [15], and hybridized piezo electromagnetic [16] mechanisms. Although, research on the vibration energy harvesting is mostly focused on the harvester's resonant analysis. Unfortunately, most real time vibrations are non-sinusoidal and are time-varying, random and stochastic in nature [17-18] as they could be of a low or mid or high frequency [19]. This concerns raises interest in achieving harvester design that could harness different operational frequencies to overcome the challenges in resonant mode while enhancing the harvestable power [19]. Different approaches that have been adopted to mitigate the above concerns are generally categorized as electrical and or mechanical tuning [22-26], frequency up conversion by converting external driving frequency to resonance frequency of the component itself [27], bi-stable harvester design which introduces nonlinearity into the design by using two oppositely poles magnet to create repulsion or use of nonlinear springs as they both affected the degree of nonlinearity on the design stiffness factor [27]. Another method reported to have enhance the power harvested is the antiphase mechanism where the coil and the magnet in the electromagnetic harvester are designed to move in opposite [28]. A hybridized piezoelectric and electromagnetic harvesting to achieve increased power output through matched damping has been reported [29].

As identified earlier, the method of nonlinear energy harvester was to address one or both limitations associated with narrow bandwidth and the low harvestable power. A novel method for nonlinear structural/electrical optimization which achieve increased bandwidth by using special S-shaped cantilever beam to reduce the stiffness factor in this design was reported in [30]. Another approach to introduce nonlinearity into a harvester system is the use of parametric excitation which is distinct from most vibrational resonance excitation because at least one of its system parameters is time-dependent modulated [20-21]. Parametric resonances are initiated when the excitation frequency is twice the natural frequency and they are of two classifications [31, 32] which are the hetero-parametric type where excitation is induced by the periodic modulation of certain system parameters in response to an external vibration force and the auto-parametric type arising

from some integer ratio relationships between different natural frequencies of a multiple degree-of-freedom system [33]. Unlike directly excited ordinary resonance, parametric resonance results in an amplitude growth that does not saturate by linear damping, hence the amplitude growth can only be truncated by either physical design/excitation constraint or the onset of nonlinearity at high amplitudes [33, 34]. Parametrically excited harvester has shown prospect to improved bandwidth due to it broadened nonlinear resonant peak and the power harvested because of resulting mechanical amplification [35]. A pendulum excited parametric harvester where the pendulum is hanged on the left-hand side of lever beam can be parametrically and or non-parametrically driven was reported [34]. In parametric mode, the excitation did not reach a steady state but was rather truncated by imposing restraint which only permitted the pendulum to exhibit a maximum angular displacement of $\pm\frac{\pi}{2}\text{radians}$ on the physical design [34]. In a similarly endeavor, an auto-parametric design using two cylindrical magnets attached on both sides of the pendulum is reported in [36]. Due to the magnetic pairs on both sides of the pendulum, a parametric effect set in such that as the amplitude of the pendulum oscillation gets increased, therefore, more vibration energy of the primary structure is transferred to the motion of the pendulum and the rotary electromagnetic harvester mounted on the pendulum's pivot will harvest more energy [36].

Asides achieving harvester design in a standalone linear or nonlinear operations by modification on the mechanical parameters of the designs, a theory of electromagnetic energy harvesting highlighted by [38] suggested that by using a nonlinear magnetic coupling could likewise broaden the frequency response of the harvester while a 2DOF electromagnetic energy harvester using magnet-coil interaction as the first SDOF and spring-magnet interaction as the second SDOF in the system achieving similar goal was reported in [39].

As a summary of the above section, a highlight of challenges and most notable limitations of vibration energy harvesting technology are mentioned below.

i. **Low/Narrow bandwidth:** The bandwidth defines the range of the frequency over which the harvester could effectively operate to harvest considerable energy for

powering sensor nodes, microelectronics and not easy to access devices such as the pacemakers etc. For most reported harvester, the operational bandwidth is fixed to a value at $\frac{1}{\sqrt{2}}$ of the resonant peak value (i.e., 3dB level).

ii. **Limited harvestable power:** The purpose of energy harvesting is to engage an autonomous operation of gadgets. Every harvester design must meet the minimum power configuration of the device to which it is connected. To overcome this limitation, tunable harvesting devices employs a tuning technique to realize the tuning; tuning is a method of regulation of the value of resonance frequency and harvestable power to coincide with the resonant and minimum power requirement of the host device.

iii. **Scalability:** There is a need for standardized and scalable approaches in the design and implementation of vibration energy harvesting systems to ensure reliability and compatibility with host infrastructure. This targets to achieve a high power density output in small designs volume.

iv. **Availability and variability of vibration source:** Availability of vibration source in a consistent and non-stochastic manner has severely compromised the rate at which this technology has evolved. This challenge severely affected the magnitude of harvestable power as identified in **ii** above.

1.2 Research question

As mentioned in the previous section, the challenges identified that affected the technology of vibration energy harvesting are enumerated. This research work will be focused on solving one or more of these identified challenges. Focusing on the electromagnetic and mechanical characteristics of the vibration harvester, a generalized research question asked in this work is given below:

What effect does the coupling parameter and different design mechanism/ parameters and stress initiated non-linearity have on the bandwidth and harvested power output of an electromagnetic vibration energy harvester?

To answer this research question, the study focuses on the several design approaches while studying their various complexities uniqueness and functionalities by leveraging

analytical and experimental approaches alongside relevant mechanical and electromagnetic software for improved harvesting/bandwidth functionalities.

1.3 Proposed vibration energy harvester (VEH) designs

This work proposed three different harvester designs as follows.

1.3.1 Cantilever design in linear and nonlinear operational modes

This is the Single degree of freedom (SDOF) cantilevered harvester. The performance characterization is undertaken both linear and nonlinear operational modes. These stages of analysis will independently establish a functional equation for predicting the stress-damping relation in the linear and nonlinear modes. The nonlinear stress in the cantilever beam is activated when the stress approached approximately 80.00 % of the fatigue level while stress below 80.00 % of the fatigue level is the linear operational mode. As a follow up, the above shall be use to effectively characterize the harvester performances in both modes.

1.3.2 Two Degree of freedom VEH

A two-degree-of-freedom (2DOF) vibration energy harvester is a device that can convert mechanical vibrations into electrical energy using a system that responds in two but mutually inclusive degree of freedom. This design typically consists of two transducer coil connected over springs in two independent DOF. When the device is subjected to vibrations, the two coils oscillate relative to each other within transduction magnet. This effect causes electrical energy to be induced in the coil through the process of electromagnetic induction. The performance analysis of the 2DOF designs is undertaken using three different connection modes of the coil over the external load resistances as individual, in-series, and in-parallel configurations. Such approach was taken to identify the most suitable mode for usage because different sensor nodes have different power, current and impedance ratings and the optimum load associated with each connection mode differs.

1.3.3 Levered, Coulomb damped VEH

This stage realizes an approach which attains either a simultaneous or standalone near resonance vibration isolation and energy harvesting on levered-dual response

mechanism through differential preloads/offsets in springs. Different level of preloads in the spring will activate a varying level of isolation or energy harvesting or both as a function of different design parameters such as the lever ratio.

1.4 Principles of energy harvesting

Due to increasing focus in the attempt to achieve sustainable energy sources, the global energy harvesting market is experiencing significant growth. The Europe market is the largest revenue holder globally at 1.1 Billion Dollars in 2022. With a compounded annual growth rate (CAGR) of 8.80 %, a forecast to reach 2.6 Billion Dollars in 2030 as Asia market overtakes the Europe market [21]. To harness the full potential of the energy harvesting architecture, a generalized principle is adopted. The general guiding law that summarizes the process of capturing and storing energy from the environment to power electronic devices is regarded as the energy harvesting principles. The basic principles involved in energy harvesting are summarized as following as shown in Fig 1.1.

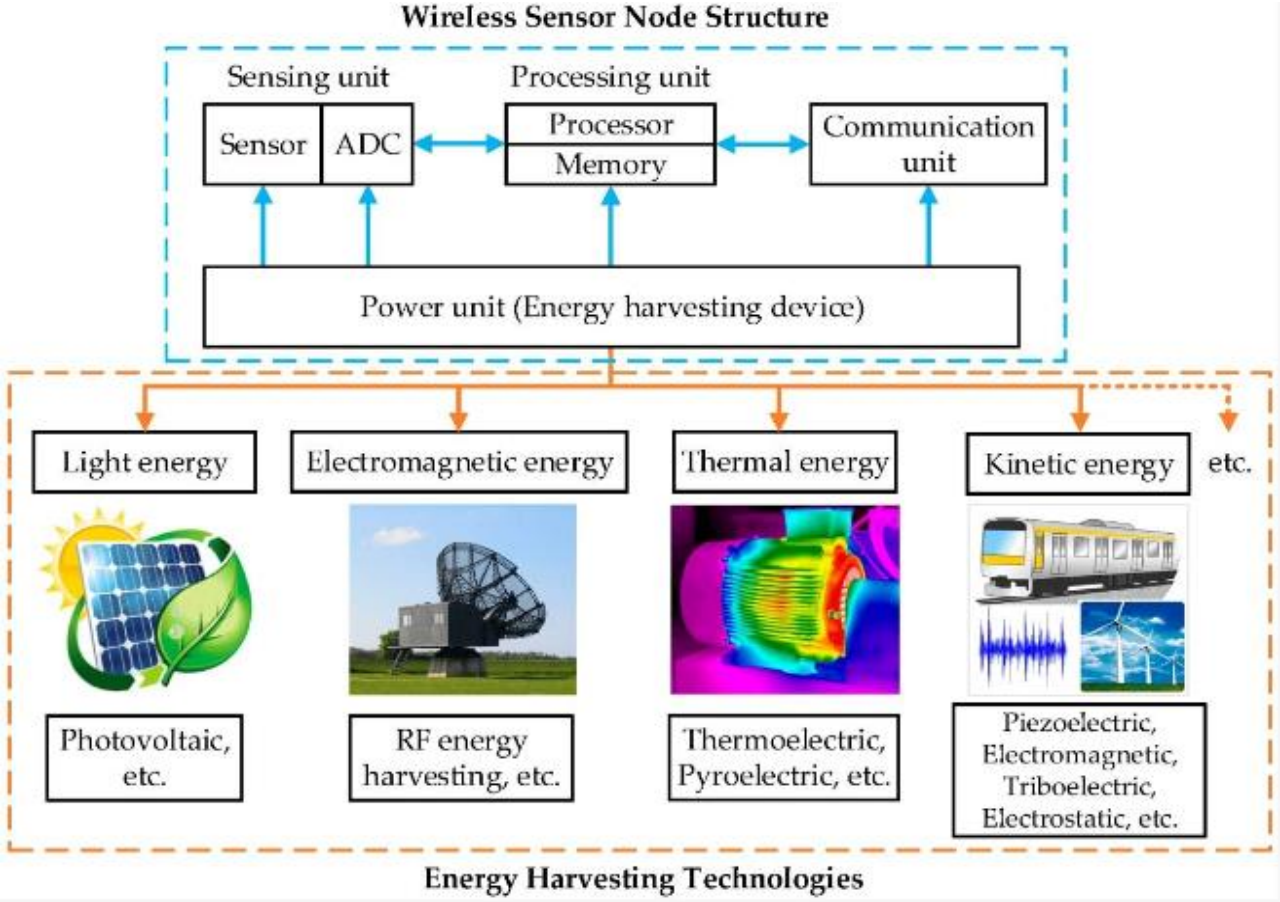

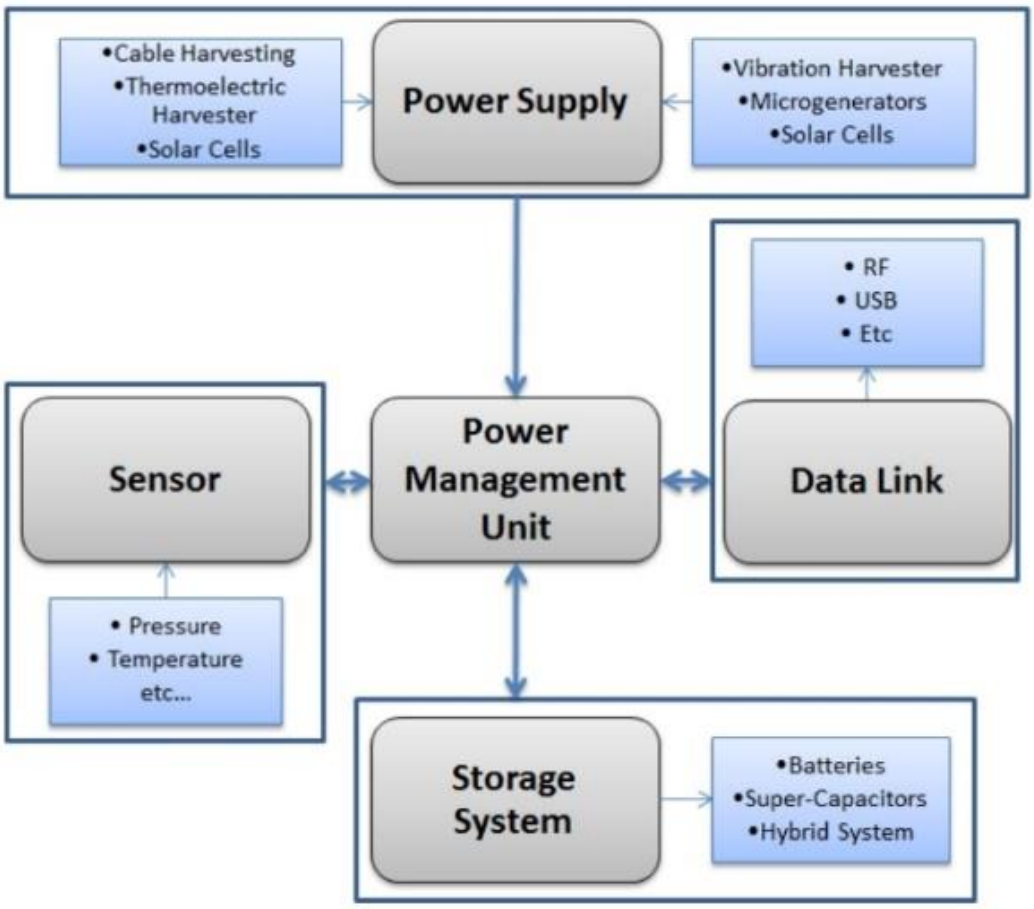

Figure 1.1 Summary of principles of energy harvester system [25] (top) and typified layout of autonomous wireless sensor nodes (bottom)

The assembled sub module team up to form an identified energy harvester principle is summarized as follows. By following these principles, energy harvesting systems can provide a sustainable and renewable source of power for various electronic devices, especially in applications where traditional power sources are not feasible or practical.

i. **Energy Source**: Energy can be harvested from various sources such as solar radiation, vibrations, thermal gradients, and radio frequency signals.
ii. **Transducer**: A transducer is used to convert the energy from the source into electrical energy. Common transducers include solar panels for converting light into electricity, piezoelectric materials/electromagnetic designs for converting

mechanical vibrations into electricity, and thermoelectric generators for converting temperature differences into electricity.

iii. **Power Management Circuit**: The power management circuit is responsible for regulating the harvested energy to match the requirements of the electronic device. It may include components such as voltage regulators, buffers, energy storage devices (e.g., batteries or super capacitors), and power conditioning circuits.

iv. **Energy Storage**: Energy harvested from the environment is often intermittent and variable. Energy storage devices like batteries or super capacitors are used to store excess energy for later use when the energy source is not available.

v. **Efficiency Optimization**: To maximize the efficiency of energy harvesting systems, it is essential to design the system to match the characteristics of the energy source and the power requirements of the electronic device. This may involve optimizing the transducer design, power management circuitry, and energy storage system.

The energy sources and the transduction principle studied in this work are the vibration sources and the electromagnetic transduction principle respectively. Taking advantages of vibrations generated during motion or other sources, Fig. 1.2 shows the summary of potential applications and usage of energy harvester architectures.

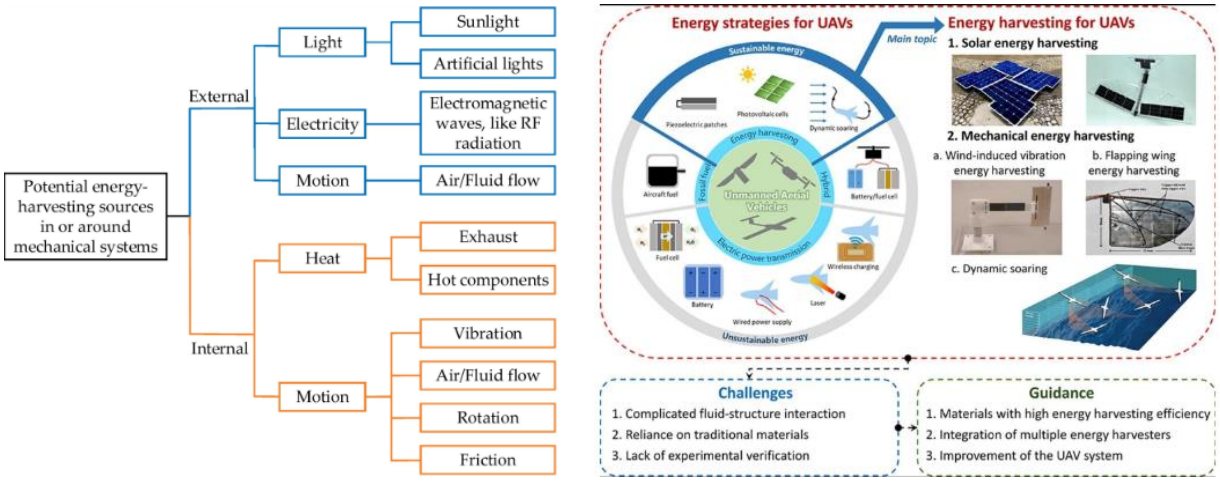

(a) (b)

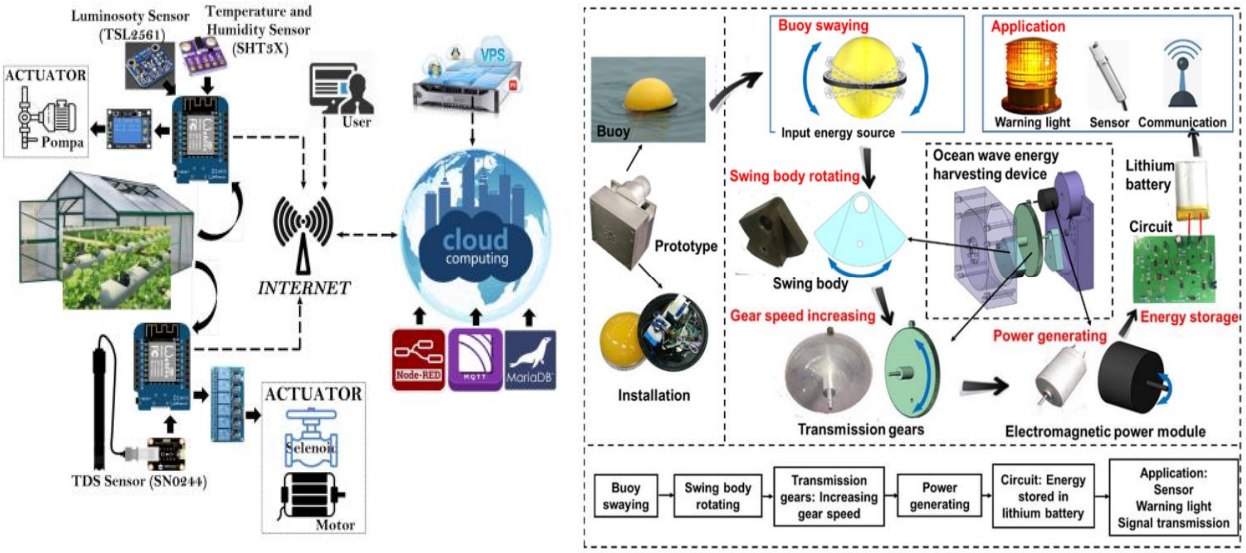

Figure 1.2 Summary of principles of energy sources in mechanical system(a) energy harvesting strategies for UAV applications [26] (b), energy harvesting strategies for smart agriculture (c) and ocean wave energy harvester driven by an efficient swing body towards the self-powered ocean buoy application [37](d)

1.5 Generalized architecture of a Vibration Energy Harvester (VEH).

The generalized architecture of a VEH can be categorically divided into mechanical and electromagnetic parts. Each identified parts has a set of generalized equations that govern their performances and can be independently described using the laws of mechanical vibrations and electrical circuits.

A. **Mechanical equations**: The equations of motion for the mechanical system describe the dynamics of the masses, springs, and dampers in the harvester and the excitation frequency. The motion of the masses can be described using differential equations that account for the displacements, velocities, and accelerations of the masses.

B. **Electrical equations**: The electrical circuit equations describe the equations that governs the conversion of mechanical energy into electrical energy. These equations typically involve parameters such as resistance, capacitance, and inductance and are related by relevant equations for circuit theory such as Ohm's law, voltage and current division laws, mesh/nodal analysis etc.

1.5.1 Transduction methods in vibration energy harvesting technology.

Transduction methods for vibration energy harvesting technology refer to different methodologies that are adopted to convert mechanical vibrations into electrical energy. The commonly adopted methods of transduction that are used in vibration energy harvesting devices are following:

i. **Electromagnetic transduction method**: This method of transduction uses the mechanical vibrations to move a magnet within a coil, coil within a magnet or both coil and magnet in relative motion. This relative motion cases an electric current to be induced in the coil through electromagnetic induction. This method is widely used in vibration energy harvesters due to its simplicity, efficiency and relatively high energy density compared to other methods of transduction. Factors such as size of the magnet, coil designs/size, and the magnetic flux are critical features to determining the power density of the electromagnetic transducer. Chapter 2 of this report gives a detail analysis on how each of this parameters affected different aspect of the electromagnetic transduction.

ii. **Piezoelectric transduction method**: Piezoelectric transduction method convert mechanical stress in various part of the piezoelectric materials such as lead zirconate titanate and zinc oxide to generate an electric charge. When subjected to vibrations, the piezoelectric material deforms, creating an electric potential that can be harvested as electrical energy. Piezoelectric transducers are commonly used in small-scale vibration energy harvesters for low-power applications. Transduction via piezoelectric configurations can achieve a relatively high energy density due to the direct conversion of mechanical stress into electrical charge over a smaller volume. Generally, their energy densities are affected by piezo material properties, resonance frequency, and geometry/volume.

iii. **Triboelectric transduction method**: Triboelectric transduction utilizes the triboelectric effect, where materials generate an electric charge through frictional contact and separation. Static electricity that is generated when two objects are rubbed against each other such that during vibration, an electric charge is generated, which can be harvested as electrical energy in triboelectric material.

Triboelectric transduction is useful for converting low-frequency and irregular vibrations into electrical power.

iv. **Capacitive/Electrostatic Transduction method**: Capacitive transduction involves using variable capacitors that change their capacitance in response to mechanical vibrations. This is a concept of electrostatic conversion involving the use of a variable capacitor that consist of two conducting plates separated by air, vacuum or a dielectric material. When the two conductors move relative to each other, the energy stored in the capacitor varies resulting in an electrical charge. Likewise, capacitive transducers are suitable for low-frequency vibration energy harvesting applications.

1.6 Some practical applications of energy harvesting in low-powered devices

The concept of energy harvesting have been studied. Several practical applications of this concept have been developed in powering low-powered devices in the following areas

1.6.1 Automotive industry

The term automotive in this context covers land, air and sea vehicles: both manned and unmanned. Vibration energy harvesters are employed in automotive applications to harvest vibrational energy from vehicle chassis, vehicle suspension, engine mounts. This harvested vibration are then converted into electrical power. This energy can be used to power onboard sensors, monitoring systems, and wireless communication devices. This effort reduces the vehicle's overall energy consumption by limiting dependence of onboard sensors on conventional energy sources such as batteries and alternators. Other applications in automotive industry include harvesting energy from vibrating train tracks to power signal lights and switches [83], UAV applications [26] and marine vehicles [37].

1.6.2 Industrial Monitoring Systems

Vibration energy harvesters can be integrated into industrial equipment and machinery to power monitoring systems, predictive maintenance sensors, and condition monitoring devices. This enables real-time data collection and analysis, leading to improved operational efficiency and reduced downtime.

1.6.3 Structural health monitoring

Structural health monitoring (SHM) plays a crucial role in the prevention of failures in civil structures and infrastructures. Vibration energy harvesters can be used in civil engineering applications to monitor the structural health of buildings, bridges, and infrastructure. By harnessing vibration energy from ambient vibrations that are naturally occurring in these building and infrastructure via energy harvester design, structural health monitoring sensors that detect structural defects, cracks, and deformations can be powered autonomously. This approach enables early detection and prevention of potential hazards by encouraging real time health data transfer and analysis for those structures.

1.6.4 Wearable electronics/body computer interface, e.g. electric wristwatches

While most wristwatches are powered by a small lithium battery [1], vibration energy harvesters can be integrated into wearable smartwatches, fitness trackers, and medical monitoring devices to harvest energy from human motion and vibrations [4]. This eliminates the need for frequent battery replacements and extends the device's operational lifespan [6]. Another wearable application is in medics using a pacemaker that requires an input supply of approximately 1.0 μW to operate.

1.6.5 Wireless sensor network

An array of sensor network usually consists of a large number of sensor nodes, which makes it costly in terms of wiring or battery usage. Hence, many micro-sized energy harvesters have been proposed and deployed in remote or hard-to-reach locations where traditional power sources are not feasible to power the sensor nodes. Vibration energy harvesters can power wireless sensor nodes used in environmental monitoring, industrial automation, structural health monitoring, and smart infrastructure applications.

1.6.6 Internet of Things (IoT) Devices

Vibration energy harvesters have been applied to operate low-power IoT devices such as smart home sensors, environmental monitoring systems, and asset tracking devices [2, 3]. By harvesting energy from ambient vibrations, these devices can operate autonomously without the need for external power sources.

1.7 Research objectives

Since VEH technology been identified as an alternate approach to generate electrical energy that could sufficiently power microelectronics and wireless sensor nodes. One probable implication of such engineering adventure on the energy sector is driving it towards sustainable energy developments. Therefore the main objectives of this thesis are as follows:

I. To investigate and analyze the performance of the electromagnetic energy harvester using system design at high coupling coefficient because the degree of coupling in the mechanical to the electrical part of the VEH will significantly affect the amount of power and voltage harvested.
II. To consider how different coupling material, electromechanical parameters, geometry and orientation of the coil-magnet transducer affected voltage and power behavior of the VEH.
III. To study the VEH performance using a 2DOF designs at different load resistance connection modes for maximizing the power harvested.
IV. To presents and analyses design that attain simultaneous harvester-isolation mechanism using levered coulomb damped system.
V. To characterize, and predict the stress-damping relationship of the linear and non-linear polymeric or non-polymeric material in the VEH system.

1.8 Thesis overview, contributions and scope

Towards attaining sustainable environments, vibration energy harvesters are innovative, and they can successfully convert mechanical vibrations into electrical energy, offering a sustainable and environmentally friendly solution for powering small electronic devices. These devices utilize the principle of electromagnetic induction or piezoelectric effect to capture and convert ambient vibrations into usable electrical power. By harnessing ambient mechanical energy from various sources such as machinery, vehicles, and human motion, vibration energy harvesters have the potential to extend the battery life and enhance the autonomy of wireless sensor networks, wearable electronics, and other low-power applications. This thesis highlights an overview of the principles, design considerations, and applications of vibration energy harvesters, highlighting their

significance in the field of energy harvesting and their promising role in advancing the development of self-powered systems. The summary of this thesis is illustrated in a flowchart shown in Figure 1.3.

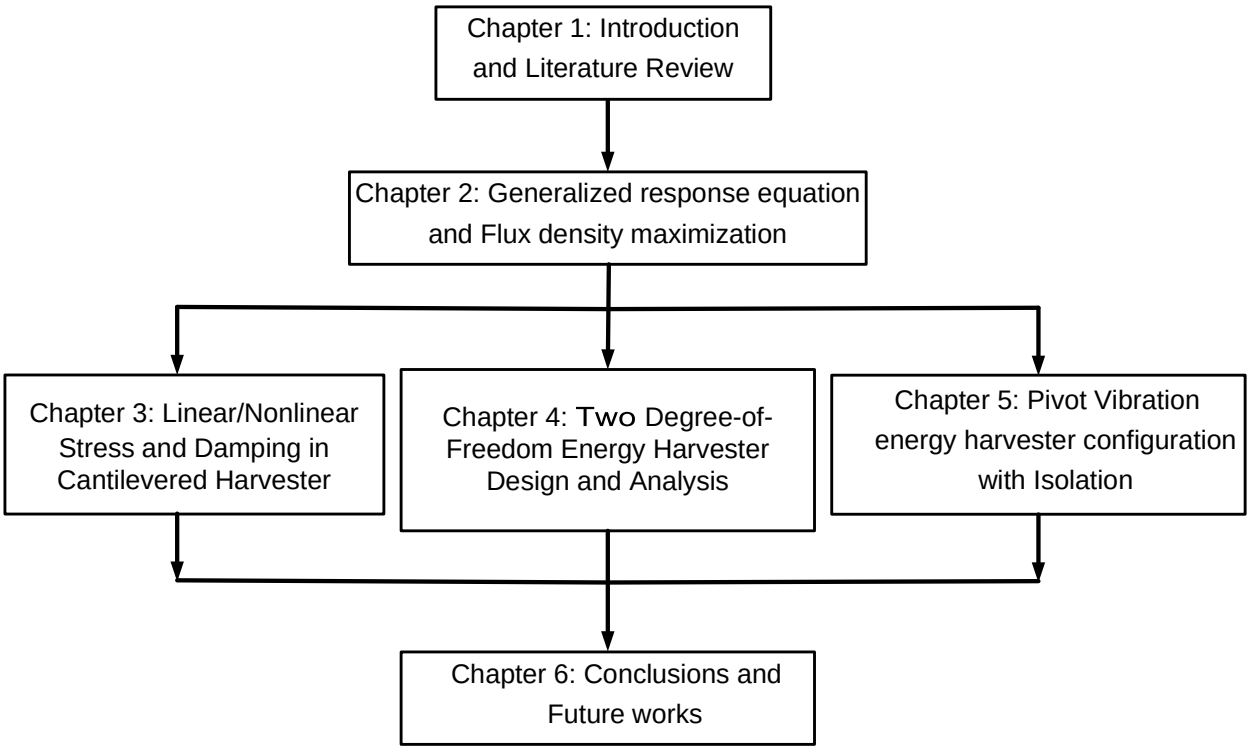

Figure 1.3 Thesis overview and flowchart

CHAPTER 2: Generalized response equation for a vibration energy harvester

2.0 Generalized architecture of vibration energy harvester

As identified earlier, a vibration energy harvester is a device that converts mechanical vibrations into electrical energy. Design considerations for vibration energy harvesters include the selection of appropriate materials for the transducer, optimizing the mechanical structure for maximum energy conversion and efficiency as well as tuning the harvester to resonate at the frequency of the ambient vibrations. By efficiently coupling the mechanical and electrical part of the harvester, a promising solution for powering low-power electronics and equipment in remote or hard-to-access locations is attained. This attainment provides a sustainable and environmentally friendly alternative to traditional power sources. The generalized architecture for an electromagnetic energy harvester is a spring-mass configuration shown in Fig 2.1 with transduction mechanisms and power management modules.

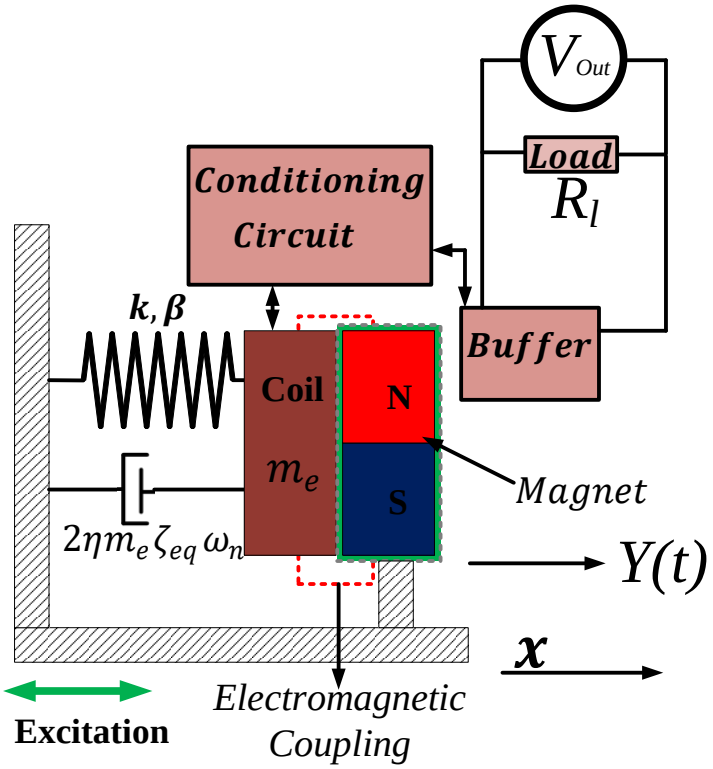

Figure 2.1 Generalized harvester design

Considering that the responses of a vibrational energy harvester design could be linear or nonlinear, the generalized equation that characteristically captures the linear and nonlinear performances is summarized as shown in Eq. (2.1).

$$m_e\ddot{Y}(t) + 2\eta m_e\zeta_{eq}\omega_n\dot{Y}(t) + kY(t) + \eta\beta Y(t)^3 \pm F_r sgn\left(\dot{Y}\right) = m_e\omega^2 F cos(\omega t) \quad (2.1)$$

where $m_e, \eta, \beta, k, \omega, \omega_n, \zeta_{eq}, F, F_r$ and $Y(t)$ are the model effective mass, nonlinear perturbation scaling parameter, nonlinear stiffness parameter, linear stiffness, excitation frequency, resonance frequency, total damping in the system, excitation amplitude, Coulomb frictions in the system and the response amplitude in the temporal coordinates.

It is important to note that the generalized governing equation are tunable by imposing certain design constraint on Eq. (2.1) as follows to achieve either linear or nonlinear applications.

1. The responses are linear if and only if $\beta = 0$, and $\eta = 1.00$.
2. The responses are nonlinear if and only if $\beta \neq 0$, hence scaling parameter $\eta \ll 1$.
3. When the harvester design has no frictional damping component, $F_r = 0.00$ N.

During dynamic testing, input vibration is transferred to the inertia mass of the model via the spring. Depending on the nature of the designs, the vibrational input force is either amplified or attenuated as linear or nonlinear. Although a generalized characterization showed that in the nonlinear mode, the response profile considerably improved the operational bandwidth compared to linear configurations [37].

To obtain the generalized solution to Eq. (2.1), the amplitude responses and the phases are derived using the harmonic balance method and plotted as a frequency response. The harmonic solution is obtained by assuming a steady state solution with harmonic terms as shown in Eq. (2.2).

$$Y(t) \cong Y_h(t) = \sum_{n=0}^{M} Y_n cos(n\omega t + n\varphi) \quad (2.2)$$

Substituting the first harmonic from Eq. (2.2) into Eq. (2.1) and equating the coefficients of $\cos(\omega t)$ and $\sin(\omega t)$ gives the frequency responses (Y) and the phases (δ) equations as shown in Eqs. (2.3) and (2.4).

$$\left(Y_n - r^2 Y_n + \frac{3\varepsilon}{4\omega_n^2}\beta Y_n^3\right)^2 + \left(2\eta\zeta_{eq} r Y_n\right)^2 = r^4 F_0^2 \tag{2.3}$$

$$\delta = \tan^{-1}\left(\frac{2\eta\zeta_{eq} r}{\omega_n^2 - \omega^2 + \frac{3\eta}{4}\beta Y_n^2}\right) \tag{2.4}$$

When $\beta = 0$ and $\eta = 1.00$ is used in Eqs. (2.3) and (2.4), the linear responses and phases of the system are correspondingly obtained. The backbone for the Duffing Eq. (2.1) shows the dependence of the nonlinear natural frequency on the amplitude of motion is obtained as shown in Eq. (2.5).

$$Y_{Backbone} = \frac{16\omega_n^2}{3\lambda}(r^2 + 2\zeta^2 - 1) \tag{2.5}$$

The Newtonian equations highlighted that each algebraically added term in the governing Eq. (2.1) is dimensionally equivalent to the Newton force. The nonlinear stiffness parameter $(\eta\beta)$ is associated with material and geometric nonlinearities in the stiffness matrix of the system, hence $\beta Y(t)^3$ is regarded as nonlinear force. Depending on the nature of the design, the stiffness matrix could be associated with spring, prebuckled cantilever, geometrical/material nonlinearity, backlashes and clearance discontinuity, nonlinear electromechanical/electromagnetic coupling etc. Using the force-stress equivalent of the nonlinear force over a unit volume of the cantilever Eq. (2.6) shows the relationship between $\eta\beta$ and force-stress equivalent for the system as shown in Eq. (2.6).

$$\eta\beta \cong \frac{\sigma_{nL}}{\delta x} \tag{2.6}$$

where β, σ_{nL}, and $\delta x \ll L$ are nonlinear stiffness, maximum nonlinear stress associated with the material nonlinearity in the cantilever during excitation, and micro extension of the cantilever beam during excitation.

In the following stage of analysis, the cantilever geometry which has the capacity to initiate material/geometric nonlinearity was used to characterize the nonlinear model in Eqs. (2.1) to (2.6) as shown in Chapter 3. During transverse vibration of a cantilever beam, geometric/material nonlinearity are initiated due to the stretching in the mid-plane when the curvature becomes too large, otherwise the response is linear.

From Eq. (2.1), the total damping in the system was represented as ζ_{eq}. This parameter is regarded as the summation of total damping energy in the harvester system. Since the energy conversion performance of electromagnetic vibration energy harvester (EVEH) is maximized by efficiently coupling the mechanical and the electrical parts, therefore, ζ_{eq} is obtained by addition of the damping contributions from the mechanical and electrical parts as shown in Eq. (2.7).

$$\zeta_{eq} = \eta(\zeta_m + \zeta_{coil}) \tag{2.7}$$

Where the expressions for ζ_m and ζ_{coil} defined as the mechanical and the electromagnetic damping ratio of the harvester design is shown in Eqs. (2.8) and (2.9).

$$\zeta_m = \frac{c_m}{2\mathrm{m}_e\omega_n} \tag{2.8}$$

$$\zeta_{coil} = \frac{8K^2{l_c}^2}{2\mathrm{m}_e\omega_n}\left(\frac{1}{R_l + R_c}\right) \tag{2.9}$$

The coupling coefficient K is defined as the number of flux line that cuts the coil is defined as shown in Eq. (2.10), where b and c_f are the flux density and the coil fill factor [40].

$$K = Nbc_f l_c \tag{2.10}$$

From Eqs. (2.8) –(2.10), $c_m, N, K, R_l, R_c,$ and l_c are the mechanical damping coefficients, coil turn number, coupling coefficient of coil-magnet configuration, external load resistance, internal resistance of the coil, and effective transduction coil length.

2.1 Flux density maximization, Electromagnetic damping and Power Equations

During harvester design, it is important that the mechanical part couples well with the electrical part to ensure high and efficient energy conversion [19]. The harvester property which determines how the mechanical and electrical parameters couples for effective performances is referred to as the coupling constant (K) as shown in Eq. (2.10). The flux density is typically measured in units of Tesla (T) or Gauss (G). Therefore, to design the magnetic and coil circuit, the flux density distribution in any harvester transducer design can be enhanced by choice of appropriate sizes and dimensions for the coil and magnets. To maximize the flux density of a vibration energy harvester, several key design considerations such as choosing the right magnetic material such as magnet with high

magnetic permeability and low hysteresis losses are important. Also, different magnetic circuit consideration such as shape and arrangement of magnets/magnetic components, design of the coil or winding with appropriate wire gauge, varying the distance between the magnets and the coil and the frequency of the vibrations are identified to notably impact the flux density in the electromagnetic transducer. Therefore, these properties needed to be independently taken into considerations to enhance and maximize the magnetic flux for improved harvesting performances. By independently taking the above flux properties into consideration, four different procedures for measuring the coupling coefficient of electromagnetic vibration energy were adequately presented [40]. Additionally, a theoretical and numerical approach for quantifying the degree of coupling was undertaken. While a two-stage coupling optimization of electromagnetic harvester for increased power as a linear function of the coupling was presented by Foong et al. [44] and [43]. The critical coupling strength(K_s) was defined as the ratio of the squared coupling constant (K) and mechanical damping ratio. Generally, K_s is reportedly categorized as weak if $K_s < 1$, moderately coupled $1 \leq K_s \leq 10$, and strongly coupled if the critical coupling strength is $K_s > 10$ [45].

Fig. 2.2 (left) shows the coil-magnet transducer model analyzed in this work. The coil-magnet parameters are coil width (c_w), coil fill factor (c_f), effective coil turn (N), effective coil length(l_c). The single magnet dimension is shown in Fig. 2.2 (right) as magnet length(l_m), magnet width(w_m) and magnet thickness (h_m). The separation distance between the symmetric magnet(D_m), clearance distance(c_d), width of the flux guiding steel (w_s).

The total volume of the magnet transduction model was obtained as shown in Eq. (2.11).

$$V_T = L_T \times w_T \times h_c \tag{2.11}$$

$$w_T = 2(w_s + w_m + D_m) \tag{2.12}$$

$$D_m = c_w + 2c_d \tag{2.13}$$

$$h_c = 2h_m + h_a \tag{2.14}$$

where L_T, w_T, h_c, c_d and θ are the length, the width/thickness, the height of the model the dynamic clearance between the symmetric half magnet and central transducer coil and the angle at which the coil cut through the field or flux of the permanent magnet.

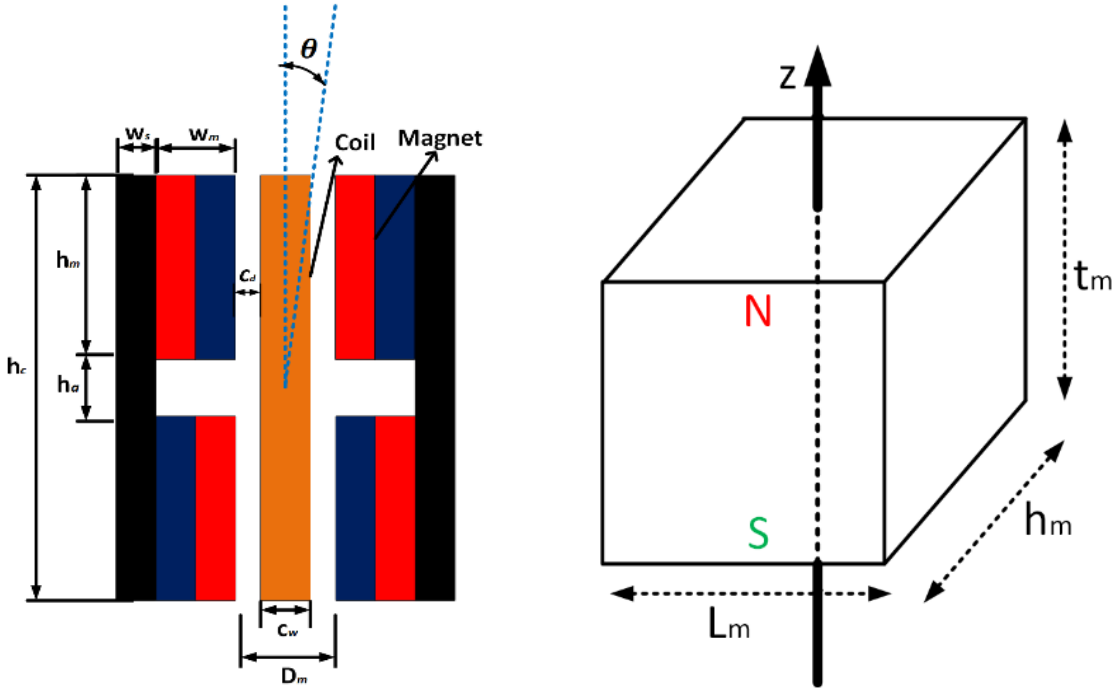

Figure 2.2 The transduction model (left), and block model for symmetric quarter magnet (right)

The effective average flux density (b) and the flux per unit volume (β_{eq}) for any given transduction coil magnet geometry of Fig. 2.2 was obtained according to Eq. (2.15) and Eq. (2.16) respectively.

$$b = \sum_{i=1}^{n} b_i \tag{2.15}$$

$$\beta_{eq} = \frac{\text{Effective average Flux Density } (\bar{b}(T))}{V_T} \tag{2.16}$$

where $n = 1, 2, 3, \ldots$ is the number of coil slots. While most literatures have considered n =1 [44, 46], this work have considered other possibilities for attaining $n > 1$ as reported in [46, 47].

From 2.2 (left), it is observed that if none of the magnetic flux couples into the coil, an approximately zero voltage is induced in the coil. Therefore, the coil materials are

carefully selected (copper in this case) to ensure that highest possible degree of coupling is realized. The selected copper wire material is wound into N turns on a nonconductive circular brace to achieve a total coil width/thickness c_w. The Maxwell theory reported that divergence and the curl of the flux density as shown in Eqs. (2.17) and (2.18) where J, H are the current, magnetic field density and μ_p is permeability of the magnetic material.

$$\nabla \cdot (\mu_p H) = 0 \tag{2.17}$$

$$\nabla \times (\mu_p H) = \mu_0 J \tag{2.18}$$

The physical meaning of Eqs. (2.17) and (2.18) asserts that for any magnetic system/magnet such as shown in Fig. 2.2, there are no isolated magnetic poles. Also, Eqs. (2.17) and (2.18) asserts that a circulating magnetic fields are produced by changing electric currents. In the eventuality of using more than one magnet, Eq. (2.17) therefore sets an order for which the transduction magnet must be aligned to allow for continuous flux linkage between the several magnets in such a manner that no pole is isolated while also giving a prediction of a non-changing flux value since external source of electric charge in the system is zero.

In the following section, different attempts to predict the variation of the flux linkages in the coil-magnet transducer when the coil-magnet geometry of Fig. 2.2 are realized in different geometry or coupling material. The fluxes are simulated using the finite element magnetic simulation (FEMM) software and the results are compared with analytical solution.

2.1.1 Flux distribution on magnet; Gauss meter versus FEMM simulation.

Before proceeding to simulate the flux density that exists between the magnet transducer geometry of Fig. 2.2 (left), an initial approach to characterize and compare the flux on a 5 mm$\times$ 10 mm$\times$ 25 mm and 15 mm$\times$ 15 mm$\times$ 1 mm magnets shown in Fig. 2.2 (right) using a Gauss meter relative to FEMM was undertaken. Using a Gaus meter, the actualized value of the flux on 5 mm$\times$ 10 mm$\times$ 25 mm and 15 mm$\times$ 15 mm$\times$ 1 mm magnets respectively measured at 0.3322 T and 0.04796 T respectively. However, the FEMM software predicted an average magnet flux density of 0.3421 T and 0.04993 T

respectively across the face marked in red line for single $25\ \text{mm} \times 10\ \text{mm} \times 2\ \text{mm}$ and single $15\ \text{mm} \times 15\ \text{mm} \times 1\ \text{mm}$ magnet are shown in Fig. 2.3 (right).

Fig. 2.3 showed that the measured value diverges from empirical value to about 4.73 %. This level of divergence is considered sufficiently accurate while Fig. 2.3 (right) shows that higher flux occurs at the edges of the magnets. Therefore, in the following analysis, results that are obtained from the FEMM simulations are acceptable to an accuracy of 95.00 %.

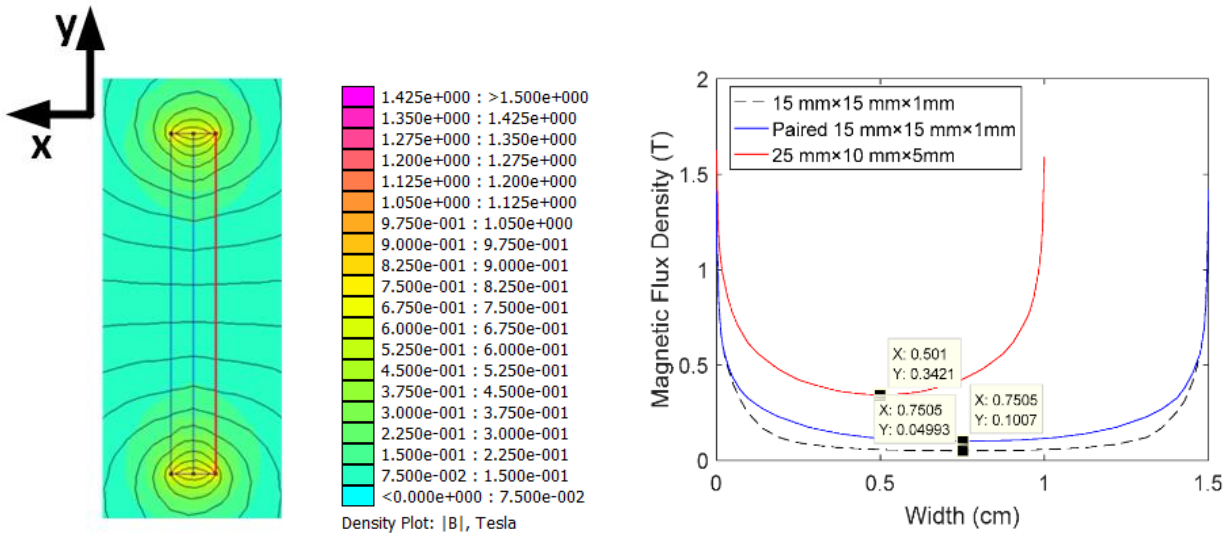

Figure 2.3 Flux density pattern from FEMM of paired 15 mm × 15 mm × 1 mm (left) and flux density line plot for different magnet arrangements (right)

2.1.2 Flux density variation with coil width (c_w)

To characterize how the flux density in the transduction coil varied with c_w, an FEMM simulation of the coil-magnet model for seven (7) coil groups using $15\ \text{mm} \times 15\ \text{mm} \times 1\ \text{mm}$ magnets was undertaken, the corresponding flux were simulated on FEMM as shown in Fig. 2.2 (left) and Fig. 2.4 (right) shows the normalized flux variation with total transducer geometry thickness.

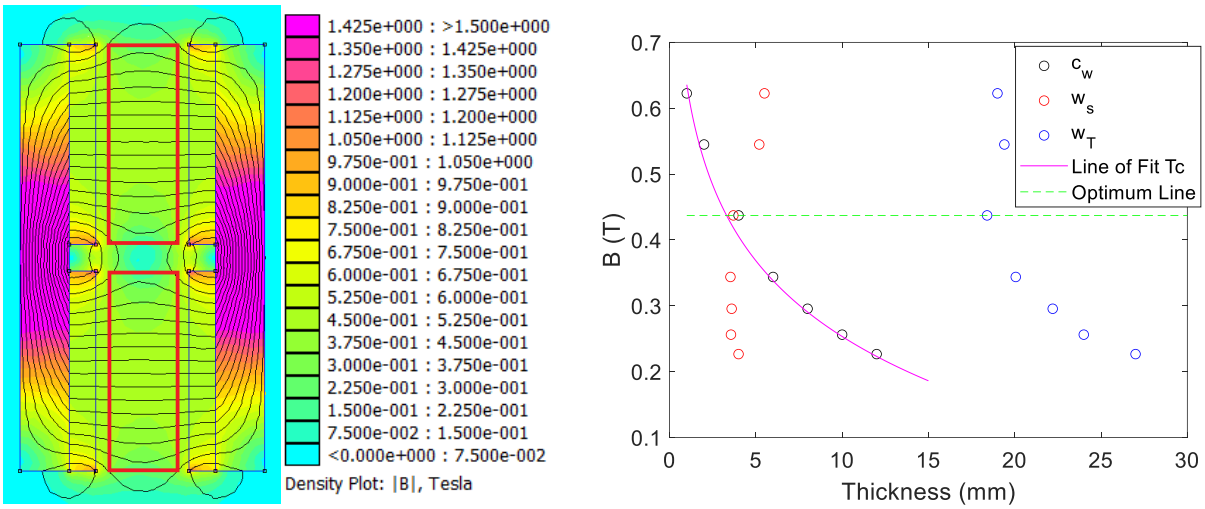

Figure 2.4 Magnet-coil simulation output on FEMM for 4 mm coil width (left), and variation of B with geometry thicknesses (right)

Generally, the magnetic flux density on any NdFeB N52 permanent magnet of known volume (V_T) was obtained as

$$b = \beta_{eq} V_T \tag{2.19}$$

where β_{eq} is the magnetic flux density per unit volume. It was obtained as the ratio of the magnetic flux density associated with each magnet geometry on the FEMM to its volume. Considering the transducer volume is variable as a function of the coil width c_w, the V_T and β_{eq} associated with configurations are therefore normalize relative to $c_w = 2.00$ mm configurations as $\overline{V_T}$ and $\overline{\beta_{eq}}$ respectively. Therefore, the normalized equation for predicting magnetic flux density in any coil geometry with volume $\overline{V_T}$ was obtained as

$$B = \overline{\beta_{eq}}\,\overline{V_T} = \overline{\beta_{eq}} c_w h_s L \tag{2.20}$$

Using the $c_w = 2$ mm as reference configuration, while keeping effective length (l_c) and packing density factor (c_f) approximately equal over different width size. To ensure that h_s remains constant as required for all coil sizes, the term N and $\bar{v}$ will approximately change with each configuration according to Eq. (2.21).

$$N_{c-i} = \mu_i N_{c-2} \ , \ i = 1, 2, \ldots n \tag{2.21}$$

where $\mu_i = (c_{w-i}/c_{w-2})$, N_{c-i} and c_{w-i} are the ratio of c_w for i^{th} coil to $c_w = 2.00$ mm, the total coil turn and width of the i^{th} coil while $N_{c-2,}$ and $c_{w-2}$the total coil turns and width of the reference coil $\mathrm{c_w} = 2.00$ mm. Also, in term of the volume ratio $\bar{V}_{c-i} = \mu_i \bar{V}_{c-2}$ also exists where Table 2.1 gives a summary of the normalized flux density (B) and respective values of flux guiding iron thickness $(\mathrm{w_s})$ coil thickness $(\mathrm{c_w})$, and total model thickness (w_T) for different design geometries.

Table 2.1 Summary of the normalized flux density (B), leakage proof iron cladding thickness $(\mathrm{w_s})$ coil thickness $(\mathrm{w_c})$, and total model thickness $(\mathrm{w_T})$ for different design geometries.

Model	$c_w(\mathrm{mm})$	$w_s(\mathrm{mm})$	$w_T(\mathrm{mm})$	N_{c-2}	$B(\mathrm{T})$	$\bar{\beta}(T\mathrm{mm}^{-3})$	$K(T\mathrm{mm})$
1	1.00	5.50	19.00	$\mu_1 N_{c-2}$	0.6226	$0.6226/(\mu_1 \bar{V}_{c-2})$	$0.5663\mu_1 l_c N_{c-2}$
2	2.00	5.20	19.40	$\mu_2 N_{c-2}$	0.5450	$0.5450/(\mu_2 \bar{V}_{c-2})$	$0.4957\mu_2 l_c N_{c-2}$
3	4.00	3.70	18.40	$\mu_3 N_{c-2}$	0.4373	$0.4373/(\mu_3 \bar{V}_{c-2})$	$0.3978\mu_3 l_c N_{c-2}$
4	6.00	3.53	20.06	$\mu_4 N_{c-2}$	0.3438	$0.3438/(\mu_4 \bar{V}_{c-2})$	$0.3127\mu_4 l_c N_{c-2}$
5	8.00	3.60	22.20	$\mu_5 N_{c-2}$	0.2955	$0.2955/(\mu_5 \bar{V}_{c-2})$	$0.2688\mu_5 l_c N_{c-2}$
6	10.00	3.56	24.00	$\mu_6 N_{c-2}$	0.2562	$0.2562/(\mu_6 \bar{V}_{c-2})$	$0.2331\mu_6 l_c N_{c-2}$
7	12.00	4.00	27.00	$\mu_7 N_{c-2}$	0.2267	$0.2267/(\mu_7 \bar{V}_{c-2})$	$0.2062\mu_7 l_c N_{c-2}$

Using Eq. (2.20), Eq. (2.10) was re-formulated as shown in Eq. (2.22).

$$K = \overline{\beta_{eq}} \vartheta N \overline{V_T} \tag{2.22}$$

Where, ϑ was obtained as the product of the fill factor (c_f), and effective length (l_c). Fig. 2.4 (left) shows a plot of variation of the flux measured on different coil geometry with thicknesses of different components of the model. From Fig. 2.4 (right) a line of fit and fit equation between B and the coil thickness (c_w) is shown in Eq. (2.23).

$$B = -0.166 \ln c_w + 0.6357 \tag{2.23}$$

From Eq. (2.10), (2.21) and (2.23) an empirical relation between the magnet flux density per unit volume of the transduction coil was obtained as shown in Eq. (2.24). Eqs. (2.23)

and (2.24) are sufficient to make a prediction of the flux density and flux density per volume of a coil on any coil geometry, respectively.

$$\overline{\beta_{eq}} = (1/\overline{V_T})(-0.166 \ln c_w + 0.6357) \quad (2.24)$$

The dotted green line in Fig. 2.4 (left) shows the level of flux at which the harvester becomes thickness optimized in term of the flux density (b) and degree of coupling (K).

From the forgone discussions and analysis, the following conclusions was reached

i. Since the flux is measured in the region where the coil is positioned, it is recommended that the inertial mass of the transducer should be concentrated in the coil to allow for resonant variation with little divergence from predicted values.
ii. A nonlinear relationship existed between *K* and β_{eq}. Both were respectively optimized at $0.3978\mu_3 l_c N_{c-2}$ Tmm and $0.4373/(\mu_3 \bar{v}_{c-2})\mathrm{Tmm}^{-3}$.
iii. Given any coil of known volume, it is possible to make a relatively accurate prediction of the magnetic flux density using Eq. (2.23) when such coil is placed in the field of permanent magnet that are paired and arranged as shown in Fig. 2.1.

2.2 Magnetic circuit design/Magnetic Flux Concentration Techniques

Another approach for enhancing the coupling in the coil-magnet transducer of an electromagnetic harvester is the use of magnetic circuit design that ensures magnetic flux concentration into the coil. The design of the magnetic circuit plays a significant role in determining the flux density within the electromagnetic harvester. This approach for magnet circuit/ flux guiding optimization is undertaken with two critical considerations:

i. Improve/compromise the magnetic coupling by geometrically adjusting the magnet dimension
ii. Design the magnetic circuit to minimize magnetic leakage and ensure a closed magnetic path for efficient flux transfer.

From the symmetric quarter magnet model of Fig. 2.2 (right), the formula for the flux density (b) for the symmetry axis of the axially magnetized block is given in Eq. (2.25).

$$b = 4\frac{B_r}{\pi}\left[arctan\left(\frac{L_m h_m}{2z\sqrt{4z^2+L_m^2+h_m^2}}\right) - arctan\left(\frac{L_m h_m}{2(t_m+z)\sqrt{4(t_m+z)^2+L_m^2+h_m^2}}\right)\right] \qquad (2.25)$$

where B_r is Remanence field also known as the residual induction (independent of the magnet's geometry) and $z = \frac{t_m}{2}$ is the distance from a pole face on the symmetry axis. While other terms holds their usual definitions, the numerical value of B_r is 10800 – 11200 Gauss (≅1.08 – 1.12 T) and 14000 – 14600 Gauss (≅1.40 – 1.46 T) for N30 and N50 neodymium magnet respectively. Fig. 2.5 shows the variation of the variation of b with V_T for the magnet geometry of Fig. 2.2 (left) at $n = 1.00$.

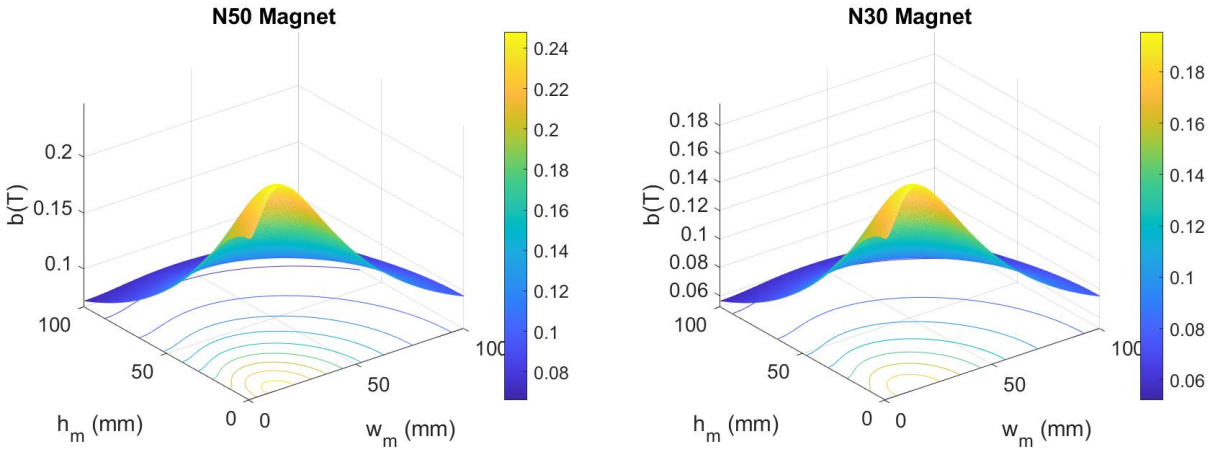

Figure 2.5 Variation of b with magnet dimension N-50 magnet (left), and N-30 magnet (right)

From Fig. 2.5, the following are concluded

a. Taking advantage of the reinforcements and cancelation of the magnetic domains, two symmetric magnets was positioned for better close circuit induction. This implies that the domain alignment results in the attractive magnetic force being always greater than the repulsive magnetic force.
b. The implication of Remanence field is that a N50 neodymium magnet will achieve a larger flux concentration than the N30 counterpart at equivalent magnet dimension with respective optimal at $w_m \cong 25.00$ mm, $h_m \cong 10.00$ mm and at $w_m \cong 25.00$ mm, $h_m \cong 8.00$ mm. Therefore, it is recommended to choose the thicknesses and widths of the transducer magnet about the values

identified above since other magnet dimension will compromise in power density and conversion efficiency as the transducer becomes bulky.

c. To prevent flux leakage during induction, the flux guiding steel width (w_s) must be chosen to have approximately equal to the magnet width (w_m), Toluwaloju et al. [47-48].
d. Incorporation of magnetic concentrators (steels) or magnetic yokes to guide and concentrate the magnetic flux towards the coil for improved energy conversion are recommended than when the spaces are air Toluwaloju et al. [48].

2.3 Coil Placement and Geometry Technique:

Another important feature for optimizing the flux linkages in the electromagnetic transducer is the consideration on the coil geometry and placement. Also, utilizing fine grade coil materials with high magnetic permeability (which reduces magnetic losses) within the magnetic field are essential for maximizing flux density are identified to be beneficial for improved coupling. To analyze how the flux density/coupling varies over different coil placement/geometries, Fig. 2.6 shows the different transducer coil wound in orthocyclic winding [51]. The implication of the different coil geometries on the flux coupling towards achieving an improved energy conversion efficiency are highlighted in the following sections.

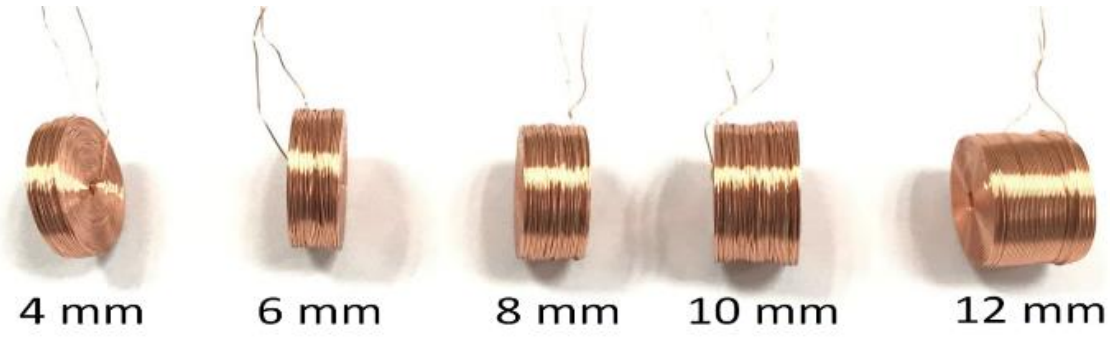

(a)

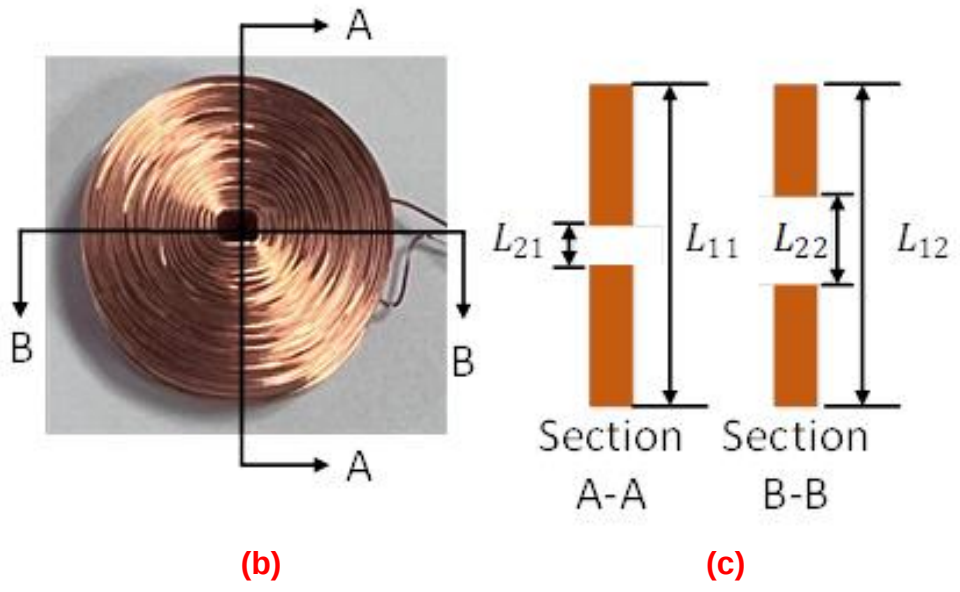

Figure 2.6 Different coil geometries (**a**), transducer coil geometry about symmetry A-A and B-B axis (**b**) and symmetric dimensioning (**c**)

Considering that the coil center is oval, therefore the packing density along the A-A symmetric half and B-B symmetric half are different. Therefore, when the coil is placed in the field of the permanent magnet, coil flux linkage and packing densities is analyzed as the average of measured values along the symmetric halves as shown in Fig. 2.6 (right). The packing density of the coil also referred to as the mechanical fill factor c_f is defined as the ratio of total wire cross-section area per slot to the effectively available slot cross-section area A_{eff} [51, 47] as shown in Eq. (2.26).

$$c_f = \frac{N*\pi*d_m^2}{4A_{eff}} \tag{2.26}$$

where $d_m, N,$ and $A_{eff} = A_T - A_I$ are the maximum wire diameter including insulation, number of coil turns, and the effective area occupied by the coil. With A_T being the total area of coil slot and liner and A_I is the cross-section area of the slot insulation with the slot liner. For different c_w of Fig. 2.6 (**A**), Table 2.2 below summarized the respective values of the c_f computed at $d_m = 0.289$ mm, at respective symmetric lengths L_{11}, L_{21}, L_{22} and L_{12} as well as the average packing density $c_{f\,Ave}$.

Table 2.2 Measured dimension of different coil geometries for different c_f and $c_{f_{Ave}}$

N	c_w (mm)	Area Section A-A			Area Section B-B			$c_{f_{Ave}}$
		L_{11} (mm)	L_{21} (mm)	$c_{f_{A-A}}$	L_{22} (mm)	L_{12} (mm)	$c_{f_{B-B}}$	
520	4.00	22.00	2.10	0.88816633	22.60	3.1	0.92638513	0.907275730
850	6.00	22.62	2.14	0.87796632	23.00	3.1	0.92297237	0.900469345
1100	8.00	21.10	2.10	0.89486574	21.62	3.1	0.90779963	0.901332685
1500	9.40	22.86	2.17	0.93629431	23.60	3.12	0.94589498	0.941094650
1850	12.00	21.03	2.11	0.93307543	23.27	3.05	0.98322825	0.943151840

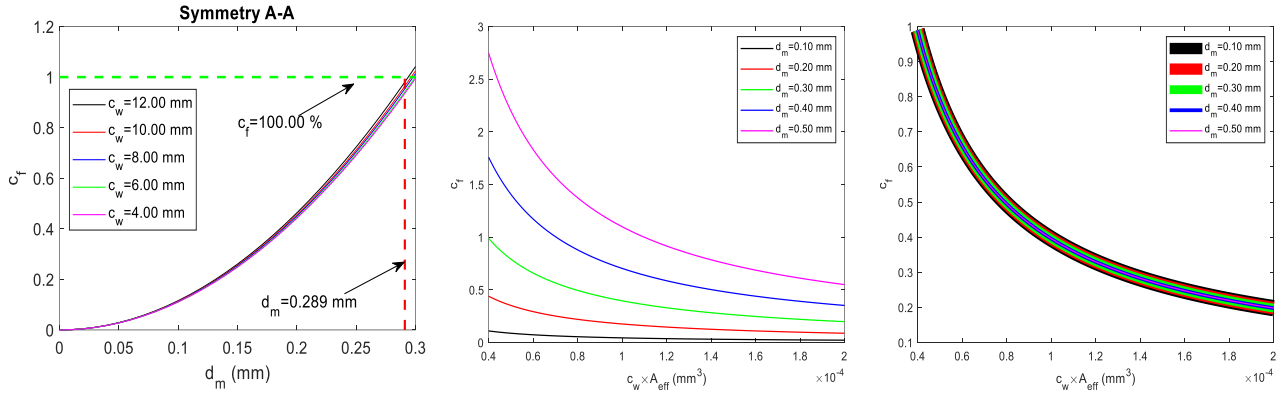

Figure 2.7 Variation of c_f with d_m for different c_w about symmetries A-A (left), c_f with coil slot volume ($c_w A_{eff}$) for different d_m (middle) and normalized c_f with coil slot volume ($c_w A_{eff}$) for different d_m (right)

Given a coil of total turn N cutting in the field of permanent magnet of flux density (b), from Fig. 2.7, the effective c_f for the copper winding diameter $d_m = 0.289$ mm at a fixed volume $c_w A_{eff}$ was realized at approximately $88.81\,\% - 93.30\,\%$ and $92.37\,\% - 98.02\,\%$ for different coil turns about symmetries A-A and B-B respectively. The average of the coil packing $c_{f_{Ave}}$ for each coil configuration was obtained at $90.72\,\% - 94.32\,\%$ about A-A and B-B symmetry. There arose the need for computing c_f about each symmetry because as shown in Table 2.2, their values about each symmetric half differs. Therefore, in the following experimental validations the average fill factor was used as $c_f = 91.04\,\%$ when the coil wire diameter $d_m = 0.289$ mm. Using $d_m = 0.298$ mm as a reference, when other values of d_m is used at fixed $c_w A_{eff}$, the packing density is

significantly lower as shown in Fig. 2.7. Therefore, to attain a reasonable packing factor of $92.00 \leq c_f \leq 100.00\ \%$ to maximize the fixed volume, the coil turn must be normalized as a function of the squared inverse of the factor that rationalize the desired d_m. For example, if the new coil diameter is $\frac{d_m}{2} = 0.1445$ mm, the coil turn N is normalized by multiple of 4.00. Also, if the new coil diameter is $2d_m = 0.578$ mm, the coil turn N is normalized by multiple of 0.25 as shown in Fig. 2.7 (middle) where the variation of c_f with coil slot volume shows that at equivalent volume, smaller d_m resulted in lower c_f. However, Fig. 2.7 (right) shows that normalizing the coil turn as a function of the squared inverse of the factor that rationalize $d_m = 0.30$ mm realized $92.00 \leq c_f \leq 100.00\ \%$.

Likewise, since the equations that govern the behavior of the electromagnetic field (Maxwell's laws) are linear, this implies that a superposition of different fields that fulfill the same equations for the total N turns of coil are possible such that if the coil of total surface area A is cutting though the magnetic field at angle θ, the flux linkage is gotten as

$$\vartheta = bANsin\theta \tag{2.27}$$

It is crucial to note that the transduction coil is always positioned in the magnet in such a manner that prevented dynamic contact with the magnet during oscillation. The minimum requirement for avoiding such contact was identified at a minimum clearance distance $c_d = 1.00$ mm with each symmetric halves of the magnet as shown in Fig. 2.2 (left). To further highlight how the flux linkage in Eq. (2.27) varies with the magnet-coil dimensions w_m, h_m and c_d, a plot that characterizes such variation is shown in Fig. 2.8. Fig. 2.8 shows the variation of flux linkage with $\mathrm{c_w}$ (left) and the variation of ϑ with angle of flux contact (θ) at different $\mathrm{D_m}$ where $c_w = 2D_m + c_d$ (middle) and fixed $\mathrm{c_w} = 6.00$ mm (right).

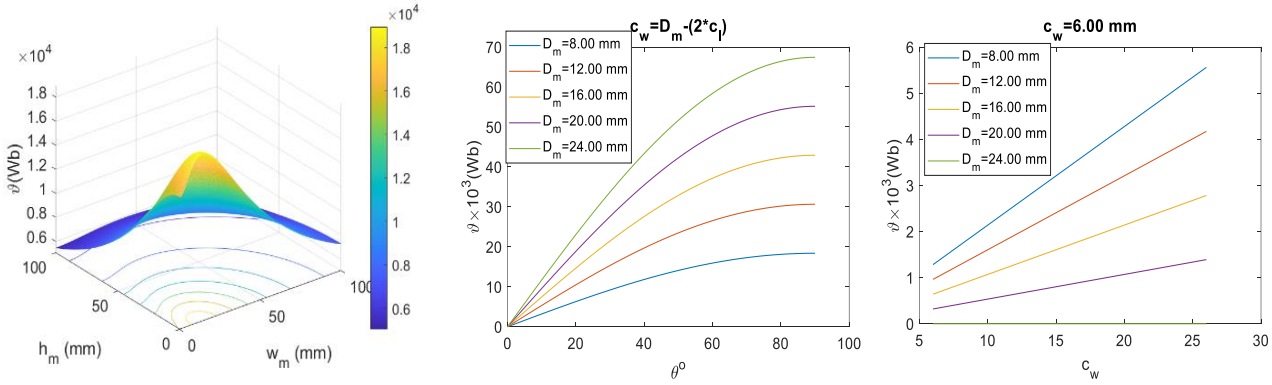

Figure 2.8 Variation of flux linkage (ϑ) with h_m and w_m (left) Variation of ϑ with angle of flux contact (θ) at different $\mathrm{D_m}$: $\mathrm{c_w} = 2\mathrm{D_m} + \mathrm{c_d}$ (middle) and $\mathrm{c_w} = 6.00$ mm (right).

From flux linkage variation of Fig. 2.8, the following are concluded

a. Smaller coil width produces lesser flux linkages at equivalent magnet geometry.
b. Using c_w that is proportionate to D_m result in larger flux linkage (ϑ).
c. The flux linkage on $c_w = 0.60$ cm and $D_m = 0.80$ cm optimizes at $w_m \cong 4.10$ cm and $h_m \cong 2.80$ cm.
d. The flux linkage (ϑ) is directly proportional to c_w and inversely proportional to D_m.
e. Positioning the coil to perpendicular linkage with the magnetic field enhances the flux linkage for better coupling and hence better harvester performances.

2.3.1 Using different coupling material in the hollows space in the coil

As a follow up to the method for maximizing flux as a function of the coil placement geometry, another approach to ensure an increased power output on a resonant energy harvester through different magnetic flux/coupling between the magnets and transduction coil design was presented in this section. Irrespective of the coupling material, the approach undertaken uses two equally tuned transduction coils vibrating inside the field of a permanent magnet. These coils are connected to a load resistance to realize a closed-circuit as shown in Fig. 2.9 (right).

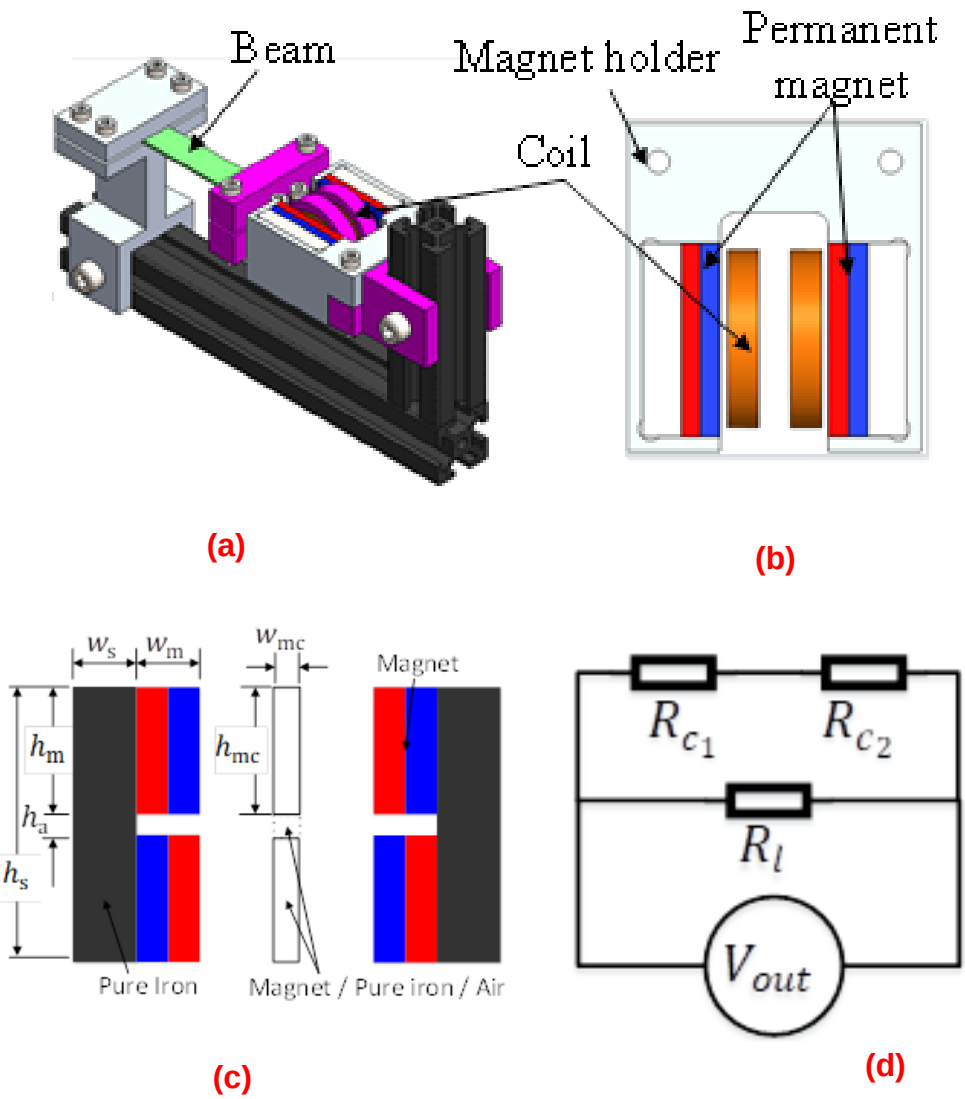

Figure 2.9 The fixed free model of SDOF cantilevered energy harvester (a) two slot coil geometry (b) the geometry of tip coil inside the magnet (c) and series connection of the slot coils (d)

From Fig. 2.9, h_s, h_m, and h_{mc} are the respective heights of cladding iron, outer magnet, and centre conductive coupling material. In addition, w_s, w_m, and w_{mc} are the respective widths of cladding iron, outer magnet, and centre conductive coupling material, while h_a is the height of the air gap between the centre conductive coupling material. Five coupling cases are considered based on the surface area and the nature of the coupling material between the two outer permanent magnets as follows. For cases 1, $w_{mc} = h_{mc} = 0$ (the coupling material is air) while w_m has a numerical value of 5 mm.

For cases 2 and 4, using magnet and pure iron as the coupling materials between the magnets space respectively, $w_{mc} = 2.00$ mm and $h_{mc} = 10.00$ mm, while w_m has a numerical value of 5 mm in both cases. Case 5 was realized by introducing two magnets with dimensions $h_a = 1.00$ mm and $w_{\mathrm{mc}} = 2.00$ mm into the space between the upper and lower symmetric center of pure iron in case 4, while case 3 was realized by introducing two pure iron with dimensions $h_a = 1.00$ mm and $w_{mc} = 2.00$ mm into the space between the symmetric center magnet in case 2. Likewise, cases 3 and 5 has the numerical values of w_{mc} and h_{mc} to be equal to those reported for cases 2 and 4 above. Other model dimensions h_s, h_{m}, w_s, and h_a have numerical values of 22 mm, 10 mm, 5 mm, and 2 mm, respectively across cases 1-5 that were considered.

As a follow up to the dimensions defined above across all the cases considered, the total surface area of the outer magnet (m_A) was obtained as

$$m_A = (4 \times h_m \times w_m) \tag{2.28}$$

The total surface area of the center conductive coupling material (m_{A_c}) was obtained as

$$m_{A_c} = (2 \times h_{m_c} \times w_{m_c}) \tag{2.29}$$

Table 2.3 gives a summary of magnet dimensions associated with cases 1-5 in discourse.

Table 2.3 Summary of magnet dimensions associated with cases 1-5

m_s (mm)	Cases	m_A (mm^2)	$\mathrm{m}_{A_c}(\mathrm{mm}^2)$	
			Magnet	Iron
14.00	1	200.00	0.00	0.00
14.00	2	200.00	40.00	0.00
14.00	4	200.00	0.00	40.00
14.00	3	200.00	40.00	4.00
14.00	5	200.00	4.00	40.00

m_s = magnet spacing, m_A= surface area outer magnet, m_{A_c}= surface area center conductive material.

Table 2.4 shows the trend of the flux density (b) variation across different cases. Across all cases, a consistent variation in *b* value at any desired point within the magnet space

showed dependence on the magnet surface area and the nature of the coupling material.

Table 2.4 Summary of the harvester flux density, electromagnetic damping ratio and optimum load

Case	$b\ (T)$	$\zeta_{coil} \times 10^{-3}$	$R_l^{opt}(\Omega)$
1	0.30862	14.89	478.60
2	0.41185	15.29	841.50
4	0.33368	15.08	554.70
3	0.41054	15.25	838.10
5	0.33558	15.07	561.60

Although it was established in Chapter 2.2 that when the separation distance between the two outer permanent magnets was shortened while using air as the coupling material, an increase in the flux density was observed, Table 2.4 shows that the model that uses a center positioned magnet (case 2) has a far better flux density of about 18.98 % than using a center positioned pure iron (case 4). Likewise, case 3 hybridized center positioned coupling material (90.00 % magnet and 10.00 % iron) achieved average flux density that is about 18.23 % far better than case 5 counterpart (10.00 % magnet and 90.00 % iron).

2.3.2 Flux feedback method

As a follow up to previous approaches for coupling/flux maximization, another methodology called the flux feedback methods was proposed. The flux feedback introduces an approach to realize an enhanced performance by feeding back leaked magnetic flux into the transduction coil-magnet configuration as shown in Fig 2.10 (left). To realize the flux feedback design approach, as earlier mentioned, two different layers of steel/iron to serve as flux convergent and flux feedback/leakage guide was used in the transducer model as shown in Fig 2.10 (left). Fig. 2.10 (left) shows the model flux feedback back model, where w_s, w_{s-con} are the respective thicknesses of the flux convergent and flux feedback/leakage guide steel. w_c, w_m and w_a are the thicknesses of the coupled coil, transduction magnet and air spaces between the symmetric transduction magnets. h_s, $h_m$and h_a are the total heights of the model, height of each transduction magnet in the model and the height of the air column between the two magnets on the

same symmetry of the model respectively.

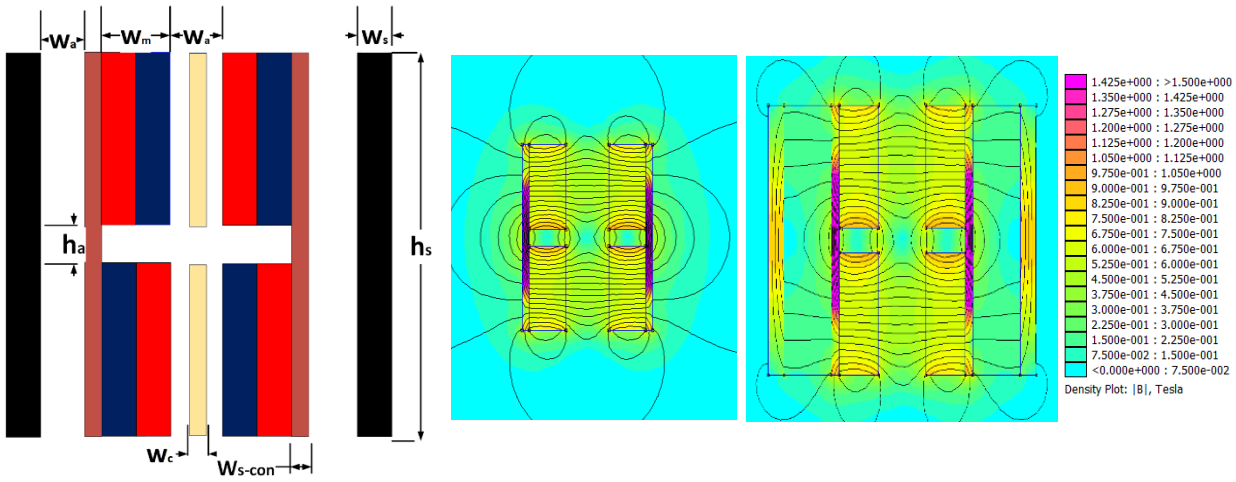

Figure 2.10 The transduction model with flux feedback model (left), FEMM simulation with no flux feedback steel (left) $w_{s-con} = 0.50$ mm, (center) $w_{s-con} = 1.00$ mm, (middle) and legend (right)

The earlier version of the coil-magnet transducer were characterized by only symmetric magnets sandwiched between a steel which acts as a flux leakage guide. The thickness of the leakage guide were carefully selected to ensure an approximately zero leakages in the magnetic flux. However, the degree of the flux density that could effectively initiate an electromagnetic induction that generate current at the maximum flux leakage guide thickness of 5.00 mm was about 0.52907 T. The additional two slots are realized in the air space between the flux feedback steel and the flux convergent steel. In comparison to the single coil configuration, the higher number of coil slot in the described feedback method is not only beneficial for realizing an effective higher harvested power over the three slotted coils when, but also expected to be beneficial for realizing improved operation in an environment much lower vibration frequency because the additional coils slightly increase the inertia mass of the model and hence a much lower operational resonant.

To adequately characterize how the feedback model performance is improved over the conventional transducer model without feedback, each transduction magnet model and average flux density distribution was queried on the FEMM software. The manner of the flux variation was investigated and compared in the two possible model configurations.

After which a test on how the relative thicknesses of the flux converging and flux feedback steels affect the average flux density and flux density per unit volume in the coil slot space of the feedback model were investigated. Fig. 2.10 (middle) shows the flux pattern in the magnet configuration when the feedback mechanism was absent. One obvious limitation with this configuration is that it is most likely characterized with severe flux leakage especially as the thickness of the leakage guide steel approaches zero. To prevent such waste of flux energy in term of leakages, the model thickness must be increases to a minimum not below 5.00 mm as the simulation result shows that the extent of the leaked flux obviously decreases as the thickness of the flux converging steel (w_{s-con}) increases.

Tables 2.5- 2.6 gives the summary of the FEMM simulated trend of the average flux value variation. Each of the test groups, has certain unique differences such as single coil slot position in the model without feedback mechanism, while those with flux feedback mechanism has three different coil slots.

Table 2.5 Summary of the flux density (b) variation with and without feedback

Feed back	w_s (mm)	b (T)	w_{s-con}		
			0.20 mm	0.50 mm	1.00 mm
No	0.00	Centre	0.37334	0.39213	0.41858
Yes	1.00	Centre	0.39359	0.41047	0.43309
		Side R	0.23570	0.20868	0.17098
		Side L	0.23583	0.20889	0.17106
	2.00	Centre	0.39544	0.41122	0.43352
		Side R	0.24500	0.21416	0.17213
		Side L	0.24456	0.21361	0.17232

** Side R = Right hand side coil Slot ** Side L = Left hand side coil Slot

Table 2.6 Summary of the flux density per unit volume (β_{eq}) variation with and without feedback

Feedback	No	Yes	
	$w_s = 0.00$ mm	$w_s = 1.00$ mm	$w_s = 2.00$ mm
w_{s-con} (mm)	β_{eq} (Tmm^{-3})$\times 10^{-5}$		
0.20	4.1390	5.1740	4.9663
0.50	4.1939	4.8565	4.6226
1.00	4.2281	4.4042	4.0414

A careful comparison of the results in Tables 2.5 and 2.6 indicates that for model without feedback, increasing the dimension of flux converging steel initiates an improved effective average flux density $(\bar{b})$ and flux density per unit volume (β_{eq}). Such was observed because as the thickness of the flux converging steel increases, the percentage of the flux leakage is reduced by directing the fluxes back to the center of the transducer magnet. However, while using the flux feedback generally improved the average flux density per unit volume relative to those without feedback, Table 2.5 shows that equal dimensional variation in the model with feedback shows an improved flux density (b) at the central coil slot but a depleted flux density (b) at the other two-sided coil slots. In essence, when the feedback steel was not present, the converging steel serves both the purpose of flux converging and flux leakage prevention noting that the leakage prevention capacity of the flux converging steel becomes dominant as $w_{s-con} \rightarrow 5.00$ mm. Taking $w_{s-con} = 0.20$ mm as reference and correlating the value of β_{eq} over model without feedback shows that the value of β increases by 1.31 % and 2.11 % for situations $w_{s-con} = 0.50$ mm and $w_{s-con} = 1.00$ mm respectively with the following conclusions

i. In comparison to the single coil configuration, the higher number of coil slot in the described feedback method is not only beneficial for realizing an effective higher harvested power over the three slotted coils although the transducer become bulky.

ii. It is interesting to note that for any level of w_s other than zero, the effective average flux density on the feedback model is almost a double of those without feedback since the inclusion of flux feedback steel into the transducer magnet geometry initiates a cascaded/double flux feedback from both the feedback steel and the flux converging steel. This approach is quite beneficial when multiple sensor nodes can be individually powered over each coil slot arrangements thus enhancing the harvested power, power density, much lower resonant operation.

iii. The model is dimensionally optimized in the flux density capacity dimension at approximately $w_s = 0.50$ mm and $w_{s-con} = 1.50$ mm. Such optimized dimension measured $\mathrm{b} = 0.41034\ \mathrm{T}, 0.21387\ \mathrm{T}$ and 0.21402 respectively for the center, left

hand side and the right-hand sided coil slot positions. The above optimized values correspond to $b = 0.83841\ \mathrm{T}$ and $\beta = 4.76367 \times 10^{-5}\ \mathrm{T}mm^{-3}$.

2.4 Damping ratio equations

Due to the complexity of VEH designs, two damping terms known as the mechanical damping ratios (ζ_{mech}) and electromagnetic damping ratio (ζ_{coil}) have been identified to be always present. The damping ratio is a measure of how quickly the vibration energy in the system decay or attenuates over time. Therefore, both ratios play a crucial role in determining the efficiency and performance of the harvester system. Both ratios are independently related to the mechanical losses (such as friction and material damping) and the electrical losses (such as eddy current losses and resistance losses) in the system respectively.

While the procedure for determining the ζ_{mech} has been justified by hysteresis model using the critical damp stress approach [44], the ζ_{coil} are formulated as a sequel to the Steinmetz theory of losses/ Statistical Theory of Losses (STL) [51-59]. The reformulated ζ_{coil} account for coupling medium ranging from weak to moderate to high. The principles of physics holds that the electromagnetic power loss is proportional to the average electromagnetic damping force. i.e.

$$P_{loss} = F\dot{z} \tag{2.30}$$

where F is damping force, and $\dot{z}$ is the velocity of oscillation noting that there exists a linear relationship between the electromagnetic damping force and the velocity [60]

$$F = c_{loss}\dot{z} = 2m_e\zeta_{loss}\omega_n\dot{z} \tag{2.31}$$

where c_{loss} is the loss constant and m_e is the effective mass of the model. Substituting (2.30) into (2.31), the ζ_{loss} for a magnet-coil system having a R_c connected to an R_l is obtained as

$$\zeta_{loss} = \frac{P_{loss}(R_l+R_c)}{2m_e\omega_n\dot{z}^2R_l} \tag{2.32}$$

If W is the electromagnetic energy loss and f is the excitation frequency, then [61]

$$P_{loss} = W * f \tag{2.33}$$

This proposed architecture thus introduces two types of electromagnetic loss namely the ferromagnetic and coil winding (copper) losses into the system. The fferromagnetic losses (P_{Fe}) arising from the ferromagnetic steel used in guiding the magnetic field and the coil winding loss called the copper losses (P_{cop}) is associated with the transduction coil winding.

Following the above, the total electromagnetic power loss (P_{coil}) and the corresponding redefined electromagnetic damping ratio (ζ_{coil}) is the sum of loss/damping from the ferromagnetic (steel) and the coil winding components in the transduction medium i.e.

$$P_{coil} = P_{Fe} + P_{cop} \tag{2.34}$$

$$\zeta_{coil} = \zeta_{Fe} + \zeta_{cop} \tag{2.35}$$

2.4.1 Ferromagnetic Loss.

The STL model demands that total ferromagnetic energy loss is the summation of the hysteresis (W_h), classical (W_{cl}) and excess (W_{ex}) energy losses [52, 59].

$$W_{Fe} = W_h + W_{cl} + W_{ex} \tag{2.36}$$

Therefore, ferromagnetic power loss in equation (2.17) can be expressed as

$$P_{Fe} = P_h + P_{cl} + P_{ex} \tag{2.37}$$

Where P_h, P_{cl} and P_{ex} are the hysteresis, the eddy and the excess power losses.

2.4.1.1 Classical/eddy current loss.

Eddy current losses refer to the energy losses that occur in conductive materials when exposed to changing magnetic fields. These losses are caused by the currents induced in the material due to the magnetic field variations, leading to resistive heating and energy dissipation. Eddy current losses is known to cause a repulsive force that is proportional to the velocity of the conductive metal. Eddy currents can be minimized by using materials with low electrical conductivity or by using laminated or segmented structures to reduce the circulating current paths. By this definition, the eddy loss is absent in our design $(\text{i.e.}, P_{cl} = 0)$ since the magnet is not moving relative to the steel neither is the coil wound on the ferromagnetic material but a 3D printed plastic to minimize weight.

2.4.1.2 Hysteresis loss

Hysteresis loss in the transducer coil-permanent magnet occurs when the coil generate an alternating magnetic current in the presence of a permanent magnet during oscillation. The hysteresis loss in this scenario is primarily due to the interaction between the alternating magnetic field generated by the coil and the magnetic domains within the permanent magnet. When the coil generates an alternating magnetic field, the magnetic domains within the permanent magnet must continuously align and re-align with the changing magnetic field. This process of magnetization and demagnetization results in energy losses due to hysteresis. The hysteresis loss in this setup is influenced by the magnetic properties of both the coil material and the permanent magnet material. To minimize hysteresis losses in the transducer coil-magnet setup, it is important to select materials with low coercively and high permeability for the coil, as well as a high-quality permanent magnet material with favorable magnetic properties. Additionally, operating the system within the optimal magnetic field range can help reduce hysteresis losses and improve overall efficiency. In the transducer geometry, it is indicative that the hysteresis loss is introduced into the transduction coil-magnet from the field interaction of the guiding ferromagnetic steel component and coil of the device. For tool steel, P_h is defined according to the equation below [55-57].

$$P_h = \eta b^n \frac{R_l}{(R_l+R_c)^2} \tag{2.38}$$

Substituting Eqs. (2.30), (2.31) and (2.32) into Eq. (2.38), the damping ratio due to hysteretic can be obtained as

$$\zeta_h = \frac{\eta b^n}{2m_e {\omega_n}^3 z^2 (R_l+R_c)} \tag{2.39}$$

where n is Steinmetz exponent, ranging from 1.5 to 2.5, while η is Steinmetz hysteresis coefficient and b is the magnetic flux density. For tool steel $\mathrm{n} = 1.6$ [55]; for Fe-3.2% Si steel $\mathrm{n} = 1.797$ and $\eta = 15.44$; for Ferrite $\mathrm{n} = 1.648$, and $\eta = 142.2$; for Fe-48% Ni, Ni–Fe–Mo alloy (mu-metal) $\mathrm{n} = 2.189$ and $\eta = 64.42$ [56]. Several values of η were reported for different materials [56, 57] but three different values determined by different hardening methodology was presented for tool steel:

1. Glass hardened tool steel; $\eta \approx 0.075$.
2. Oil hardened tool steel; $\eta \approx 0.027$.
3. Annealed tool steel; $\eta \approx 0.019$

2.4.1.3 Excess loss

Excess loss in a coil-magnet arrangement refers to additional energy losses beyond the expected hysteresis and eddy current losses that occur in the system. These losses can be caused by various factors such as mechanical vibrations, stray magnetic fields, imperfect alignment of the coil and magnet, and other non-ideal conditions in the system. Excess losses can result in reduced efficiency, increased heat generation, and performance degradation of the transducer coil-magnet arrangement. It is important to identify and minimize excess losses in systems to improve overall efficiency and reliability. To reduce excess losses in a coil-magnet arrangement, considerations such as proper design, material selection, shielding techniques, and minimizing mechanical stresses can be implemented. Likewise, excess power loss P_{ex} is defined according to the equation below [55-57].

$$P_{ex} = \frac{8.76}{\rho_{coil}} \sqrt{\sigma G A v_0 (bf)^3} \frac{R_l}{(R_l + R_c)^2} \tag{2.40}$$

Substituting (2.30), (2.31) and (2.32) into (2.40), the damping ratio due to excess loss is

$$\zeta_{ex} = \frac{8.76\sqrt{\sigma G A v_0 (fb)^3}}{2 m_e \omega_n{}^3 z^2 \rho_{coil} (R_l + R_c)} \tag{2.41}$$

where ρ_{coil} is density of coil, and v_0 is the statistical parameter lumping the effect of the local coercive field in the STL as defined in [53-54]:

$$v_0 = \frac{1}{9\sigma A G b^2 f_n} \tag{2.42}$$

2.4.2 Coil winding loss (ζ_{cop}) and harvested power equation.

Coil winding loss in a magnet coil transducer refers to the energy loss that occurs in the coil winding due to various factors such as resistance of the wire, skin effect, proximity effect, and other resistive losses. When an electrical current flows through the coil winding, these losses result in the conversion of electrical energy into heat. The resistance of the wire used in the coil winding is a primary factor contributing to coil winding losses. As

current flows through the wire, resistance causes a voltage drop, leading to power dissipation in the form of heat. The skin effect, which causes current to flow predominantly on the surface of the wire at high frequencies, and the proximity effect, which causes non-uniform current distribution in multi-strand conductors also increase coil winding losses.

Techniques to reduce coil winding losses include using high-conductivity wire, optimizing the wire diameter, and minimizing the length of the winding. Additionally, proper design considerations such as minimizing the number of turns and optimizing the coil geometry can help reduce losses in the coil winding of a magnet coil transducer.

When the system is set into vibration by an external excitation of amplitude F, and frequency ω, the coil component couples into the magnetic field of the permanent magnet in an oscillatory manner thereby inducing a voltage in the coil as it cuts through the flux of the permanent magnet. The voltage induced in the coil as it cuts the magnetic field of the magnets is given as

$$\varepsilon = \frac{d\phi}{dt} \tag{2.43}$$

while the magnetic flux (ϕ) through a single coil turn is

$$\phi = Kl_c z \tag{2.44}$$

The product $l_c z$ is defined as the effective cross-sectional area (A) mapped by the coil during the oscillatory motion in the magnetic field of the permanent magnet; l_c is the effective coil length and z relative coil displacement. Substitute (2.44) into (2.43) gives the induced voltage per unit length of the coil as

$$\varepsilon = Kl_c \dot{z} \tag{2.45}$$

Considering the magnet configuration, it would be observed that two oppositely directed but equal magnitude coupling forces independently act on the cross sectional areas of the coil. Since the geometry of the coil is circular, $l_c = 2\pi r_e$ and $\dot{z} = \omega_n r_e$ is defined as a function of the radial distance r_e, the voltage induced in the effective coil length as the coil of total internal resistance (R_c) cuts the magnetic field of the magnets when connected in series to an external load resistance (R_l), is given as

$$v_{out} = 4Kl_c\omega_n z\left(\frac{R_l}{R_l+R_c}\right) \tag{2.46}$$

According to Ohm's law, the harvested power at the load resistance is obtained as

$$P_{out} = 16K^2{l_c}^2(\omega_n z)^2\frac{R_l}{(R_l+R_c)^2} \tag{2.47}$$

Substituting (2.30), (2.31) and (2.32) into (2.47), the coil winding damping ratio is obtained as

$$\zeta_{cop} = \frac{8K^2{l_c}^2}{m_e\omega_n}\left(\frac{1}{R_l+R_c}\right) \tag{2.48}$$

While the redefined electromagnetic ratio obtained as the sum of coil winding damping ratio (ζ_{cop}), hysteresis damping ratio (ζ_h) and excess damping ratio (ζ_{ex}), the redefined new total damping (ζ) is the sum of mechanical damping (ζ_m), and the redefined electromagnetic damping ratio as shown in Eq. (2.49)

$$\zeta = \zeta_m + \zeta_{cop} + \zeta_h + \zeta_{ex} \tag{2.49}$$

Fig 2.11 shows the variation of excess loss (left) and hysteresis loss (right) components of the redefined electromagnetic damping ratio versus frequency for different load resistance and the variation of coil winding loss components versus frequency for different load resistance. The plot in Fig. 2.11 suggest that for any given coil geometry and R_l, $\zeta_h \cong \zeta_{ex}$ while $\zeta_{cop} < \zeta_{ex} < \zeta_h$. The inequality suggests that the effect of loss ratios due to hysteresis and excess loss has a negligible effect on the effective electromagnetic damping as show in the next section.

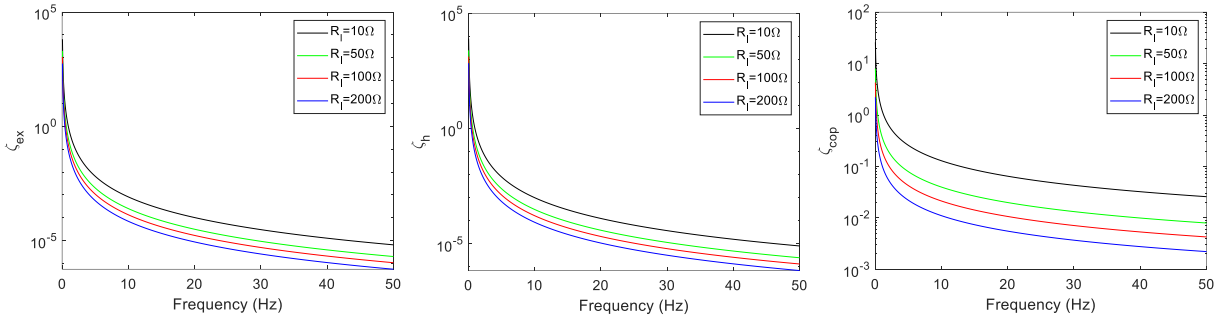

Figure 2.11 Variation of loss components versus frequency for different load resistance; excess loss (left) hysteresis loss (middle) and copper winding loss (right)

2.4.3 Experimental verification of the redefined damping model.

Using the redefined damping ratio Eq. (2.49) in the generalized response solution for a non-Coulomb damped linear cantilever Eq. (2.1) with constraint $\beta = 0$ and $\eta = 1.00$. The experiment set up to validate the redefined electromagnetic damping equations was set up as shown in Fig 2.12. The harvester system is configured as a fixed-free beam. The fixed end of the beam is clamped to a table firmly fixed to a shaker while a tip coil is mounted on the free end of the beam.

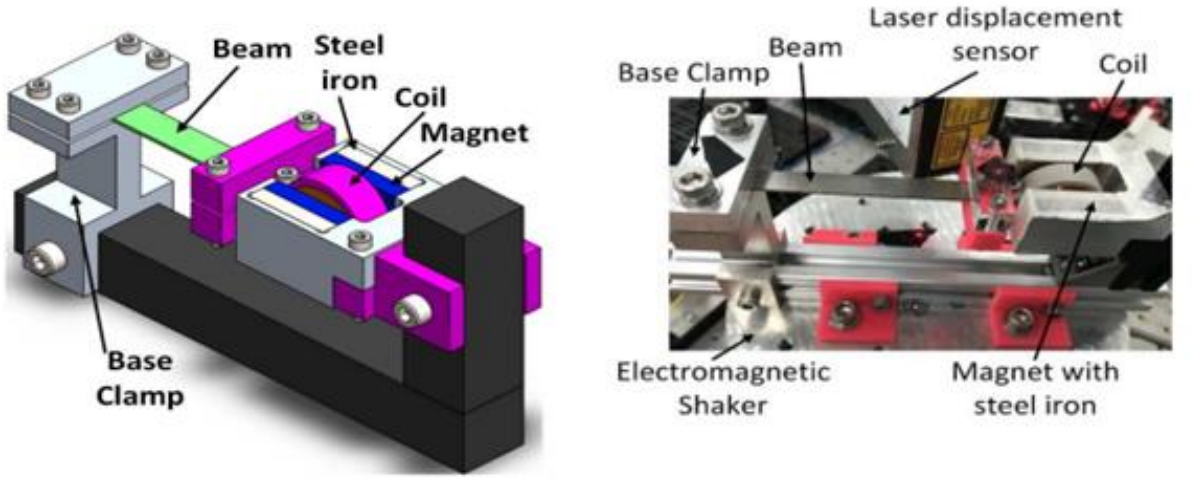

Figure 2.12 SDOF cantilever type vibration energy harvester: Model (Left) and experiment set-up (Right)

Defining the critical coupling strength as $K_s = \frac{K}{\zeta_m}$ and noting that coupling is respectively weak, moderate and strong when $K_s < 1$, $1 \leq K_s \leq 10$, and $K_s > 10$ [45]. Fig. 2.13 (left) shows that while the old damping ratio equation is valid for low and fairly moderate coupling since both are approximately equal at $K_s \leq 1.50\ \mathrm{Wbm}^{-1}$, the deviation of the new electromagnetic damping equation toward a smaller value further from the old $K_s > 1.50\ \mathrm{Wbm}^{-1}$ validates its usefulness for computing the electromagnetic damping ratio in all regions of coupling since the existing electromagnetic ratio shows a faster approach to unity as the coupling K_s increases. Also, Fig. 2.13 (right) however shows that the contribution of ζ_h and ζ_{ex} to the total electromagnetic damping ration can be neglected as shown in Fig. 2.11. This is suggestive that over 99.08 % of the total electromagnetic damping ratio is associated with the coil winding loss.

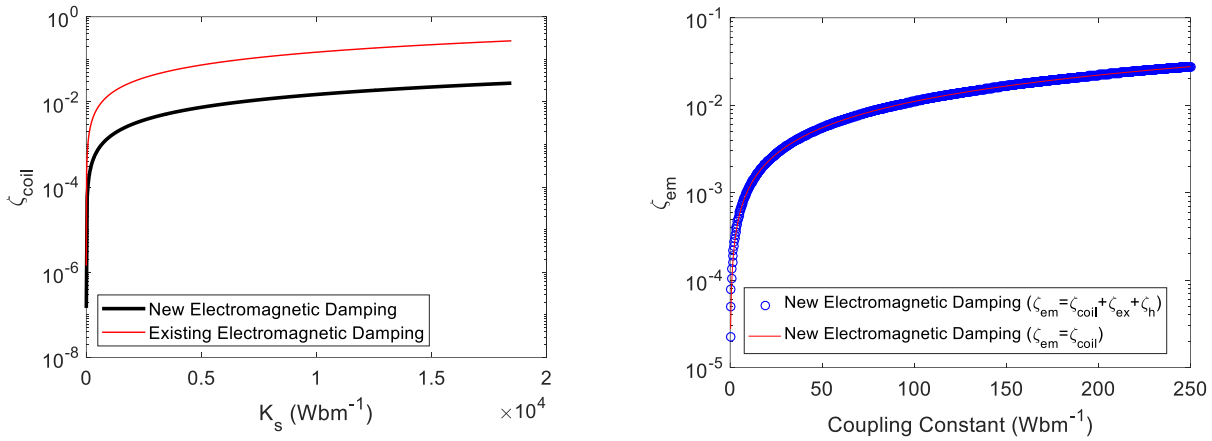

Figure 2.13 Variation of electromagnetic damping ratio with critical coupling (left) and comparison of electromagnetic damping ratio against coupling constant at $\zeta_h = \zeta_{ex} = 0$ with $\zeta_h \neq \zeta_{ex} \neq 0$ (right)

During experimental validation, the cantilever beam to which the transduction coil was attached is fabricated from a stainless-steel material with mechanical and thermoplastic properties reported in [27]. The accuracy of the redefined electromagnetic damping ratio equation was tested on two coil geometries. The beam geometry used on the two coil has a length (L) of 86.5 mm, width (W) of 10.00 mm and a thickness of 1.00 mm. When the shaker is triggered, the tip coil freely oscillates in the field of the permanent magnet. The electrical power whose magnitude was computed based on Faraday's law of electromagnetic transduction was then harvested over an external load resistor. The masses of the test coils are 22.06 g and 20.73 g. The coil fill factor, number of coil turn, flux density and the magnet spacing are identical for both geometries as 90.96 %, 570, 0.2319 T and 14 mm, respectively for the two geometries that were tested. The displacement response and the accompanying induced voltage over the coil connected to external load resistance 110.00 Ω of the system was captured using two Keyence LK-H050 laser displacement sensors which were connected to a USB-6001 National Instrument data acquisition (DAQ) card and obtained the response in LabVIEW.

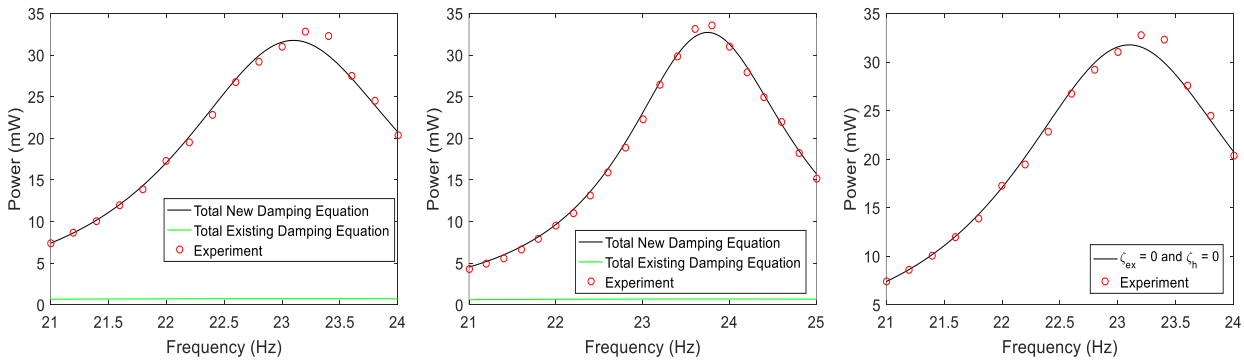

Figure 2.14 Maximum power; coil geometry 1 (left), coil geometry 2, (middle) and Maximum power harvested coil geometry 1 for $\zeta_{\mathrm{h}} = 0$ and $\zeta_{\mathrm{ex}} = 0$ (right).

Using the new damping equation Eqs. (2.49) and power equation Eq. (2.47), Fig. 2.14 show that the power harvested at resonant is $31.76\,\mathrm{mW}$ and $32.72\,\mathrm{mW}$ for coil geometries 1 and 2, respectively. The experimental harvested power matched well with the analytical solution to approximately 99.98% compared to the power harvested using the existing damping equation which yielded an agreement 0% for this medium coupling operation. This degree of agreements further validates of the veracity of the redefined electromagnetic damping equation. The redefined electromagnetic damping equation was also identified to remains valid to approximately 99.08% when the hysteresis and excess damping components were set to zero as shown in Fig. 2.14 (right).

2.5 Power density and efficiency analysis of electromagnetic vibration harvester

2.5.1 Power Density (PD):

The power density can be defined as the power harvested per unit volume or unit area of the harvester. For a given harvester design of total practical volume (V_p), the effective power density is computed as shown in Eq. (2.50)

$$P_D = \frac{P_{out}}{V_p} \tag{2.50}$$

2.5.2 Energy Harvesting Efficiency (ϱ):

The energy harvesting efficiency of the harvester is calculated as the ratio of the harvested power to the total available power in the vibration source. For a vibration source

with total power P_{source}, the effective harvester efficiency is computed as shown in Eq. (2.51)

$$\varrho = \frac{P_{out}}{P_{source}} \tag{2.51}$$

2.6 Summary

Chapter 2 illustrates the theoretical aspects of vibration energy harvesters, focusing on the generalized response equation that governs their operation and the strategies for maximizing harvester power output and flux. By examining the dynamic response of the harvester system to external vibrations, the generalized response equation provides a fundamental framework for predicting the electrical output of the harvester under different operating conditions. Furthermore, the chapter explores various techniques and optimization methods aimed at maximizing harvester power and flux, including structural and electromagnetic transducer design enhancements. Through a comprehensive analysis of these optimization strategies, this chapter provided insights into the key principles and methodologies for enhancing the performance and efficiency of vibration energy harvesters, ultimately advancing their practical implementation in energy harvesting applications.

The flux/coupling variation reported achieved various optimal value with different coupling material such as air, steel, smaller magnets, or hybrid of the fore mentioned between the outer magnet spaces where the transduction coil oscillated during excitation. Also, another methodology for achieving varied coupling/flux presented was using a larger/smaller outer magnet dimension. The coupling/flux variation was investigated and the effective magnetic flux density on each different model was computed using the Finite Element Magnetic Methods (FEMM) software concluding that using iron as the coupling material raised the flux density and power harvested by 8.37 % and 1.76 % respectively compared to air. Also, using magnets as the coupling material increased the flux density and power harvested by 25.06 % and 3.99 %, respectively. Although it was established in Chapter 2.2 that when the separation distance between the two outer permanent magnets was shortened while using air as the coupling material, an increase in the flux

density was observed, Table 2.4 shows that the model that uses a center positioned magnet (case 2) has a far better flux density of about 18.98 % than using a center positioned pure iron (case 4). Likewise, case 3 hybridized center positioned coupling material (90.00 % magnet and 10.00 % iron) achieved average flux density that is about 18.23 % far better than its case 5 counterpart (10.00 % magnet and 90.00 % iron). Similarly, it was highlighted that for any two coils, the coupling coefficient is not only a function of the flux density, but also a function of the coil fill factor while an approach to make a relatively accurate prediction of the magnetic flux density as a function of the coil width was presented.

As a follow up, the electromagnetic damping ratio was redefined and the solution of the new damping equation displayed a good agreement of approximately 99.98 % with experimental results compared to the old damping equation which yielded an agreement 0% for the medium coupling working condition of the proposed design. This degree of agreements further confirms the veracity of the redefined electromagnetic damping equation. Further analysis shows that the redefined electromagnetic damping equation remains approximately valid to a percentage ratio of 99.98% when the hysteresis and excess loss components were set to zero.

CHAPTER 3: Theoretical Analysis of Linear/Nonlinear Stress and Damping in Cantilevered Harvester

3.0 Introduction

Cantilever vibration energy harvester is a device designed to convert mechanical vibrations into electrical energy for powering small electronic devices or sensors. The cantilever structure for the energy harvesting consists of a fixed-free beam that responds to external mechanical vibrations by response at the free end. As the beam undergoes cyclic bending due to vibrations as shown in Fig. 3.1, it generates electrical power through the appropriate transduction mechanism such as piezoelectric or electromagnetic methods. However, in the operation of a cantilever vibration energy harvester, the stress level experienced by the beam can approach fatigue limits, especially under high-frequency or high-amplitude vibrations. This can affect its mechanical behavior and energy harvesting performance as a result of material and geometric nonlinearities that are initiated due to changes in the stiffness matrix of the beam structure.

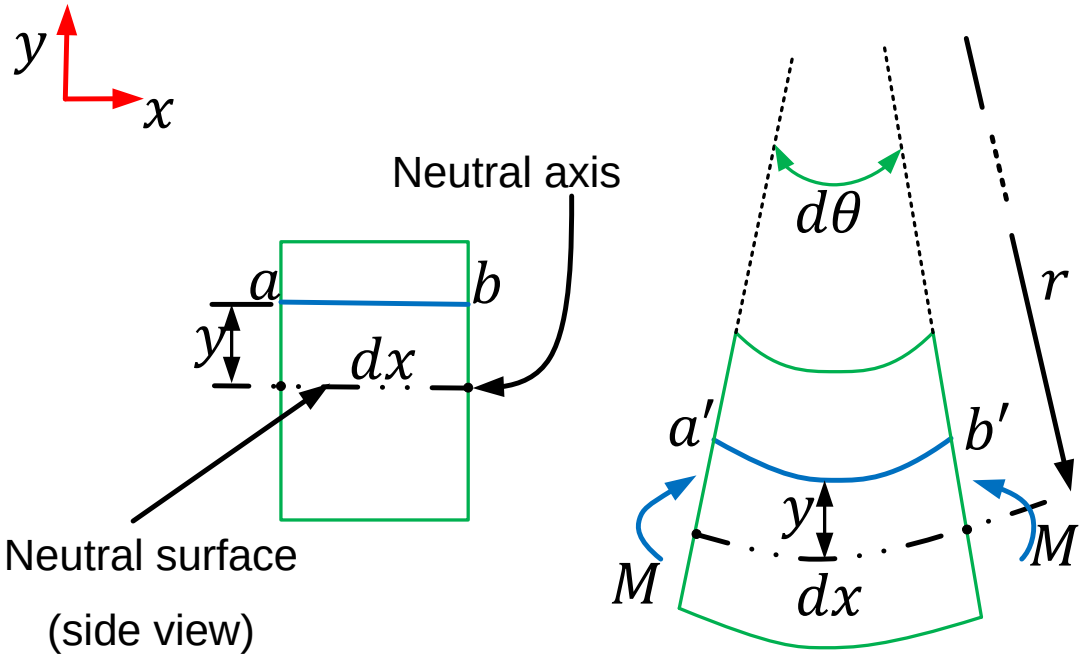

Figure 3.1 Deformation of an infinitesimal beam segment; before deformation cross sectional view (left), after deformation elevation view (right)

Although, most reported application of cantilevered harvester design with different material is centered about achieving a linear stress distribution in the cantilever beam such that the maximum stress that are attained during operation are always far away from the fatigue stress level (σ_f) of the material from which the cantilever laminate are fabricated. By implication, most damping equation that have been reportedly formulated for analyzing the energy harvesting behavior of cantilever beam are only valid in the linear domain. Therefore, as the response of the cantilever design initiate geometric or material nonlinearity, those linear equations fail. This section focus to both analytically and experimentally investigate how the harvester performance of cantilever structure behaves as the stress approaches the σ_f. To undertake the above objectives, initial procedure that was adopted for analyzing of the linear and nonlinear stress-damping relationship in a cantilevered harvester is summarized as follows:

1. **Linear Stress Analysis**:

    i. Start by modeling the cantilevered harvester as a beam structure subjected to external loads, such as tip mass sizes and acceleration.
    ii. Applying the principles of mechanics the stress distribution along the beam, considering factors like material properties, geometry, and loading conditions are computed.
    iii. Using analytical methods Euler-Bernoulli beam theory, hysteresis damping, Lazan's theory and a generalized assumption for proportionate damping in the linear domain, the linear stress distribution along the tip loaded beam and their critical/fatigue relationship with the mechanical damping ratio are determined using the critical damped stress model.

2. **Nonlinear Stress Analysis**:

    i. For nonlinear stress analysis, a consideration for material properties that exhibit nonlinear behavior, such as plasticity or large deformations is a choice. The material choice for considerations are the fiber glass, and polyether ether ketone (PEEK) laminate.

ii. Incorporate nonlinear effects, such as geometric nonlinearity (large deflections) or material nonlinearity into the stress analysis to capture the behavior of the harvester more accurately by formulating a stress-damping relationships different from 1 (iii) above.

3. **Damping Analysis**:

   i. Damping in a cantilevered harvester affects its dynamic response and energy dissipation characteristics.
   ii. Determine the damping mechanisms present in the harvester, such as material damping, structural damping, or viscous damping.
   iii. Analyze the damping behavior of the harvester under different loading frequencies and amplitudes to quantify the energy dissipation and dynamic response of the system as a function of the linear/nonlinear stresses in the cantilever.

4. **Experimental Validation**:

   i. Subject to whether the cantilever laminate material properties exhibit nonlinear behavior, such as plasticity or large deformations or not, consider the dynamic response of the harvester under harmonic vibrations.
   ii. Validate the theoretical stress-damping analysis results through experimental testing, such as modal analysis and vibration testing.
   iii. Compare the experimental data with the theoretical predictions to assess the accuracy and reliability of the analytical nonlinear/linear stress-damping models.
   iv. Use the experimental results to refine the analytical models and improve the understanding of the stress and damping characteristics of the cantilevered harvester.

Generally, the stress level in cantilever electromagnetic vibration energy harvesters approached the fatigue level when material and geometric nonlinearity occur, this can impact its resonance frequency, energy conversion efficiency, and overall reliability.

Therefore, understanding these nonlinear effects are crucial for optimizing the design and performance of cantilever vibration energy harvesters when laminate with plastic and elastic behavior are used. While material nonlinearity refers to the deviation of the material properties from linear elastic behavior, the geometric nonlinearity arises from large deformations or displacements in the structure. By considering the nonlinear behavior of the beam and implementing appropriate design strategies, such as material selection, structural optimization, and control algorithms, the efficiency and durability of the energy harvester can be enhanced, leading to improved energy harvesting capabilities in various applications relative to linear counterparts [12].

In the linear response regime, the behavior of cantilever-based electromagnetic vibration energy harvesters has been extensively studied. Kim et al. [73] investigated the design and optimization of a cantilever harvester using a magnetic circuit approach. Linear cantilever systems, utilizing piezoelectric or electromagnetic transduction mechanisms, have been extensively studied for their efficiency in converting mechanical vibrations into electrical energy [74]. They highlighted the importance of maximizing magnetic flux density for improved power generation efficiency. Additionally, Smith and Johnson [75] explored the impact of varying cantilever dimensions on the resonant frequency and power output of the harvester. Their work emphasized the need for precise tuning of parameters to achieve optimal performance. Moving into the realm of nonlinear responses, Li et al. [76] delved into the dynamics of a nonlinear cantilever harvester under broadband excitation. Their study revealed the occurrence of multiple resonances and the potential for enhanced power generation through nonlinear effects. Furthermore, Yang and Wang [77] proposed a nonlinear modeling approach for cantilever harvesters, considering the impact of magnetic damping and nonlinear stiffness. Their findings demonstrated the complex interplay between nonlinear phenomena and energy harvesting efficiency. Integrating linear and nonlinear aspects, Chen et al. [78] conducted a comprehensive study on a cantilever electromagnetic harvester with a tunable magnetic field. By dynamically adjusting the magnetic field strength, they achieved improved performance across a wide range of excitation frequencies, showcasing the benefits of hybrid linear-nonlinear strategies. Moreover, Liang and Zhang [79] explored the use of

nonlinear dynamics to enhance the bandwidth of cantilever harvesters, enabling efficient energy extraction from varying vibration sources. In addition, Daqaq et al. [80] has explored the use of nonlinear structures, such as bistable and tristable configurations, to improve energy harvesting performance by leveraging nonlinear dynamics while most studies only studies focus on the linear stress-power relationship of cantilevered design, no known approach that efficiently analyzed the nonlinear stress-strain-harvester performance of harvester cantilever beam has been rigorously undertaken. In the following analysis, the generalized governing equation modelled as an equivalent of the duffing nonlinear equations are solved analytically using the perturbation method of the harmonic balance.

For small oscillations, the responses of a deformable body are analytically and numerically characterized by set of linear equations and boundary conditions. However, as the amplitude of oscillations rises, nonlinear effect sets in, hence the linear set of equations are no longer sufficient to describe the motion of the body. Factors contributing such nonlinearity have been associated with the material, geometric, loading/inertia. As earlier identified, appropriate design strategies, such as material selection, structural optimization, and control algorithms, the efficiency and durability of the energy harvester can be enhanced, leading to improved energy harvesting capabilities in various applications. The focal design strategy adopted in this stage of analysis is centered on the material selection while establishing how the stress-damping relation evolves as the beam configuration changes from one that exhibit nonlinearity to those without. The possible material choices for testing the behavior of the cantilever as the stress distribution attains the fatigue level in this work are aluminum, steel, fiber glass, polyvinylchloride laminate (PVC) and polyether ether ketone (PEEK) [41]. These choice is necessary because their respective elastic and plastic properties varies with their modulus of elasticity thus the stress spectrum from varies from easy to late approach to fatigue stress levels (σ_f) as the excitation testing evolves. For example, steel laminates having highest level of yield, modulus of elasticity and lowest damping coefficient will attain σ_f level later than other material composites and some types of alloys as shown

later by formulating relevant equation using the stresses-strain-deformation-energy relationship in the cantilevered harvester configuration.

The stresses caused by the bending moment are known as bending stress, or flexure stresses. The neutral axis passes through the axis of the beam and is perpendicular to the plane of symmetry, as shown in Fig. 3.1. The xy-plane that contains the neutral axes of all the cross sections is known as the neutral surface of the beam.

In deriving the flexure formula, the following assumptions as made:

i. The beam has an axial plane of symmetry, which we take to be the x-y plane as shown in Fig. 3.1

ii. The applied tip loads lie in the plane of the symmetry and are perpendicular to the axis of the beam (the x-axis).

iii. Plane sections of the beam remain plane (do not warp) and perpendicular to the deformed axis of the beam.

iv. Change in the cross-sectional dimensions of the beam are negligible.

v. Because the shear stresses caused by the vertical shear force will distort (warp) an originally plane section, discussion here is limited to the deformations caused by the bending moment alone.

vi. The deformations due to the vertical shear force are negligible in the slender beams compared to the deformations caused by bending

The above assumptions lead to the following conclusion:

i. The cross section of the beam rotates as a rigid entity about the neutral axis.

ii. Upon deformation, the neutral surface becomes curved as shown in Fig.3.1 (right).

iii. During excitation, the longitudinal cantilever laminate on the neutral surfaces are not deformed. However, laminate above and below the surfaces are respectively compressed and stretched

During excitation, the fiber form are arc $a'\,b'$ of radius$(r-y)$, subtended by the angle $d\theta$ has a deformed length $\overline{a'\,b'}=(r-y)d\theta$. The original length of this fiber is $\overline{ab}=dx=rd\theta$. The normal strain ε of the laminate is given as

$$\varepsilon=\frac{\overline{a'\,b'}-\overline{ab}}{\overline{ab}}=-\frac{y}{r} \tag{3.1}$$

The negative sign indicates that positive bending moment causes compressive stress when y is positive (fiber above the neutral surface) and tensile stress when y is negative (fiber below the neutral surface). Assuming that the stress is less than σ_f of the material we can obtain the normal stress in the segment $\overline{ab}$ from Hook's law was obtained as.

$$\sigma_{max}=-\frac{E}{r}y \tag{3.2}$$

Eq. (3.2) shows that the normal stress of a longitudinal fiber is proportional to the distance y of the fiber from the neutral surface such that at $y=0$ (neutral axial line), $\sigma_{max}=0$ MPa and E is the modulus of elasticity for the material.

3.1 A semi-empirical determination of η and β as a function of σ_{nL} from generalized cantilever equation

In chapter 2, an equation that adequately captured the influence of η on the generalized motion of the vibration energy harvester is given in Eq. (2.1) subject to relevant conditions. The generalized governing equation is nonlinear if $\eta \ll 1, \beta \neq 0$ and linear if $\eta=1\,,\beta=0$. From, Eqs. (2.1), the expression for the linear and nonlinear viscous damping coefficients that measure the energy dissipation property of the system is as shown in Eq. (3.3)

$$\eta c\left(\dot{Y}\right)=2\omega_n\zeta_{eq}\dot{Y}(t)\left|\dot{Y}\right|^{n-1}\begin{cases}n=1,\eta=1\,,\beta=0 & \text{Linearly damped}\\ n>0,\eta\ll 1,\beta\neq 0 & \text{Nonlinearly damped}\end{cases} \tag{3.3}$$

where the modulus *n* is used to maintain the dissipative characteristic of the nonlinear damping force. The appropriate values of *n* were reported as $n=1$, $n=0$, $n=2$ and $n=1.5$ for a linear viscous damped system, for system with dry friction between two surfaces,

for system with quadratic damping at high Reynold number, and for oscillating fluid through an orifice respectively.

From Eq. (2.1), the nonlinear damping ratio $(\eta\zeta_m)$ and nonlinear stiffness (β) terms are strong factors that influence the nonlinear characteristics. To effectively model a mathematical relations between nonlinear damping ratio $(\eta\zeta_m)$ and nonlinear stiffness (β) as a function of the nonlinear stress (σ_{nL}) associated with material/geometric nonlinearity as stress approached σ_f during excitation, the stresses are independently analyzed for linear and nonlinear applications by a semi-empirically fitting a damping-stress relationship in the cantilever over different level of excitation in the linear and nonlinear mode of operations.

In the linear domain, Fig. 3.2 (left) shows the strain-stress distribution in the cantilever in the loading and unloading cycle of the beam using the hysteretic damping model [63, 64]. Lazan [67] proposed a method to identify the mechanical damping of a structure based on its maximum stress response during vibration. He then developed a generalized the damping stress equation to predict the damping of metals. A similar equation was also derived by Kume et al. [68]. Defining linear critical stresses (σ_c), maximum linear stress (σ_{max}), their relationship with the total strain energy (W_0) and total damping energy (D_0) is given as shown in Eqs. (3.4) – (3.5).

$$D_0 = \oint D dv = \frac{\pi\sigma_{max}\sigma_c}{tan\theta} = \frac{\pi}{E}\sigma_{max}\sigma_c \tag{3.4}$$

$$W_0 = \frac{\sigma_{max}^2}{2E} \tag{3.5}$$

In the linear domain, the loss factor ϵ is the ratio of the total damping energy to the total strain energy as shown in Eq. (3.6).

$$\epsilon = \frac{\sigma_c}{\sigma_{max}} \tag{3.6}$$

Lin [67] and Zhu [69] stated that in case of proportional damping, an exact relationship exists between the hysteretic loss factor ϵ and mechanical damping ratio (ζ_m) as shown below.

$$\zeta_m = \frac{\sigma_c}{2\sigma_{max}} \tag{3.7}$$

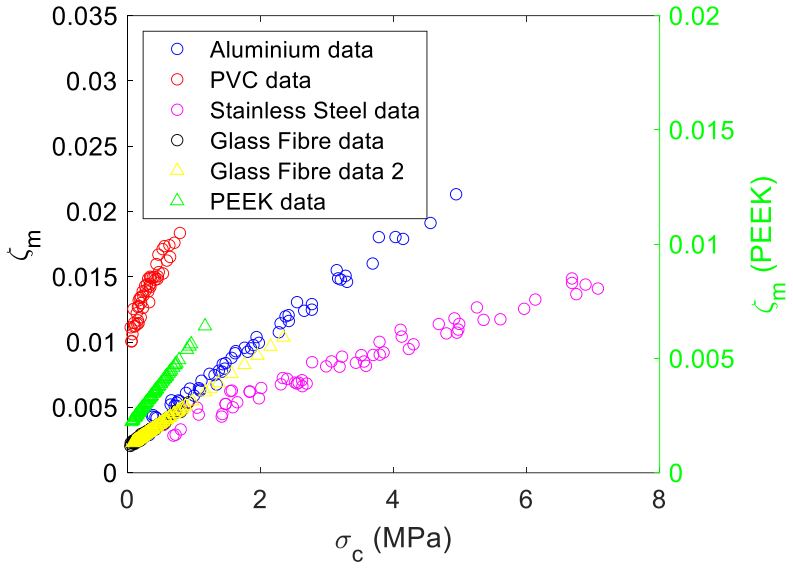

Figure 3.2 ζ_m versus σ_c for different material (right)

By duplicating the experimental procedures outlined in Foong et al. [49], Fig. 3.2 (right) shows the variation of the mechanical damping ratio (ζ_m) with the critical stress in the system for five (5) different choices of materials when the cantilever structure are operated in linear domain i.e., $\sigma_{max} \ll \sigma_f$. Fig. 3.2 (right) shows that the steel laminates having highest level of yield, modulus of elasticity attained the lowest damping coefficient at equivalent stress level hence the tendency to initiate material or geometric nonlinearity are insignificant compared to composite materials such as fiber glass, polyether ether ketone, and polyvinylchloride laminate (PVC) respectively. Therefore, steel laminate are not the proper candidate for testing the material/geometric nonlinear effects in cantilever structure since it will attain σ_f later than other material composites and some types of alloys when subjected to equal load distribution/excitations.

The equation that generalizes the variation of ζ_m with σ_c where σ_{max} and σ_c are related by Eq. (3.7) for different material grade is shown in Eq. (3.8) with respective fit parameter shown in Table 3.1

$$\zeta_m = a\sigma_c^b + c \tag{3.5}$$

Table 3.1 Summary of fit parameters for variation of ζ_m with σ_c for different materials

Material	$E(GPa)$	$a \times 10^{-6}(Pa^{-b})$	$b \times 10^{-23}$	$c \times 10^{-3}$
Fiberglass	22.500	0.003567	1.0000	2.001
PEEK	3.6447	0.003792	1.0000	2.001
Aluminium	63.000	0.015270	0.9114	1.828
Stainless Steel	225.00	0.021090	0.8447	1.662
PVC	3.1000	7.116000	0.5345	8.068

In the last section, appropriate fit equation for predicting the variation of the damping ration as a function of the stress distribution in the cantilever laminate are obtained as shown in Eq. (3.8), this section emphasized the nonlinear relationship between both. Although, Eq. (2.6) shows that both β and η are functions of σ_{nL} while Eq. (3.6) shows linear damping ration as a function of linear critical stresses(σ_c) and maximum linear stress (σ_{max}), there is however, a need to understand how the nonlinear stress distribution (σ_{nL}) in the tip loaded cantilevered affected the nonlinear stiffness (β) and nonlinear damping ($\eta\zeta_m$). Sequel to conclusion inferred from Fig. (3.2), to effectively compare the nonlinear stress distribution as a function of damping for a cantilever structure, the material choice considered are glass fiber and peek subject to the Osborne Goodman approach [65].

To start with, the mechanical properties of the cantilever strips were tested using tensile and flexural tests based on ASTM D638 Type I using the INSTRON universal testing machine at the loading speed was 9.46 mm/min as reported [50]. Once the material has been specifically shaped according to the standard dimension, it is loaded into tensile grips of the INSTRON device. The test begins as the grips separate, pulling the sample from both ends at a constant rate of speed of 9.46 mm/min. The flexural modulus, reported in the Matweb material property data sheet as 20.70Gpa, and 3.64GPa respectively for Fiberglass and Peek laminate [65]. The result of specimen tensile and flexural tests as a function of the strain rates with other fit parameters for effective stress characterization are shown in Fig. 3.3 below.

The stress-strain plot of Fig. 3.3 shows the linear fit for the stress-strain distribution with the yield point highlighted as the departure from linearity. The secant slope is the slope of the stress-strain plot at break point to 2.0 % strain offset. Using the Osborne Goodman theory, the nonlinear stress in the cantilever was approximated as shown in Eqs. (3.9) – (3.10).

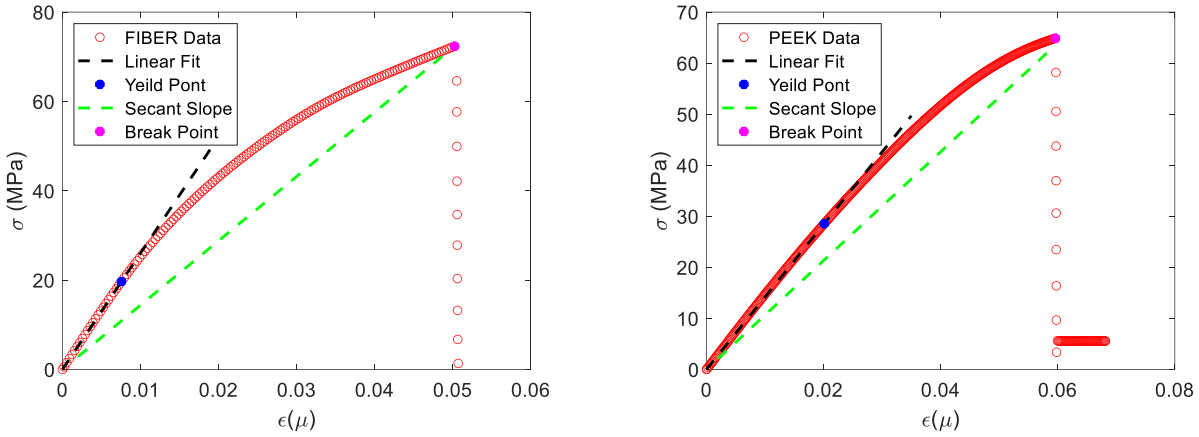

Figure 3.3 Stress-strain profile from Instron testing fiberglass (left) and PEEK (right)

$$\sigma_{nL} = \frac{1.92p\varepsilon E}{q\sigma_q^{1-n}} \tag{3.9}$$

$$n = \frac{1+log\left(\frac{1.92p}{q}\right)}{log\left(\frac{\sigma_q}{\sigma_p}\right)} \tag{3.10}$$

where, σ_p, and σ_q are the stresses at yield and break points and , p and q are the ratio of secant slope to modulus at yield point and the ratio of secant slope to modulus at break. Now that an adequate expression for the nonlinear stress σ_{nL} has been obtained, an equivalent approximated expression for η over different stresses (σ_{nL}) level was undertaken using a semi-empirical method by duplicating the experimental procedure for the linear analysis as shown in Fig. 3.4. The semi-empirical approach approximated a fit solution for $\eta\zeta_{mech}$ versus σ_{nL} and η versus σ_{nL} using different geometrical parameters W, L, f_n^2, and g as the normalizing factor to obtain a dimensional equivalent of Eq. (2.6).

The plot in Fig. 3.4 shows that at equivalent damping, the stress level in the fiber glass configurations is significantly larger than those on the PEEK material. The implication of the above observation is that at equivalent excitations, and resonance, the stress in the

fiberglass cantilever is larger to achieve a quick approach to fatigue and hence the operational life is shortened as later shown in Fig. 3.7 (middle) and Fig. 3.7 (right).

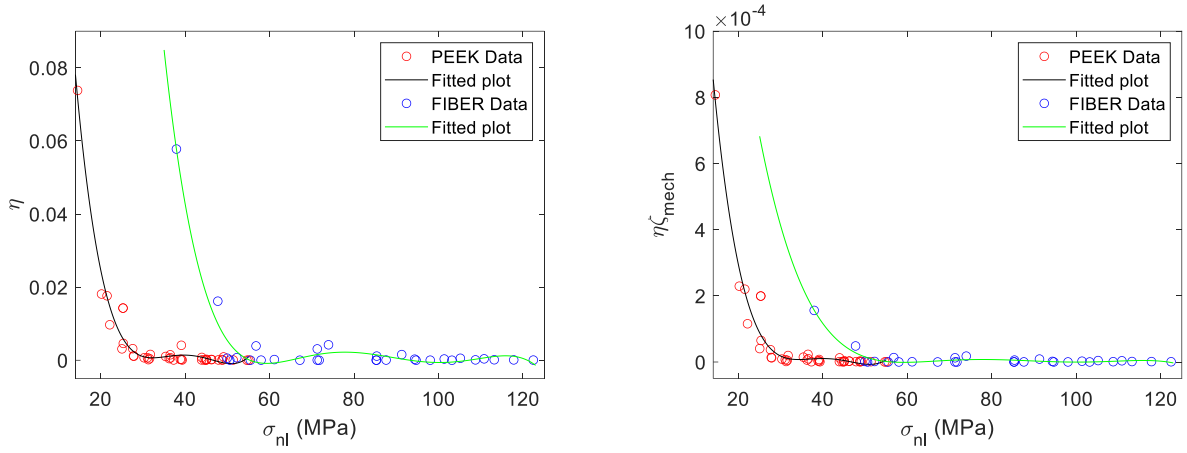

Figure 3.4 Variation of $\eta\zeta_m$ versus σ_{nL} (left) and $\eta\zeta_m$ versus σ_{nL} (right) for different choice of materials

The resulting fit equation that generalizes the variation of η with σ_{nl} for different material grade is shown in Eq. (3.11) with respective fit parameter shown in Table 3.2.

$$\eta = \frac{1}{\beta\zeta_m}\left(\frac{WLf_n^2}{g}\right)\left(a\sigma_{nl}{}^5 + b\sigma_{nl}{}^4 + c\sigma_{nl}{}^3 + d\sigma_{nl}{}^2 + e\sigma_{nl} + f\right) \tag{3.11}$$

Table 3.2 Summary of fit parameters for different materials

Material	$a \times 10^{-40}$	$b \times 10^{-31}$	$c \times 10^{-23}$	$d \times 10^{-15}$	$e \times 10^{-07}$	$f \times 10^{-00}$
Peek	0	0.754	-1.645	1.328	-0.471	0.621
Fiber	-3.866	1.707	-2.956	2.505	-1.037	1.668

The term $\left(\frac{WLf_n^2}{g}\right)$ used in Eq. (3.11) are the normalizing parameters used to capture the geometric nonlinearity initiated in the cantilever during excitation. The normalizing parameters are defined as beam width (W) and beam length (L) as well as the excitation acceleration (g) and resonant squared f_n^2 to obtain a dimensional equivalent of Eq. (2.6). β in Eq. (3.11) approximated as the Modulus of elasticity for respective material.

To obtain the effective solution for the responses and phases of the cantilever beam when material nonlinearity is present according to Eq. (2.3) and Eq. (2.4), the nonlinear stiffness term $\eta\beta$ is obtained using Eqs. (3.8) - (3.10).

3.2 Fatigue stress analysis of the cantilever beam.

The last section both analytically and semi-empirically presented the solution to various nonlinear parameters of the cantilever beam as a function of the linear and nonlinear stress when material nonlinearity are absent and present respectively. Eqs. (3.4) - (3.8) effectively computed the variation of the linear damping ratio with the linear stress in the beam while Eqs. (3.9) - (3.11) effectively computed the variation of the nonlinear damping ratio with the nonlinear stress in the beam.

This section consequentially to the previous stages of analysis presents the stress/damping variation in the cantilever harvester design. During transverse vibration of a cantilever beam, geometric/material nonlinearity are initiated due to the stretching in the mid-plane when the curvature becomes too large, otherwise the response is linear. By calculating the mid-plane stretching, engineers can assess the structural integrity of the beam and ensure that it can withstand the applied loads without failure during energy harvesting applications.

The harvester configuration is a fixed-free cantilever beam with geometric nonlinearity. Geometrical nonlinearity are initiated as a function of the changes in the bend curvature of the cantilever during loading. The mathematical governing equation for the cantilever having material and geometric nonlinearity is presented as shown in Eqs. (2.1) – (2.39) and Eqs. (3.4) – (3.11). A cantilever beam in vibration energy harvesting application is a type of beam that is fixed at one end and free at the other end as shown in Fig. 3.5.

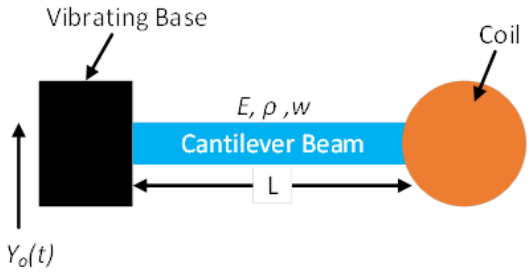

Figure 3.5 Single degree of freedom (SDOF) fixed-free cantilever structure

The transducer coil that is fixed at the free end of the cantilever is places in the field of a permeant magnet. The coil serves as a mechanism to convert the dynamic responses of

the cantilever free end into electrical energy by electromagnetic induction when it cuts the field of permanent magnet. In Fig. 3.5, E, ρ, w, L and $Y_0(t)$ are the Young modulus, density, width length of the cantilever beam and the excitation amplitude. In the context of linear cantilever harvester design, the structural mechanist uses the Euler-Bernoulli beam theory as a fundamental theory to analyze the behavior of beams. Generally, the occurrence of geometric nonlinearity in a mechanical system often demonstrated complex behaviors such as bi-stability, period doubling sequence, chaos and sometimes unbounded motions in the presence of harmonic forcing and damping [12]. Therefore, the implications of the choice of material for efficient energy harvesting on cantilever design for achieving efficient linear and nonlinear applications must be carefully studied as they can forecast a catastrophic consequence for the system being modelled when requisite knowledge is lacking.

It was earlier identified that in the linear domain, the total stress level in the beam are obviously far from the fatigue stress level while initiating material nonlinearity is implication of the stress being closer to fatigue level, although, to this point, no known approach to quantifying the fatigue stress limit (σ_f) of the cantilever design has been presented. To achieve an accurate prediction of σ_f in the linear and nonlinear mode, a 2-segmented curve fitting for $log(D_0)$ versus $log(\sigma_{max})$ defined in Eqs. (3.4) – (3.5) was undertaken. Eq. (3.4) shows that $D_0 \propto \sigma_{max}$, such that the stress variation with the damping energy divides into two region of linear and nonlinear fit as shown Fig. 3.6 while at the intersection the linear and nonlinear segments of the curve fitted data is the fatigue stress level measure at $0.8\sigma_f$. Fig. 3.6 shows that below and above the intersection point, the logarithms of total the damping energy $(\log D_0)$ versus the logarithm of maximum stress $(log\sigma_{max})$ are respectively linear and nonlinear.

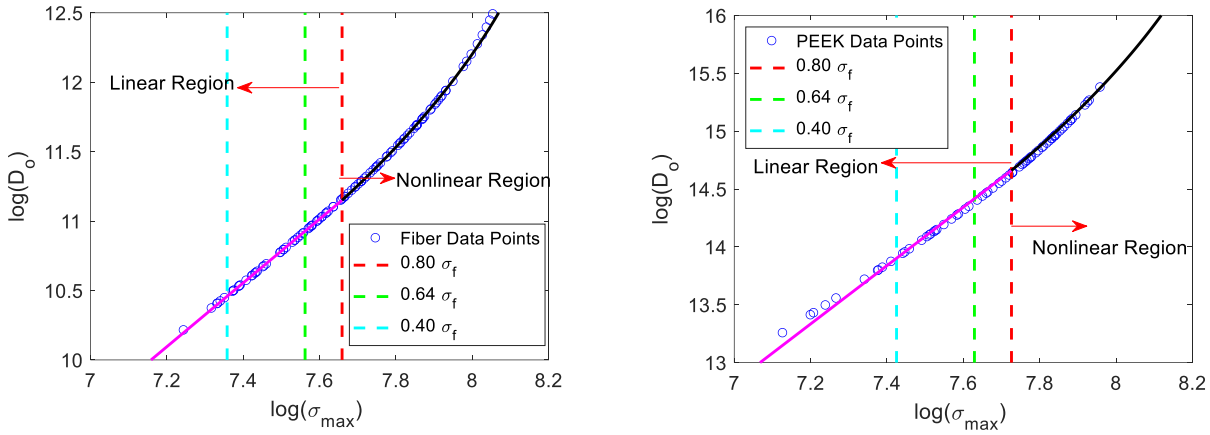

Figure 3.6 Variation of log(D_0) versus log(σ_max): fiber glass (left) and peek (right)

From Fig. 3.6 above, the $0.8\sigma_f$ the fiber and peek materials were independently obtained as 45.614 MPa and 53.670 MPa respectively. Also, $0.64\ \sigma_f$ and $0.40\ \sigma_f$ of each materials are measured at 29.193 MPa and 18.246 MPa and 34.348 MPa and 21.467 MPa respectively for fiber and peek cantilever configurations. The above suggests that when a cantilever structure of equal geometry made from fiberglass and peek material are subjected to equal level of excitation, the peek material will achieve a better stress distribution than the fiber material hence a lager fatigue limit, improved damping and larger responses at equal geometry and excitation. Similarly, while the intersection point on the 2 segment fit is the maximum fatigue point approximated at (σ_f), when the cantilever structure is subjected to vibrations such that the stress distribution approached $0.8\sigma_f$, the responses becomes nonlinear. Since the cantilever structure are fairly loaded and homogenous, therefore, the identified nonlinear behaviors in the stress and damping energy relationship is attributed to material and geometric nonlinearity which onset as σ_{max} approaches$0.8\sigma_f$ typically at$0.4\ \sigma_f \leq \sigma_{max} \leq 0.80\ \sigma_f$.

To further elucidate on how the variation of the stress level in the cantilever structure initiated material nonlinearity and the associated approximations for the linear and nonlinear damping at $\sigma_{max} < 0.8\sigma_f$ or $\sigma_{max} > 0.8\ \sigma_f$, a plot of the variation of the $log\left(\frac{\sigma_{max}}{\sigma_c}\right)$ with $log(\sigma_{max})$ over $0.40\ \sigma_f, 0.60\ \sigma_f, 0.80\ \sigma_f$ and $> 0.80\ \sigma_f$ fatigue level is shown in Fig. 3.7 below.

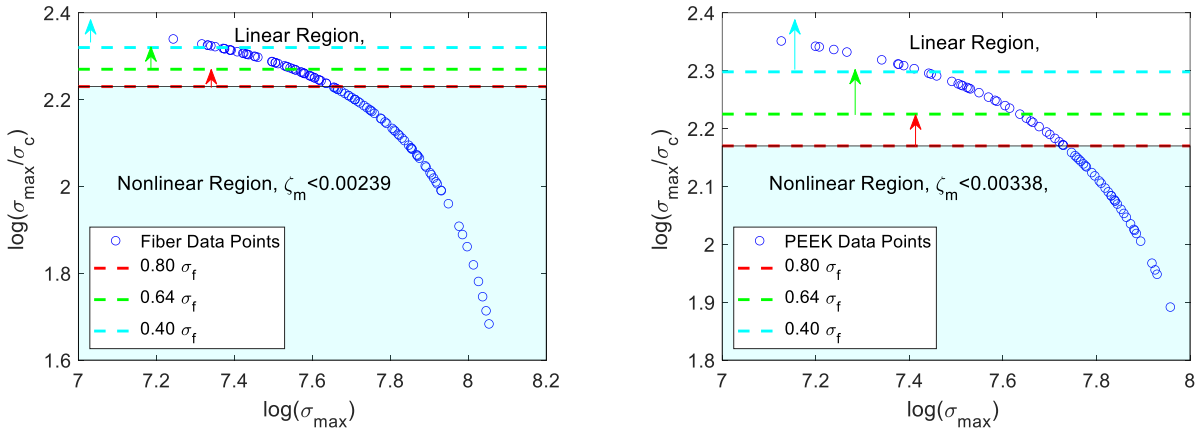

Figure 3.7 Variation of log(σ_max/σ_c) versus log(σ_max): fiber glass (left), and peek (right)

From Eq. (3.6), the half ratio of σ_c to σ_{max} is ζ_m. Taking the log inverse to base 10 of $\left(\frac{\sigma_{max}}{\sigma_c}\right)$ and necessary algebra shows that nonlinear responses sets in at $\zeta_m < 0.00239$ and $\zeta_m < 0.00338$ for fiber and peek cantilever structure respectively, where ζ_m is computed using Eq. (3.8). The implication of the above procedures on the energy harvesting behavior of the cantilever with geometric nonlinearity is shown in the following section.

To obtain a generalized approach for quantifying the operational life time of the cantilevered configuration operated at resonance frequency (f_n) for vibration energy harvesting applications, the Basquin equationor the power law equation [70] as shown in Eq. (3.12) was adopted.

$$\sigma_{max} = \sigma_f (2N_s)^z \tag{3.12}$$

where $\sigma_{max}, \sigma_f, N_s$ and z are the maximum stress, fatigue stress, number of cycles, and the Basquin stress exponent [70]. Another method that was reported to have obtained the fatigue and the cycle is the Palmgren-Miner's rule [71]. The Basquin stress exponent (z) for a fiber glass has been reported as -0.22096 for PVC and $-0.071 - 0.130$ for fiber glass [72]. Taking the logarithm of both sides of Eq. (3.12) gives the expression for obtaining the loading cycle as shown in Eq. (3.13).

$$N_s = \frac{1}{2} log^{-1}\left(\frac{1}{z} log\left(\frac{\sigma_f}{\sigma_{max}}\right)\right) \tag{3.13}$$

When the cantilever beam is operated at resonance (f_n), the average operational time (t) is approximated as the ratio of the loading cycle to the resonance (f_n) as shown in Eq. (3.13).

$$t \cong \frac{N_s^{|z|}}{f_n} \tag{3.13}$$

Using the generalized Eqs. (2.1) – (2.39) and Eqs. (3.7) – (3.11), Fig. 3.7 (left) shows the plot of the response profile of the cantilevered harvester system when both linear and nonlinear responses are initiated subject to respective constraint and boundary conditions. Fig. 3.8 (left) shows that when responses is nonlinear due to geometric nonlinearity associated with the stress distribution in the cantilever, two types of nonlinearity namely; hardening (β is positive) and softening (β is negative) are identified. Hardening nonlinearity occurs when a material becomes stiffer (or harder) as it experiences increasing excitation force inputs, i.e., the material's resistance to deformation increases as the excitation forces or deformation increases. On the other hand, the softening nonlinearity occurs when a material becomes less stiff (or softer) as it experiences increasing excitation; in this case, the material's resistance to deformation decreases with continued loading. Although, initial theoretical analysis shows that the nonlinear jumps in the response profile are not severe, however, their implication of this (i.e., hardening or softening nonlinearity) on the harvester behavior using peek and fiber material shall be investigated and comparatively analyzed in the experimental and parametric section of this chapter.

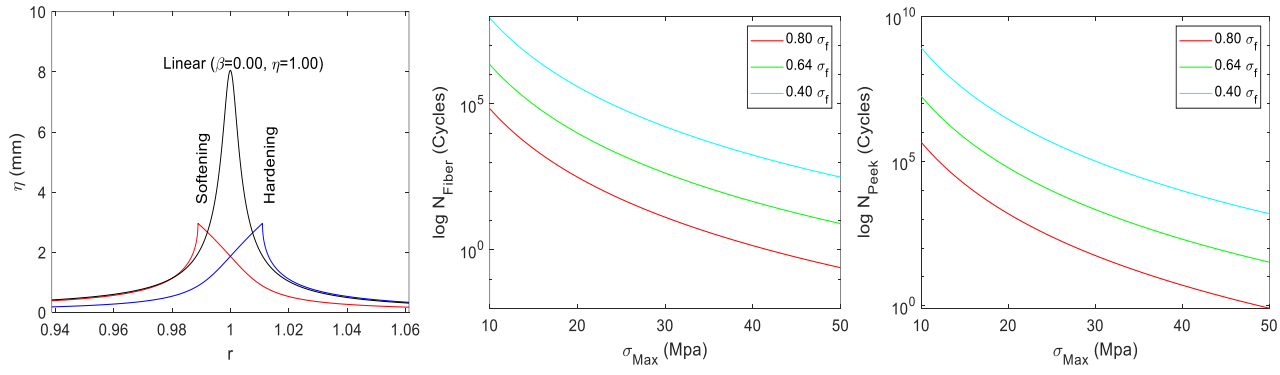

Figure 3.8 Response profile of cantilevered harvester for linear and nonlinear responses (left), variation of σ_max with σ_max over different σ_f for fiberglass (middle) and peek (right)

A plot of the fatigue cycle N computed as functions of σ_{max} obtained at fatigue stress levels $0.8\,\sigma_f, 0.64\,\sigma_f$ and $0.40\,\sigma_f$ for cantilever beam is shown in Fig. 3.8 (middle and right). Fig. 3.7 (middle and right), showed that at equivalent stress level, the peek material achieve a longer loading cycle of $\cong 50$ multiple of the fiber glass counterpart. The figure further highlighted that operating the cantilever structure at lesser stress levels i.e., $\sigma_{max} < 0.8\sigma_f$ will significantly enhance the loading cycle and hence the operational time (t) as shown in Fig 3.9.

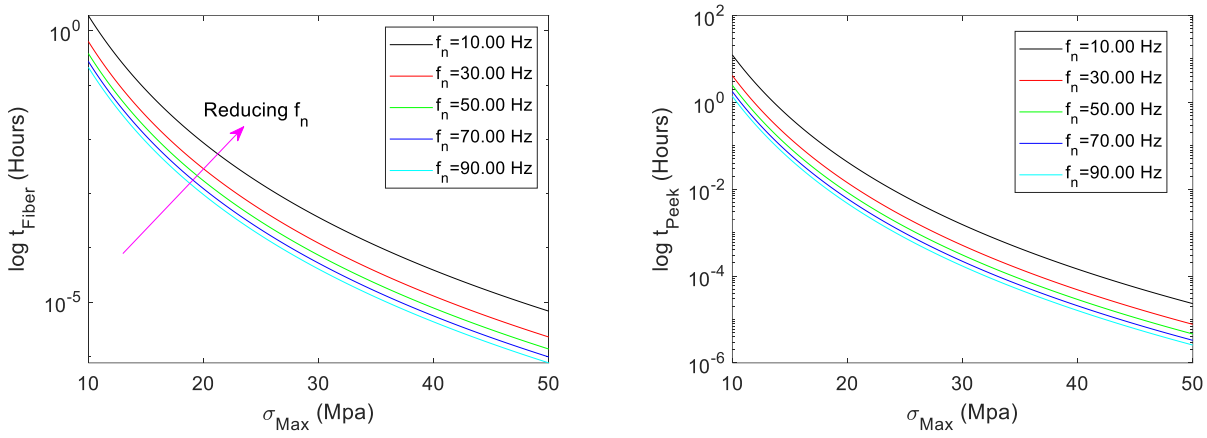

Figure 3.9 Variation of t with σ_f for different f_n, fiberglass (left) and peek (right)

Fig. 3.9(left) and Fig. 3.9(right) respectively showed the variation of the operational time for fiber and peek at σ_f level for different f_n. Peek is generally classified as a high-performance thermoplastic known for its excellent mechanical properties, chemical resistance, and high temperature resistance. Fiberglass, on the other hand, is a composite material made of glass fibers embedded in a polymer matrix, known for its strength and stiffness. The strength-to-weight ratio in Peek is higher than fiber glass, therefore, while both exhibit a linear elastic behavior up to a certain point, the stress profile of Fig. 3.9 showed that while the end of linearity in peek is followed by elastic deformation, the fiberglass composite materials typically exhibit plastic deformation/damage accumulation and eventual failure after the stress exceed the $0.8\sigma_f$ level, hence a shorter operational lifetime of $t \cong 2.00$ hours at $f_n = 10.00$ Hz and $\sigma_{max} = 10.00$ MPa compare to $t \cong 12.50$ hours at $f_n = 10.00$ Hz and $\sigma_{max} = 10.00$ MPa for peek as shown in Fig. 3.9.

To conclude this Chapter, Figs. 3.8 – 3.9 is that peek attained a good fatigue resistance, low creep deformation and good impact resistance. It can withstand cyclic loading for a large number of cycles without failure, thus making it suitable for applications requiring durability under repeated loading. On the other hand, the fiberglass composites can have lesser and varying fatigue resistance depending on the fiber orientation, matrix material, and manufacturing process. Therefore, peeks are generally best options in applications where chemical resistance, high temperature stability, corrosion resistance, and wear resistance are critical compared to fiberglass configurations.

3.2.1 Experimental Verification

The sub-chapter present an approach to experimentally validate the accuracy of the analytical Eqs. (3.4) - (3.12). In a cantilever beam with geometric nonlinearity the damping of the system is computed as a function of the nonlinear stress distribution using the Osborne Goodman's method as earlier stated while the damping in a linear cantilever model is typically constant and does not change significantly at resonance according to Eq. (3.8). When material/geometric nonlinearity is present, changes in stiffness matrix affects the dynamic response of the system and the damping behavior are observed as shown in Eqs. (3.9) – (3.11) causing the damping to change across the excitation profile. The experimental model that was used to validate the accuracy of the equation is shown same as shown in Fig. 2.12. Although the observed nonlinearity is weak, Fig. 3.10 shows the response profile for a peek cantilever configuration with $m_{Tip} = 51.40$ g, $L = 40.05$ mm; 0.10 g (left) and 0.20 g (right) and respective performance parameters shown in Table 3.3. Likewise, Fig. 3.10 shows the response profile for a peek cantilever configuration with $m_{Tip} = 25.75$ g, $L = 56.81$; 0.10 g (left) and 0.20 g (right) and respective performance parameters shown in Table 3.4.

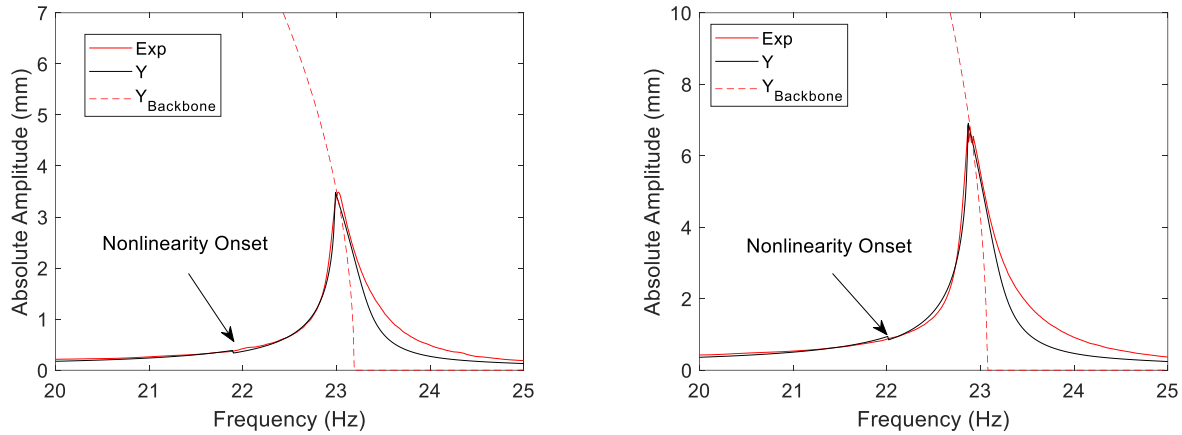

Figure 3.10 Response profile $\mathrm{m_{Tip}} = 51.40$ g, $\mathrm{L} = 40.05$ mm 0.10 g (left) and 0.20 g (right)

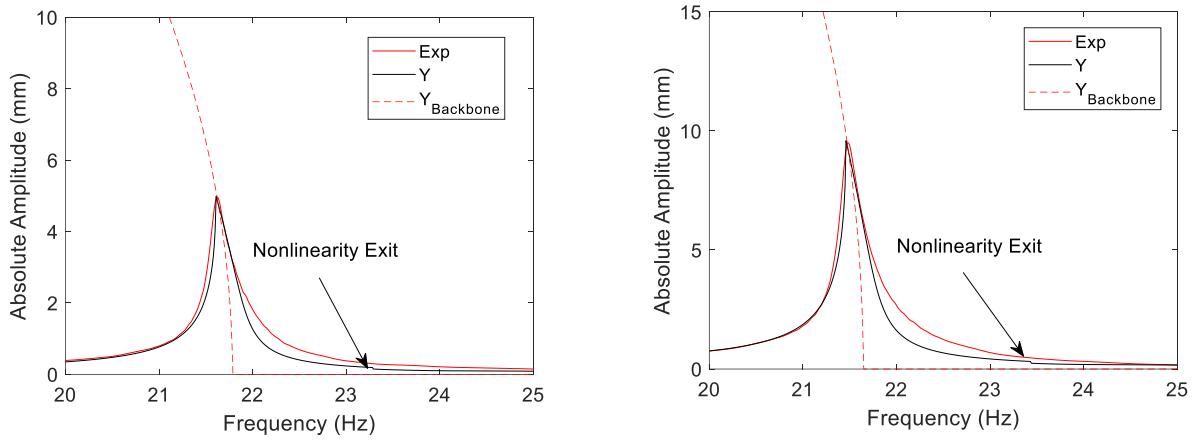

Figure 3.11 Response profile $\mathrm{m_{Tip}} = 25.75$ g, $\mathrm{L} = 56.81$ mm 0.10 g (left) and 0.20 g (right)

Similarly, parameters $\eta, \zeta_m, \eta\beta$, and $\eta\zeta_m$ were observed to be inversely consistent with g and σ_{nl} such that when the acceleration is high, the nonlinear stress in the beam is likewise high, but the $\eta, \zeta_m, \eta\beta$, and $\eta\zeta_m$ reducing as shown in Tables 3.3 and 3.4. Likewise, the micro extention during excitation due to the elastic nature of the cantilever was observed as a linear function of g and σ_{nl}. This implies that as the excitation increased, the beam becomes thinner about the point of moment due to geometrical nonlinearity, hence the resonance is shifted down by approximately 0.85 % for every 50.00 % rise in g.

The fitted plots in Figs. 3.10 – 3.11 shows that the fit equations obtained for characterizing the variation of the nonlinear stress with damping is accurate to approximation of 93.44

%. Generally, for the nonlinear beam under investigation, results indicated that when the excitation frequency (ω) approaches the resonance frequency, deflection are mitigated by the nonlinear damping effect which manifested as a function of the elastic property of the beam resulting in a softening nonlinearity as shown in Figs. 3.10 and 3.11. Figs. 3.10 and 3.11 which manifested as a point of jump in the response profile. These points are characterized as onset or exit of nonlinear which is observed to vary for different configuration such that while $m_{Tip} = 51.40$ g, $L = 40.05$ mm activated nonlinearity onset before resonance while the $m_{Tip} = 25.75$ g, $L = 56.81$ mm exited nonlinearity just after resonance. The characterized onset or exit of nonlinearity is identified as a function of the pre-stress in the beam at static equilibrium such that longer beam $L = 56.81$ mm has a larger static pre-stress and axial extension (δx) than $L = 40.05$ mm as shown in Tables 3.3 to 3.4 where σ_{nL} for larger beam length is higher at equivalent excitations although the tip mass (m_{Tip}) is smaller.

It was earlier identified in Figs. 3.5 and 3.6 that the stress in the cantilever beam approaches nonlinear as it approach the fatigue level i.e., σ_{nL} occurs when $\sigma_{max} \rightarrow \sigma_f$ From Tables 3.3 and 3.4 the stress level for nonlinear onset (σ_{nL}) always lies about $0.5\,\sigma_f < \sigma_{nL} < 0.8\,\sigma_f$ in agreement to the range identified in Figs. 3.5 and 3.6 such that below this identified range, the responses becomes linear hence, the stress-damping analysis is undertaken using the linear Eqs. (3.4) – (3.8).

Table 3.3 Summary of fit parameters for $\mathrm{m_{Tip}} = 51.40$ g, and beam length $\mathrm{L} = 40.05$ mm

g	$f_n(Hz)$	n	η	ζ_m	$\eta\zeta_m \times 10^{-3}$	$\sigma_{nL}(MPa)$	$\delta x\ (\mu m)$	$\eta\beta \times 10^6(Nm^{-3})$
0.10	23.188	3.42	0.0196	0.0137	0.2560	24.965	0.651	10.715
0.20	23.072	3.22	0.0047	0.00975	0.0463	33.8705	2.646	2.744

Table 3.4 Summary of fit parameters for $\mathrm{m_{Tip}} = 25.75$ g, and beam length $\mathrm{L} = 56.81$ mm

g	$f_n(Hz)$	n	η	ζ_m	$\eta\zeta_m \times 10^{-3}$	$\sigma_{nL}(MPa)$	$\delta x\ (\mu m)$	$\eta\beta \times 10^6(Nm^{-3})$
0.10	21.78	3.42	0.01488	0.0138	0.2063	25.137	0.953	5.707

0.20	21.64	3.22	0.00395	0.00932	0.0368	34.127	3.885	1.612

3.2.2 Vibration energy harvesting of cantilever with nonlinear stress

To validate the energy harvesting performances and advantages in the nonlinear domain, the initial condition $0.5\,\sigma_f < \sigma_{nL} < 0.8\,\sigma_f$ as identified above must be satisfied. Below those stress level, the linear analysis is used to illustrate the analytical model of the cantilever. However, above the range, the response becomes chaotic especially as $\sigma_{nL} \geq 0.8\,\sigma_f$.

3.2.2.1 Peek cantilever laminate

Using the governing Eqs. (2.1) – (2.39) and Eqs. (3.4) – (3.11), the responses and power harvested at 0.20 g, and 0.40 g is shown in Figs. 3.12 to 3.15 respectively for different dimensions of the beam and Table 3.5 – 3.6 shows the respective performance indicators for mechanical and electrical properties of the design.

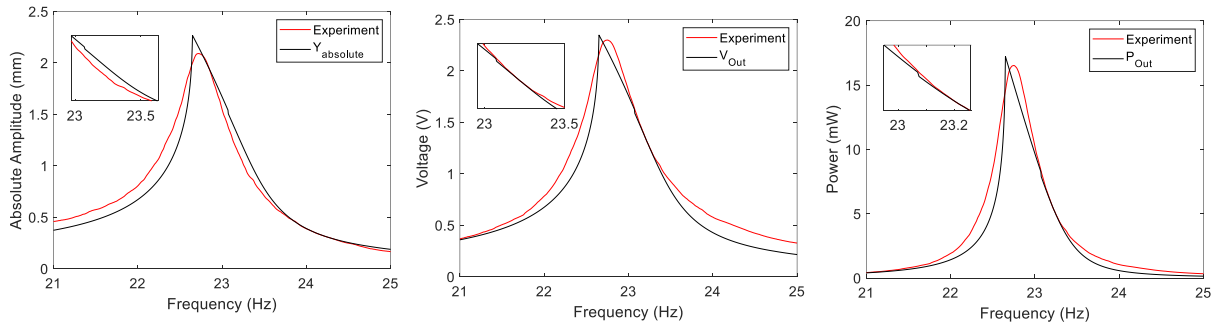

Figure 3.12 Energy harvesting with PEEK for $W = 15.35$ mm at 0.20 g response profile (left) voltage (middle) and power (right)

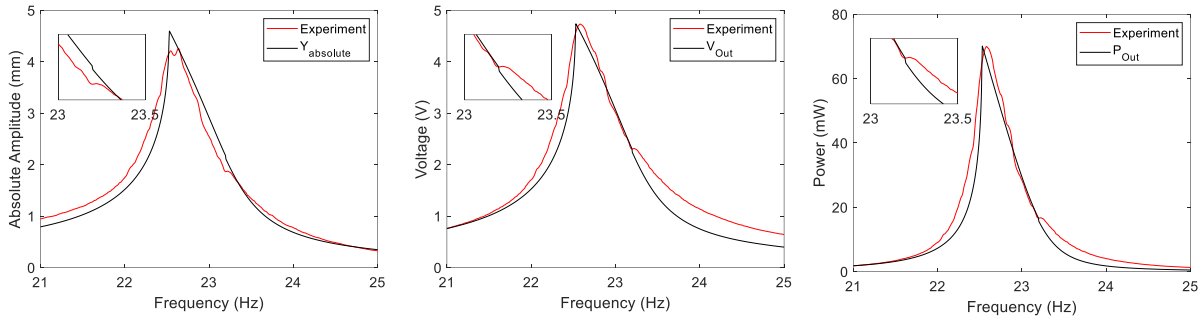

Figure 3.13 Energy harvesting with PEEK $W = 15.35$ mm at 0.40 g response profile (left) voltage (middle) and power (right)

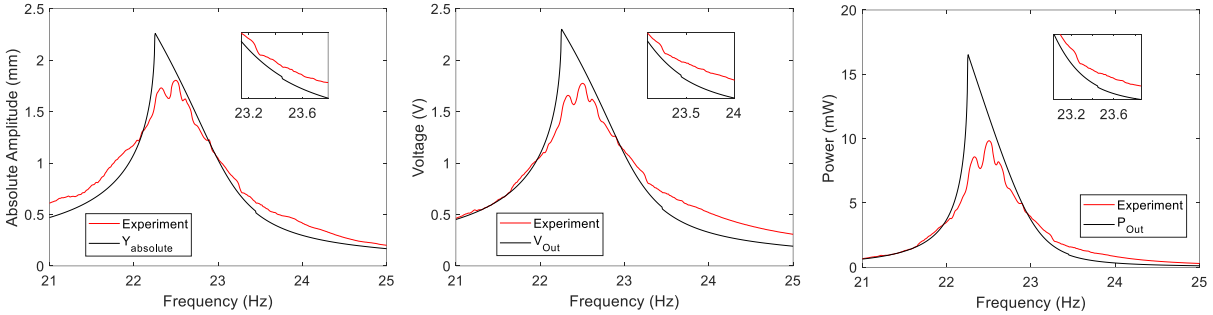

Figure 3.14 Energy harvesting with PEEK $W = 20.22$ mm at 0.20 g response profile (left) voltage (middle) and power (right)

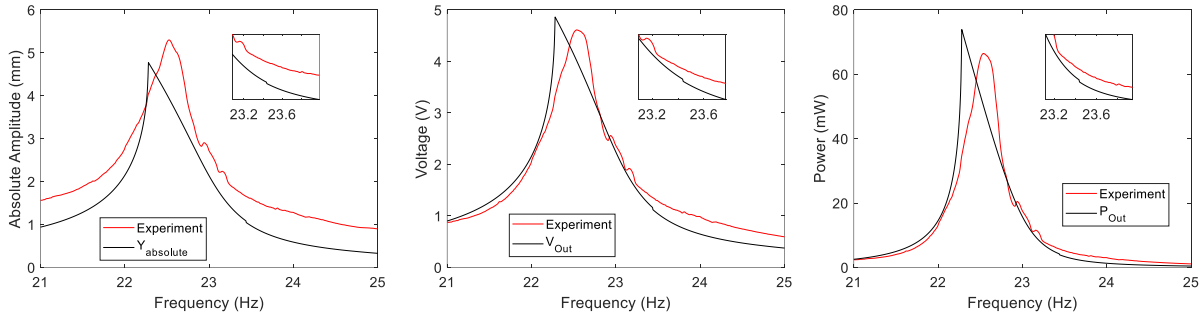

Figure 3.15 Energy harvesting with PEEK $W = 20.22$ mm at 0.20 g response profile (left) voltage (middle) and power (right)

The performance profiles of Figs. 3.12 to 3.15 shows that the governing equations is fitted to an approximated 96.22 % irrespective of the acceleration and the beam dimension. Also the response, voltage and power profile shows obvious deviation from the nonlinear stress-damping analysis to linear stress-damping equivalent at $f \geq 1.02 f_n$. This characterized point for exit of nonlinearity $f \geq 1.02 f_n$ is identified as a function of the pre-stress in the beam at static equilibrium due to the beam length.

Table 3.5 shows the summary of nonlinear mechanical parameters for PEEK at $g = 0.20$, and 0.40. At different g the variation of σ_{nL} region $0.64\sigma_f < \sigma_{nL} < 0.8\sigma_f$ as earlier identified such that below this identified region, the response is characterized in the linear domain.

Table 3.5 Summary of nonlinear mechanical parameters for $g = 0.20$, and 0.40

$L(mm)$	$W(mm)$	$T(mm)$	g	$f_n(Hz)$	$\zeta_m \times 10^{-3}$	n	$\eta \times 10^{-2}$	$\sigma_{nL}(MPa)$	δx (μm)
43.14	15.35	2.193	0.20	23.13	3.01	2.33	4.47	24.26	0.69
		2.185	0.40	23.00	4.04	2.92	1.33	51.24	20.95
49.44	20.22	2.18	0.20	22.76	2.87	2.21	4.34	23.06	9.23
		2.17	0.40	22.72	3.75	2.32	0.97	41.64	28.34

Table 3.6 shows the variation of the electromagnetic parameter, harvested voltage and power at optimum load resistance $R_l^{opt} = 320.00\ \Omega$. Table 3.6 shows that the nonlinear stress in the beam is likewise a linear function of ζ_{coil}, v_{out}, and P_{out}.

Table 3.6 Summary of nonlinear electromagnetic parameters and power harvested for $g = 0.20$, and 0.40

$L(mm)$	g	$f_n(Hz)$	$\zeta_{coil} \times 10^{-2}$	$Y\ (mm)$	$v_{out}(V)$	$P_{out}^{max}\ (mW)$
43.14	0.20	23.13	2.32	2.404	2.347	17.221
	0.40	23.00	2.32	4.881	4.738	70.159
49.44	0.20	22.76	2.26	2.393	2.299	16.523
	0.40	22.76	2.26	5.063	4.864	73.935

3.2.2.2 Fiberglass cantilever laminate

Using the governing Eqs. (2.1) – (2.39) and Eqs. (3.4) – (3.11), the responses and power harvested at 0.20g, and 0.40g is shown in Figs. 3.12 to 3.15 respectively for different dimensions of the beam fitted to an approximated 96.22 % irrespective of the acceleration

and the beam dimension and Tables 3.7 – 3.8 shows the respective performance indicators for mechanical and electrical properties of the design.

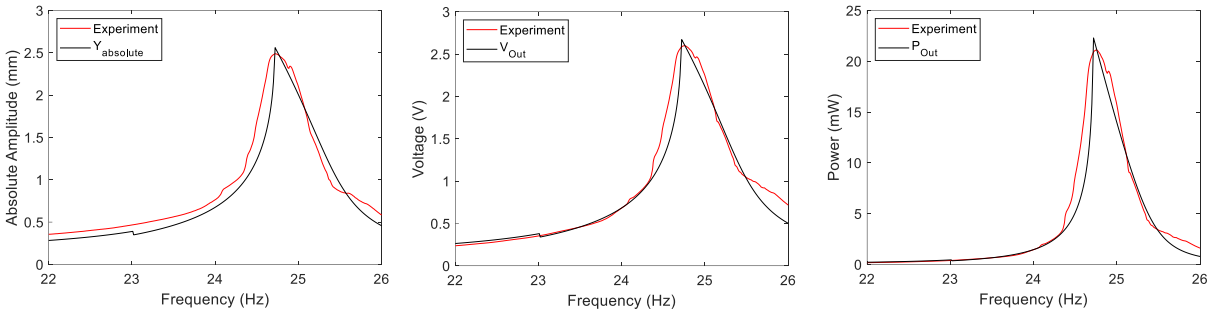

Figure 3.16 Energy harvesting with PEEK for $W = 12.00$ mm at 0.20 g response profile (left) voltage (middle) and power (right)

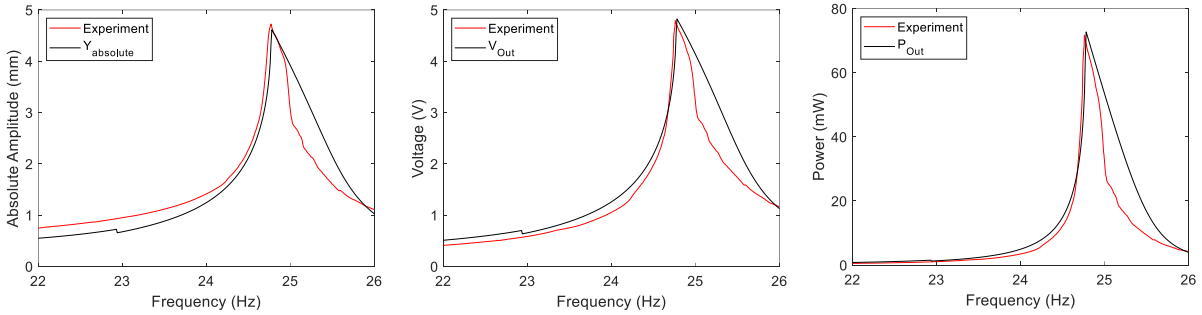

Figure 3.17 Energy harvesting with PEEK $W = 12.00$ mm at 0.40 g response profile (left) voltage (middle) and power (right)

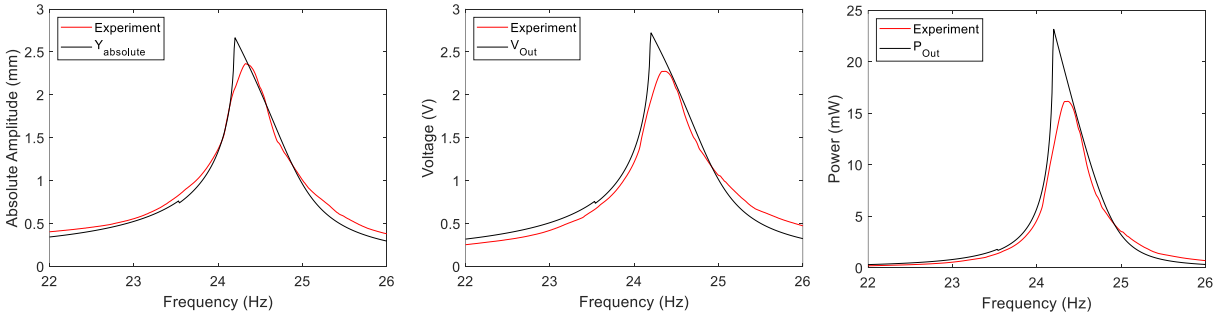

Figure 3.18 Energy harvesting with PEEK for $W = 15.00$ mm at 0.20 g response profile (left) voltage (middle) and power (right)

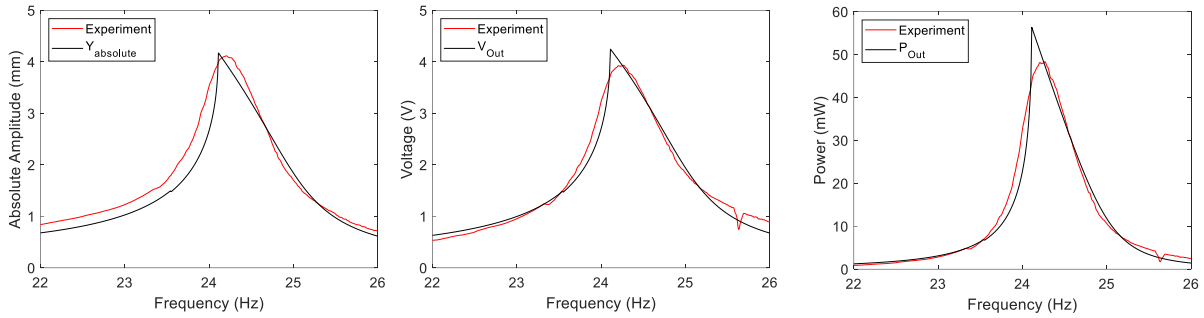

Figure 3.19 Energy harvesting with PEEK for $W = 15.00$ mm at 0.40 g response profile (left) voltage (middle) and power (right)

Table 3.7 shows the summary of nonlinear mechanical parameters for fiberglass at $g = 0.20$, and 0.40. At different g the variation of σ_{nL} region $0.64\sigma_f < \sigma_{nL} < 0.8\sigma_f$ as earlier identified such that below this identified region, the response is characterized in the linear domain

Table 3.7 Summary of nonlinear mechanical parameters for fiberglass at $g = 0.20$, and 0.40

$L(mm)$	$W(mm)$	$T(mm)$	g	$f_n(Hz)$	$\zeta_m \times 10^{-3}$	n	$\eta \times 10^{-2}$	$\sigma_{nL}(MPa)$	δx (μm)
73.52	12.00	2.093	0.20	25.173	0.1344	3.480	0.649	72.952	7.721
		2.099	0.40	25.281	0.0451	3.885	1.990	105.173	20.295
81.82	15.00	2.095	0.20	24.706	0.1116	3.450	0.552	71.153	9.877
		2.095	0.40	24.706	0.0649	3.520	0.294	102.159	26.705

Table 3.8 Summary, nonlinear electromagnetic parameters and power for fiberglass at $g = 0.20$, and 0.40

$L(mm)$	g	$f_n(Hz)$	$\zeta_{coil} \times 10^{-2}$	$Y\ (mm)$	$v_{out}(V)$	$P_{Out}^{max}\ (mW)$
73.52	0.20	25.173	1.661	2.772	2.599	21.106
	0.40	25.281	1.654	5.038	4.791	71.743
81.82	0.20	24.706	1.637	2.984	2. 753	23.684
	0.40	24.706	1.637	4.151	3.933	48.347

To characterize the harvester preferential comparison of the PEEK and fiber laminate, three indicators were compared in terms of the harvested power, design volume and power density analysis.

The power density of an energy harvested was computed from Eq. (2.50) as the ratio of the harvested power to the system design volume. The actual practical volume of the harvester (V_p) during operation defined as shown in Eq. (3.14).

$$V_p = LW(h_A + Y) \tag{3.14}$$

where, L, W, and h_A are the actual practical length, width, and height of the design. Also, Y is the maximum response of coil during excitation.

Likewise, the normalized power density (NPD) which is the power output density of the device normalized to base acceleration and frequency as shown in Eq. (3.15).

$$NP_D = \frac{P_D}{fg^2} \tag{3.15}$$

From Fig. 3.90, the respective values of L, W, and Y for each design configuration is shown in Tables 3.5 and 3.7 where $h_A = 15.50\ \mathrm{mm}$. Table 3.9 shows the summary of V_A, P_{Out}^{max}, P_D, and NP_D for each configurations at an applied load of $R_l = 320.00\ \Omega$.

Table 3.9 Summary of power and power density comparison for different material

Material	Configuration			$f_n(Hz)$	g	Y (mm)	P_{Out}^{max} (mW)	V_p (cm^3)	P_D ($mW\mathrm{cm}^{-3}$)	NP_D ($\mathrm{Wm}^{-1}\mathrm{s}^{-5}$)
	$L(\mathrm{mm})$	$W(\mathrm{mm})$	$T(\mathrm{mm})$							
PEEK	43.14	15.35	2.19	23.13	0.20	2.404	17.221	10.26	1.6778	362.69
			2.19	23.00	0.40	4.881	70.159	11.86	5.9176	643.22
	49.44	20.22	2.18	22.76	0.20	2.393	16.523	20.37	0.8109	178.16
			2.17	22.76	0.40	5.063	73.935	17.89	4.1334	454.02
FIBER	73.52	12.00	2.09	25.17	0.20	2.772	21.106	18.14	1.1634	231.08
			2.10	25.28	0.40	5.038	71.743	16.12	4.4505	440.10
	81.82	15.00	2.10	24.71	0.20	2.984	23.684	25.21	0.9396	190.16
			2.10	24.71	0.40	4.151	48.347	22.69	2.1312	215.66

Table 3.9 shows the power density comparison of fiberglass configurations with the PEEK design transduction methods. The table generally shows that at an approximate equivalent excitation and resonance, the fiberglass configuration always attain a larger design volume, lesser power densities and lesser normalized power densities while approaching fatigue stress level earlier than PEEK design. The above is indicative that using the PEEK laminate in a cantilever harvester design is desirable in term of power density, power and operational volume. Since the PEEK is often characterized by much better plastic/elastic properties than fiberglass, it is therefore intuitive to conclude that material that operation cantilever design with material that shows more plastic behavior will enhance the power density performances while reducing practical volume for practicable smart applications. The following section shows the performance comparison of the harvester performance using a PEEK material with linear steel configurations.

3.2.3 Energy harvesting comparisons of nonlinear with linear laminates

By comparing harvesting performances at nonlinear stress with linear stress in cantilever beams for energy harvesting applications, valuable insights into the limitations, preferences and challenges associated with nonlinear behavior can be gleaned. The results in this section will give an understanding of how nonlinear stress affects the mechanical response and energy conversion capabilities of the beam as an essential factor for optimizing the design, performance, and durability of energy harvesting systems. To ensure effective comparison of the linear and nonlinear performances, comparison is undertaken at equivalent resonances as shown in Fig. 3.16 while the performance comparison is shown in Table 3.7.

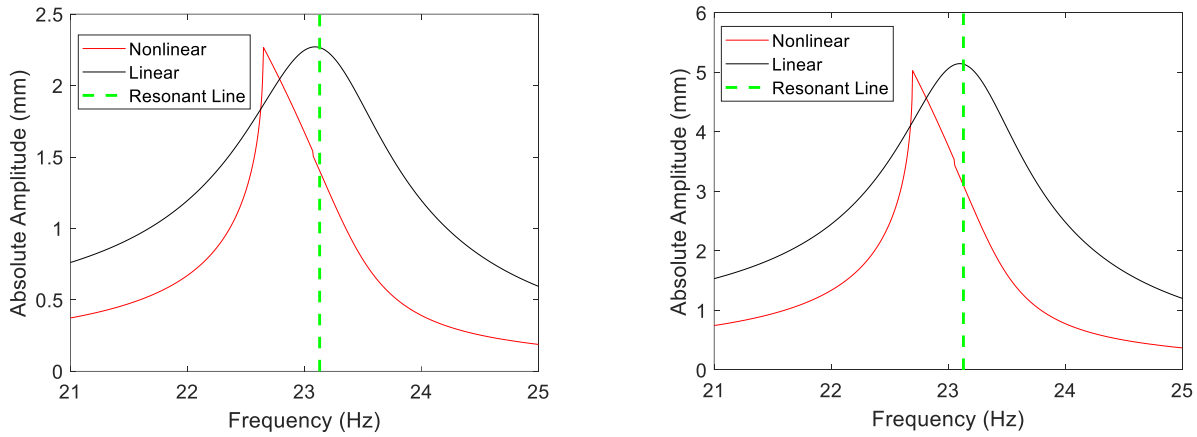

Figure 3.20 Response comparison of linear and nonlinear cantilever design; 0.10 g (left) and 0.20 g (right)

Fig. 3.15 shows that although the response profile showed a compromise on the operational bandwidth relative to the nonlinear model, Table 3.7 however showed that longer beam length compromised on the power density is attained on the linear model at equivalent resonances since the effective length that realized equivalent resonances on the linear configuration is approximately a double of the nonlinear design. This observation further confirms the preference of materials with more elastics/plastic behaviors for enhanced power density as shown in the last section.

Table 3.10 Summary of nonlinear mechanical parameters for $g = 0.10$, and 0.20

Mode	g	L (mm)	E (GPa)	f_n (Hz)	δx (μm)	n	σ_c (MPa)	σ_{nL} (MPa)
Linear	0.20	70.20	175.00	23.13	-	-	0.26	-
	0.40	70.20	3.644	23.13	-	2.33	0.53	-
Nonlinear	0.20	43.14	175.00	23.13	0.69	-	-	24.26
	0.40	43.14	3.644	23.00	20.95	2.92	-	55.00

3.2.4 Parametric Analysis

In this section, a parametric analysis with a cantilever beam with material nonlinearity was undertaken by studying the effects of varying beam parameters on the behavior and performance of the harvester. The parameters considered are the beam length (L), beam

width (W) and beam thickness (T). This section attained systematically varying the parameters and analyzing their impact on the system performances; mainly the response peak/harvested power and the operational bandwidth. Undertaking the above analysis makes it possible to identify optimal configurations that maximize energy harvesting capabilities as shown in Fig. 3.17.

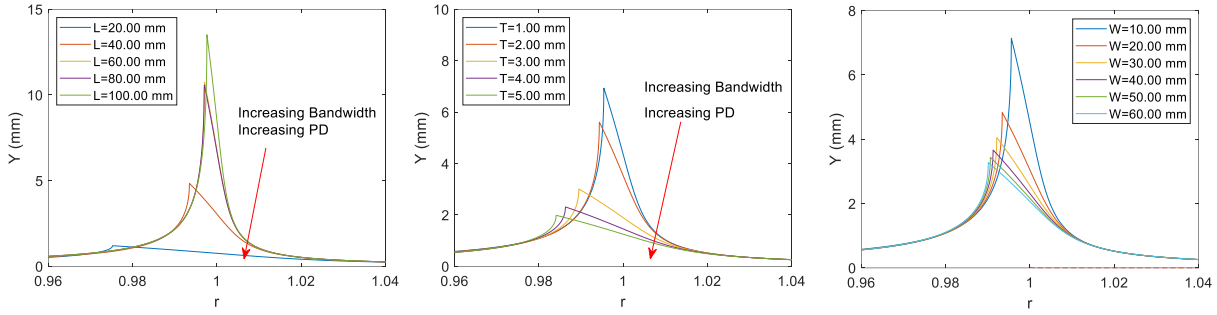

Figure 3.21 Parametric comparison of the response performance with L (left), T (middle) and W (right)

The results in Fig. 3.17 showed that reducing the length, width and thickness of the beam independently led to a broadening of the bandwidth while reducing the response peak, indicating an improved ability to capture a wider range of vibration frequencies at a compromised resonant maximum power output although the power density will be enhanced. However, changing the beam width did not produce significant changes in the bandwidth compared to length and thickness. Therefore, the length and thickness of the beam are more influential in determining the performance of the harvester in capturing vibration energy across a range of frequencies while enhancing the power density of the design.

3.3 Summary

Chapter 3 delves into the intricate dynamics of linear and nonlinear stress and damping in cantilevered energy harvesters, providing a comprehensive theoretical framework and analysis of these critical aspects. By examining the behavior of cantilevered structures under varying stress conditions, the chapter elucidates the impact of linear and nonlinear stress on the performance and efficiency of energy harvesters. The discussion on damping mechanisms sheds light on how energy dissipation influences the overall system response and potential power generation capabilities.

Through detailed theoretical models and analytical approaches, the chapter explores the interplay between stress, damping, and harvester behavior, offering valuable insights into the design optimization and performance enhancement of cantilevered energy harvesters. By elucidating the complexities of linear and nonlinear dynamics in these systems, this chapter contributes to a deeper understanding of the underlying principles governing energy harvesting mechanisms, paving the way for advancements in the development of efficient and robust harvester designs when material nonlinearity are present in cantilever harvester designs highlighting the following

i. Characterized onset or exit of nonlinearity is identified as a function of the pre-stress in the beam at static equilibrium such that longer beam $L = 56.81$ mm has a larger static pre-stress and axial extension (δx) than $L = 40.05$ mm as shown in Table 3.3 to 3.4 where σ_{nL} for larger beam length is higher at equivalent excitations although the tip mass (m_{Tip}) is smaller.
ii. Nonlinear geometric effect occurs when the stress distribution in the beam approached σ_f . The interval $0.64\sigma_f < \sigma_{nL} < 0.8\sigma_f$ corresponds to stress level where geometric nonlinearity occurs in the configuration, below such levels the responses becomes linear. However, above the range, the response becomes chaotic especially as $\sigma_{nL} \geq 0.8\,\sigma_f$.
iii. Power analysis showed that although the nonlinear configuration was disadvantaged in terms of the operational bandwidth relative to the linear design, the power density are significantly compromised on the linear domain. Therefore, material that operation cantilever design with material that shows more plastic behavior will enhance the power density performances while reducing practical volume for practicable smart applications.
iv. Parametric analysis showed that reducing the length, width and thickness of the cantilever beam significantly enhances the operational bandwidth and the power density of the design.
v. Although no competitive advantages is observed in the peak output of the linear design compared to the design with material nonlinearity at equivalent excitation, the nonlinear design however shows prospect for achieving a higher power density

and down shifting of the peak output resonances because the effective length required for equivalent resonances is half those required for linear applications

CHAPTER 4: Dynamic responses of the 2DOF electromagnetic vibration energy harvester through different electrical coil connections

4.0 Introduction.

The dynamic response of a 2-degree-of-freedom (2DOF) electromagnetic vibration energy harvester can be influenced by the electrical connections of the coil. The electrical connections determine how the induced voltage from the coil is utilized and can significantly impact the performance of the harvester. While the coils in the 2DOF designs could be connected independently, one common configuration is the series connection of the coils, where the induced voltages from each coil are added together. This configuration can increase the overall voltage output of the harvester but may also introduce additional impedance and affect the resonant frequency of the system. Another configuration is the parallel connection of the coils, where the induced voltages are combined in parallel. This configuration can reduce the impedance of the system and potentially improve the overall power output, but may also introduce challenges in matching the impedance of the electrical load. Additionally, the cross-connection of the coils, where the induced voltages are connected in a cross pattern, can offer a compromise between the series and parallel connections. This configuration can provide a balance between voltage output and impedance matching, leading to optimal performance of the harvester. Overall, the electrical coil connections play a crucial role in determining the dynamic response and performance of a 2DOF electromagnetic vibration energy harvester. Careful consideration and optimization of the electrical connections are essential to maximize the energy harvesting efficiency and ensure the successful operation of the device.

A two degree of freedom (2DOF) system has been analyzed and presented in literatures as a system having two independent directions/axes of response to external vibration. Engineering applications of a 2DOF system among others include a quarter-vehicle model which has found practical applications in the modelling and analysis of suspensions (shock absorbers) in automobiles, helicopter cockpits, vibration

isolators/absorbers, etc. One unique feature of a 2DOF system is that the system has two normal vibration modes corresponding to two natural frequencies such that if an arbitrary initial excitation is imposed on the system, the resulting free vibration will be a superposition of the two normal modes of vibration corresponding to both natural frequencies. Most of the harvester type reported in literature is a resonant single-DOF (SDOF) system such that the performance of such an SDOF system is optimum when the external excitation coincides with the predefined resonance. While noting that the concept of resonance is likewise applicable to 2DOF system, readily available sources of vibrations include, among others, those induced from train motion, vehicle suspensions, air conditioning systems, vibrations in cockpits and wingspans of flying vehicles etc. Real life applications of energy harvesters tap from this vibration sources to either monitor the structural health or power up sensors and micro gadgets operational on the vehicles. A review, analysis and comparison of methods for harvesting train induced vibration was investigated using electromagnetic, piezoelectric, triboelectric and hydraulic transduction methods by harvesting considerable amount out of the total 14% energy loss associated with vibration, traction and heat during train motion to achieve a power supply for the structural health monitoring sensors on the track line and the vehicle while mentioning limitations such as stability, durability and economy as problems that are yet to be fully resolved in current research literatures [81]. An efficient and approximate method for computation of the harvested energy for train induced bridge vibrations was presented [82] as equivalent to the analytical modal solutions of the simply-supported Euler-Bernoulli beam transverse response under moving loads, while conceptualizing the train as a moving load it concludes that the harvested energy is strongly dependent on the rail traffic and a clear succinct mathematical model for the energy harvested found the optimum amount of energy harvested per unit mass is proportional to the product of the square of the input base acceleration amplitude and the square of the input duration [83]. Similarly, a conceptualization and optimization of a real life electromagnetic harvester using rail was demonstrated [84] and validated using the multi-physics model, and an average electrical power of $6.5\,\mathrm{mW}$ was obtained experimentally. Likewise, various morphologies and designs of energy harvester; mostly electromagnetic based was reported to have been incorporated into various parts of automobiles like the suspension

[85], [86] and [87], rack and gear transmission [88] etc., and tested to give satisfactory performance to have harvest considerable vibration energy useable by payload and other micro gadgets/sensors on the automobiles.

Most of the harvester design reported in literature are resonant energy harvesters such that once they are factory tuned to a resonant, they cannot self-adjust to the dominant frequency of its environment in the event of spurious and stochastic vibration discharge. This situation constitute the major limitations to the efficient and autonomous operation of energy harvesting devices since such resonant harvesters are characterized by a narrow bandwidth, however, recent advances undertaken to overcome the demerits of such resonant systems [89], [90]. In an attempt to ensure a consistent, high, broadband and autonomous power supply is available to remote sensors, authors have reported on various methodologies of achieving such a novel ambition by varying the harvester's design parameters to achieve higher response or frequency tuning/up conversion using pair of magnets [91], [92], stoppers [90], [93], [94] spring [95], parametric pendulums [96], antiphase motion [97] etc. One recent approach to achieving a better response culminating in harvesting a higher power at a lower resonant frequency in using a multi-DOF energy harvester. A novel example of such approach is the wave energy converter (WEC) that uses a spherical submerged body to increases the average captured power by 26 % for the WECs going from 2DOF to 4DOF while a 19% decrease going from 2DOF to 5DOF was observed in the resonant frequency. These results translate to capturing power more efficiently at a lower resonant frequency [98] while another approach resulted in an increased bandwidth [99]. The use of a six degree of freedom (6 DOF) triboelectric Nano-generator (TENGs) designed to mimic the petal of a flower floating on ocean to harvest the chaotically stochastic ocean waves along the six possible DOFs was demonstrated to capture blue (ocean/sea) energy. The impressive device triggered by a water wave frequency of about 1.3 Hz and a wave height of about 8 cm charged a capacitor of $220\ \mu F$ to a voltage of $1.3\ V$ in 1 minute while the harvested power was used to power a watch, a calculator, and a hygrometer thereby showing promising applications in developing self-powered smart marine sensors and distributed power systems in oceans [100]. Likewise a novel approach to harvest vibrational energy in the freight cable

was introduced in [101]. The systems were demonstrated to be highly efficient, portable, and reliable but plagued by two main challenges. These challenges as reported are capturing arbitrary random/stochastic vibrational energy efficiently and increasing the output power so that the system is suitable for cableway equipment that requires high power.

A parametrically excited harvester was demonstrated to have resulted in a large amplitude response and a potential buildup of harvested power because unlike the conventional harvesting technology that depends on the direct activation of the fundamental modes of resonance. The parametric excitation introduces a paradigm shift distinct from the normal resonant excitation because at least one of the system parameters is modulated to be time dependent. However, such feats come at potentially expensive limiting factors of requiring the excitation amplitude to exceed a certain initiation threshold prior to onset of the parametric resonant regime. A novel mechanism and design to reduce the short-comings of a parametrically excited vibration energy harvester (PEVEH) for practical realization are investigated [102]. As stated earlier, it was iterated in Ref. [102] that the wideband performance of a parametric harvester was limited by the nature of the ambient excitation whose amplitudes are often not high enough to initiate a parametric excitation. An attempt to reduce the potential barrier that initiates a parametric excitation includes a wideband two-element piezoelectric energy harvester with both bi-stability and parametric resonance characteristics employing magnetic coupling effects between a parametrically excited beam with another directly excited beam [103]. The use of nonlinear stress-strain curves to achieve desired nonlinearities through field-induced striction by magnetostriction or electrostriction different from existing approaches, where external fields are harvested using strictive effects, the authors reported employing external fields that manipulate the effective Young's modulus to achieve parametric excitations [104]. Using a pendulum-based harvester-absorber that allows for an improved vibration suppression and harvesting simultaneously by fixing the same poled cylindrical magnet to the sides of the pendulum hinged on a rotor and stator mechanism to initiate electromagnetic transduction, while other sets of same poled magnets are fitted to the primary structure in a position such that their field could interact

with those on the pendulum was reported [105]. Thus, additional vibration energy of the primary structure can be transferred to the motion of the pendulum if properly tuned hence energy will be harvested by the electromagnetic harvester mounted on the pendulum's pivot [105].

At this point it becomes necessary to state that some harvester system prototypes, including the one presented in this work, are fully dependent on friction, since friction is introduced into the system due to the gliding/relative movement of the free parts. Friction is usually an unwanted feature in a mechanical system since it is mostly the cause of energy waste manifested as wear and tear, unnecessary noise, and heat. However, in energy harvesting systems, they could be beneficial to achieve an enhanced performance in term of response or bandwidth if properly tuned. For the majority of the work reported, it was found that the Coulomb damping model was able to produce the closest match to the experimental data although the LuGre model proved more suitable in one case having a relatively high level of friction [106].

It was earlier stated that frictional force is a major but unwanted part of the harvested system whose disadvantage could be exploited to achieve a better performance and or enhanced bandwidth, several attempts that describe a correct model to characterize the friction forces were explored and presented by authors. The smooth Coulomb friction was adequately modelled [107], and was found to suppress the vibration response and effectively dissipate vibration response. Responses of mechanical system under different friction models was reported [106], [107] and [108]. Here, the Coulomb friction models were observed to give a result with the closest match to the experiment. Hence, such a model can be adopted to characterize the nature of the friction in our design, while noting that the design approach adopted in this work ensured that this predatory friction type is reduced to the possible minimum in the moving parts as it has the capacity to limit/reduce the systems response.

In this chapter, the focus will center on the design, modeling, verification, and experimentation with a 2DOF electromagnetic vibration energy harvester. The analysis of the harvester's performance was investigated under three different coil connection configurations: individual, series, and parallel connections to ascertain which

configuration type is the most appropriate to ensure a suitable impedance matching between the sensor and the harvester. A detailed analysis of the 2DOF system presented here opens a new potential for a performance trade-off in the power harvested, power density and operational bandwidth of vibration energy harvester.

The analysis of the harvester's performance was investigated under three different coil connection configurations: individual, series, and parallel connections to ascertain which configuration type is the most appropriate to ensure a suitable impedance matching between the sensor and the harvester. The system design reported in this work demonstrates practical applicability such as harvesting vibration energy on automobile body and suspension during motion to power sensors used for monitoring the structural health and working condition of the vehicle, as well to power the Light Emitting Diode (LED) lightning systems since recent car designers have opted for LEDs as lightning to ensure energy optimization [86]. The proposed design and its geometrical and electromagnetic damping are yet to be optimized, noting that the optimization will further reduce the overall mass and further enhance the systems performance thereby expanding the scope of usability of the harvester design to cover a wide spectrum of applications, including for powering micro gadgets and wearable electronics.

The chapter presented here is organized as follows. Chapter 4.2 introduces the governing equation of forced coulomb-damped 2DOF system where the analytical solution for the steady state responses and the associated phase of each degree of freedom was obtained. The steady state response analysis of each mass was investigated to assert the extent and nature of the response while the dynamic nature of the coulomb friction on the response was imposed as a tool for response tuning, hence categorizing the response as either continuous, stick or stick-slip in nature. Derivation of the electromagnetic damping ratio, voltage, and power equation for different connections configurations were introduced in Chapter 4.3. In Chapter 4.4, a five-stage experimentation on the determination of the spring's stiffness, mechanical damping, optimum load resistance, system response and the harvested voltage/power was undertaken and compared with the theoretical results introduced in Chapter 4.2. The harvested power and power densities using optimum load resistance was considered and normalized with respective

mass accelerations and frequencies and compared with those reported in recent literatures in Chapter 5. Finally, the work was concluded in Chapter 4.6.

4.1 Governing equation and theory of forced Coulomb-damped 2DOF harvester.

An exact solution for the steady forced vibration of a 2DOF system with two viscous and Coulomb dampers subjected to a simple harmonic ground excitation is presented in this work. Den Hartog [108] and Luca Marino [109], [110] reported the exact solution of steady forced vibration of a single DOF system with combined viscous and Coulomb damping. Whereas both authors consider an SDOF approach, this work shall extend the approach presented for the implementation to a 2DOF energy harvester system while characterizing the dynamic friction and finally optimizing the power harvested base the connection types of an external load resistance.

The response of the system described above requires two independent coordinates, x_1 and x_2, to fully characterize the respective responses of masses, m_1 and m_2, such that for each response coordinate, the governing equation is in the form of a coupled differential equation. If the harmonic solution is assumed for each coordinate, the solution of the coupled differential equation causes the system to respond in two distinct vibration modes such that an arbitrary initial excitation applied to the system will result in free vibration having the superposition of the two normal vibration modes. However, if the system vibrates under the action of an external harmonic force, the resulting forced harmonic vibration takes place at the frequency of the applied force.

A simplified model for a 2DOF spring-mass is shown in Fig. 1, which is investigated under four different design geometrical configurations (cases); noting that each design variation was achieved by varying the numbers and positions of coulomb friction contacts between the masses and the joined base-wall. The case 4 design was achieved when coulomb (friction) contacts F_{r_1} and F_{r_2} are present on both the lower and upper masses respectively, while both coulomb contacts are absent in the case 1. In cases 2 and 3, either coulomb contact F_{r_1} or F_{r_2} is absent in the respective mass.

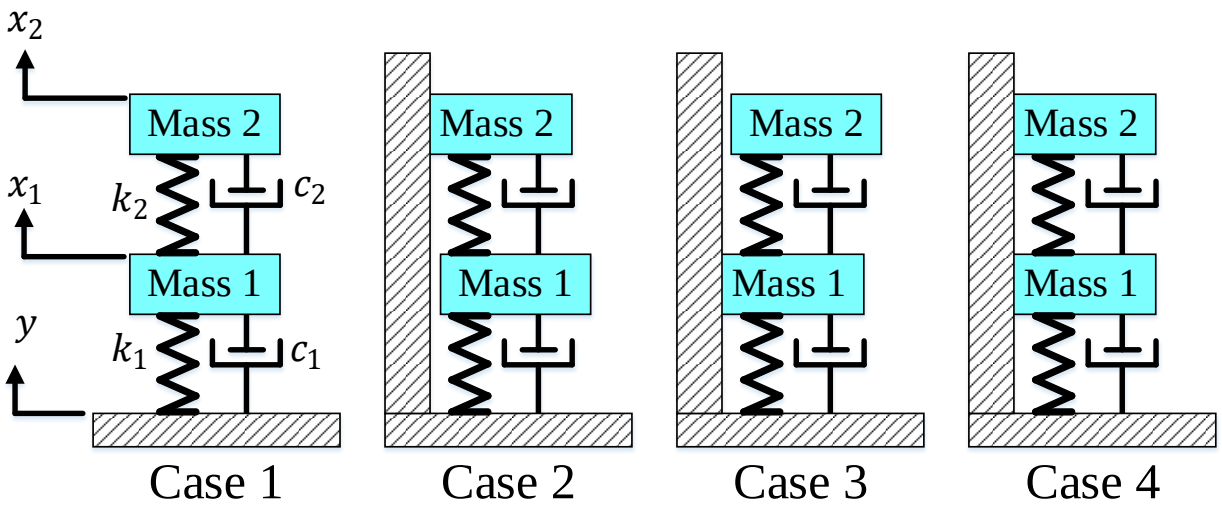

Figure 4.1 Four different configurations for joint base wall interaction of 2DOF system

Although frictions are usually undesirable in mechanical systems, they became unavoidable and important design considerations in the harvested design proposed here since the 2DOF system has a linear guide rail as a mechanism to achieve a constrained response in the desired DOF, this constrained response from the guiderail likewise prevents an unwanted bending/buckling in the linear spring. The purpose of the guide rail is to provide a vertical motion in the experiment since it will be impractical for the masses to move vertically without a support because of bending/buckling in the spring. During an excitation, a dynamic friction effect modeled as a coulomb friction is set up between the moveable parts of the guiderails. A theoretical approach and friction modeling was undertaken to investigate the response of the harvester design under all four different possible constraints and since the guiderails used are identical, it is assumed that the magnitude of the dynamic friction force on the preload contact space of the guide rails is equal since the upper and lower masses have identical masses.

In the following analysis of the 2DOF system, x_i, c_i, k_i, F_{r_i} and Y refers to the absolute vertical motion of each mass under a sinusoidal base excitation input of $Ye^{i\omega t}$. The viscous damping coefficient, spring stiffness, the magnitude of the frictional force (between the mass and the joint base wall's surface) and the amplitude of sinusoidal base excitation input associated with each respective mass m_1 and m_2 (considered under 4 different mass-joint base wall's configurations) as shown in Fig 4.1. A general solution

that encapsulates the whole model (case 4) will be presented while the necessary constraints will be imposed on the said generic case 4's solution to realize other configurations. For example, to realize cases 3, 2 and 1 from case 4, $F_{r_2} = 0, F_{r_1} = 0$, and $F_{r_1} = F_{r_2} = 0$, respectively.

Using the Newton's second law of motion on the generic proposed model (case 4), a free body diagram was obtained as shown in Fig 4.2. From the free body diagram, the equations of motion for the viscous and coulomb damped 2DOF forced system are obtained as

$$m_1\ddot{x}_1 + (c_1 + c_2)\dot{x}_1 + (k_1 + k_2)x_1 - c_2\dot{x}_2 - k_2x_2 + F_{r_1}\,\mathrm{sgn}(\dot{x}_1) = m_1\ddot{y} + c_1\dot{y} \qquad (4.1)$$

$$m_2\ddot{x}_2 - c_2x_1 - k_2x_1 + c_2\dot{x}_2 + k_2x_2 + F_{r_2}\mathrm{sgn}(\dot{x}_2) = 0 \qquad (4.2)$$

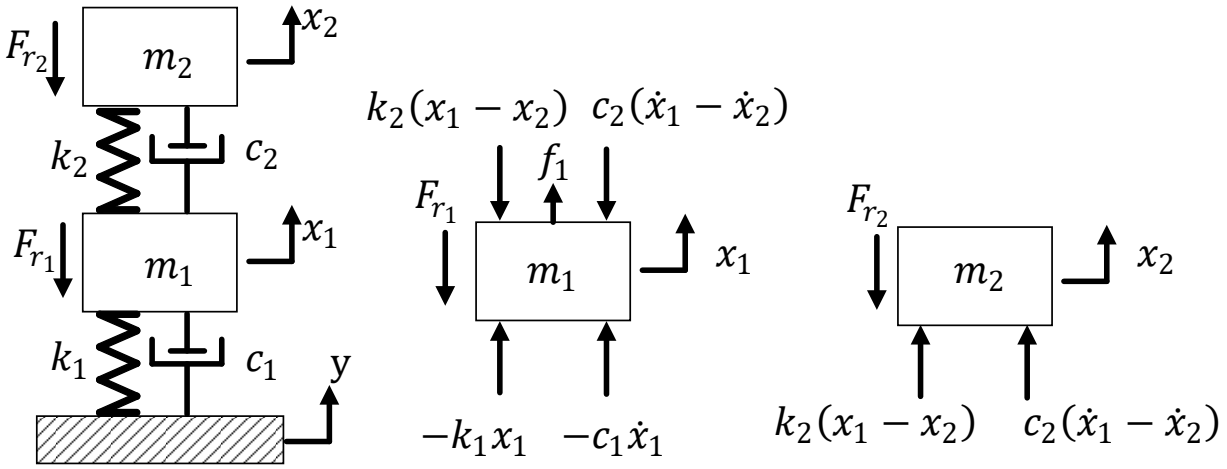

Figure 4.2 Free body diagram for the joint base-wall interaction of 2DOF system

where f_1 is the summation of excitation and viscous damping forces applied on m_1 i.e., $f_1 = m_1\ddot{y} + c_1\dot{y}$, x_1 and x_2 are the respective responses of m_1 and m_2; $\ddot{y}$ is the base acceleration, F_{r1} and F_{r2} are the friction forces on each DOF and $\dot{y}$ is the base velocity. When friction is ignored, the masses m_1 and m_2 respond harmonically to the input base excitation y, however, the focus in this work is based on the harmonic response of the 2DOF fiction bases system. The desired steady-state absolute harmonics responses x_1 and x_2 associated with i^{th} mass could be expressed as

$$x_i = X_i e^{i\omega t} \qquad i = 1, 2.$$

where x_i is the steady state response. The coupled responses given in Eqs (4.1) and (4.2) can be written in the matrix form as shown below

$$|[k_i] + \omega[\mathrm{c}_i] - \omega^2[\mathrm{M}_i]\,||X_i|=[F_i] \tag{4.3}$$

where $[\mathrm{M}_i]$, $[\mathrm{c}_i]$, $[k_i]$ and $[F_i]$ are the mass, viscous damping, stiffness, and external force matrices. Eq. (4.3) reduces to an eigenvalue problem with the external force is set to zero. A nontrivial solution is obtained if and only if the determinant of the eigenvalue problem is zero, so the natural frequencies (ω_1 and ω_2) corresponding to both vibration modes can be obtained as shown below:

$$\omega = \sqrt{\left(\left(\left[\frac{k_1+k_2}{2m_1}\right] + \left(\frac{k_2}{2m_2}\right)\right) \pm \sqrt{\frac{k_1^2+k_2^2+(2k_1k_2)}{4m_1^2} + \left(\frac{k_2}{2m_2}\right)^2 + \left(\frac{k_2^2-k_1k_2}{2m_1m_2}\right)}\right)} \tag{4.4}$$

Using the definition of mass, viscous damping, stiffness, and external force matrices in Eq. (4.3), the uncoupled steady state responses of masses m_1 and m_2 are obtained as follows:

$$X_1 = h_{11}F_{11} + h_{12}F_{21} \tag{4.5}$$

$$X_2 = h_{21}F_{11} + h_{22}F_{21} \tag{4.6}$$

where $h_{ij}(\omega)$ is a complex valued function of frequency obtained from the inverse of the impedance function matrix of the characteristic equation. It indicates the relationship between a response associated with the DOF i, and a force acting at the mass associated with the DOF j, such that a typical frequency response function h_{ij} (ω) for a 2DOF system can be expressed as:

$$h_{11} = \frac{(i\omega c_{22}+k_{22}-m_{22}\omega^2)}{(i\omega c_{11}+k_{11}-m_{11}\omega^2)(i\omega c_{22}+k_{22}-m_{22}\omega^2)-(i\omega c_{12}-k_{12})(-i\omega c_{21}-k_{21})} \tag{4.7}$$

$$h_{12} = \frac{-(i\omega c_{12}+k_{12})}{(i\omega c_{11}+k_{11}-m_{11}\omega^2)(i\omega c_{22}+k_{22}-m_{22}\omega^2)-(i\omega c_{12}-k_{12})(-i\omega c_{21}-k_{21})} \tag{4.8}$$

$$h_{21} = \frac{-(i\omega c_{21}+K_{21})}{(i\omega c_{11}+k_{11}-m_{11}\omega^2)(i\omega c_{22}+k_{22}-m_{22}\omega^2)-(i\omega c_{12}-k_{12})(-i\omega c_{21}-k_{21})} \tag{4.9}$$

$$h_{22} = \frac{(i\omega c_{11}+k_{11}-m_{11}\omega^2)}{(i\omega c_{11}+k_{11}-m_{11}\omega^2)(i\omega c_{22}+k_{22}-m_{22}\omega^2)-(i\omega c_{12}-k_{12})(-i\omega c_{21}-k_{21})} \tag{4.10}$$

Also, for i^{th} DOF, j is the DOF on which the excitation force is acting, and is always unity i.e., fixed on 1st DOF mass and the phase associated with each frequency response function h_{ij}(ω) obtained as

$$\phi_{ij} = \tan^{-1}\left(\frac{\mathrm{Im}(h_{ij})}{\mathrm{Re}(h_{ij})}\right) \tag{4.11}$$

The implication of the above statement in a simpler term is that the phases ϕ_{11} and ϕ_{21} could only be computed in reference to frequency response functions h_{11} and h_{21} for the respective masses 1 and 2. Now that an expression for the absolute steady state response and the phase of the 2DOF system, the relative response of the i^{th} mass was obtained as

$$z_i = \sqrt{{X_i}^2 + Y^2 - 2X_i Y\cos\phi_{ij}} \tag{4.12}$$

Considering the general architecture of the harvester design presented, it becomes very crucial to investigate and analyze the friction model for the four different cases in the following section.

4.2 Friction analysis on a 2DOF system

The governing equations that characterized the vertical displacement response of a forced Coulomb-damped 2DOF system had been discussed. The 2DOF system was configured into four (4) different cases as shown in Fig. 4.1 and the general equation that governs the four (4) cases was formulated and reported in Chapter 4.2. It was concluded that the response of each case could be gotten by imposing certain case-specific constraint i.e., presence or absence of i^{th} degree friction force $\left(F_{r_i}\right)$ induced from the guiderail (HIWIN MGN5C mechanical slider) on the general equation earlier presented in Chapter 2.

The pre-pressure applied to the guide rail falls in the light preload group whose pre-pressure falls in the 0-2% of the dynamic load capacity of the HIWIN MGN5C mechanical slider [111]. The dynamic load capacity and the coefficient of friction force of the mechanical slider was reported as $c_{dyn} = 0.54\ kN$and the coefficient of friction computed as $\mu = 4.99 \times 10^{-3}$. This friction coefficient correlates to the kinetic friction coefficient

since the friction is assumed to be fully converted to kinetic friction when steady-state vibration is achieved. The device geometry shows that the mechanical slider is positioned vertically, hence, a general assumption that the preload force and the friction coefficient between the slider and the guiderail is independent of the mass attached to the slider (so that it must not be too heavy to detach the slider from the rail). Using the above definitions, the constant friction force was calculated to have a magnitude of $F_{r_i} = c_{dyn} \times \mu \cong 0.0539\ \mathrm{N}$.

Also, the generic system is modelled as a 2DOF system with friction introduced between the mass and the wall due to the presence of the guiderails. The wall and the base form a joint system referred to as joint base-wall system, where the friction will be dynamics in nature depending on the relative motion between the magnet and the wall. The dynamic characteristics of the friction are such that its magnitude and direction determine the response type that has been categorized as either continuous, stick-slip or full stuck, based on the following sign convention:

$$\mathrm{sgn}(\dot{x}_m) = \begin{cases} 1 & \text{if } \dot{z}_i > 0 \\ [-1\ 1] & \text{if } \dot{z}_i = 0 \\ -1 & \text{if } \dot{z}_i < 0 \end{cases} \tag{4.13}$$

(i) when $\dot{z}_i > 0$ correspond to a positive relative velocity between the mass and the wall. This corresponds to a positive friction since $\mathrm{sgn}(\dot{z}_m)$ is positive hence the response is continuous.

(ii) when $\dot{z}_i < 0$ correspond to a negative relative velocity between the mass and the wall. This correspond to a negative friction since $\mathrm{sgn}(\dot{z}_m)$ is negative hence the response is stick.

(iii) when $\dot{z}_i = 0$ correspond to the fact that the relative velocity is zero between the mass and the wall, and $\mathrm{sgn}(\dot{z}_m)$ function assumes any value between -1 and 1. The actual value will be such that the system is in equilibrium, i.e., the vector sum of the spring forces and of the friction force is zero [110], [112].

According to the Newton's law of motion, the static friction model asserts that an object on a friction surface will initiate or maintain a continuous motion only when the net force $|F|$ exerted on the object is larger than the frictional force acting to oppose the motion of

the object. Otherwise, the object would remain stuck to the friction surface. Noting that the following friction analysis was conducted using the equation that governed the case four (4) and the dynamic model of the harvester system was formulated based on the consideration of the relative velocity between the object and the frictional surface in Eq. (4.13).

Using Eqs. (4.1) and (4.2), according to the Newton's second law, the stick condition of a Coulomb-damped, base-excited 2DOF system is obtained as

$$|F_1| = (k_1 + \omega c_1)Y \mp F_{r_1} < 0 \tag{4.14}$$

$$|F_2| = \mp F_{r_2} < 0 \tag{4.15}$$

Eqs. (4.14) and (4.15) imply that the required condition for stick i.e., $|F_1| < 0$ and $|F_2| < 0$ will occur if and only if the frictional forces F_{r_1} and F_{r_2} on the respective m_1 and m_2 have a negative sign with a magnitude greater than $(k_1 + \omega c_1)y$ while the friction force (Fr_2) on m_2 has also a negative sign. However, the slip condition for the system according to Eqs. (4.16) and (4.17) requires that $|F_1| > 0$ and $|F_2| > 0$. Both conditions $|F_1| > 0$ and $|F_2| > 0$ are possible only for when the frictional forces F_{r_1} and F_{r_2} on m_1 and m_2 respectively are positive valued.

$$|F_1| = (k_1 + \omega c_1)Y \mp F_{r_1} > 0 \tag{4.16}$$

$$|F_2| = \mp F_{r_2} > 0 \tag{4.17}$$

In summary, the sufficient condition for dynamic stick response is that F_{r_i} has a negative sign while the necessary condition for a continuous response for each DOF is that F_{r_i} has a positive sign. These observations further confirm the earlier reported friction model summarized in Eq (4.13).

The positions maintained based on Eqs. (4.14) to (4.17), are further established that the Coulomb fiction force could be employed to achieve suitable response tuning of a 2DOF harvester system. Previous works on the SDOF coulomb damped system reported that such system is often characterized by one isolation frequency and the friction always shows an inverse damping effect on the response i.e., the higher the friction, the lower

the response. The 2DOF coulomb damped system, also shows an inverse damping response with magnitude of the friction force but the isolation may often exceed one [95].

Literatures [95], [107] have reported that the Coulomb friction can be modeled as either: (i) static in nature, i.e., the frictional force resists force that is applied to an object, and the object remains at rest until the static friction force is overcome, or (ii) dynamic in nature where the frictional force resists the motion of an object. The dynamic interaction is realized with a joint base-wall such that the friction direction becomes dependent on the relative motion between the wall and the mass. In this model, the friction model employed

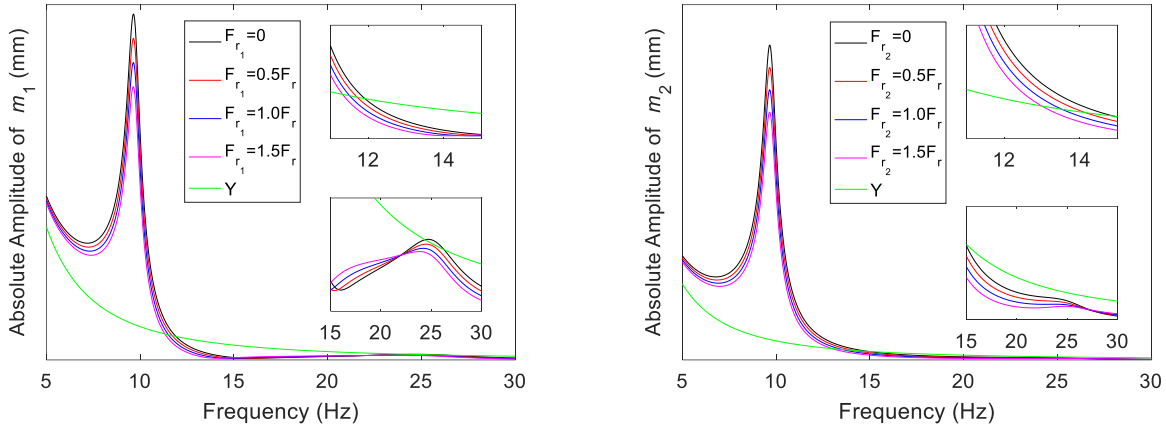

Figure 4.3 Response with the static model, m_1 (Left) and m_2 (Right)

Using Eqs. (4.5), (4.6) and (4.12), the response of the 2DOF harvester was obtained when the friction was modeled to have a static nature as shown in Fig. 4.3. According to Newton's second law, the conditions for stick and slip on the static model will straight forwardly depend on the balance between the excitation force and friction force such that the sufficient condition for a continuous response is that F_{r_i} has a positive sign and $x_i > Y$. When the converse of the above holds valid, the system enters the stick situation. As shown above, the responses of the two masses goes into the stick mode after the first isolation. On the contrary, the characterization of the dynamic friction model does not only depend on the force balance but also depends on the relative motion between the wall and mass m_i. During excitation, the relative motion between the wall and the masses will influence the direction of the friction according to Eq. (4.13).

However, Fig. 4.4 shows the response of the i^{th} DOF when the friction surface is modeled to have a dynamic nature. Fig. 4.4 shows that the dynamic friction could achieve a tuning effect on the response and harvested power since Fig. 4.4 also shows that the higher the dynamic friction, the higher and earlier is the occurrence of the isolation jump i.e., the isolation point shifts to a lower frequency but with higher isolation jumps and a lower response amplitude. Introducing friction into the system implies the difficulty in forcing the system into a stick mode i.e., the isolation frequency asides the response could be enhanced using friction.

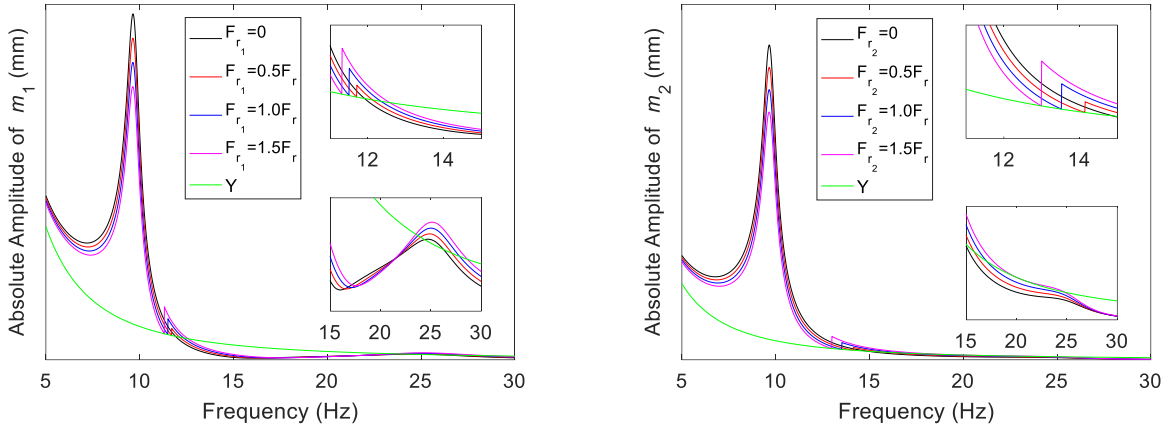

Figure 4.4 Response of the dynamic friction model, m_1 (Left) and m_2 (Right)

4.3 Response analysis on a 2DOF system

The next approach to this work is to model the response of the 2DOF system and hence determine which configuration (out of the four cases presented) is most suitable for real life energy harvesting. The vertical axis of the response was plotted to a log scale to give a clear view of the response and isolation in each of the four cases considered while the isolation frequencies associated with each case was indicated using colored marker. In this system, the change in the direction and magnitude of the friction force was only considered at isolation points while at other frequencies, the friction force magnitude is assumed to be equal to F_{r_i}. Fig. 4.5 shows that for every i^{th} DOF, each of the four cases analyzed was characterized by at least one isolation point where the friction changes direction thereby forcing the motion from a continuous state to a stick or vice versa. The isolations for m_1 and m_2 was independently considered as shown in Fig. 4.5. Fig. 4.5

(Left) shows that for each case considered, case 1 was the first to reach its first isolation frequency. Until the first isolation the response of m_1 is always continuous for the four (4) cases since the friction is modeled to be positive i.e., $X_i > Y$, according to Eq. (4.16). However, the dynamic nature of the friction force which maintains a positive sign initiates an isolation jump hence the motion is yet continuous after the first isolation frequency. After the first isolation the response of m_1 is yet in the slip/continuous domain until after the second isolation where the friction changes sign to negative. Hence, the response becomes stick-slip except in case 2 where the response of m_1 will permanently enter a stick mode after its own second isolation because its response becomes lower than the excitation amplitude. This condition certainly limits the response of m_1 in the case 2 configuration although the response before the first isolation is quite good.

Fig. 4.5 (Right) shows the response of m_2 is always continuous before the respective first isolations are attained as marked for each case. The vertical dotted lines indicate the first isolation points of m_2 on each cases considered.

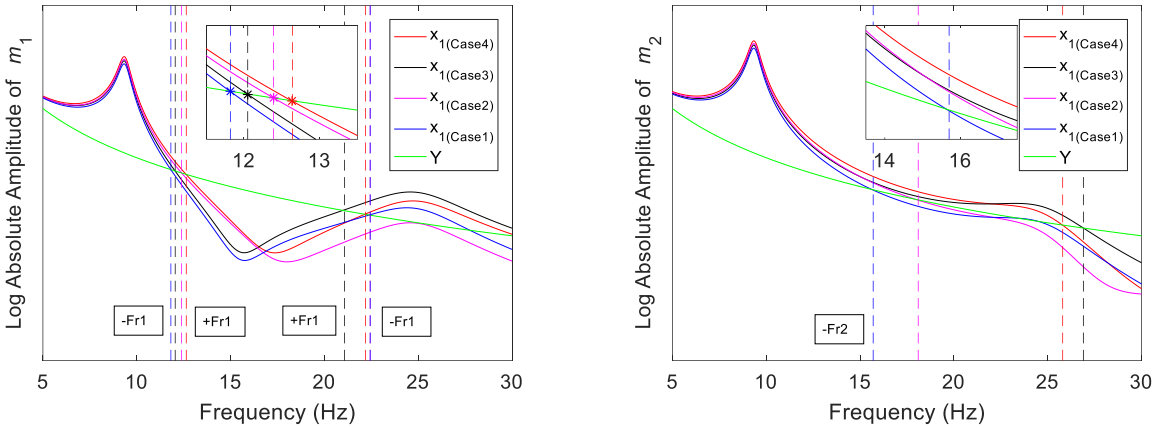

Figure 4.5 Evaluation of the isolation points m_1 (Left) and m_2 (Right)

Unlike m_1 response for which the first and second isolations are shown, the second isolations for m_2 could not be shown over the frequency considered because they are significantly far from the first isolation frequency, hence showing the friction transition sign becomes impossible. As observed from Fig. 4.5 (Right), cases 1 and 2 were the first to attain their first and second isolations after which they both enter the stick domain because the friction sign becomes negative, and the response becomes lower than the

excitation amplitudes. However, cases 3 and 4 attained their first isolations shortly after the cases 1 and 2 have entered a full stuck situation i.e., after their second isolation frequency.

In conclusions, the response characteristics of m_1 and m_2 above indicates that cases 2 and 1 will not be beneficial for energy harvesting because they are too quick to enter isolation. Whereas cases 4 and 3 shows the potential for a better response and never too quick to enter isolation, albeit case 4 is still preferable because m_1 and m_2 has a far better and desirable response than case 3. However, it is also noted that response in an unwanted DOF axis may be introduced in case 3 because of the absence of a linear guiderail on m_1.

4.4 Derivation of the electromagnetic damping ratio, voltage, and power equation through different electrical connections

The dynamic interaction of a 2 DOF system have been fully characterized in the previous section. In this section, the forced coulomb-damped 2DOF system as an electromagnetic vibration energy harvester using three different harvesting configurations, determined by the manner of external load resistors, will be discussed.

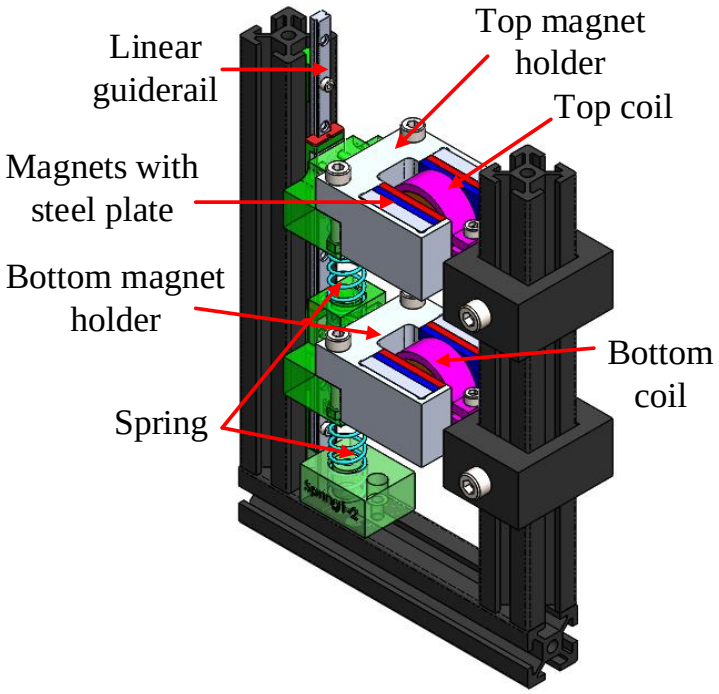

Figure 4.6 The 2DOF electromagnetic energy harvester diagram

The harvester model is a 2 DOF electromagnetic vibration energy harvester, and the design composes of two independent bottoms and top coils (hereafter referred to as m_{c_1} and m_{c_2}, respectively) and two identical springs mounted to the bottom and top magnets (hereafter referred to as m_1 and m_2, respectively) as shown in Fig. 4.6. Each coupled top-top magnet-coil and bottom-bottom magnet-coil represent an SDOF harvester configuration such that during excitation, each coil couples into the magnetic field of the corresponding spring mount magnet, thereby inducing voltage whose magnitude is obtained using the Maxwell's principle of the electromagnetic transduction in the coil loop.

Following the initial definitions of the damping, voltage and power equation in section, the electromagnetic parameters of the harvester such as the coupling factor, the electromagnetic damping ratio, the electromagnetic damping coefficient, and the induced voltage for each coupled section of this 2DOF harvester design was redefined as follows.

$$\zeta_{e_i} = \frac{8K_i^2 l_{c_i}^2}{m_i \omega_{n_i}} \left(\frac{1}{R_l + R_{c_i}} \right) \; i = 1,2. \tag{4.18}$$

$$c_{e_i} = 2m_i \omega_{n_i} \zeta_i \tag{4.19}$$

$$V_{coil_i} = 4K_i l_{c_i} z_i \omega_{n_i} \tag{4.20}$$

where K_i is the coupling coefficient of the i^{th} coil, z_i is the relative displacement of the i^{th} magnet and the wall, l_{c_i} is the effective length of the i^{th} coil, m_i is the mass of the i^{th} magnet, ω_{n_i} is the resonant frequency of the i^{th} DOF, R_l is the external load resistance and R_{c_i} is the internal resistance of the i^{th} coil.

To properly characterize and optimize the full potential of the 2 DOF harvester is presented in this work. Aside the individual external load connection, the consideration and characterization of other connection types, such as the external load connected in series and parallel circuit to the harvester system, will be undertaken in this work.

4.4.1 Individual connection of load resistor

When an external load resistor R_l is connected across each coil with internal resistance R_{c_i} as shown in Fig. 4.7, such connection is herein referred to as the individual connection. The electromagnetic damping ratio, the electromagnetic damping coefficient, and the induced voltage across each external resistance in series with the coil resistor are expressed in Eqs. (4.18) – (4.20), respectively.

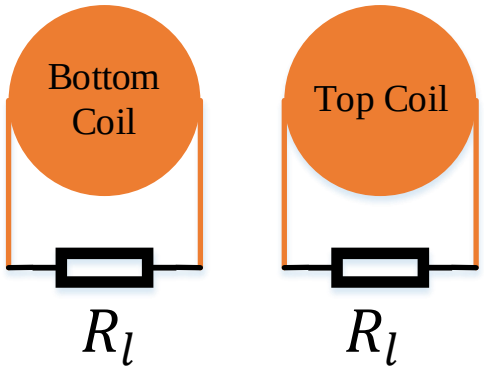

Figure 4.7 Individual connection of load resistor to energy harvester

The parameters ζ_{e_i}, c_{e_i} and V_{ind} described in Eqs. (4.18) – (4.20) will be used to compute the respective electromagnetic damping ratio, the electromagnetic damping coefficient, and the induced voltage on each i^{th} individual coil when the external load resistor is individually connected across the i^{th} coil.

For the individual connection, the voltage harvested across the load resistor over each i^{th} DOF coil was obtained using the voltage division law as

$$V_i = 4K_i l_{c_i} z_i \omega_{n_i} \left(\frac{R_l}{R_l + R_{c_i}} \right) \tag{4.21}$$

According to Ohm's electrical law, the total power harvested over the entire coil length is the square of the induced voltage in Eq. (4.21), divided by the sum of the external load resistance and the coil resistance:

$$P_i = 16\omega_{n_i}^2 {z_i}^2 \frac{{K_i}^2 l_{c_i}^2}{\left(R_i + R_{c_i}\right)} \tag{4.22}$$

where z_i is the relative amplitude of m_i given in Eq. (4.12).

4.4.2 Series connection of load resistor

The series connection is realized when an external load resistor R_1 is connected in series across the coils of internal resistance R_{c_i} as shown in Fig. 4.8. From the circuit theory, when two or more resistances are connected in series, the effective resistance of the circuit is the summation of all resistances of connected resistors. The closed-circuit series connection of the coil resistances, R_{c_1}, R_{c_2} and R_l, and its equivalent is shown in Fig. 4.8 (Right) such that the equivalent circuit resistance is obtained as

$$R = R_l + R_{c_1} + R_{c_2} \tag{4.23}$$

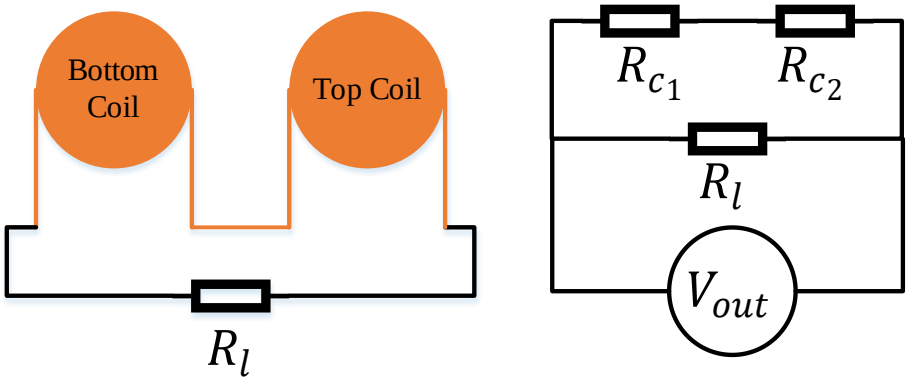

Figure 4.8 The connection of 2DOF coil in series (Left) and the equivalent closed-circuit connection (Right)

where V_{coil} is the voltage induced in each coil. The circuit theory asserts that the effective voltage across the series connected resistors is equal to the sum of voltage across each resistance with equal current flowing through them.

When the coils of the energy harvester system described above are connected in series, the effective electromagnetic damping ratio will be expressed just in the same manner as the electric current. Therefore, following the definition in [113] effective electromagnetic damping ratio associated with each coil when connected in series becomes:

$$\zeta_{series} = \sum_1^2 \zeta_{e_i} = \zeta_{e_1} + \zeta_{e_2} \tag{4.24}$$

where ζ_{e_i} is the electromagnetic damping ratio associated with the i^{th} DOF. Hence,

$$\zeta_{e_1} = \frac{8{k_1}^2 l_{c_1}^2}{m_1 \omega_{n_1}} \left(\frac{1}{R_l + R_{c_1}}\right) \tag{4.25}$$

$$\zeta_{e_2} = \frac{8{K_2}^2 l_{c_2}^2}{m_2 \omega_{n_2}} \left(\frac{1}{R_l + R_{c_2}}\right) \tag{4.26}$$

Also, the voltage harvested across R_l due to each i^{th} DOF associated with the arm of the coil is obtained by dividing the induced voltage over R_l and R_{c_i} as

$$V_i = 4K_i l_{c_i} z_i \omega_{n_i} \left(\frac{R_l}{R_l + R_{c_2}}\right) \tag{4.27}$$

Likewise, from Eq. (20), the equivalent electromagnetic damping coefficient is

$$c_e = c_{e_1} + c_{e_2} \tag{4.28}$$

Since two independent coils are connected in series in the system, the effective voltage harvested over R_l is the summation of the voltages on R_l due to each coil i.e.

$$V_{out} = V_1 + V_2 \tag{4.29}$$

The effective power harvested over the two coils connected in series is obtained as

$$P_{out} = \frac{V_{out}^2}{R_l} \tag{4.30}$$

4.4.3 Parallel connection of load resistors

To achieve a parallel connection, an external load resistor R_l is connected in parallel across the coils of internal resistance R_{c_i} as shown in Fig. 4.9.

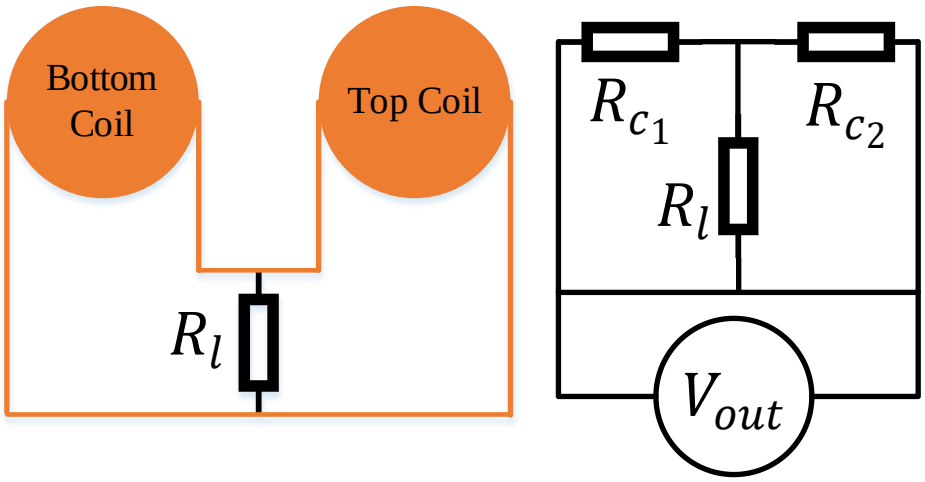

Figure 4.9 The connection of 2DOF coil in parallel (Left) and the equivalent closed-circuit connection in parallel (Right)

The closed-circuit parallel connection of the coil resistances R_{c_1}, R_{c_2} and R_l and its equivalent closed-circuit connection is shown in Fig. 4.9 (Right). According to the circuit theory, the voltage across each parallel connected resistor is equal while the current flowing through each coil is different.

The electromagnetic damping ratio (ζ_{e_i}) associated with each DOF in the parallel connection mode is likewise obtained from Eqs. (4.25) and (4.26). From the circuit theory, when two or more resistances R_1 and R_2 are connected in parallel, the effective resistance (R) of the circuit is the averaged summation of all resistances of the resistors connected. Since different current flows in each arm of the circuit due to different coil, then the electromagnetic damping ratio for each arm is likewise obtained according to Eqs. (4.25) and (4.26) and the voltage induced across each i^{th} DOF arm of the coil is given in Eq. (4.21).

If the voltage induced across each parallel connected coil is given as V_i, the analysis of the parallel connection circuit Fig. 4.9 (Right) shows that the voltage harvested over R_l

can be obtained using the mesh current or nodal analysis to give the following circuit equations:

$$V_1 = i_1\left(R_l + R_{c_1}\right) + i_2 R_l \tag{4.31}$$

$$V_2 = i_1 R_l + i_2\left(R_l + R_{c_2}\right) \tag{4.32}$$

where, i_1 and i_2 are the current induced in the circuit due to the excitation of coils 1 and 2, respectively. Solving Eqs. (4.31) and (4.32) simultaneously give the expression for i_1 and i_2 as

$$i_2 = \frac{V_1 - i_1\left(R_l + R_{c_1}\right)}{R_l} \tag{4.33}$$

$$i_2 = \frac{(V_2 R_l) - V_1\left(R_l + R_{c_2}\right)}{R_l^2 - [(R_l + R_{c_1})(R_l + R_{c_2})]} \tag{4.34}$$

The total current flowing through R_l is obtained as i:

$$i = i_1 + i_2 \tag{4.35}$$

Hence the voltage and power harvested over the load resistor R_l are obtained as shown in Eqs. (4.36) and (4.37), respectively

$$V_{out} = iR_l \tag{4.36}$$

$$P_{out} = \frac{V_{out}^2}{R_l} \tag{4.37}$$

4.5 Experimental verification

It is recalled that the frequency response functions are dependent on the resonant (ω), spring constant (k_i) and the viscous damping (c_i). The viscous damping (c_i) coefficient can be described as the sum of the mechanical damping coefficient and the electromagnetic damping coefficient, and it is yet to be fully defined because the mechanical damping coefficient associated with each DOF (c_{m_i}) is unknown. The total damping coefficient of an electromagnetic system has been defined as the sum of the mechanical damping coefficient and the electromagnetic damping coefficient given as

$$c_i = c_{e_i} + c_{\mathrm{m}_i} \qquad i = 1, 2. \tag{4.38}$$

Eq (4.19) established that the electromagnetic damping ratio depends on the load resistance such that in the limit of a very large external load resistance, the electromagnetic damping ratio value converges towards zero. This expectation was employed to characterize the approximate value of c_{m_i} of the 2DOF harvester by setting up an experimental rig as shown in Fig. 4.10.

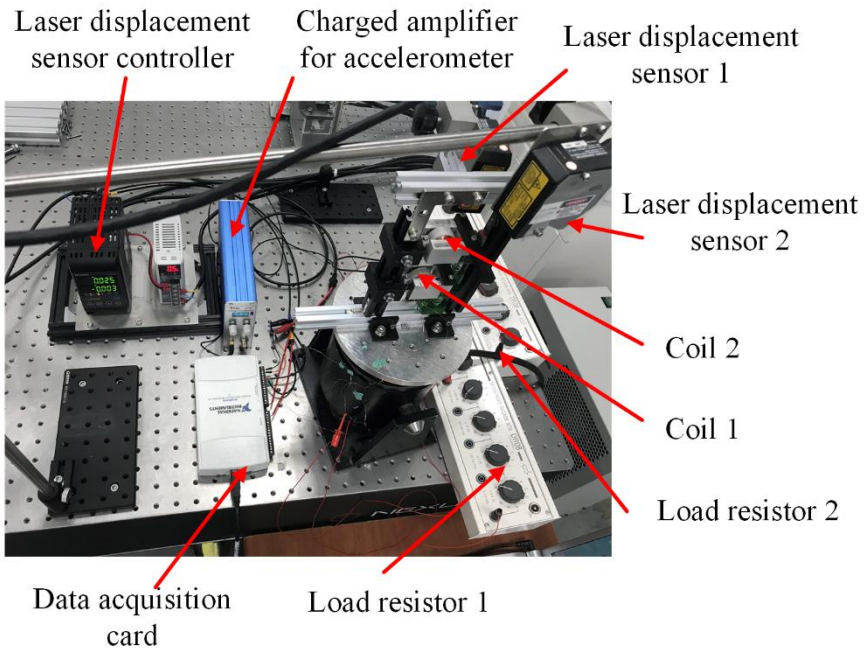

Figure 4.10 Experiment set up 2DOF vibration energy harvester

When the shaker is started, the displacement responses of the magnets were captured using two Keyence LK-H050 laser displacement sensors, which are connected to the controller and an accelerometer connected to the charged amplifier, was used to capture the base excitation response. Both output data were connected to a USB-6210 National Instrument data acquisition (DAQ) card and the response was obtained in LabVIEW. The data of the voltage and the power harvested over each DOF of the coil, when they are connected either individually, series or parallel to an external load resistor, was acquired over the load resistance wired into the DAQ device.

Table 1 gives a summary of the 2DOF harvester parameter where N is the number of coil turns, b the magnetic flux density cutting through the coil from the magnetic field, l_{c} is the effective coil length, c_{f} is the coil fill factor, R_{c} is the coil internal resistance, ζ_{m} is the

mechanical damping ratio and ζ_e is the electromagnetic damping ratio associated with the oscillation of the coil inside the field of the coupled magnetic field during excitation.

Table 4.1 Summary of the 2DOF harvester parameters

Position	f_n (Hz)	Magnet/Spring parameter		Coil parameter					
		Mass (g)	k ($\mathrm{Nm^{-1}}$)	N	$b\ (T)$	l_c (mm)	c_f	$R_c\ (\Omega)$	F_r (N)
Top	9.69	136.18	1316.60	1100	0.2438	0.7351	0.9097	13.50	0.0539
Bottom	9.69	135.83	1328.10	1500	0.2587	0.7603	0.9097	19.50	0.0539

4.5.1 Determination of mechanical damping associated with each DOF $(\boldsymbol{c_{\mathrm{m}_i}})$.

Before taking an attempt to determine the mechanical damping coefficient associated with each DOF, the mechanical stiffness associated with i^{th} spring DOF was first empirically determined using the set up shown in Fig. 4.11. During experimentation, increasing/decreasing the free length of the i^{th} resulted in a corresponding change in the force and length of the spring while the i^{th} spring constant was then obtained using the Hooke's equation.

The result of the experiment gave the values for the spring constant as $k_1 = 1316.6\ \mathrm{Nm^{-1}}$ and $k_2 = 1328.1\ \mathrm{Nm^{-1}}$ for lower and upper springs respectively. Although, the springs was made from same material and of the same dimension, the empirical values of k_1 and k_2 was observed to be slightly different.

This difference owns up to the fact that since the spring was glued to the 3D printed spring holder, the length of the portion of the spring wire and the effective number of spring turn that was glued slightly differs, therefore a slight difference in the spring constant value such that the one in lesser effective turn will have a higher stiffness. It is important to note that twist/torsional displacement of the spring associated with masses 1 and 2 may occur during coupling or excitation. To avoid these, two different and separate approaches were taken to mitigate each following: During the system's coupling, the top and bottom spring

holders were carefully aligned in parallel before the glue was applied to prevent a twist in the spring when securing to the rail blocks. Also, during excitation, the spring's twisting/buckling effect became obvious especially when the excitation exceeds certain thresholds (i.e., 0.34 g, 0.31 g and 0.37 g for individual, series, and parallel connections as observed during experimentation) even when the coil masses 1 and 2 were operated at optimum load resistance. To avoid the said mass twist, the harvester's performance as reported in this work was verified at carefully selected external excitations of 0.3025 g, 0.3028 g and 0.3006 g for individual, series, and parallel connections during the experimental verification.

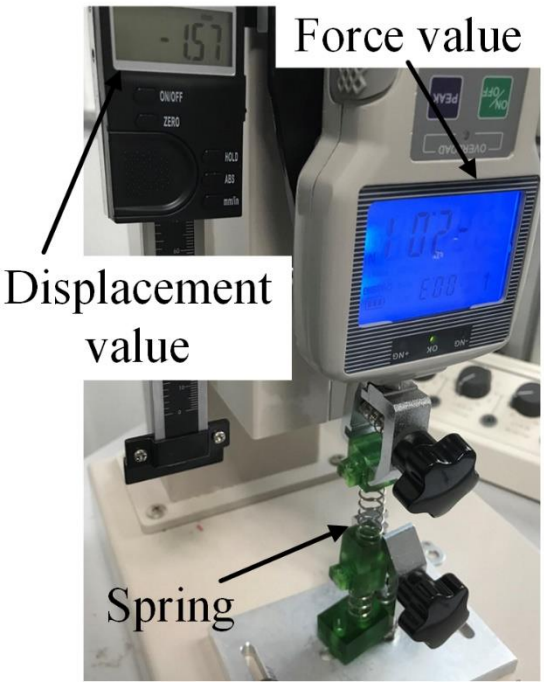

Figure 4.11 Experiment set up for obtaining the spring constants k_1 and k_2

The mechanical damping ratio of the spring (with friction) was obtained from the experiment by finding a best-fit between the experimental and theoretical results for the voltage and power harvested when the electromagnetic damping was approximately zero. The vibration harvesting procedure was then performed by setting the external load resistance at $R_l = 50\,\mathrm{k}\Omega$, to ensure that the system response was purely mechanical. When the shaker is triggered, the spring mount magnet begins to oscillate, thereby inducing a voltage in the fixed coil while the electrical power whose magnitude was

computed based on Faraday's law of electromagnetic transduction was then harvested over the external $50\,\mathrm{k\Omega}$ load resistor and voltage was captured through the data acquisition card. Fig. 4.12 shows the plot of the theoretical and experimental results in the limit of approximately zero electromagnetic damping.

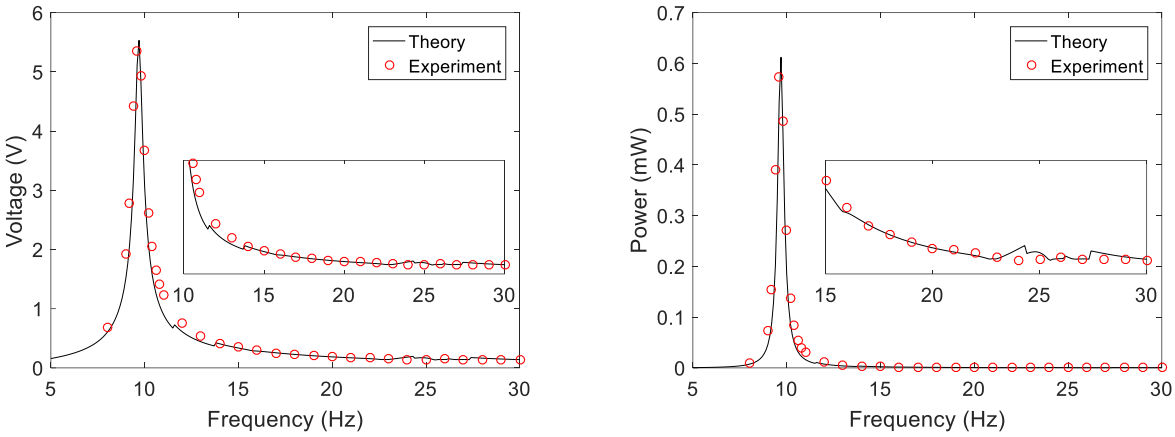

Figure 4.12 Voltage (left) and Power (right) harvested when the load resistance is 50 kΩ

Using the experimentally validated values of spring constant in Eq. (4.4) gives the first and second vibration mode resonant as 9.692 Hz and 25.410 Hz, respectively. The values of c_{m_1} and ζ_{m_1}associated with the lower spring that adequately fit the experimental data was found to be 0.651 Nsm^{-1} and 1.2679×10^{-2} , respectively.

Now that a value for the mechanical damping ratio of the lower spring has been obtained by predicting a reasonable value which fits the voltage and power curve as shown in Fig. 4.12 in the limit $\zeta_{\mathrm{e}_i} = 0$, now a new methodology for obtaining the mechanical damping ratio of k_2 is highlighted in the following section.

To accommodate mechanical damping coefficient (c_{m_i}) and ratio (ζ_{m_i}), Eq. (4.20) was redefined as follows for each DOF.

$$c_{\mathrm{m}_i} = 2m_i\omega_{n_i}\zeta_{\mathrm{m}_i} \tag{4.39}$$

Substitute $i = 1, 2$, into Eq. (4.35)

$$c_{\mathrm{m}_1} = 2m_1\omega_{n_1}\zeta_{\mathrm{m}_1} \tag{4.40}$$

$$c_{\mathrm{m}_2} = 2m_2\omega_{n_2}\zeta_{\mathrm{m}_2} \tag{4.41}$$

Dividing Eq. (4.41) by Eq. (4.40) gives

$$c_{\mathrm{m}_2} = \frac{m_2\omega_{n_2}\zeta_{\mathrm{m}_2}}{m_1\omega_{n_1}\zeta_{\mathrm{m}_1}} \times\ c_{\mathrm{m}_1} \tag{4.42}$$

Recall that for any SDOF system

$$\omega_{n_i} = \sqrt{\frac{k_i}{m_i}} \tag{4.43}$$

Substitute Eq. (4.43) into Eq. (4.42) gives

$$c_{\mathrm{m}_2}^2 = \frac{m_2k_2\zeta_{\mathrm{m}_2}^2}{m_1k_1\zeta_{\mathrm{m}_1}^2} \times c_{\mathrm{m}_1}^2 \tag{4.44}$$

Eq. (4.44) gives the general expression for obtaining the mechanical damping coefficient associated with k_2. The solution of Eq. (4.44) can be considered under four (4) different situations as follows:

A. CASE 1: $m_1 = m_2$ and $k_1 = k_2$

This is a very special case when the top and bottom springs, made from the material with the same mechanical, electrical and thermoelastic properties, are stressed under equal loads of m_1 and m_2. This situation is desirable because the conditions $m_1 = m_2$ and $k_1 = k_2$ will cause the two masses to vibrate with the equal damping ratio for the two modes associated with the 2DOF system. For this situation the mechanical damping coefficient of m_2 according to Eq. (4.44) reduces to

$$c_{\mathrm{m}_2} =\ c_{\mathrm{m}_1} \tag{4.45}$$

B. CASE 2: $m_1 = m_2$ and $k_1 \neq k_2$

The implication of the condition here is that the resonant of m_1 and m_2 can never be equal for any vibration mode according to Eq. (4.39), hence, $\zeta_1 \neq \zeta_2$. Therefore Eq. (4.40) reduces to

$$c_{\mathrm{m}_2} = \sqrt{\left(\frac{k_2\zeta_{\mathrm{m}_2}^2}{k_1\zeta_{\mathrm{m}_1}^2} \times c_{\mathrm{m}_1}^2\right)} \tag{4.46}$$

C. CASE 3: $m_1 \neq m_2$ and $k_1 = k_2$

Just as in case 2, the implication of the condition here is that the resonant of m_1 and m_2 can never be equal for any vibration mode according to Eq. (4.43), hence, $\zeta_1 \neq \zeta_2$ Therefore, Eq. (4.44) reduces to

$$c_{\mathrm{m}_2} = \sqrt{\left(\frac{m_2\zeta_{\mathrm{m}_2}^2}{m_1\zeta_{\mathrm{m}_1}^2} \times c_{\mathrm{m}_1}^2\right)} \tag{4.47}$$

D. CASE 4: $m_1 \neq m_2$ and $k_1 \neq k_2$

Case 4 is a typical situation presented in Eq. (4.44) and very much applicable to the 2DOF harvester analyzed. In the experiment setup, the masses and spring constants are $m_1 = 136.18\,\mathrm{g}$, $m_2 = 135.83\,\mathrm{g}$, $k_1 = 1316.6\,\mathrm{Nm}^{-1}$ and $k_2 = 1328.1\,\mathrm{Nm}^{-1}$ and substitute into the Eq. (4.44), the value of c_{m_2} can be determined. It is noted that $\frac{\omega_2}{\omega_1} = 1$ for the same excitation mode in a 2DOF system and $\frac{m_2}{m_1} \cong 1$ for the harvester design presented in this work. If the above situation holds valid, therefore $\zeta_{\mathrm{m}_2} \cong \zeta_{\mathrm{m}_1}$ for the same modal responses of m_1 and m_2. Using the above conditions in Eq. (4.44) gives the expression for obtaining the mechanical damping coefficient associated with m_2 as

$$c_{\mathrm{m}_2} = \sqrt{\left(\frac{m_2k_2}{m_1k_1} \times c_{\mathrm{m}_1}^2\right)} \tag{4.48}$$

As a follow up to the last section, it is important to clearly state that for the design considered in this work, case 4 is applicable and the mechanical damping coefficient of such a system was obtained using Eq. (4.39).

4.5.2 Verification of a 2DOF system in different load resistance connection types

Before a deliberate attempt was made to verify harvester performance, it became necessary to ensure that due to the protrusion of the magnet on the guide rail, additional friction other than those associated with the preload was not introduced into the guide

rail. To clarify this uncertainty, the static moment of the center of mass of the magnet will be computed and compared to those reported in the HIWIN data sheet [31]. The guide rail was reported to have a basic static loading and static moment of 0.84 kN and 1.3 Nm, respectively, along the y- axis [31]. The mass and the static moments of the top and bottom magnets in the same y-axis was calculated as 0.0129 kN and 0.0452 Nm, and 0.0130 kN and 0.0456 Nm, respectively. A careful comparison of the computed values and the data sheet values of the basic static loading and the static moment, shows that the computed values of the static load and static moment are much smaller than those in the datasheet. Hence, it is safe to conclude that no additional friction other than those associated with the preload will exist in the guiderail.

The experiment was set up as discussed in Chapter 4.4. The mathematical model was investigated for the three different connection configurations of the coils. The first connection type is when the coils are independently connected to an external load resistance, while the other two connection types referred to as the series and parallel connections.

Figs 4.13. and 4.14 show the absolute amplitude response of a 2DOF energy harvester using different connection types.

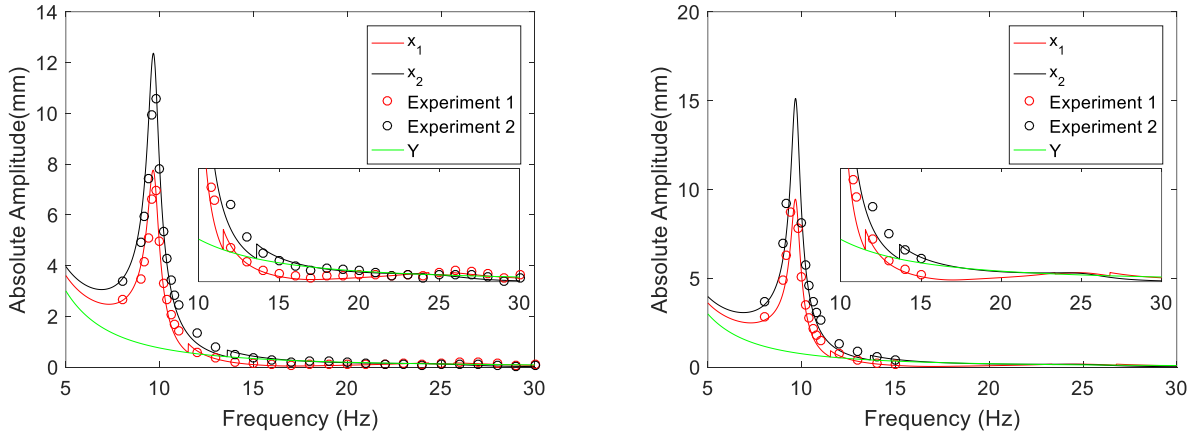

Figure 4.13 Absolute amplitude for different individual load resistor connections R_l=40 Ω (Left) and R_l=70 Ω (Right)

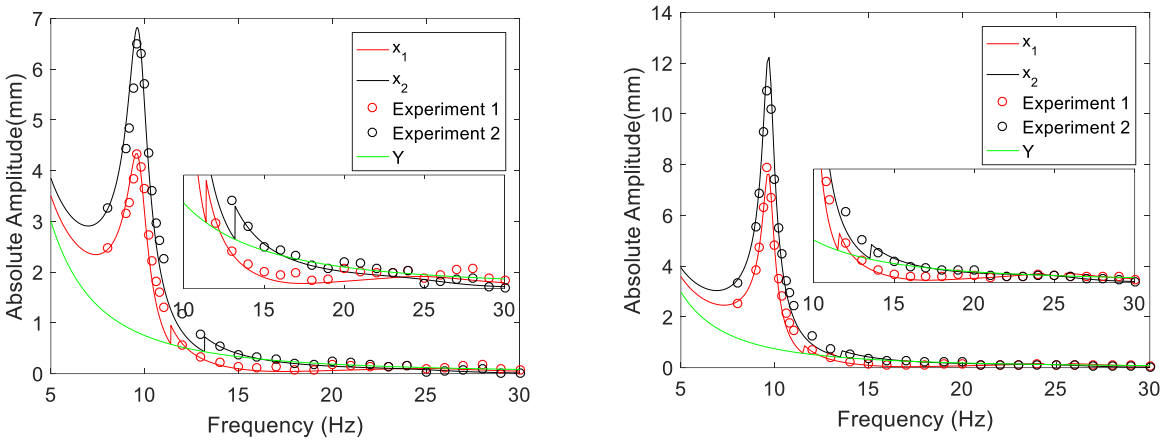

Figure 4.14 Absolute amplitude for different load resistor connections, R_l=40 Ω, series (Left) and parallel (Right)

Fig. 4.13 shows that when the individual connection was tested using two different external load resistors $70\ \Omega$ and $40\ \Omega$, the response of both coils 1 and 2 on the individual connection using $R_l = 70\ \Omega$ has a higher amplitude response because the higher external load resistance causes a considerable reduction in the electromagnetic damping.

However, upon comparing all three different connection types over an equal external load resistance of $40\ \Omega$, Figs. 4.13(Left) and 4.14 shows that the amplitude response of m_1 and m_2 in both parallel and individual connections is better than those for the series connection because for equal excitation and external load resistance, the electromagnetic damping ratio for the parallel and individual connections are equal but lower than those for the series connection. Therefore, in agreement to Eqs. (4.18) to (4.22) and (4.31) to (4.37), when the connection types were tested on equal external load resistances, the parallel and individual connection with the least electromagnetic damping ratio will harvest the highest power because the damping ratios (mechanical and electromagnetic) (Table 2) and responses Fig. 4.13 (Left) and Fig. 4.14 (Right) of the parallel connection is equal to those of the individual connection under such configurations.

However as shown in Fig. 4.15 (Left) and Fig. 4.16, such a trend does not occur because the highest harvestable power was registered on coil 2 pertaining to the individual connection. This digression from the expected trend may simply be associated with two possible causes: Firstly, according to the closed-circuit results in Eqs. (4.31) - (4.36), the

voltage harvested over the two coils in the parallel connection can be considered as the average of those harvested over each individual coils. Secondly, the power harvested over each connection mode is optimized at different R_l values such that each connection will operate at its own best when the external load becomes optimum, as will be discussed in the next section.

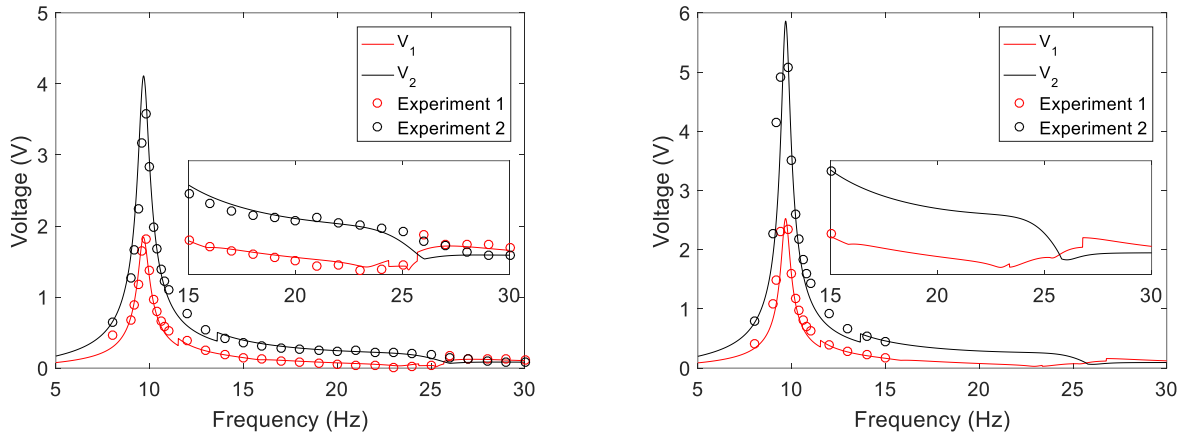

Figure 4.15 Harvested voltage for different individual load resistor connections R_l=40 Ω (Left) and R_l=70 Ω (Right)

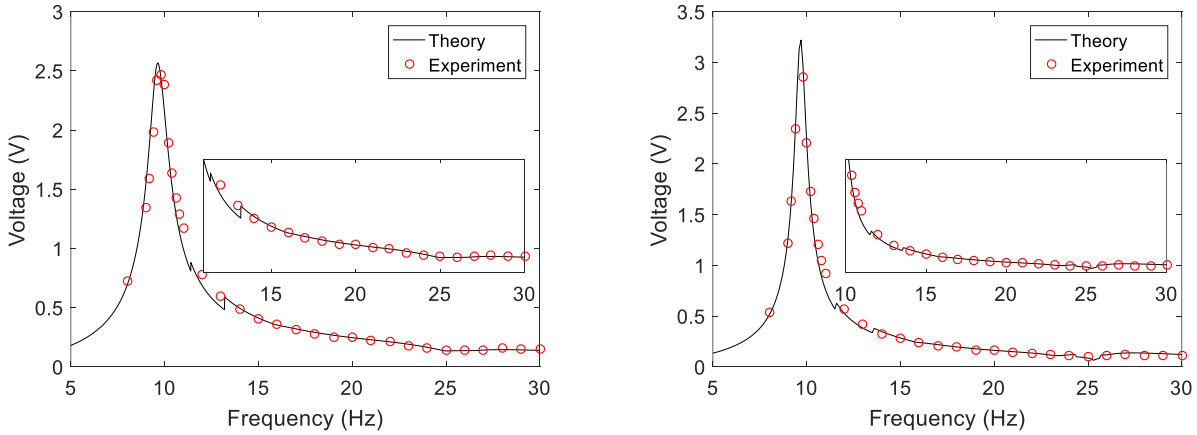

Figure 4.16 Harvested voltage for different load resistor connections, R_l=40 Ω in series (Left) and in parallel (Right)

The experimental errors were further analyzed in this work. It is interesting to note that coils 1 and 2 used in the individual connection with load resistors $40\,\Omega$ and $70\,\Omega$ generated the respective percentage errors of about 2.25 % and 1.09 % from the experiment 1, and 2.12 % and 0.99 % from the experiment 2. In addition, the series and

parallel connection with an external load resistor of $40\ \Omega$ gave the respective percentage errors of 2.19 % and 3.08 % for experiment 1 and 1.07 % and 3.15 % for experiment 2.

Also, Figs. 16 (Left) and 18 (Left) show that the empirical voltage/power harvested in the series connection matched the theory given in Eqs. (4.29) and (4.30) to an accuracy of about 99.30 %. Figs. 4.16 (Right) and 4.18 (Right) also show that the empirical voltage/power harvested in the parallel connection matched the theory given in Eqs. (4.36) - (4.37) to an accuracy of about 97.80 %, where in both cases, each of the coils used have an internal resistance $R_{c_1} = 13.5\ \Omega$ and $R_{c_2} = 19.5\ \Omega$.

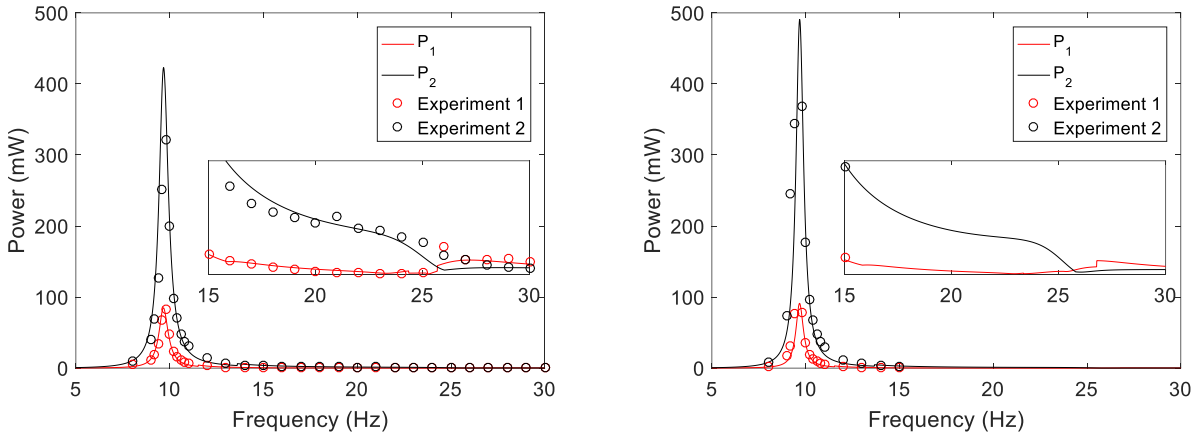

Figure 4.17 Harvested power for individual load resistor connection, R_l=40 Ω (Left) and R_l=70 Ω (Right)

The empirical power harvested over different connection types was reconciled with the theory as shown in Figs. (4.17) and (4.18). Both were found to be consistent to an accuracy of about 98.2 % on the average. Since the power plot presented here was harvested over an external load resistance, it does not give a clear description of the optimum capacity of the harvester. To achieve this optimum capacity, the 2DOF system must operate over an external load resistor called the optimum load as discussed in the next section.

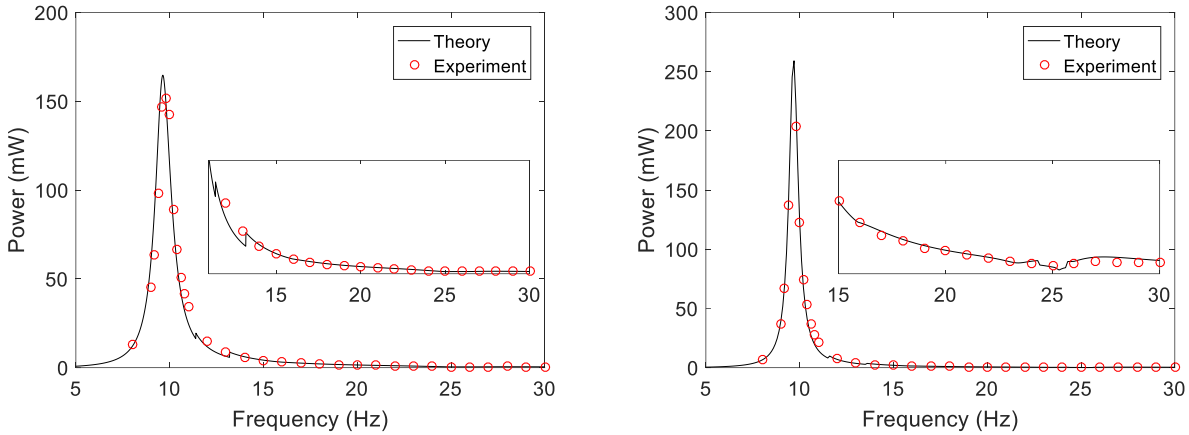

Figure 4.18 Harvested power for load resistor connection, R_l=40 Ω in series (Left) and in parallel (Right)

For each DOF, Table 4.2 gives a summary of the base acceleration, electromagnetic and mechanical damping ratio associated with the different load connection where, ζ_{m_i}, and ζ_{e_i} is the mechanical and electromagnetic damping ratio associated with the i^{th} DOF respectively and ζ_e is the equivalent electromagnetic damping ratio for the series connection as given in Eq. (4.24).

Table 4.2 Summary of the parameters associated with the different load connection

Connection	Load resistance (Ω)	Base acceleration (g)	Damping ratio ($\times 10^{-2}$)						
			c_{m_1}	c_{m_2}	ζ_{m_1}	ζ_{m_2}	ζ_{e_1}	ζ_{e_2}	ζ_e
Individual	40	0.3025	65.091	65.290	1.2678	1.2750	1.195	2.581	-
	70	0.3006	65.091	65.290	1.2678	1.2750	0.766	1.716	-
Series	40	0.3028	65.091	65.290	1.2678	1.2750	1.012	2.186	3.217
Parallel	40	0.3006	65.091	65.290	1.2678	1.2750	1.195	2.581	-

It is important to state at this point that irrespective of the connection type, the mechanical property of the harvester system is strongly independent of the electrical properties namely external load resistance, internal load resistance, coil fill factor the connection type etc. in agreement to Eqs. (4.38) and (4.39) confirming that ζ_{m_i} is purely a mechanical parameter. As shown in Table 4.2, the values obtained for the mechanical damping coefficients c_{m_1} and c_{m_2} associated with springs 1 and 2, respectively is approximately

equal across different connections for the different base excitations considered. This analysis presented here could be furthered extended to investigate effect of swapping the position of the top and bottom coils on the performance of the 2DOF system.

In summary, the experimental analysis suggests that when the system is tested under an equal load resistance, the response, voltage, and power harvested are inversely proportional to the electromagnetic damping ratio. The analysis conducted on the voltage/power harvested at a fixed value of external load resistance $R_l = 40\ \Omega$ shows that the coil 2 individual connection could harvest higher voltage/power for equal external load resistance followed by the parallel connection that also shows a good operational output while the harvested power on the series connection is not too satisfactory except for some low power operation. To determine which configuration that is the most efficient, it is important to characterize the system response at optimum external load resistance corresponding to each configuration, as investigated next.

Unlike certain harvester designs which require some initial energy to overcome a threshold associated with bio-stability, hence requiring a need for a priori knowledge of the working environment [115], and pre-experimentation to determine the magnitude of damping parameter [116], the device reported here shows the potential for operation under any level of excitation. A little modification such as engaging a stopper to limit the response level to prevent twist on masses 1 and 2 may be needed as the excitation exceeds the limit earlier mentioned in Chapter 4.1. Likewise, it was shown in Ref. [116] that the driving speed and normal load can significantly affect the dynamic and energy harvesting characteristics of the friction system. In contrast, the work reported here not only establishes that the friction in the guiderail is independent of the harvester load, but also characterizes the friction in the guiderail to be dependent on the sign of the relative velocity between the guiderail slider and the slider beam.

4.6 Optimum load resistance

Several authors have reported on the existence of an optimum load resistance $\left(R_l^{opt}\right)$ that will result in harvesting maximum power/voltage output on a vibration energy harvester [117],[118]. In the literatures, works have been done to determine the optimum

load resistance R_l^{opt} that can provide the highest load power, considering the maximum power transfer theorem related to $\frac{\partial P_{ave}}{\partial R_l} = 0$ [117],[118].

Using the above condition in Eq. (4.22) and using the quotient rule of differentiation gives the value of load resistance for which the maximum/optimum power is transferred for individual connection as

$$R_l^{opt} = \frac{16K^2 {l_c}^2}{\zeta_{e_i}} + R_c \tag{4.49}$$

When the load resistor was connected individually as shown in Fig.4.19, the variation of the harvested average power with the external load resistance and the peak of the plot shows the maximum harvestable power at a corresponding resistance called the optimum load resistance. The Fig. 4.19 shows an agreement of about 98.23 % between the theory and experiment, and the power harvested optimizes at $R_l^{opt} = 56.3\ \Omega$ and $39.10\ \Omega$ for coil 2 and coil 1, respectively when the excitation frequency was 10 Hz.

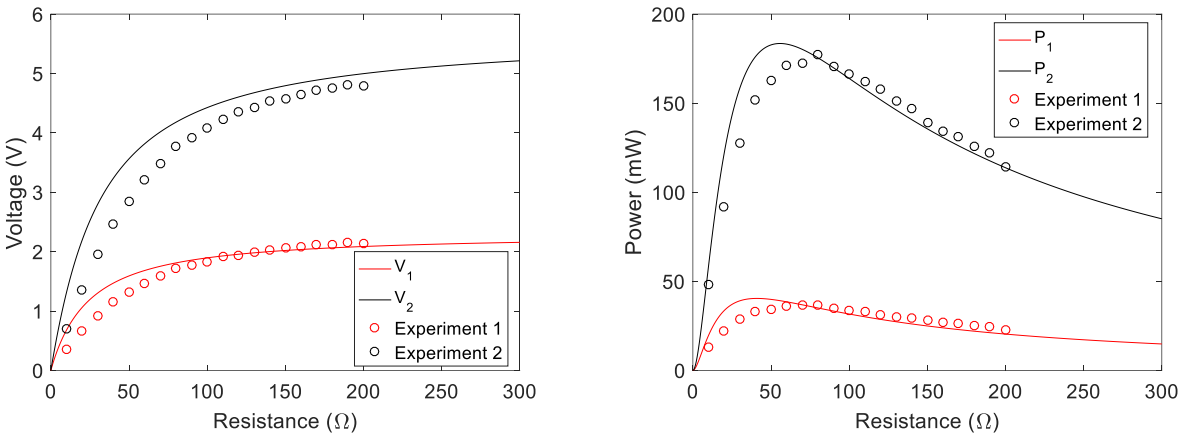

Figure 4.19 . Verification of the optimum resistance for individual connection, voltage (Left) and power (Right)

Similarly, Figs. 4.20 shows that harvested maximum power in the series connection optimizes at $R_l^{opt} = 221.50\ \Omega$ while the power harvested in parallel connection optimizes at $R_l^{opt} = 43.29\ \Omega$ and $0 \leq R_l^{opt} < 2.32\ \Omega$.

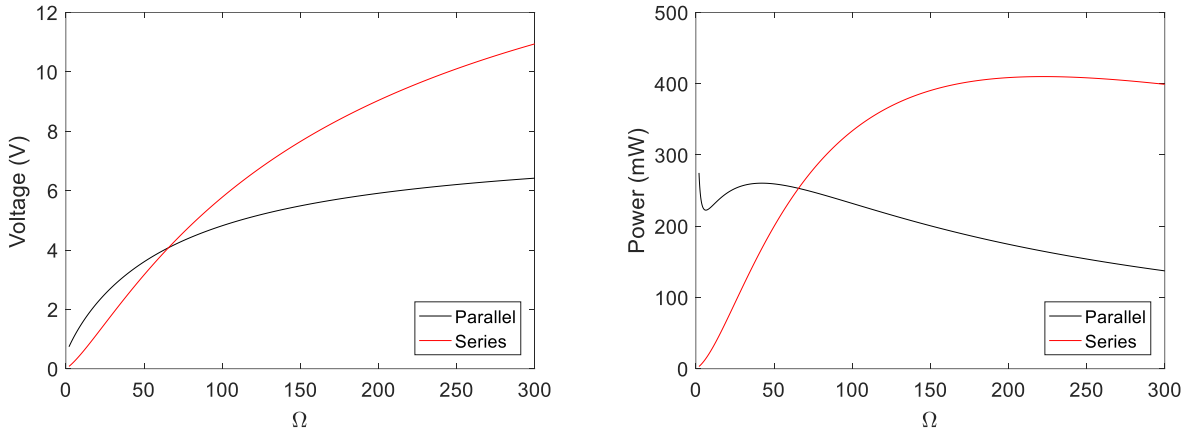

Figure 4.20 Variation of voltage with $\mathrm{R_l}$ (Left) and optimum load resistance (Right) for series and parallel connection

These values of the optimum load agree with the theoretical values computed from Eq. (4.49) and the values obtained for each configurations suggests that the individual and parallel connection is mostly applicable to power low impedance devices/sensors. In addition, Fig. 4.20 (Right) shows that the parallel connection also a rapid and progressive increases in the power harvested from about $261.8\ \mathrm{mW}$ to about $25.2\ \mathrm{W}$ for extrapolations of the load resistances at $0 \leq R_l^{opt} < 2.32\ \Omega$. Fig. 4.20 (Right) shows that the 2 DOF series connection has the potential to harvest energy to power moderately high impedance sensors.

Table 4.3 Optimum load resistance for each configuration

Connection	Coil position	Base acceleration (g)	Optimum load resistance (Ω)
Individual	2	0.3024	56.30
	1	0.3024	39.10
Series	-	0.3006	221.50
Parallel	-	0.3006	< 2.32 and 43.29

4.7 Relative amplitude between two masses

As stated previously, the excitation of the 2DOF system will produce two vibration modes for which each mode response is sufficiently defined by two resonances ω_1 and ω_2. However, during experimentation with 2DOF system, an unexpected observation made

was that the magnet starts touching during excitation at ω_1 when the external load resistance becomes generally higher than the optimum load value for all connection types in such situations. For the system, it is assumed that the two masses will not hitting each other as the spring free length is sufficient.

Upon excitation at a base acceleration of $0.3006\ \mathrm{g}$, the phase the 2DOF system shows that m_1 and m_2 are vibrating in phase until the first resonance ω_1 hence m_1 and m_2 were never expected to touch each other during excitation. However, it was observed that when the external load resistance is a bit above the optimum value for each connection types, and excitation approaches resonance, the responses of m_1 and m_2 will initiate a nonlinear dynamic interaction between them such that they begin to collide/touch. This collision causes the mechanical impact on m_2 to transfers a secondary shock to m_1 and vice versa (in the form of impulsive force), this effect was expected to trigger a nonlinear frequency up-conversion mechanism.

To characterize such nonlinearity that was initiated by touching, considerations shall be anchored on the maximum compressible limit of the springs (l_s) during excitation. l_s is defined as the maximum distance between the two fixed ends of the spring when they are fully compressed during excitation because of the relative responses between m_1 and m_2 as shown in Eqs. (4.50) and (4.51). In the experiment setup shown in Chapter 4.40, Fig. 4.10 the l_s was measured to be $6.2\ \mathrm{mm}$ since the wire diameter of each spring is 1 mm with a total effective turn of 6.2. The general condition that determines if m_1 and m_2 will collide was obtained as shown in Eqs. (4.50) and (4.51)

$$x_2 - x_1 \geq l_s; \qquad \text{Collision between } m_1 \text{ and } m_2 \tag{4.50}$$

$$x_2 - x_1 \geq l_s; \qquad \text{No Collision between } m_1 \text{ and } m_2 \tag{4.51}$$

As earlier stated, the need to formulate the condition that determines whether m_1 and m_2 will initiate a dynamic interaction as a function of the springs maximum compressible distance (l_s) becomes necessary to ensure that there is no existence of other dynamic interaction of m_1 and m_2 asides those associated with the spring response. Figs. 4.21-

4.22 shows the result of the dynamic analysis using different load resistances and R_l^{opt} for different connection configurations.

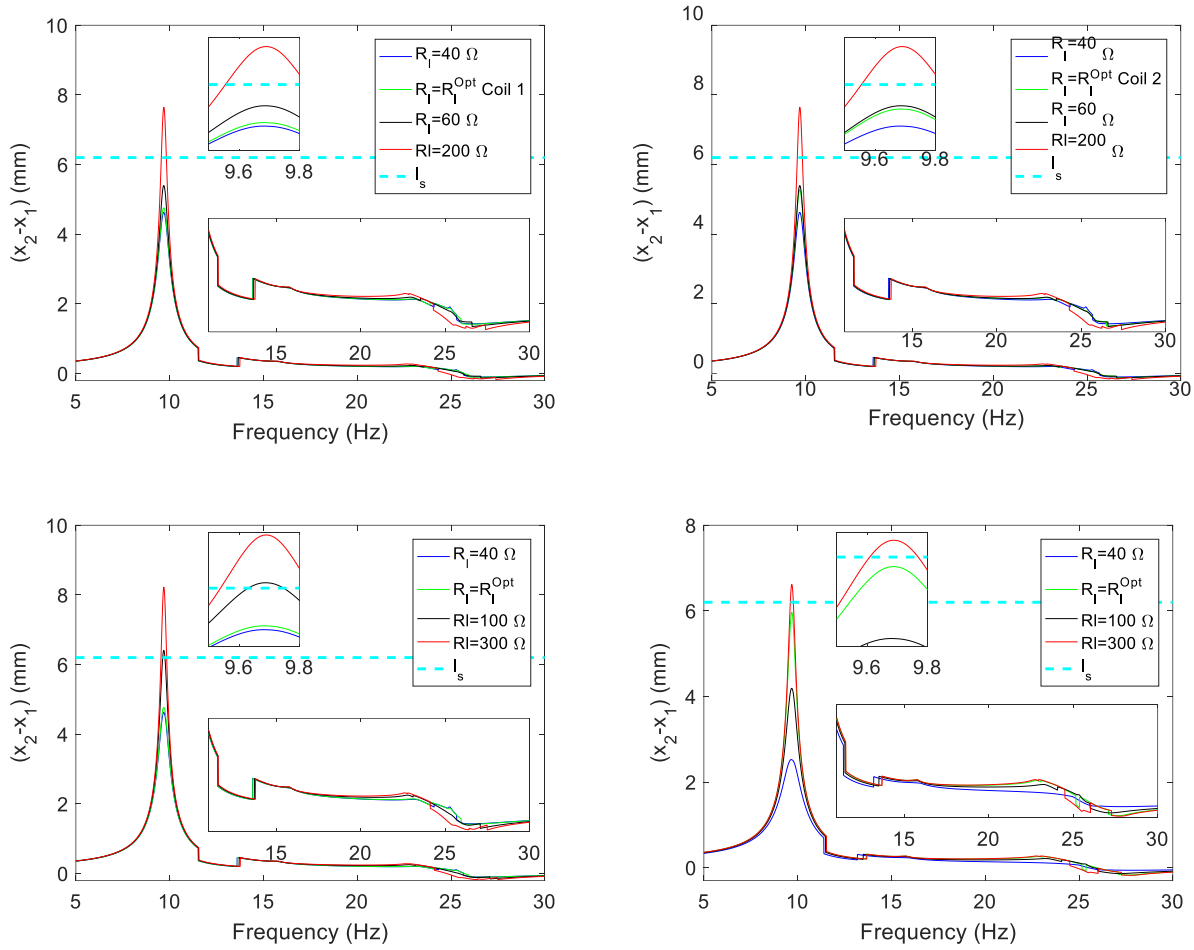

Figure 4.21 Difference in absolute amplitude of m_1 and m_2 individual coil 1 optimum (Top left), individual coil 2 optimum (Top right), parallel connection (Bottom left), series connection (Bottom right)

Figs. (4.21) shows that when the harvester is connected to an external load resistor whose value is equal to or less R_l^{opt} across all the connection types the harvester will sustain the condition needed for the non-dynamic interaction of m_1 and m_2, i.e., they will not touch. The above position indicates that if the harvester is operated at load resistance that is below or equal to the optimum values of the external load resistance an efficient operation void of interaction between m_1 and m_2 is guaranteed.

Also, Fig. (4.21) shows the occurrence of dips around 11.0 Hz to 14.5 Hz while 23.0 Hz to 27.0 Hz shows a mixed region of dips and jumps. These are the effect of the isolations

jumps for each of mass because the lower and upper limits of the dip/jumps correspond to individual isolations of m_1 and m_2, respectively. It is noted that the region of dips implies that the response of m_1 is greater than m_2, while dips imply that the response of m_2 is greater than m_1.

To this point, the analysis of the 2 DOF harvester considered under different configurations suggests that each configuration type has its own merits and demerits. The individual, series and parallel connection shows a prospect for harvesting power which is optimal only at $R_l^{opt} = 56.30\ \Omega$, $221.5\ \Omega$ and $43.29\ \Omega$, respectively. As shown in Fig. 4.20 (Right), the power harvested on the series connection becomes optimized at a moderately high resistance, hence a safe conclusion that the series connection is mostly beneficial for powering high impedance sensors and microelectronics because its performance becomes optimum at a resistance of $221.50\ \Omega$. However, it is unsatisfactory for low resistance operation unlike the parallel and individual connections for which the harvested power is optimal at low resistance while the parallel connection shows an added advantage for usage at ultra-low resistances.

4.8 Power density

Aside of setting the possibility for choice on the operational impedances by using different connection configurations, the proposed design shows a considerable improvement of the power density. The average power density is obtained by dividing the average power harvested by the actual practical volume of the energy harvested. Hence, one practical way of ensuring a high-power density is to ensure the system volume is as low as possible.

The power density is an important indicator of the energy harvester performance, which is often used to represent the overall quality of energy harvesting systems. An energy harvesting system with higher power density harvests more energy per unit volume of the system. In energy storage/ charging system, it is very important that the system be characterized by the high-power density since they are quick to release their energy and can also recharge quickly.

The power density of the 2DOF system considered was obtained as

$$P_D = \frac{P_{out}^{max}}{V_A} \tag{4.52}$$

where, P_{out}^{max} is the resonant optimum power output and V_A is the actual practical volume of the harvester during operation defined as

$$V_A = L_A W_A \left(h_A + x_2^{opt}\right) \tag{4.53}$$

where, L_A, W_A, h_A and x_2^{opt} are the actual practical length, width height and maximum response of coil 2. From Fig. 4.22 $L_A = 75.98\,\text{mm}, W_A = 38.00\,\text{mm}$, $h_A = 125.00\,\text{mm}$ and x_2 has values different R_l^{opt} depending on connection types as shown in Table 4.4.

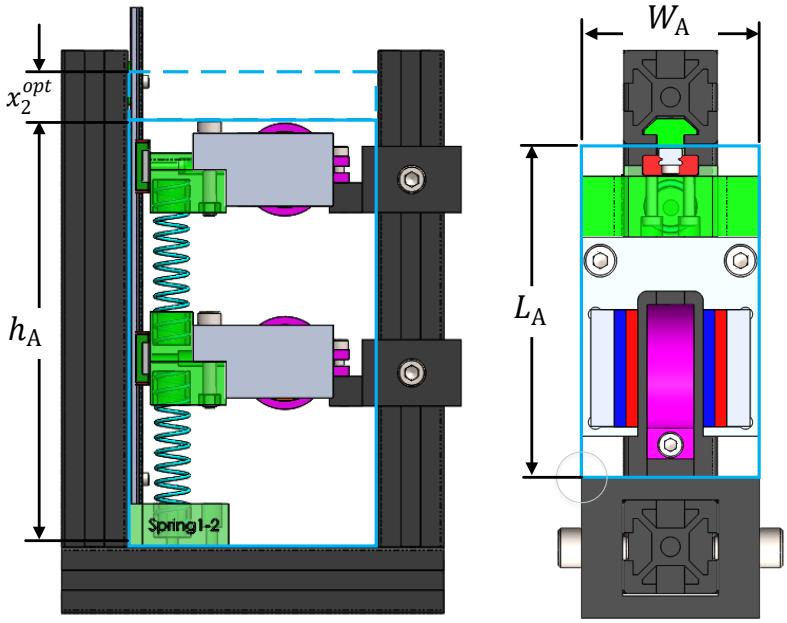

Figure 4.22 Geometry of the harvester design under non-vibrating condition

Table 4.4 shows that the harvester design shows a reasonably high-power density across all the considered configuration in comparison with other harvester design.

Table 4.4 Summary of power and power density across different connection

Configuration	Coil position	R_l^{opt}	x_2^{opt} (mm)	P_l^{max} (mW)	$V_p(\times 10^{-4})$ (m^3)	$P_D(\text{Wm}^{-3})$
Individual	2	56.30	12.66	85.71	4.01	213.60
	1	39.10	12.66	470.40	4.01	1172.28

Series	-	221.50	15.78	410.40	4.07	1009.03
Parallel	-	43.29	12.65	261.60	3.97	658.38

Apart from the harvester's power density characterization, the power density could be normalized; the normalized power density (NPD) which is simply the stated power output of the device normalized to base acceleration level and frequency and divided by the volume [119]

$$NP_D = \frac{P_D}{fg^2} \tag{4.54}$$

Table 4.5 shows the power density comparison of present work with other but current state-of-the-art vibration energy harvester using different transduction methods.

Table 4.5 Comparison of present work with current state-of-the-art vibration energy harvesters

Author	Transducer	f_n (Hz)	Base acceleration (g)	P_l^{max} (mW)	V_p (cm^3)	$P_D(\times 10^{-6})$ ($mWcm^{-3}$)	NP_D ($Wm^{-1}s^{-5}$
Alwathiqbelah et al [120]	T	17.80	1.4000	0.01223	1646.00	7.43	< 0.001
Iqbal et al [121]	P and E	11.10	0.6000	2.21	272.00	8.14	0.014
Milad et al [122]	E	27.00	4.0000	999.70	463.00	2159179.27	0.052
Wan et al [123]	P	5.80	-	1.58	450.00	3511.11	-
Yucheng et al [124]	E	4.50	3.5000	23.20	310.00	74838.71	0.141
Yasar et al [125]	E	10.00	0.5000	0.24	7.00	34285.71	0.143
Yili et al[119]	P	46.00	2.0000	0.97	0.32	3031250.00	0.171

This work coil 1	E	9.69	0.3006	85.71	401.30	213580.86	2.540
This work Parallel	E	9.69	0.3006	261.60	397.30	658444.50	7.829
This work Series	E	9.69	0.3006	410.40	406.70	1009097.62	11.999
This work coil 2	E	9.69	0.3006	470.40	401.30	1172190.38	13.941

***E – Electromagnetic; P – Piezoelectric; T – Triboelectric

The above observations as reported in Table 5 conclude that although the non-optimized dimension of the harvester reported in this work is moderately high in comparison to other works in selected literatures, the proposed harvester however has been demonstrated to have a better performance because of its practical applications for harvesting highest possible power density even at excitations far lower than those in selected literatures. To enhance the system performance to accommodate larger external excitations, a slight feature modification such as using larger spring stiffness will be sufficient. The above feature is well desirable in any vibration energy harvester device because the system showed that they are well cut to harvest significant energy to power sensor even at low frequency excitations.

4.9 Summary

This work has proposed a 2DOF vibration electromagnetic harvester modeled as a coupled coil-magnet system. The modeling of the 2DOF energy harvester system was investigated using four different design configurations. Analysis on the friction dependent response and isolations was conducted and the results indicated that the case 4 presented in this work has a much better performance than other.

The other three cases are considered not fit for a 2DOF vibration energy harvester because the occurrence of observable effect such as single isolation point means the masses will spend most of their operational bandwidth in the stick mode as well as the introduction of unwanted degree of freedom in their response due to the absence of the linear guiderail that helps to constrain the response to one response axis for each of the

vibrating masses. Since the system has two coils independently associated with each of the 2DOF of the system, an approach to ascertain the types of connection between the two coils that will yield the best output performance was also undertaken.

Before optimizing its performance based on the connection type, the initial approach was to determine the spring constants and the mechanical damping ratio as reported in Chapter 4.4.1. It was hence observed that the mechanical damping ratio of the system is independent of the harvester's electrical parameter, thus opening a gap for electrical and or mechanical base power optimization. As stated, the response was investigated using three different connection types reported in Chapters 4.3.1 – 4.3.3 and Chapter 4.4.3 reported the optimum load for which the harvested power becomes maximum for each connection configurations.

The overall theoretical and mathematical background to the harvester's performance was presented in Chapter 4.3 and later compared with the experiment in Chapter 4.4.2. Both theoretical and experimental results agree to a limit of 98.85 %. While noting that the individual and series connections clearly cut well to power low impedance sensors, the parallel connection however would be most suitable for powering high impedance sensors/micro gadgets. The power densities and the normalized power densities for each connection configuration (summarized in Tables 4.4 and 4.5 respectively) are quite promising to ensure continuous and autonomous supply of power to both onsite and remote sensors. The power densities for coils 1 and 2 individual connection, series connection and parallel connections were obtained as $213.60\ \mathrm{Wm^{-3}}$, $1172.28\ \mathrm{Wm^{-3}}$, $1009.03\ \mathrm{Wm^{-3}}$ and $658.38\ \mathrm{Wm^{-3}}$, respectively, while the normalized power densities were shown in Table 4.5. These values are comparably much higher than those realized in selected literatures.

Another significant uniqueness of this design lies in the fact that a single 2DOF harvester presented here could be operated over different load impedances by a choice of connection modes such that this observed characteristic opens a new way for maximizing the harvested power by allowing for a clear-cut impedance matching between the sensors/ micro gadgets and the harvester by using a suitable connection types over different selectable impedances (individual coil 1, individual coil 2, series connection of

coils 1 and 2 and the parallel coil connection of coils 1 and 2). This novel proposed approach offers a good economic advantage over conventional SDOF resonant harvesters which usually require a new harvester design for different sensors.

CHAPTER 5: Isolation point shift for simultaneous energy harvesting with levered Coulomb damped electromagnetic vibration energy harvester.

5.0 Introduction

Isolators are essential components in instrumentation and measurement systems to ensure accurate and reliable data acquisition. A general application for payload usage considered in this work aims to achieve a reduction noise and interference in measurement systems by isolating the signal path from external disturbances. This ensures that the measured data is accurate and reliable. In another view, most isolated payloads also need efficient and uninterrupted power supply for optimal operation. Since vibration is always exists in buildings, machinery parts, automations, and even human motion. The unwanted vibration sources which affects payload operations may include reactions in the wheels, optical tables, thermal gradient, etc. [126, 127], the accuracy of optical payloads and interference sensitive devices are questionable. By pursuing the sustainable development goal for attaining sufficient energy infrastructure, reducing dependency on fossil fuels while encouraging the use of renewable energy to the intent of reducing greenhouse gas emissions this work attains the following objectives. While efficiently attaining a near resonant isolation of the payload from interfering vibrations, it simultaneously and efficiently converted the external vibration into electrical energy to meet the power requirements of isolated payload, sensor nodes, structural health monitoring IoT and smart devices [128-131].

In another projection, the design will prove worthiness in region plague with energy crisis. For example, a simple laboratory/industrial procedure that requires simultaneous power generation for data acquisition and vibration isolation on optical devices, sensor nodes and payloads may suffer a severe setback in most developing countries where energy issues are dominant since power outage are often inevitable in case of source failure or battery drain. Hence, the implemented mechanism reported in this work will efficiently tackle these identified challenges by efficiently shield the payload by isolating it form

unwanted vibrations while simultaneously providing power for autonomous operation of the payloads by electromagnetic transduction method. The scope of application of the design presented in this work is limited to small payload usage to avoid an operational compromise and hence an eventual failure on the stiffness matrix of the design. The harvester-isolation design reported in this works is referred to as the Levered Coulomb Damped Dual Response single shunted (LEDAR-SS) mechanism or levered design for short. The dual response characteristics is associated with the ability of the design to simultaneously trigger responses on the LHS and the RHS of the design during excitation. Also the single shunted definition is used to characterize the fact that the design is connected over a shunt resistor to successfully harvest power for the payload while isolating vibrations.

To successfully harness the contra-wise implication of vibration on systems while generating autonomous energy application, vibration energy harvesting-isolator devices can successfully convert undesirable vibration into useable electrical energy for optical devices, wireless sensor node and payload while shielding them from vibration are encouraged. In the design of mechanical systems, friction has been identified as one of the design parameter introduced due to associated joints and bearings although they have been regarded as unwanted phenomenon in mechanical systems because they reduce the overall system's performance by wasting energy in the form of noise and heat [132, 133]. Initial analysis shows that, the LEDAR-SS design successfully took the advantages of friction as a design parameter in two aspects. Firstly, the friction as well as the transducer coil in the system set the bound for earlier onset of near resonant vibration isolation while harvesting relative to conventional isolator design. Secondly, as shown in later sections the configurations with larger friction successfully broadened the band over which isolation occurs although friction has been identified to induce a stick-slip response that causes a non-uniform response in vibrating structures [134]. While necessary boundaries conditions that marks the onset of stick-slip coulomb response in a system was well reported [135, 136]. Marino and Cicirello (2020) formulated necessary conditions for multi degree of freedom (MDOF) coulomb damped system noting that that such motion

controlled effect of friction synergized with appropriate electrical/automation could realize an electro-mechanical tuning for enhanced bandwidth, isolation and harvested power.

Also, the implication of the presence friction on the energy harvesting in the capacity of designs has been effectively presented analyzed and reported by Zhang et al, [137] and Lin, et al, 2018 [138]. Both design approaches harvest vibrational energy by collecting energy from rail track vibrations over mechanical vibration rectifiers. While Zhang et al achieved an anchored design where the prototype is attached to the rail track, Lin et al (2018) however, uses a anchorless design where a spring preload and reset pin are used to eliminate the need for an anchor. The power harvested in both situations reached an average power of 7.00 W and the maximum power of 56.00 W from freight trains traveling at 64 km/h under a 5.7 mm deflection. While both anchored and anchorless localized and dedicated designs above are quite novel for dedicated applications on rail tracks, non-dedicated usability of energy harvester is a concern such as highlighted for LEDAR-SS design finding non-localized harvester isolation applicability.

In another radical adventure, Hosseinkhani et al [139] demonstrated energy harvesting design that characteristically activate linear and nonlinear harvesting of sound and vibrational energy for application while Liu et al [140] identified that to a large extent, the isolation capacity of nonlinear vibration isolators generally depends on the selection of design parameters (including structural, geometric, preloads and excitation parameters). The approach adopted to characterize the isolation/harvesting performances of the levered configuration reported in this work shall likewise undertake a parametrized analysis of the performances as a function of relevant mechanical and electrical parameters. To effectively convert the vibrational kinetic energy into electrical energy, different transduction mechanisms has been reported such as the electromagnetic method presented by Sun et al [124], piezoelectric method reported by Xie et al [141] and triboelectric (TENG) method analyzed by Adonijah et al [142]. A earlier noted, some identified usage for dedicated applications of energy harvester include wind turbine harvesting [143] and electromagnetic vibration harvesting for train and rail applications [144, 145], smart water system metering [146] etc.

Asides a generalized approach that realized standalone harvester performances via a single transduction method, other design approach are achieved that uses the hybridization of two different transduction mechanisms to improve the harvested power. The need for the derivation of the electromagnetic damping ratio from Maxwell's equations and the Faraday's law based on the statistical theory of losses to an accuracy of 99.54 % was presented [147]. An example of such hybridized transducer attempt was a compact hybrid solar and electromagnetic design. The packaged solar cell used as the substrate is sandwiched between a meshed patch and a rectifying circuit that absorbed solar energy which is then converted to DC power separately or simultaneously with the electromagnetic configuration [148]. Another design that incorporated hybrid transducing is a synergistic system that uses thermoelectric-piezoelectric approach utilizing ambient thermal mechanical energy flows as reported by Kim et al [149]. While amplifying the thermoelectric efficiency using a new approach of actively adjusting thermal energy flows through the piezoelectric beam dynamics, the combined operation only harvested an optimal power of 7.619 mW at 0.5 g. A separate hybridized approach which take the advantage of biomechanical energy to actualize a shaft-shared triboelectric-electromagnetic hybrid portable energy harvester is proposed to drive functional LEDs with a wide range of wavelengths was achieved and reported by Ra et al [150]. Although the design achieved the set objectives, it is required to be operated by human over an optimally designed gearbox which is susceptible to wear and tear and hence failure; such are undesirable for efficient applications in energy harvesting technologies. Also, a breathable and woven hybrid energy harvester that is knitted with a textile TENG and fiber BFCs with a power management circuit is specially designed to amplify the power by 46 times and lower the effective internal impedance of the power source was reported by Zhuo et al [151] as another wearable device with efficient hybrid method of transduction.

While other sections of this review has highlighted different approach to attain certain degree of standalone harvester or isolation performances and either a hybrid or non-hybridized transduction. Performance tradeoffs such has the harvested power, isolation capacities, design compatibility and other has pioneered some research endeavor to

consider a hybrid system of vibration isolations and energy harvester. Such approach efficiently incorporated both vibration isolation and energy harvesting system into a single unit as reported in this work. These hybridized isolator-harvester configurations clearly demonstrated the capacity to simultaneously isolate vibration while converting the certain degree of response registered in the model into electrical energy in the transduction medium. For a low resonance vibration energy harvesting and isolation application, two different designs i.e., a tri-stable nonlinearity-enhanced mechanism [152] and a dual-functional metamaterial by Lu et al [153] has been proposed. Both designs used the energy transfer through resonant inter-well oscillations to achieve a larger bandwidth. Noting the complexity and limitations of low resonant vibration harvesting, Xu et al [154] and Lu et al [155] identified that quasi-zero stiffness (QZS) configuration is widely used in vibration isolation at low frequency (< 5 Hz) and ultra-low level (< 0.05 g). Another method which attains a simultaneous vibration energy harvesting and isolation via quasi-zero-stiffness support and radially distributed piezoelectric cantilever beams was shown by Liu, Zhao, and Liao [155]. Because the peaks for simultaneous isolation and harvester for the design presented by Liu et al [155] falls on different spectral bands tuning is thus required for each specific application in other to attain a close match in the two regions. However, such tuning is quite unnecessary in the LEDAR-SS configuration which always attain a near resonant simultaneous vibration isolation and energy harvesting. Yan et al [156] presented a levered configuration with magnetic spring using a negative resistance shunts to compensate for inherent resistance, the effect of levered vibration isolators with electromagnetic shunt damping was successfully improved. Different from using the magnetic spring, Wang et al [157] reported a similar levered harvester-isolator configuration using a high-static-low-dynamic-stiffness spring to effect vibration isolator with electromagnetic shunt damping. Although both designs have the non-linear responses, the isolation point is still far beyond the resonance.

This work presented a novel vibration harvesting and isolation on a levered mechanical system. The simultaneous vibration isolator-harvester functions is designed to both isolate a payload from external vibrations and harvest energy from these vibrations to power the payload. By combining these two functions in a single device, the hybrid

vibration isolator harvester is able to both protect the payload from vibrations and provide it with a sustainable source of power. This makes it an ideal solution for applications where both vibration isolation and power generation are required. In Chapter 5.2, a generalized model and the governing equations in different design configurations was presented. Chapter 5.3 introduces a generalized performance theory that characterizes the response comparison analysis of the two design strategies relative to the conventional isolator designs when the transduction coil was both present and absent while later establishing a generalized rule for enhanced isolation and energy harvesting performance as a function of the different damping ration parameters. In Chapter 5.4, the potential and the restoring in the model was characterized as a function of the static preloads and offsets in the spring over different levels of lever ratio and preloads affected the isolation-harvester performances in the model. Chapter 5.5 focused on the experimental verification for the analytical equations reported in Chapter 5.2 while Chapter 5.6 parametrically investigated the simultaneous harvesting-isolation performance over different mechanical and electrical parameter of the model. In Chapter 5.7, the conclusion summarizes the significant contribution in terms of isolation, energy harvesting and hybrid performance.

5.1 Generalized LEDAR-SS model designs and operations

The generalized model configuration considered in this work uses a rigid lever pivoted over some bearing while its response is constrained to a desired DOF using a guiderail. Beside the guiderails, the bearings used in the model also introduce Coulomb friction force during operation. The derivation of the governing equation for the SDOF levered configuration was based on the Lagrange equation premised on the generalized energy change in the associated coordinate of the system during excitation.

The hybridized vibration energy harvesting and isolation effect of the LEDAR-SS mechanism considered in this work was investigated using two design configurations as shown in Figs. 5.1 and 5.2, strategy A (presence of both vertical and horizontal guiderails) and strategy B (no guiderails).

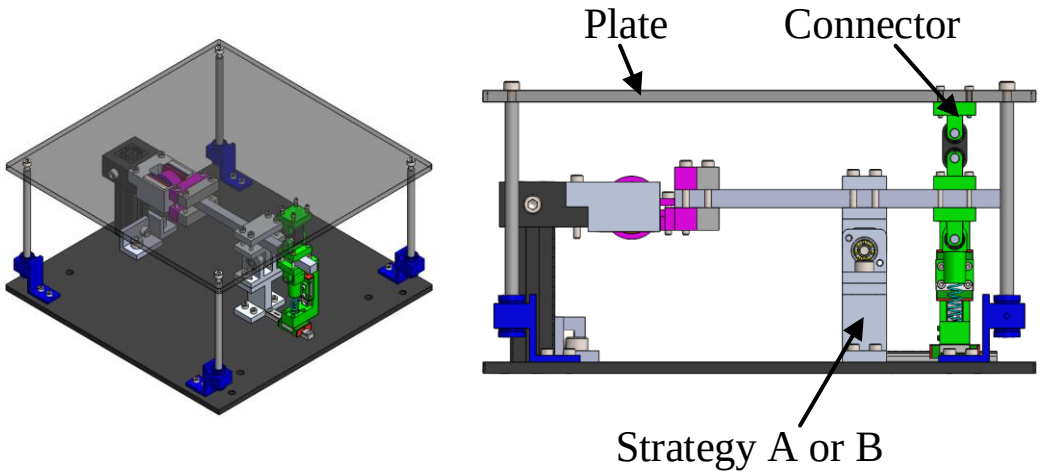

Figure 5.1 Isolator-harvester design with transduction coil; 3D view (left) and side view (right)

The decoupled view of the model in Fig. 5.1 from the isolator platform to show the lever configuration framework is presented as shown in Fig. 2.

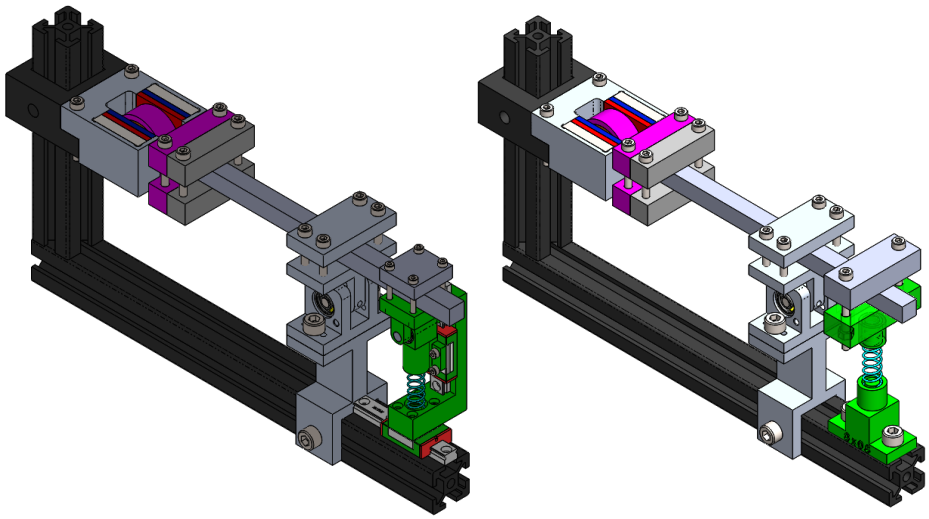

Figure 5.2 Strategy A (left) and strategy B (right)

The respective generalized model is shown in Figs. 5.1and 5.22 has a center pivot which realized a relative amplitude amplification/attenuation over the left-hand side (LHS) and the right-hand side (RHS), trigonometry shows that the response amplitude on the RHS of the lever is larger if the effective beam length on the right-hand side (X_R) is longer than the effective length on the left-hand side (X_L) and vice versa.

From Fig.5.1, the position of the connector could be moved to either LHS or the RHS clamps on the lever. The implication of such possibilities shall be discussed in the later sections. The LHS of the generalized model comprises of two guiderails, restoring spring and a small bearing. All these components on the LHS of the model are coupled as a single unit strapped onto a 3D resin printed material using different and appropriate sizes of screws and nuts. The two bearings in the model are radially loaded and the load distribution on then are carefully symmetrized to reduce any possibility for axial force during dynamic operations. The vertical guiderail strapped to the 3D printed part over a spring was aligned to realize vertically constrained non-stochastic response of lever tip end. However, the horizontal guiderail is a mechanism for dissipating strain force from the 3D printed part especially at much larger excitations. The relative performances of the model in the presence and absence of the fore- mentioned guiderails will be compared in the work to draw specific performance tradeoffs and preference for real life physical applications. Although the presence of the horizontal rail was proposed to dissipate strain forces in the spring via horizontal motion, their absence however will initiate certain degree of impulsive responses which often arise in mechanical systems due to strain, collision, impact, joint clearances, machine tool interaction, and material handling as shown in the later sections. Impulsive events dissipates energy via components such as bearings and sliders that has certain degree of loose fittings/unnecessary stick motion.

5.2 Governing equation of the lever model

The schematic representation and the generalized spring mass LEDAR-SS mechanism in consideration for the levered Coulomb damped system is shown in Fig. 5.2. The decoupled view of the model in Fig. 5.1 from the isolator platform to show the lever configuration framework is presented with various geometrical parameters shown in Fig. 3. In the following analysis, the parametric terms M_f, ω_n $F_{r_{gry}}$, $F_{r_{grx}}$, $F_{r_{b_1}}$, and $F_{r_{b_2}}$ are the effective mass of the model, angular resonance, frictions in the vertical and the horizontal guiderail, frictions in the central pivot bearing and the frictions in the small bearing respectively. F_{r_s} is however defined as other force component associated with the straining in the 3D printed part. The sinusoidal base excitation is $y = F_0 \sin(\omega t + \delta)$, $\ddot{y}$ is

the excitation acceleration defined as $\ddot{y} = \omega^2 y$, F_0 is the maximum amplitude of the base excitation and δ is the phase difference between the response and excitation.

The dynamic generalized governing equation of the levered model as obtained using the Lagrange of the system is shown in Eq. (5.1).

$$\ddot{Y} + \frac{v}{2\epsilon m_e}(c_{mech} + c_{coil})\dot{Y} + \omega_n^2 Y \pm \frac{1}{\mathrm{M}_f} F_r \mathrm{sgn}(\dot{Y}) + F_0 = \ddot{y} \tag{5.1}$$

where ω_n is the the resonant angular frequency, F_r is the total friction in the system and c_{mech} and c_{coil} are the mechanical and the electromagnetic damping coefficients respectively.

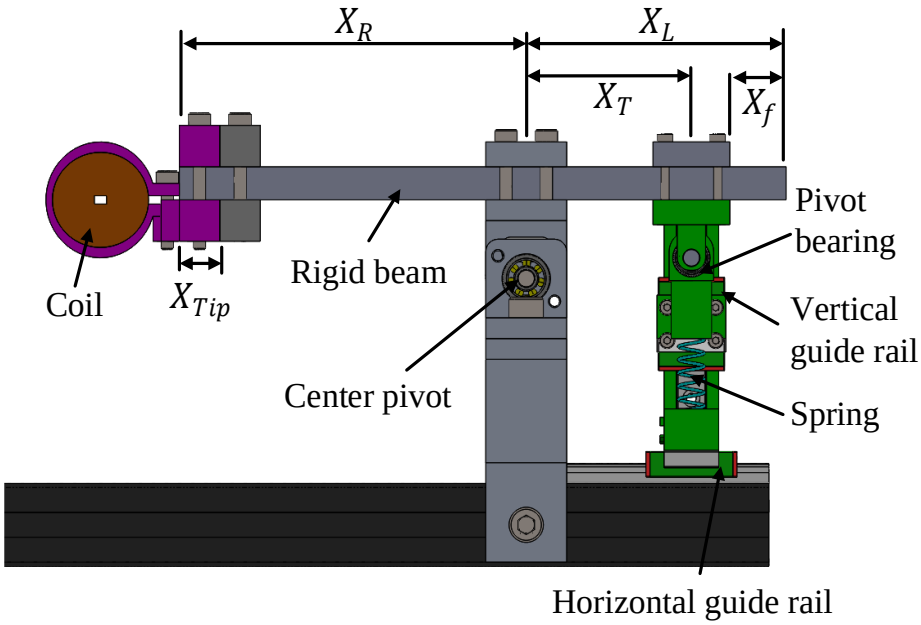

Figure 5.3 Design for the forced Coulomb-damped lever-type configuration

The dimensionless amplification factors v and ϵ was defined as shown in Eqs. (5.2) and (5.3). Both equations define the ratios of the lever about the central pivot and the smaller bearing to the left-hand side (LHS) of the beam respectively.

$$v = \frac{X_T}{X_L} \tag{5.2}$$

$$\epsilon = \frac{X_R}{X_L} \tag{5.3}$$

where X_T, X_R, and X_L are the length of the beam on the LHS of the pivot lying between the central pivot and the smaller pivots and the total length of the lever to the right side and left sides of the central pivots respectively. Taking the moment about the central pivot, the effective mass of the model (M_f) was obtained as shown in Eqs. (5.4) - (5.6).

$$\mathrm{m}_e = \frac{1}{X_T}\left(\mathrm{m}\frac{p}{2} + \left(\mathrm{M}_2 + \frac{\mathrm{m}_2}{2}\right)X_T - \mathrm{M}_{2\mathrm{G}}\frac{X_T}{2} - \mathrm{m}_1\frac{X_R}{2} - \mathrm{M}_{Tip}\mathrm{q} - \mathrm{M}_{coil}\left(X_R + X_{cog-Coil}\right)\right) \quad (5.4)$$

$$p = X_L - X_T \quad (5.5)$$

$$q = \left(X_R - X_{cog-Coil} - \frac{X_{Tip}}{2}\right) \quad (5.6)$$

where X_T, X_R, and X_L are the length of the beam on the LHS of the pivot lying between the central pivot and the smaller pivots, the total length of the lever arm to the right side, and left sides of the central pivots/lever respectively. Also, $\mathrm{m}, \mathrm{m}_2, \mathrm{M}_2, \mathrm{M}_{2G}, \mathrm{m}_1, \mathrm{M}_{Tip},$ and M_{coil} are the mass of the beam portion of length from the LHS end to the the smaller bearing on spring, mass of the beam portion of length X_T, mass of the clamp supported on the smaller bearing on the spring, the effective lumped mass; from the bearing holder, guiderail block, and bearing pin as highlighted in Fig. 5.3, effective mass of the beam of length X_R, the mass of the coupled tip mass and effective mass of the transduction coil respectively. $X_{cog-Coil}$ is the center of mass of the coil along x-axis. The coupled tip mass size was carefully selected to realize a mechanism for static equilibrium in the model, thereby preventing a static preload stress in the spring.

To ensure that no signficant momentum/inertia redistribution during excitation occur as a function of the masses of the load plate, the mass of the load bearing plate, was chosen to be quite negligible. Otherwise, if the load bearing plate and the isolating payload has a significant mass, it will alter the natural frequency of the isolator device due to inertia redistribution and stiffness matrix alteration. This alteration often leads to a shift in the resonance frequency of the system to a lower spectrum since M_f in Eq. (5.4) will become larger in such circumstances thus initiating a more excessive responses and eventual failure of the system. This concerns forms the limits for the application of the isolator system for small pay load application such as small precision measuring instruments,

gyroscopes, microelectromechanical sensors, small optical components, microfluidic devices etc. to avoid initiating unwanted levels of static preloading in the springs.

The Lagrange (L), in the generalised coordinate for the model is as shown in Eq. (5.7), and the potential energy (V) and kinetic energy (T) of the levered model was obtained as shown in Eqs. (5.8) and (5.9).

$$L = T - V \tag{5.7}$$

$$V = \left(\frac{1}{2}F_s + F_{r_{gry}} + F_{r_{grx}} + F_{r_{b_1}} + F_{r_{b_2}}\right) sgn(\dot{Y})Y + M_f gY + I\ddot{\theta}\theta\frac{Y}{X_L} + \int F_{r_s}\, dY \tag{5.8}$$

$$T = \frac{1}{2}\mathrm{m}_e\dot{Y}^2 \tag{5.9}$$

Using Eqs. (7)–(9), the Lagrange of the system was obtained as shown in Eq. (10).

$$L = \frac{1}{2}M_f\dot{Y}^2 - \left(\frac{1}{2}F_s + F_{r_{gry}} + F_{r_{grx}} + F_{r_{b_1}} + F_{r_{b_2}}\right) sgn(\dot{Y})Y - M_f gY - I\ddot{\theta}\theta\frac{Y}{X_L} - \int F_{r_s}\, dY \tag{5.10}$$

where F_s, $F_{r_{gry}}$, $F_{r_{grx}}$, $F_{r_{b_1}}$, $F_{r_{b_2}}$, F_{r_s}, and *I* are the damping force in the spring, Coulomb frictional force in the vertical guiderail, frictional force in the horizontal guiderail, frictional force in the central pivot bearing, friction force in small bearing located on the spring, strain force in the 3D printed part of model, and the mass moment of inertia. The generalized equation of motion for the model from the generalized Lagrange is shown in Eq. (5.11).

$$\frac{d}{dt}\left(\frac{\partial L}{\partial \dot{x}_i}\right) - \left(\frac{\partial L}{\partial x_i}\right) = F_i \tag{5.11}$$

where F_i is the generalized force coordinate acting on the system. In this case, F_i is the force function associated with the external excitation defined as $F_i = \mathrm{M}_f\ddot{y}$ where y is the excitation force defined as $y = F_0\sin(\omega t + \delta)$ and $\ddot{y}$ is the excitation acceleration defined as $\ddot{y} = \omega^2 y$. The trigonometric identity $\sin\theta = \left(\nu\frac{Y}{X_L}\right)$ and appropriate first and second derivatives have been used noting that when θ is very small, $\sin\theta \approx \theta$. Therefore, using this definition and Eq. (2), $\theta = \nu\frac{Y}{X_L} = \frac{X_T Y}{X_L^2}$, thus the terms $I\ddot{\theta}\theta\frac{Y}{X_L}$ in Eq. (8) equivalent to $I\ddot{\theta}\frac{X_T Y^2}{X_L^3}$ is approximated to zero since $X_L^3 \gg X_T Y^2$.

The damping force (F_s) which is the sum of damping contribution from the stiffness and the viscous parameter of the system is defined as $F_s = \frac{\nu}{\epsilon}\left(c\dot{Y} + kY\right)$ is defined in Eq. (5.12).

$$F_{res} = \frac{\nu}{2\epsilon} F_s \tag{5.12}$$

Using the definition of L and appropriate derivative by substituting Eq. (5.10) into Eq. (5.11) gives the generalized equation of motion as shown in Eq. (5.13).

$$\mathrm{M}_f \ddot{Y} + \frac{\nu}{2\epsilon}(c_{mech} + c_{coil})\dot{Y} + \frac{\nu}{2\epsilon} kY + F_r \mathrm{sgn}\left(\dot{Y}\right) + \mathrm{M}_f g = \mathrm{M}_f \ddot{y} \tag{5.13}$$

where F_r is defined as shown in Eq. (5.14).

$$F_r = \left(F_{r_{gry}} + F_{r_{grx}} + F_{r_{b_1}} + F_{r_{b_2}} + \mathrm{F}_{r_s}\right) \tag{5.14}$$

Eq. (14) is valid for the strategy A. For strategy B, the $F_{r_{gry}}$, $F_{r_{grx}}$, and $F_{r_{b_2}}$ will be consider as zero. With the definition of the effective mass M_f in Eq. (5.4), angular resonance ω_n of the system was then obtained as shown in Eq. (5.15).

$$\omega_n = \sqrt{\frac{\nu}{2\epsilon \mathrm{M}_f} k} \tag{5.15}$$

To obtain an explicit solution to Eq. (5.13), a generalized assumption that the response during excitation is symmetric with respect to the equilibrium natural axes of the lever due to the symmetric loading during excitation. Hence, the following initial conditions were used to characterize the response of the model defining frequency ratio (r) as the ratio of excitation frequency to the resonant frequency.

A. At $t = 0$,

$$Y = Y_m \quad \text{and} \tag{5.16}$$

$$\dot{Y} = 0 \tag{5.17}$$

B. At $t = \frac{T}{2} = \frac{\pi}{\omega}$,

$$Y = -Y_m \quad \text{and} \tag{5.18}$$

$$\dot{Y} = 0 \tag{5.19}$$

Using the condition above on Eq. (5.13) gives the simplified matrix Eq. (5.20)

$$\begin{bmatrix} p & q \\ t & u \end{bmatrix} \begin{bmatrix} \sin\delta \\ \cos\delta \end{bmatrix} = \begin{bmatrix} g \\ h \end{bmatrix} \tag{5.20}$$

where

$$p = \left(\varphi \sin(\tau) - \cos(\tau) - e^{-\lambda}\right) \tag{5.21}$$

$$q = -\frac{\omega}{\beta}\sin(\tau) \tag{5.22}$$

$$t = \left((\gamma - \varphi\beta)\cos(\tau) - (\varphi\gamma + \beta)\sin(\tau)\right) \tag{5.23}$$

$$u = \left(\omega\cos(\tau) + \omega e^{-\lambda} + \frac{\omega}{\beta}\gamma\sin(\tau)\right) \tag{5.24}$$

$$g = \left(\varphi \sin(\tau) - \cos(\tau) - e^{-\lambda}\right)\frac{Y_m}{F_0 r^2 Q} + \left(\cos(\tau) - \varphi\sin(\tau) - e^{-\lambda}\right)\frac{\left(\frac{\nu}{\omega_n^2 \mathrm{M}_f}F_r + \frac{g}{\omega_n^2}\right)}{F_0 r^2 Q} \tag{5.25}$$

$$h = \left((\gamma - \varphi\beta)\cos(\tau) - (\varphi\gamma + \beta)\sin(\tau)\right)\frac{\left(Y_m - \frac{\nu}{\omega_n^2 \mathrm{M}_f}F_r sgn(\dot{Y}) - \frac{1}{\omega_n^2}g\right)}{F_0 r^2 Q} \tag{5.26}$$

Adequate expression for $\sin\delta$ and $\cos\delta$ was obtained by solving the matrix in Eq. (5.20) to give

$$\sin\delta = \frac{uE - qF}{pu - tq} \tag{5.27}$$

$$\cos\delta = \frac{pF - tE}{pu - tq} \tag{5.28}$$

Using the trigonometric identity, $\sin^2\delta + \cos^2\delta = 1$ after substituting appropriate expressions for p, q, t, u, E, and F into Eq. (5.27) and Eq. (5.28) gives the solution of the second order nonhomogeneous response for Eq. (5.13) as

$$Y_m = -\frac{H}{2G}\left(\frac{\nu}{\omega_n^2 \mathrm{M}_f}F_r + \frac{g}{\omega_n^2}\right) \pm \frac{1}{2G}\sqrt{H^2\left(\frac{\nu}{\omega_n^2 \mathrm{M}_f}F_r + \frac{g}{\omega_n^2}\right)^2 - 4G(F_0 r^2 Q)^2\left(M\left(\frac{\left(\frac{\nu}{\omega_n^2 \mathrm{M}_f}F_r + \frac{g}{\omega_n^2}\right)}{F_0 r^2 Q}\right)^2 - N\right)} \tag{5.29}$$

where,

$$G = \left[\left(\varphi - \frac{\gamma}{\beta}\right)^2 e^{-2\lambda}\sin^2(\tau) + 4e^{-2\lambda}\cos^2(\tau) + e^{-4\lambda} + 1 - 4\left(\varphi - \frac{\gamma}{\beta}\right)e^{-2\lambda}\sin(\tau)\cos(\tau) - 2\left(\varphi - \frac{\gamma}{\beta}\right)e^{-3\lambda}\sin(\tau) - 2\left(\varphi - \frac{\gamma}{\beta}\right)e^{-\lambda}\sin(\tau) + 2e^{-3\lambda}\cos(\tau) + 2e^{-\lambda}\cos(\tau) + 2e^{-2\lambda}\right] \quad (5.30)$$

$$H = \omega^2\left[2e^{-4\lambda} + 2\left(2\frac{\gamma}{\beta}\sin(\tau) + 2\cos(\tau)\right)e^{-3\lambda} - 2\left(\left(\frac{\gamma}{\beta} + \varphi\right)^2\sin^2(\tau) + 4\left(\frac{\gamma}{\beta} + \varphi\right)\sin(\tau)\cos(\tau)\right)e^{-2\lambda} - 2\left(2\cos(\tau) - 2\frac{\gamma}{\beta}\sin(\tau)\right)e^{-\lambda} - 2\right] \quad (5.31)$$

$$M = \omega^2 + \omega^2 e^{-4\lambda} + 2\omega^2\left(\frac{\gamma}{\beta} + \varphi\right)\sin(\tau)\,e^{-3\lambda} + \left(\left(\frac{\gamma}{\beta} + \varphi\right)^2\sin^2(\tau) - 2\right)\omega^2 e^{-2\lambda} - 2\left(\frac{\gamma}{\beta} + \varphi\right)\omega^2 e^{-\lambda}\sin(\tau) \quad (5.32)$$

$$N = \omega^2\left(\frac{4\gamma^2}{\beta^2}\sin^2(\tau)\cos^2(\tau) - 4\frac{\gamma}{\beta}\sin(\tau)\cos(\tau) + 1\right) - \left(\left(\varphi - \frac{\gamma}{\beta}\right)^2\sin^2(\tau) - 4\cos^2(\tau) - \left(4\omega\frac{\gamma^2}{\beta^2} + \frac{2\gamma}{\beta}\omega - 4\frac{\gamma}{\beta} + 4\varphi\right)\sin(\tau)\cos(\tau) - 2\omega\left(\varphi - \frac{\gamma}{\beta}\right)\sin(\tau) + 4\omega\cos(\tau) + 3\omega\right)\omega^2 e^{-2\lambda} - \left(2\left(\frac{2\gamma}{\beta}\varphi - \frac{2\gamma^2}{\beta^2}\right)\sin^2(\tau)\cos(\tau) - 8\frac{\gamma}{\beta}\sin(\tau)\cos^2(\tau) + 4\cos(\tau)\right)\omega^2 e^{-\lambda} + \omega^4 e^{-4\lambda} \quad (5.33)$$

where, $\varphi = \frac{\nu\zeta_m}{2\sqrt{1-\frac{\nu^2\zeta_m^2}{4}}}$ and $\gamma = \frac{\nu\omega_n\zeta_m}{2}$, $\beta = \omega_n\sqrt{1-\frac{\nu^2\zeta_m^2}{4}}$, $\tau = \frac{\pi\sqrt{1-\frac{\nu^2\zeta_m^2}{4}}}{r}$, $Q = \left[\frac{1}{(\omega_n^2-\omega^2)^2+(\alpha\omega)^2}\right]^{\frac{1}{2}}$

From particular solution of Eq. (5.13), the associated phase (δ) was obtained according to Eq. (5.34) such that the effective phase difference for the LEDAR-SS model was obtained as

$$\delta_{LHS,RHS} = \pm\tan^{-1}\left(\frac{\nu\zeta_m\omega}{\omega_n\left(1-\left(\frac{\omega}{\omega_n}\right)^2\right)}\right) \quad (5.34)$$

It is crucial to note from Eq. (5.8) that the potential function from which the Lagrange was deduced has a gravity dependent term whose effect further goes on to affect the model responses as shown in Eq. (5.29). If the gravity induced potential in neglected and with a consideration to conventional no levered SDOF configuration, $\nu = 1$ and defining $\omega_n^2 \mathrm{M}_f = k$, Eq. (5.34) reduces to the form in Eq. (5.35)

$$Y_m = -\frac{H}{2G}\left(\frac{F_r}{k}\right) \pm F_0\sqrt{Q^2 r^4 \frac{N}{G} - \frac{(4GM - H^2)}{4G^2}\left(\frac{F_r}{F_0 k}\right)^2} \quad (5.35)$$

5.3 Damping ratio equations

Vibration energy harvesting is a promising technology for generating electrical power from ambient vibrations, with applications in wireless sensor networks, IoT devices, and wearable electronics. The respective mechanical damping ratio (ζ_{mech}) and the electromagnetic damping ratio (ζ_{coil}) in the system as reported by Toluwaloju et. al [158] was obtained as shown in Eqs. (5.36) - (5.37). The mechanical damping term is often associated with the viscous damping and the Coulomb friction damping (if friction is present in the system). The addition of the ζ_m and ζ_{coil} gave the total damping (ζ_T) of the system.

$$\zeta_m = \frac{c_{mech}}{2M_f \omega_n} \quad (5.36)$$

$$\zeta_{coil} = \frac{8K^2 {l_c}^2}{2M_f \omega_n}\left(\frac{1}{R_l + R_c}\right) \quad (5.37)$$

where c_{mech}, N , $K, R_l, R_c,$ and l_c are the mechanical damping coefficients, coil turn number, coupling coefficient of coil-magnet configuration, external load resistance, internal resistance of the coil, and effective coil length. The coupling coefficient K is defined as the number of the flux line that cuts the coil is defined as shown in Eq. (38), where b and C_f are the flux density and the coil fill factor [147].

$$K = NbC_f l_c \quad (5.38)$$

The spring constant of each design model were determined experimentally, on a force-displacement testing module as *k* = 940.00 Nm^{-1} and *k* = 1314.10 Nm^{-1}.

5.4 Equations of harvested voltage and power

The equations for computing voltages and power harvested in the levered design when the coil is connected to the tip end of the RHS of the lever is presented in this section. During excitation, the transduction coil freely oscillates in the magnetic field of the

permanent magnet, and the voltage induced in the coil was obtained using the Faraday's principle of electromagnetic induction as shown in Eq. (5.39).

$$v_{ind} = \frac{d\phi}{dt} = Bl_c Y_m \omega \tag{5.39}$$

The magnet configuration was designed using symmetric coupled configurations. Each symmetric half uses two magnets of equal flux density. Hence, the total induced voltage per effective length of the coil was obtained as shown in Eq. (5.40).

$$v_{ind} = 4Kl_c Y_m \omega_n \tag{5.40}$$

where K, l_c, ω_n, and Y_m are function earlier defined as the coupling coefficient in Eq. (5.38), effective coil length, resonant frequency, and the response of the coil about the desired DOF. The close circuit configuration of the coil with internal resistance R_c was connected in series to an external zero inductive load resistor R_l, and the voltage harvested across external resistance was obtained using the voltage division rule as shown in Eq. (5.41).

$$V_{Out} = 4Kl_c z\omega_n \left(\frac{R_l}{R_l + R_c}\right) \tag{5.41}$$

5.5 Characterizing harvesting and isolation of lever device relative to conventional designs

To quantify the harvester and isolation preferences of the model, the performances were respectively compared with the SDOF harvester/isolation configurations as shown in Fig. 5.4. The transmissibility (τ) is defined as the ratio of the amplitude response of the model to the base excitation amplitude at any level of excitation. τ is a property that measures the degree of mechanical isolation in a mechanical system such that when $\tau < 1$, the system is isolating and when $\tau > 1$, the system is amplifying while $\tau = 1$ implies a passive function. The frequency ratio (r) in the following analysis is defined as the ratio of the excitation frequency (f) to frequency at resonance (f_n). Justification on the isolation performances relative to conventional designs highlights the early onset of isolation in the lever design near resonant frequencies compared to conventional designs shown in Fig. 5.4. While conventional designs often rely on passive or active isolation mechanisms to

mitigate the effects of external vibrations, typically onset at about $\sqrt{2}f_n$. LEDAR-SS however, shows capacity for near resonant self-isolation characteristics when harvesting energy by leveraging on the mechanical advantage of a lever arm to amplify the displacement of the proof mass in response to vibrations, thereby increasing the harvested energy compared to conventional design needing a passive or an active isolation mechanisms. Vibration isolators are devices that prevent the transmission of vibration from one component of a mechanical system to another. The procedure for isolation that uses mechanical springs and rubber pads called passive isolation have been used for application on industrial equipment such as pumps, motors, heating, ventilation and air conditioning (HVAC) systems, washing machines, sensitive laboratory equipment, sensors, payloads, high-end audio etc. Both linear and nonlinear approaches has been adopted to achieve passive vibration isolation in a mechanical system attaining onset of isolation at $\sqrt{2}f_n$ where f_n is the operational resonance The nonlinear vibration isolation devices (NLVIDs) approaches reported in literature are either negative stiffness vibration isolation devices (NSVIDs) positive stiffness vibration isolation devices (PSVIDs) or quasi-zero stiffness vibration isolation devices (QZSVIDs) by using compressed springs, pre-buckled beam, magnetic element, geometrically nonlinear structure as well as composites or metamaterials to initiate nonlinear effects. For any given NLVIDs, the three types of stiffness mentioned above could exist independently or simultaneous depending on the geometrical designs. One of the focuses on NLVIDs has been on developing system with very low resonant frequencies so that low frequencies can be isolated at high static load bearing capacities on very sensitive instrumentation devices while noting that isolating higher frequencies compromised on the static load bearing capacities conventional linear isolator which attained isolation onset at $r > \sqrt{2}$ where r is the ratio of excitation frequency to frequency at resonance. With a consideration to the operational compromise on the conventional linear and NLVIDs, the levered isolator realizes two novel distinct advantages over them as shown in Fig 5.4.

In general, Fig. 5.4 highlighted that while SDOF configurations attained isolation at $r \geq \sqrt{2}$, the levered configuration onset a banded isolation at $r < 0.901, r < 0.946$ and $1.099 < r < 1.639, 1.078 < r < 1.482$ on the LHS and the RHS lever when the

coil is present and absent, respectively showing that the coil further enhances the bands of isolation. Likewise, Fig. 5.4 highlights that both LHS and the RHS attained isolation characteristics before and after the resonances in a consistent manner with the phase equation (5.34) as shown in Fig. 5.4 (right) showing that while the phases of the LHS of the lever is consistent with the SDOF such that it is always in and out of phase with the base before and after resonance, those for the RHS attained a reversed phase. The reversed phases initiated a slight delay in the responses and hence a slight variations in the resonant peaks in the response profile of the levered system on the RHS relative to the LHS.

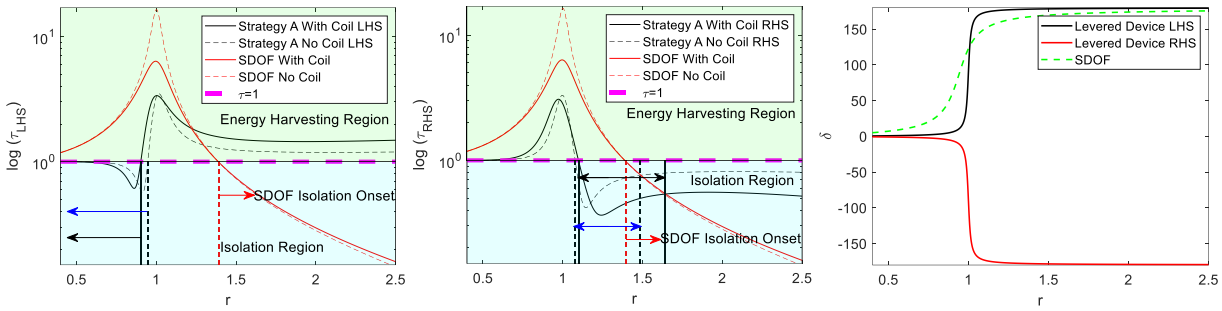

Figure 5.4 Transmissibility comparison with a conventional SDOF harvester configuration; LHS (left), RHS (middle) and phase (right)

When the system is in static equilibrium, the rig is such that zero preload compression or tensile existed in the spring, however, as the dynamic testing advances toward resonances, the preloads becomes a sudden compression. The early onset of isolation in the lever design near resonant frequencies can be attributed to the amplification of the displacement of the proof mass and the mechanical advantage provided by the lever arm such that as excitation approaches resonance, the amplification of the displacement due to the lever ratio and the clamp mass sizes further enhances or compromise sudden compression preload. This effect hypothetically alters the stiffness matrix of the spring resulting in pre and post near resonance on the LHS and RHS of the lever respectively. Post resonance in the RHS due to phase reversal. This characteristic of the lever design by tuning the lever ratio not only enhances isolation efficiency but the energy harvesting capacity also.

Noting that the lever system presented in navigate a path for near resonance double banded vibration isolation and energy harvesting, this section gives insight to quantifying the practicable range for resonance choice for the design at any desirable τ. If the operating or disturbing frequency to be isolated is identified as f, reference to Fig. 5.4 shows the onset of isolation on NLVIDs and conventional designs occurred at ratio $(r) = \sqrt{2}$ and $r \cong 1$. The generalized expression for obtaining the level of transmissibility at a desired f_n and disturbing f to be isolated was then obtained as shown in Eq. (5.42).

$$\tau = \left| \frac{1}{\left(\frac{f}{f_n}\right)^2 - 1} \right| \tag{5.42}$$

A sequel to Eq. (5.42) by the plot of f_n versus τ at different desired f and f_n versus f is shown in Fig. 5.5. From Fig. 5.5, dotted red and black lines marks the bound of region $f/\sqrt{2}$ or $\pm 0.015\, f$ and $\delta f_n / \delta\, \tau = 0$ are defined as the minimum and maximum windows for the choice of f_n for any design. The area bounded within these two lines highlighted the regions where the τ of the system changes significantly such that beyond those areas, any choice of f_n will not produce any considerable change τ. The above suggests that, available bandwidth for choice of resonant always lies between $f/\sqrt{2}$ or $\pm 0.015\, f$ and $(\delta f_n / \delta\, \tau)_f = 0$ where Fig. 5.5(left) shows that as f increases, the band available for choice of f_n consequentially increases.

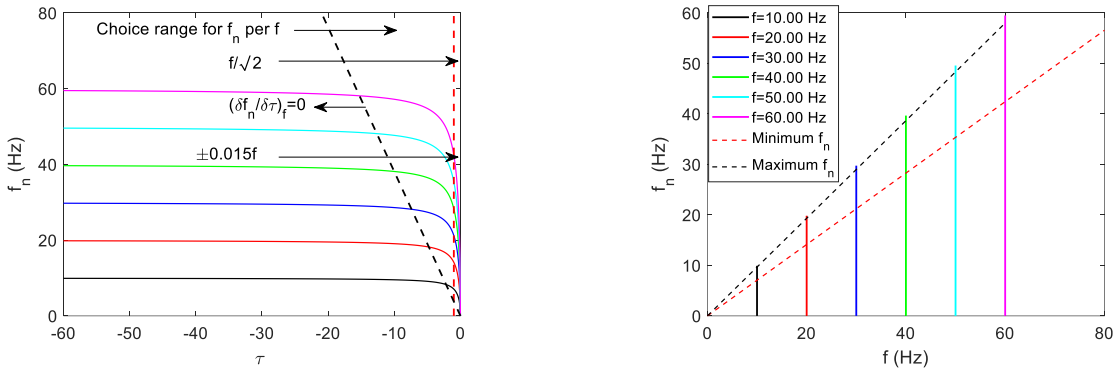

Figure 5.5 Resonant versus transmissibility at different f (left) and resonant versus f (right)

To further clarify the variation of the available bands/window for choice of f_n, Fig. 5.5 (right) shows that as the disturbing frequency to be isolated (f) approaches a lower spectrum, a challenge of coincidence with operational resonant arose. Most conventional isolator handle such challenge by designing low static device. Although such innovations successfully achieve it purpose, two main challenges are however, identified. First, in other to achieve lower operational resonance $f_n = f/\sqrt{2}$ earlier than f, the static load bearing capacity(stiffness) of the conventional nonlinear designs are significantly compromised, however, the levered device in discussion here shows capacity for low frequency small payload vibration isolation performances without compromising static stiffness although the high-static-low-dynamic-stiffness (HSLDS) nonlinear isolators have likewise proven to have an advantage over linear isolators by attaining low-frequency vibration isolation without compromising the static stiffness, however their isolation onset is still far from resonance. Secondly, in addition to its high-static stiffness characteristic (i.e., good load bearing capacity), the lever design presented successfully showed capacity for isolation in the region where $f_n \cong f$ realizing a banded isolation at $r \mp 0.015$ on the LHS and the RHS of the lever respectively as an advantages over NLVIDs and conventional linear vibration isolators which only showed onset of isolation at $r = \sqrt{2}$.

While damping plays a critical role in vibration energy harvesting-isolation of a systems by dissipating energy and influencing the overall performance. The total damping in any electromechanical system (ζ_T) is shown in Eq. (5.43).

$$\zeta_T = \zeta_{mech} + \zeta_{coil} \tag{5.43}$$

This following section aims to characterize transmissibility (τ) variation relative to the total damping in the system, highlighting the implications and knowledge of direct relationship between damping, amplification, and isolation (anti-resonance) depth shown in Fig. 5.6.

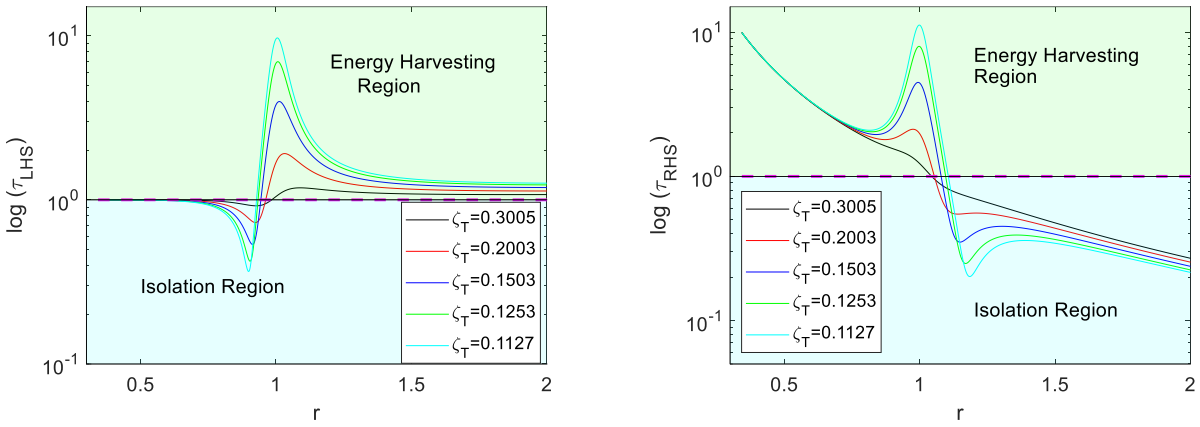

Figure 5.6 Transmissibility comparison lever configuration at different damping level; LHS (left) and RHS (right)

To justify the observed trend for direct proportionality between amplification height and isolation (anti-resonant) depth and the total damping in the system, this work identifies that the isolation depth in the system becomes larger due to increased compressive preload in the spring about resonance, thus compromising the energy dissipation capacity as a linear function of the spring compression and vice versa as shown in Fig. 5.6. Taking advantage of such compromise, the simultaneous near resonant vibration energy harvesting-solation capacity is effectively enhanced by achieving different level of ζ_T by simultaneously or independently tuning ζ_{mech} and ζ_{coil}.

5.5.1 Mechanical and electromagnetic tuning for improved/compromised performance

Since it has been identified that lowering the total damping ratio by independently or simultaneously down tuning the mechanical and electromagnetic damping ratios will effectively reduce the amount of energy dissipated during the vibration harvesting-isolation process. Down tuning the damping ration was observed to generally allow more energy to be harvested with improved anti-resonance depth for better near resonance isolation while compromising the operational bandwidth as shown in Fig. 5.7.

The electromagnetic damping ratio is associated with the parasitic effect of the coil winding and load resistances leading to heating/skin effect in the coil while Eqs. (5.36) and (5.37) shows that the tunable parameter for achieving different levels of ζ_{mech} and

ζ_{coil} are M_f and b. The following section efficiently characterized the condition for minimum ζ_{coil} while ω_n, N, l_c and c_f are fixed in the configuration. Fig. 5.7 shows the variation of ζ_{coil} and ζ_{mech} which are both an inverse function of $\omega_n$with M_f over different flux values.

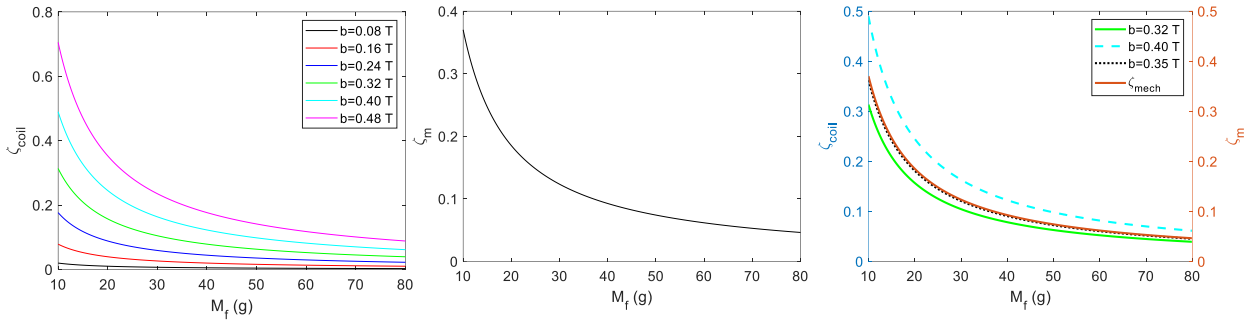

Figure 5.7 ζ_{coil} versus $\mathrm{M_f}$ at different flux level (left) and ζ_{m} versus $\mathrm{M_f}$(middle) and superimposed plots of ζ_{coil} and ζ_{m}(right)

Simulation results shows that at equivalent M_f, while ζ_{coil} changes over different b, ζ_{mech} however does not since it is independent of electrical parameters since it is a mechanical parameter. Super imposing the ζ_{coil} and ζ_{mech} plots in Fig. 5.7 (left) and (middle) resulted in Fig. 5.7 (right) showing that $\zeta_{mech} \cong \zeta_{coil}$ at $b \cong 0.35$ T. At this equivalence, a balanced damping effect within the system, which helps to control vibrations and oscillations leads to improved stability and enhanced performance capabilities is observed [159].

To further compromise the energy dissipation characteristic of the design, Fig. 5.7 and Eq. (5.43) requires that ζ_{coil} must be down tuned from the identified point of equivalence by geometrical or electrical approach. Both are respectively done by tuning the geometric or the coil/load resistances.

Given an electromagnetic transducer of dimensions t_m, h_m, and c_w i.e., magnet thickness, magnet width, and the effective coil width simulated in FEMM software, Fig 5.8 (left) shows the flux variation over the tunable magnet parameter the h_m, and t_m axis i.e., magnet thickness, magnet width, and the effective coil width simulated in FEMM software. Fig. 5.8 (right) showed the variations of the flux over t_m and h_m divides into three regions $\zeta_{coil} = \zeta_{mech}$, $\zeta_{coil} > \zeta_{mech}$ and $\zeta_{coil} < \zeta_{mech}$. The equivalence, $\zeta_{mech} \cong \zeta_{coil}$ occurring at optimal $h_m \cong 0.45$ mm and $t_m \cong 0.45$ mm as shown in Fig. 5.8 (right).

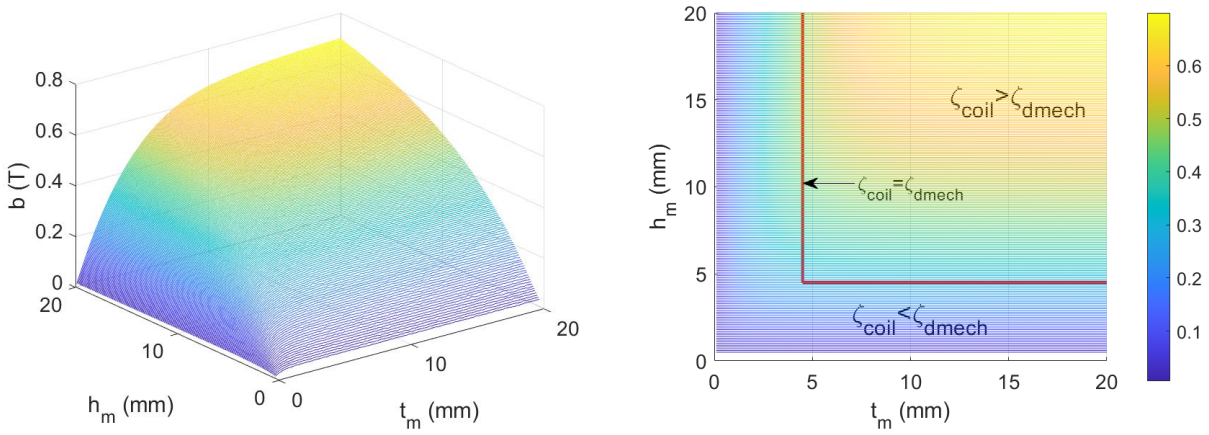

Figure 5.8 Differential variation of b with t_m and h_m, (left) and 2D view b (right)

Each identified region has unique engineering applications. The interval $\zeta_{coil} = \zeta_{mech}$ corresponding to 0.45 mm$\leq t_m \leq 0.99$ mm and 0.45 mm$\leq h_m \leq 0.99$ mm is the point of equivalence on the mechanical and electromagnetic damping ratio realizing 0.34 T$\leq b \leq 0.36$ T. These points attain most stable harvesting performance with higher energy conversion efficiency while regions $\zeta_{coil} > \zeta_{mech}$ are clearly identified for efficient energy harvesting since the flux attained in those regions are high. Lastly the regions $\zeta_{coil} > \zeta_{mech}$ attained enhanced near resonant harvester-isolation performances of the lever design due to the sudden approach of the spring preload to compression as the responses approaches resonances while significantly compromising the total energy dissipation capacity of the system.

The above approach could be generalized to capture how the electromagnetic damping ratio varied in the system when the resonances are tuned to activate $\zeta_{coil} < \zeta_{mech}$ since M_f, ω_n, ζ_{mech}, and ζ_{coil} shows a tractable relationship according to Eqs. (5.13), (5.15), (5.36) and (5.37).

5.5.2 Differential potential and preloads in the spring as a function of design parameter

The static spring preload $(\pm y_{off})$ manifest as the spring potential energy and the restoring force. The y_{off} is negative when the preload is compression and y_{off} is positive when the preload is tensile while $y_{off} = 0.00$ mm implies that the static preloads in the spring is zero During dynamic testing, this preload is further increased or compromised

as a function of different geometric parameters of the design such as the lever ratio (ϵ), tip clamp mass $\left(\mathrm{M}_{Tip}\right)$, and effective beam length (L_b).

Using definition from Eq. (5.6), ϵ >1, ϵ <1 and ϵ =1 implies $X_L < X_R$is $X_L > X_R$ and $X_L = X_R$ respectively corresponds to positive offset (tensile preload) and negative offset (compressive preloads) and no preloads. The offset are further highlighted to vary with M_{Tip} resulting in lever arm to be displaced above or below the neutral axis in the static equilibrium by shifting the inertia of the system. Fig. 5.9(left) showed that larger ϵ i.e., tensile preload implies a larger restoring force and vice versa. Also, the corresponding variation of the potential as a function of ϵ shown in Fig. 5.9(right) highlighted that y_{off} likewise varies with different value of ϵ such that $\epsilon \cong 1$ corresponds to $y_{off} = 0.00$ mm while $\epsilon > 1$ and $\epsilon < 1$ is positive and negative offsets are respectively. Computing the slope $\delta V = \frac{\partial V}{\partial y_{off}}$ from Fig. 5.9(right) showed that δV is maximum due to tensile preloads and vice versa, hence more energy is dissipated during dynamic testing for ϵ >1 than ϵ <1. The above implies a compromise in the isolation depth and vice versa. This effect becomes more obvious as the magnitude of y_{off} is increased.

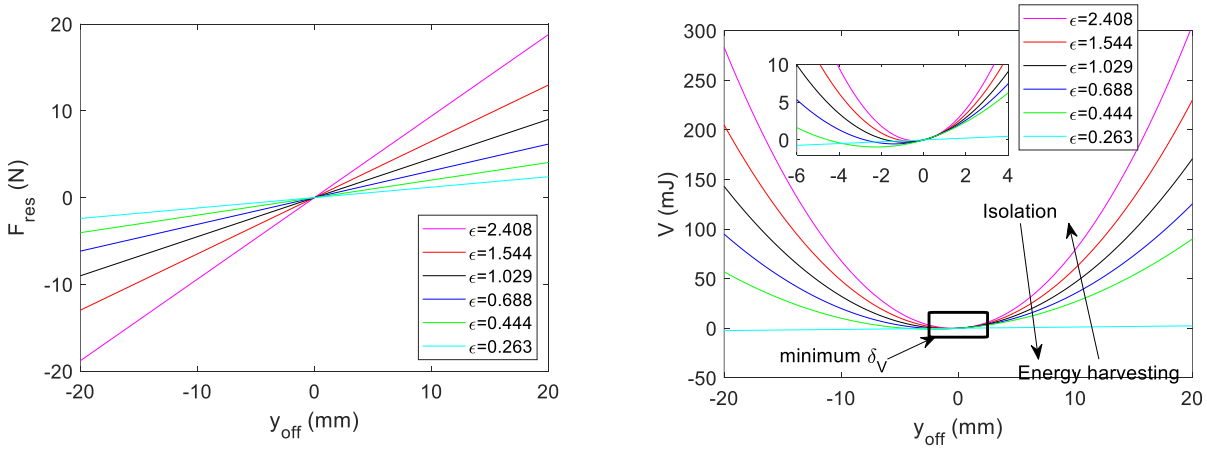

Figure 5.9 Restoring force vs absolute response amplitude (left) and potential energy vs absolute response amplitude (right) by variation of ϵ

Also, the effect of the Coulomb friction forces (F_r) on how friction affected the restoring forces and the potential distribution in the spring as shown in Fig. 5.10.

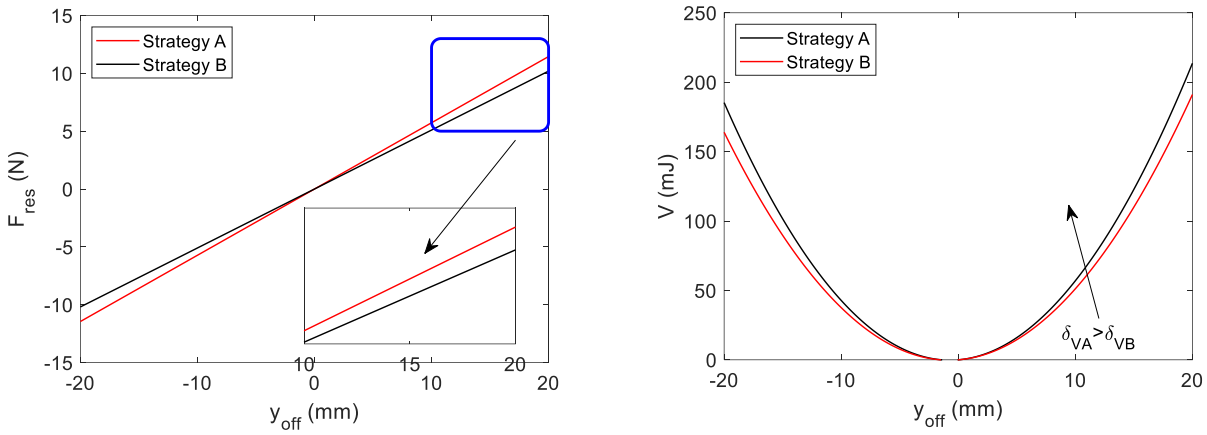

Figure 5.10 Restoring force vs absolute response amplitude (left) and potential energy vs absolute response amplitude (right) for strategies A and B

Fig. 5.10 identified that the design with larger friction (strategy A) attained a larger potential decay relative to those with lesser friction (strategy B) i.e., $\delta_{V_A} > \delta_{V_B}$. The implication of $\delta_{V_A} > \delta_{V_B}$ as a follow up to Fig. 7 is that strategy A with higher potential decay becomes the best option for earlier onset of vibration isolation while strategy B most efficient for vibration energy harvesting.

5.6 Experimental verification

The design of the strategies A and B enumerated was experimentally validated in this section. The vibration was simulated in the laboratory using an EMIC 9514 AN/AS electromagnetic vibration shaker as shown in Fig. 5.11. Two accelerometers were used as feedback to control the desired acceleration and the displacement responses of the harvester on the LHS and the RHS of the lever was captured using a Keyence LK-H050 laser displacement sensor which has a measuring range of ±10 mm. All post experimental analysis of the acquired data are analyzed in MATLAB.

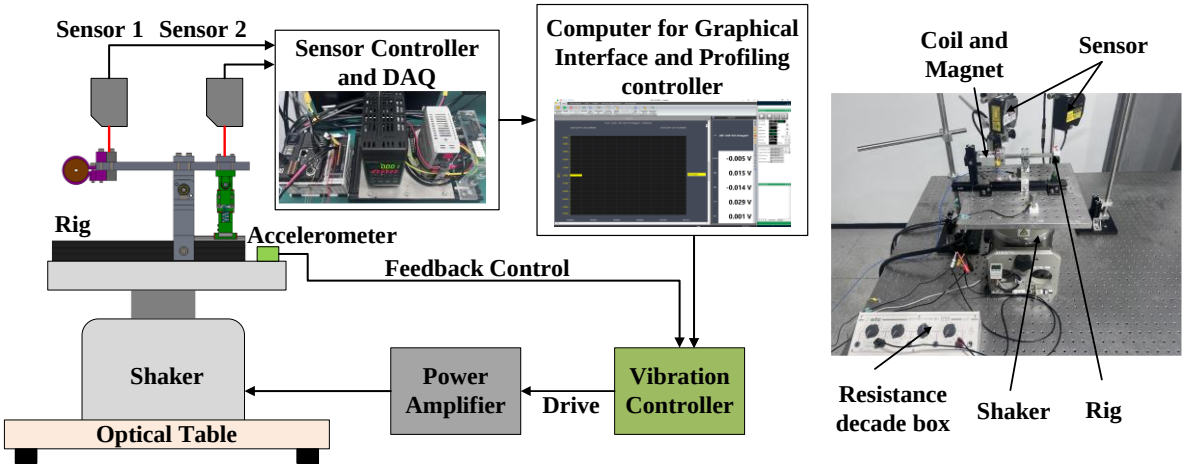

Figure 5.11 Experimental flow chart (left) and rig setup (right) for the laboratory testing

The effective friction in each model was defined as shown in Eqs. (5.14) and (5.15). The pre-pressure applied on each of the guide rail falls in the light preload group of 0–2 % of the dynamic load capacity of the HIWIN MGN7C mechanical slider [160]. The static load capacity, dynamic load capacity and the coefficient of friction force of the mechanical slider was reported as C_{static}= 0.84 kN, C_{dyn}= 0.54 kN and the coefficient of friction computed as 4.99× 10^{-3} resulted in $F_{r_{gx}} = (0-2\%)C_{static} \times \mu \cong 0.0622$ N and $F_{r_{gy}} = (0-2\%)C_{dyn} \times \mu \cong 0.0539$ N respectively.

Likewise, using the generalized definition of friction in two sliding surfaces in contact the friction in the bearings $F_{r_{b_1}}$ and $F_{r_{b_2}}$ were computed as shown in Eq. (5.43).

$$F_{rb1} = \mu_r M_f g \tag{5.43}$$

where μ_r is defined as the coefficient of friction in the bearing has a numerical value of $\mu_r = 0.0015$ obtained from SMB bearing datasheet [161]. The friction in the smaller bearing $(F_{r_{b2}})$ was then obtained as a rationalized function of $F_{r_{b1}}$ as shown in Eq. (5.44) where the terms $D_{pivot} = 12.00$ mm (pivot bearing diameter) and $D_{spring\ bearing} = 9.00$ mm (spring top bearing diameter).

$$F_{r_{b2}} = \frac{D_{pivot}}{D_{spring\ bearing}} F_{r_{b1}} \tag{5.44}$$

The axial load should be less than 20.0 % of the radial load and the load should be purely axial for thrust bearings for efficient bearing performances [161]. Since no known approach is known for determining the strain/buckling force $\left(\mathrm{F}_{r_s}\right)$, their values are predicted in the following analysis.

When, $c_w = 6.00$ mm and $D_m = 14.00$ mm, $t_m = t_s = 5.00$ mm, $w_m = 10.00$ mm, $w_s = 22.00$ mm, and $l_m = l_s = 25.00$ mm, Table 1 gives a summary of the electromagnetic transduction parameters for the coil-magnet transducer using appropriate equations.

Table 5.1 Summary of tip coil parameter

Strategy	N	b (T)	l_c (mm)	c_f	R_c (Ω)	R_l (Ω)	ζ_{coil}
A	870	0.2557	76.7548	0.9097	11.6000	50.0000	0.0513
B	870	0.2557	76.7548	0.9097	11.6000	50.0000	0.0421

ζ_{coil} in Table 1 for strategies A and B obtained from Eq. (5.36), are observed to be different due to differences in geometry and respective stiffness and hence the effective masses and the resonances on strategies A and B. In the following sections, the experimental data obtained for strategies A and B were compared to the analytical solutions presented in Eqs. (5.1) – (5.44) for verification and analysis.

To compute the degree of fit between analytical solutions and the experimental data, calculating the coefficient of determination, also known as R-squared (R^2) is sufficient. R-squared is a statistical measure that represents the proportion of the variance in the dependent variable that is predictable from the independent variable(s) in a regression model according to Eq. (5.45).

$$R^2 = 1 - \frac{\sum_{i=1}^{n}\left(y_i - y_{Theoryi}\right)^2}{\sum_{i=1}^{n}(y_i - \bar{y})^2} \tag{5.45}$$

where $y_{Theoryi}$ is the predicted value from the theoretical model for each data point, y_i is the observed experimental data, $\bar{y}$ is the mean of the observed experimental data and n is the number of the observed data points.

5.6.1 Response validation of Strategy A

The response of design strategy A at different levels of excitations when $X_f = 0.00$ mm, $X_L = 81.780$ mm, $X_R = 61.069$ mm, $X_T = 72.130$ mm, and $\epsilon = 0.832$ is shown in Fig. 11. The responses of the LHS and the RHS was clearly identified at frequency < 13.79 Hz and frequency > 15.48 Hz, respectively. Considering the drive frequency spectrum 13.20 Hz to 20.00 Hz, the experimental results show a strong agreement of about R^2 =90.41 % with the analytical solutions. A 90.41 % degree of fit between analytical and experimental data indicates a relatively good level of agreement between the two datasets. This level of fit suggests that the analytical model is capturing a significant portion of the variability present in the experimental data. While there may still be some discrepancies between the analytical predictions and the actual experimental results due to rig inconsistencies especially at drive frequencies below 13.20 Hz because of certain misalignments in various parts of the rig, a 90.41% fit implies a solid correlation and predictive capability of the analytical model. Further refinement of the rig with precision manufacturing to reduce spalling effects in the bearing and eliminating impulsive events etc. will potentially improve the degree of fit.

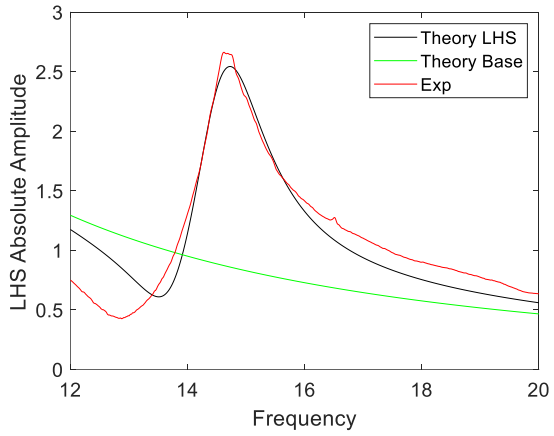

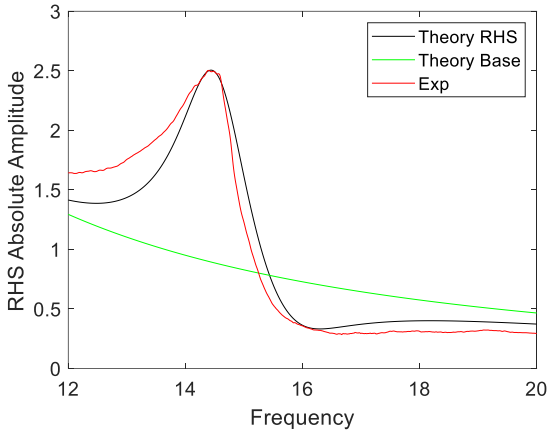

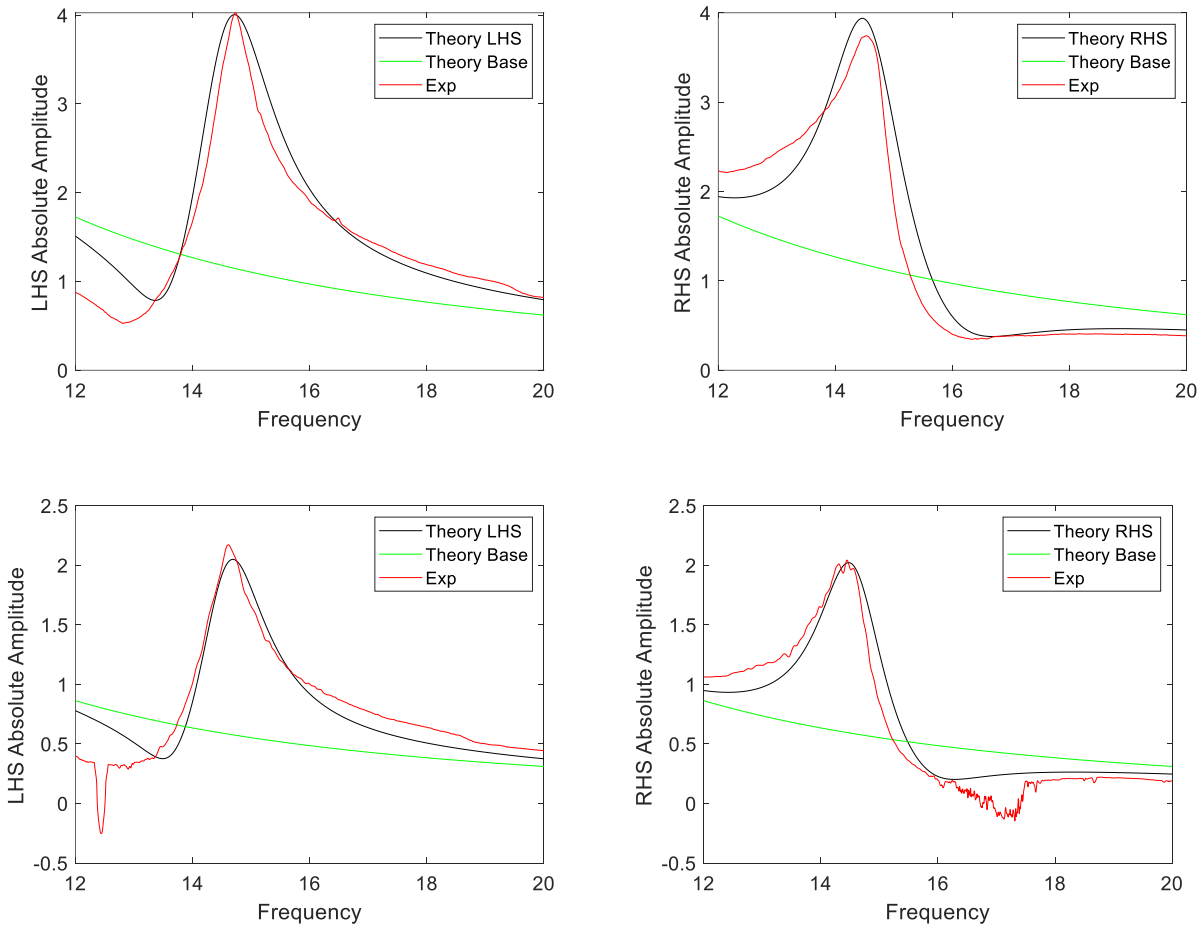

Figure 5.12 Absolute amplitude (mm) strategy A at $\mathrm{X_f} = 0.00$ mm for 1.00 g (top), 0.75 g (middle), and 0.50 g (bottom)

Table 5.2 shows the summary of the performance parameters for strategy A where F_{r_s} was obtained to vary linearly with excitation acceleration. Using Eqs. (5.43) and (5.44), the $F_{r_{b1}}$ and $F_{r_{b2}}$ on strategy A was computed as 0.6062 mN and 0.4547 mN, respectively.

Table 5.2 Summary of performance parameter for strategy A

g	k $(\mathrm{Nm^{-1}})$	f_n (Hz)	ζ_{mech}	F_{r_s} (N)
0.50	940	14.68	0.0772	0.0655
0.75	940	14.68	0.0907	0.1568
1.00	940	14.68	0.1002	0.2481

5.6.2 Response validation of Strategy B

Fig. 5.13 shows the response of design strategy B at excitation levels of 0.75 g and 0.50 g when $\mathrm{X}_f = 0.00$ mm, $X_L = 81.000$ mm, $X_R = 68.069$ mm, $X_T = 73.250$ mm, and $\epsilon = 1.189$. The profile shows that design strategy B has a larger responses than strategy A under equivalent excitation levels because it has a lesser Coulomb frictional damping.

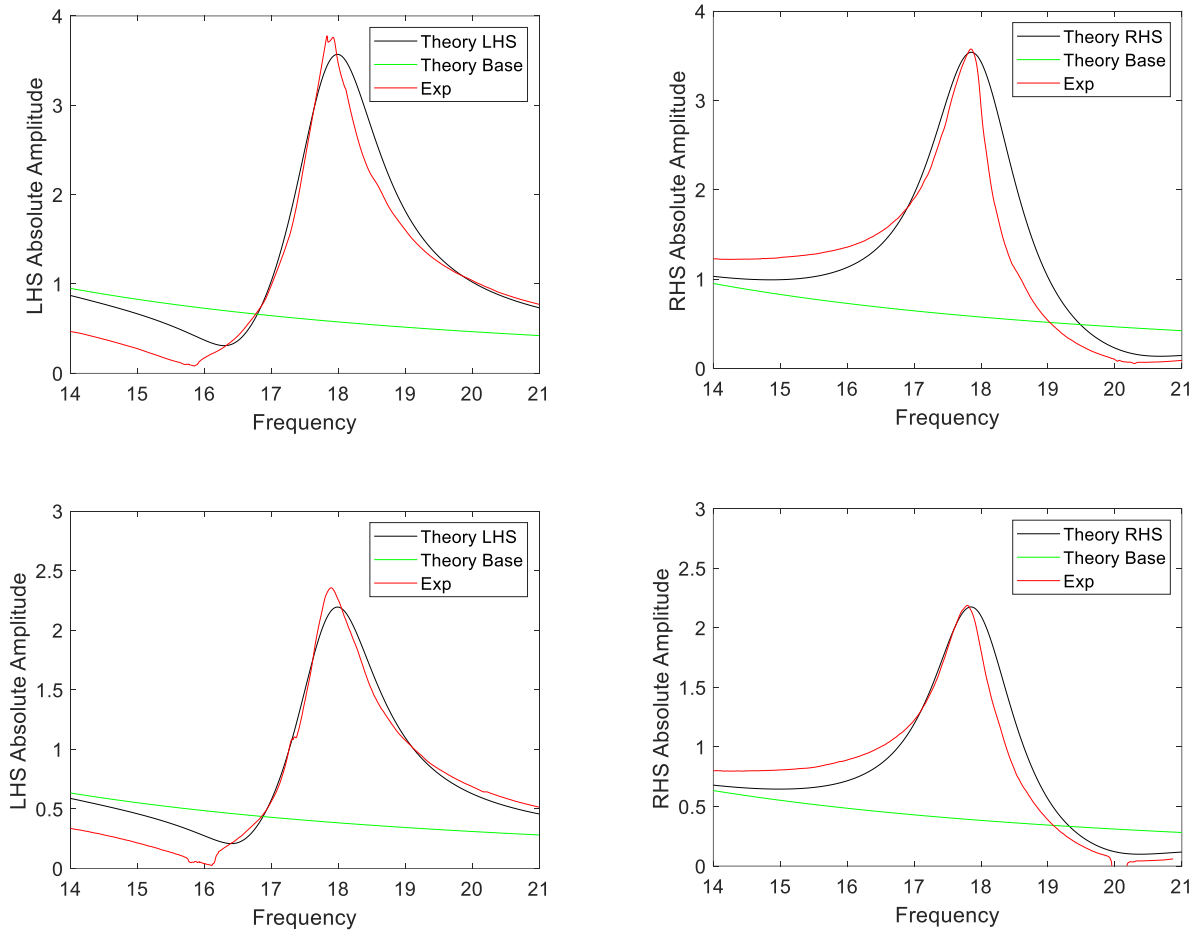

Figure 5.13 Absolute amplitude (mm) strategy B at $\mathrm{X_f} = 0.00$ mm for 0.75 g (top) and 0.50 g (bottom)

Using Eq. (5.42), the $F_{r_{b1}}$ on strategy B was computed as 0.6265 mN and $F_{r_{b2}} = 0.00$ mN because the smaller clamp bearing was absent in B. Table 5.3 shows the performance parameters for strategy B. Comparing Tables 5.2 and 5.3 shows that $\mathrm{F}_{r_{sB}} > \mathrm{F}_{r_{sA}}$ because there are no mechanism to restrain the response in desired DOF, hence a larger buckling in the spring at equivalent excitations.

Table 5.3 Summary of performance parameter for strategy B

g	k (Nm^{-1})	f_n (Hz)	ζ_{mech}	F_{r_s} (N)
0.75	1300	18.01	0.0907	0.2498
0.50	1300	18.01	0.0851	0.1663

During rig testing the rig set for strategy B showed stochastic multi degree responses when the excitation acceleration excced certain thresshold identified at g≥ 1.20 since the stiffness characteristic is severly compromised. However, strategy A, overcome such limitation until g≅ 4.21 because the guiderail and bending the the 3D printed part further constrained the responses.

5.6.3 Experimental validation of the harvested power on A and B

The harvested voltages and powers in strategies A and B when $\mathrm{R}_{\mathrm{l}} = 50.00\ \Omega$ is shown in Figs. 5.14 and 5.15 to an accuracy of about 93.52 % across all levels of excitations.

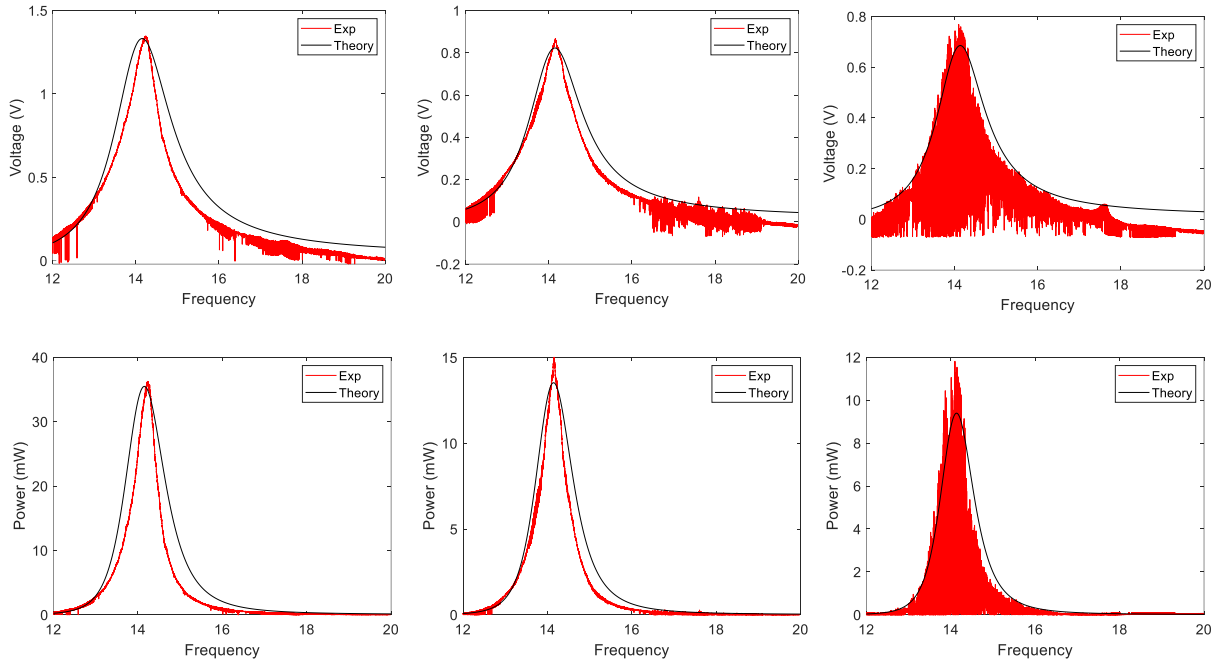

Figure 5.14 *Strategy A harvested voltage (top) and power (bottom) at 1.00 g (left), 0.75 g (middle), and 0.50 g (right)*

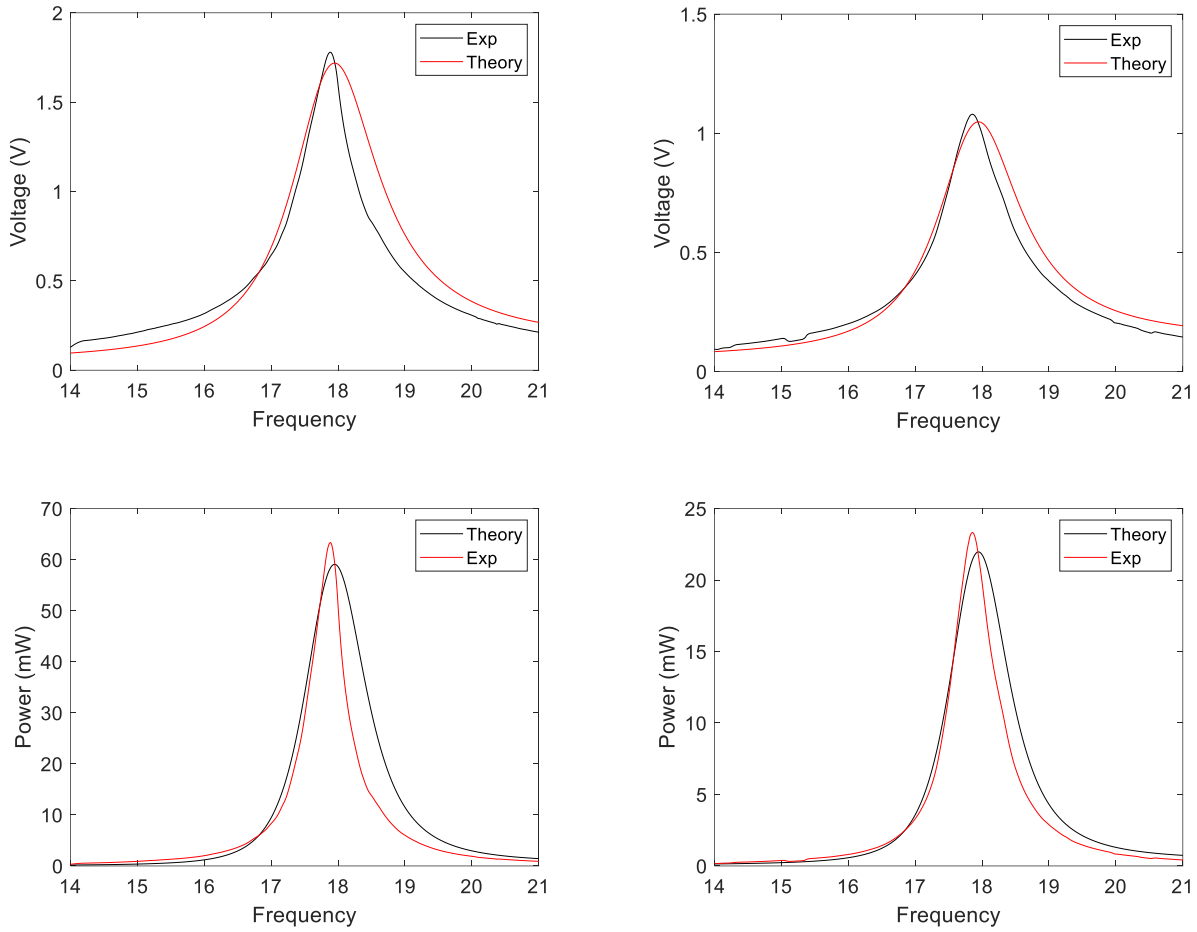

Figure 5.15 Strategy B harvested voltage (top) and power (bottom) at 0.75 g (left) and 0.50 g (right)

The summary of harvested power and voltage on strategies A and B from Figs. 5.14 and 5.15 are given in Table 5.4. Table 4 shows that irrespective of the degree of acceleration, the voltages and power harvested in strategy B is always higher than those on strategy A thus further confirming the preference of B as better candidate for vibration energy harvesting.

Table 5.4 Summary of maximum power and voltage on strategies A and B at $X_f = 0.00$ mm

g	Strategy	f_n (Hz)	V_{Out} (V)	P_{Out} (mW)
0.50	A	14.72	0.732	10.703
	B	18.01	1.686	56.802
0.75	A	14.72	0.892	15.899

	B	18.01	1.026	21.128
1.00	A	14.72	1.343	36.073

5.7 Semi-empirical variation of F_{r_s} versus g.

To this point, no known approach for quantifying and analyzing the variation of the strain forces F_{r_s} in the 3D printed part is known as they were predicted to fit the experimental data in Chapter 5.6. The following section however undertake a semi-empirical approach to quantify their variation in strategies A, and B as a function of the excitation accelerations by using the accurately determined fitted values from Tables 5.2 to 5.3 for strategies A, and B and other test values of F_{r_s} when the transduction coil were absent. The two independent approaches were necessary to independently quantify the variation of F_{r_s} with g when the design are functioning as either an energy harvester or a standalone isolator. Fig. 5.16 showed the plot of a semi-empirical variation of F_{r_s} versus g for strategies A, and B when $X_f = 0.00$ mm (left) and $X_f = 10.00$ mm (right).

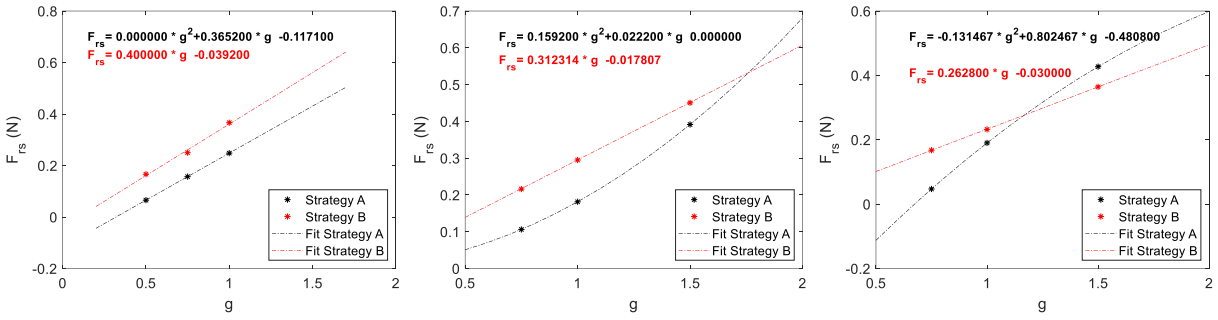

Figure 5.16 Semi-empirical variation of F_{r_s} versus g for strategies A, and B; with transducer coil when $X_f = 0.00$ mm (left), without transducer coil when $X_f = 0.00$ mm (middle) and without transducer coil when $X_f = 10.00$ mm (right)

Fig. 5.16 showed that although the F_{r_s} on strategy B is a linear function of g according to the Hooke's law, F_{r_s} is consistently larger on strategy B for $X_f = 0.00$ mm and $X_f = 10.00$ mm when g<1.76 and g<1.17 respectively such that the range of g over which F_{r_s} in B is consistently larger over A therefore narrows down with increasing X_f. This observation is

consistent with the fact that while increasing X_f, the inertia of the model is distributed to initiate a much lower response because of larger tensile preload in the spring.

A general comparison on the variation of the F_{r_s} trends on strategies A, and B for $X_f = 0.00$ mm with and without the transduction coil Fig. 5.16 (left and middle) shows that although the F_{r_s} on strategy B is a linear function of g, the introduction of the transduction coil successfully linearize F_{r_s} on strategy A. This observation is consistent because the introduction of the transducer coil added to increases the total damping of the system hence the effective response amplification is lower. Noting that strategy B has none of the rails in the configuration, it is easy to conclude that the variation of F_{r_s}(pure buckling force) is consistent with the Hooke's theory since the response is directly proportional to g. Therefore, it is reasonable to conclude the following:

i. The strain force profile of the 3D printed material generally has a nonlinear response to excitation when the transducer coil is absent since their presence shifts F_{r_s} to linear variation with g, therefore, it enhances isolation.
ii. Presence of the horizontal rail successfully dissipated the nonlinear stain force in the 3D printed part by horizontal motion hence a less nonlinear strain force profile.
iii. While the F_{r_s} in strategy B is linear and could be characterized by Hooke's law, those on A are not. This implicate a compromise on the band for vibration isolation and amplification on B relative to A.
iv. Comparing Fig. 5.16 (middle and left) shows that at equivalent g increasing X_f correspondingly reduced the F_{r_s}. This observation is consequential to the mass inertia distribution which varies inversely with X_f such that increasing X_f correspondingly lowers the compressive preload offset. Numerical extrapolation suggests that as X_f further increases, the preload migrated from compressive (better isolation effect) to tensile preloads, hence lesser responses.
v. In the absence of the horizontal rail, F_{r_s} the 3D printed part to approach permanent deformation faster until it is permanently deformed as g increases.

5.8 Combined harvester-isolation tradeoff over electromechanical property.

To this point, the standalone harvester and isolation characteristics of the system has been considered. This section investigates the simultaneous vibration isolation-harvester performances of strategies A and B in Fig. 5.1 for small precision payload.

To ensure that no signficant momentum/inertia redistribution existed during excitation, the mass of the load bearing plate must be negligible otherwise, it will alter the stiffness matrix of the isolator-harvester design. Major alteration will often leads to a shift in the resonance frequency to a lower spectrum according to definition of M_f in Eq. (5.4) and whether the load plate is connected to the LHS or RHS of the connector. This concerns forms the limits for the application of the isolator system for small pay load application such as small precision measuring instruments, gyroscopes, microelectromechanical sensors, small optical components, microfluidic devices etc. to avoid initiating unwanted levels of static preloading in the springs.

At an external load resistance of $R_l = 50.00\,\Omega$, Fig. 5.17 shows the comparison of the transmissibility and the harvested voltage/power plot of the modified models A and B when $f_n = 14.72$ Hz, $\epsilon = 0.832, X_L = 81.78$ mm, X_R =68.06 mm, and $k = 940\ \mathrm{Nm}^{-1}$.

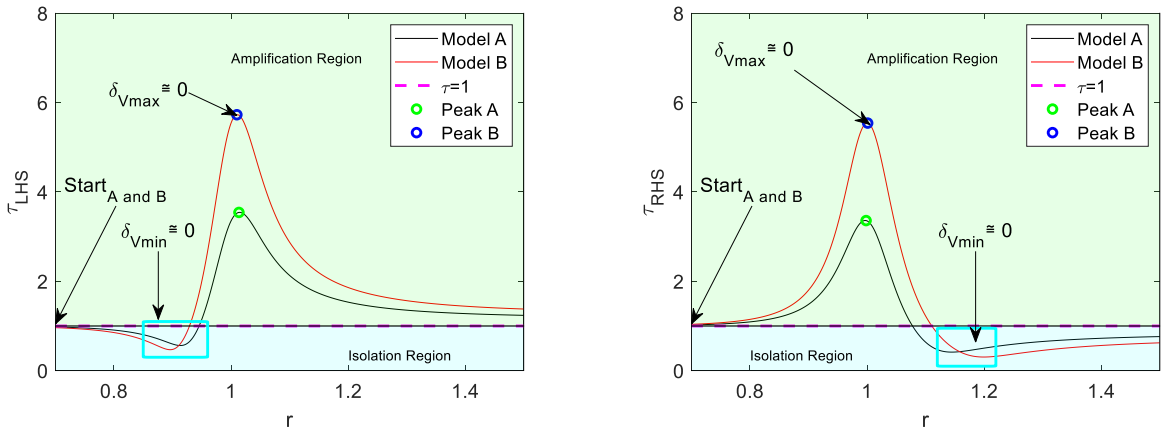

Figure 5.17 Isolation-harvester comparison of modified models A and B; LHS (left) and RHS (right)

Comparing the relative transmissibility (τ) of models A and B from Fig. 5.17 shows that the model A attained a better band of isolation with lesser amplification capacity relative B due to larger Coulomb damping and vice versa as evidenced with larger amount of

harvestable power on strategy B in Fig. 5.18. Table 5.5 gives a summary of the power harvested.

The above performances indicated that while model A shows capacity for standalone vibration isolation in term of the early onset of the isolation (i.e., larger isolation band), model B however, at equivalent excitation is preferable for standalone vibration energy harvesting.

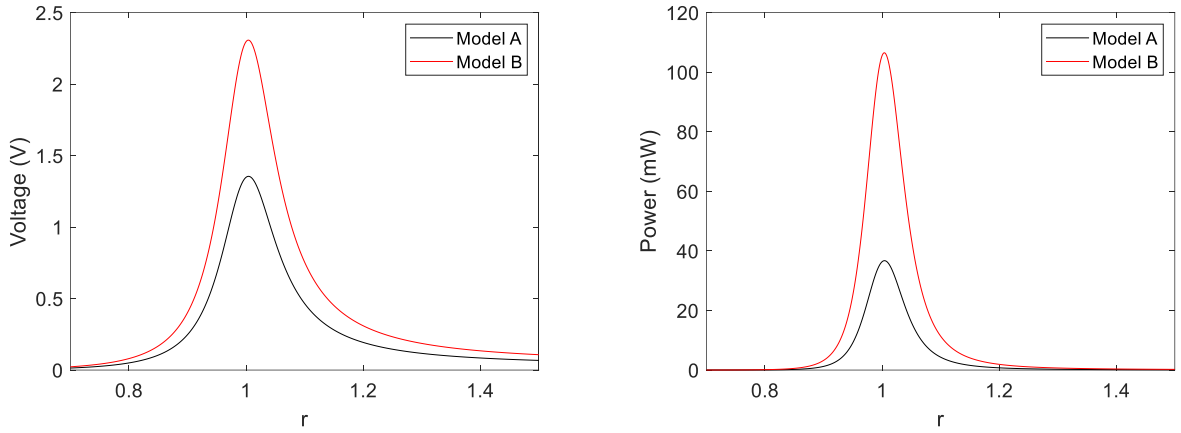

Figure 5.18 Performance comparison of modified models A and B; Harvested voltage (left) and power (right)

Table 5.5 Summary of stand-alone energy harvesting performance on strategies A and B

g	Model	k (Nm^{-1})	ζ_{mech}	ζ_{coil}	V_{Out} (V)	P_{Out} (mW)
1.0	A	940	0.1090	0.0505	1.355	36.701
1.0	B	940	0.0960	0.0533	2.307	106.515

To investigate the practicability of the model for hybrid performances, a decoupled parametric analysis on the variation of the transmissibility and vibration energy harvesting over different range of mechanical (stiffness) and electrical (electrical) parameters was necessary as shown in Chapters 5.6.1 and 5.6.2.

5.8.1 Different spring stiffness

The stiffness of the spring is a mechanical parameter which determines the static loading capacity as well as the resonance of the system. A system with high *k* value is often

characterized with high static, high resonance, a high load bearing capacity. Figs. 5.18 and 5.18 shows the transmissibility curves of the lever isolator with transduction coil and the harvested voltages/power respectively at different spring stiffness and a fixed external load of R_l =50.00Ω, $L_{Beam} = 150.00$ mm, and $\epsilon = 0.8323$. The plots in Fig. 5.17 (left and middle) and Fig. 5.19 showed that smaller stiffness enhanced isolation and energy harvesting performances with a compromise on the isolation band and vice versa. The variation of the operational band for A and B at different *k* is shown in Fig. 5.19 (top right) and Fig. 5.19 (bottom right) respectively. It shows that the bandwidth of model A is approximately 1.35 multiple of B because the effect of the Coulomb damping necessitated a much energy dissipation in A at equivalent stiffness.

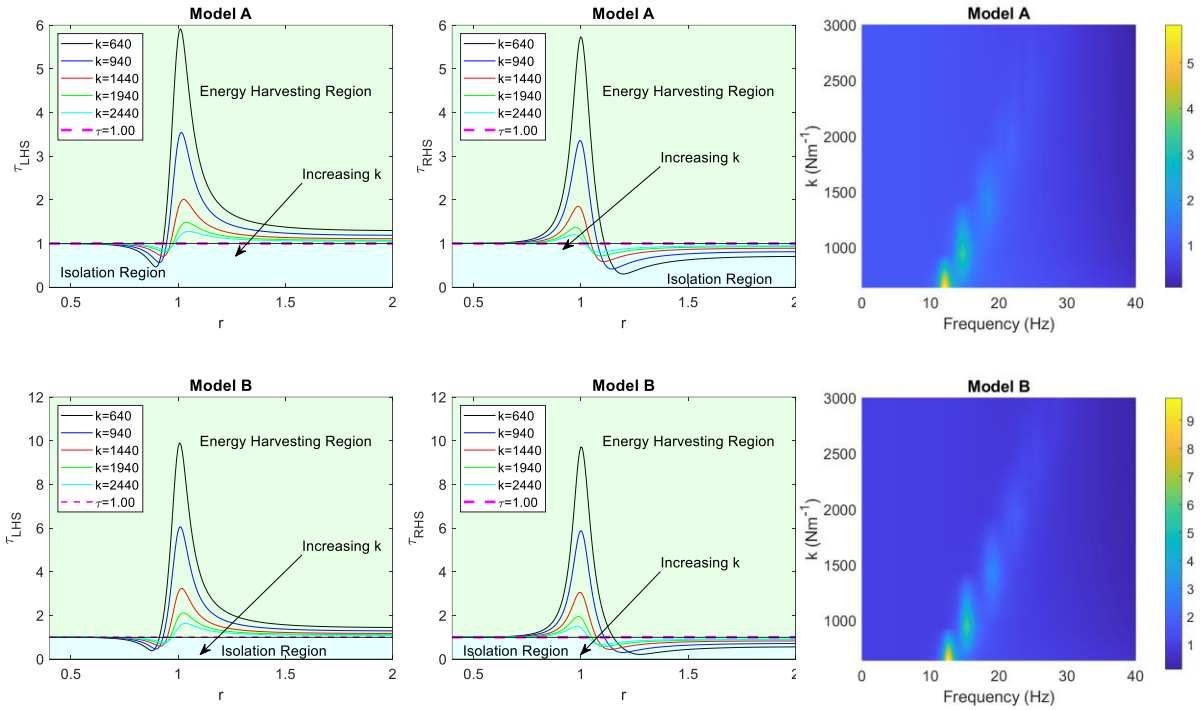

Figure 5.19 Transmissibility vs frequency ratio at different stiffness LHS (left), RHS (middle) and 2D plane view of k vs frequency (right) of transmissibility; model A (top) and model B (bottom)

This observations is consistent with the application of the design for small payload application such that by taking advantages of power harvested as shown in Fig. 5.20, the small payload is powered simultaneously while isolating it from harmful vibrations.

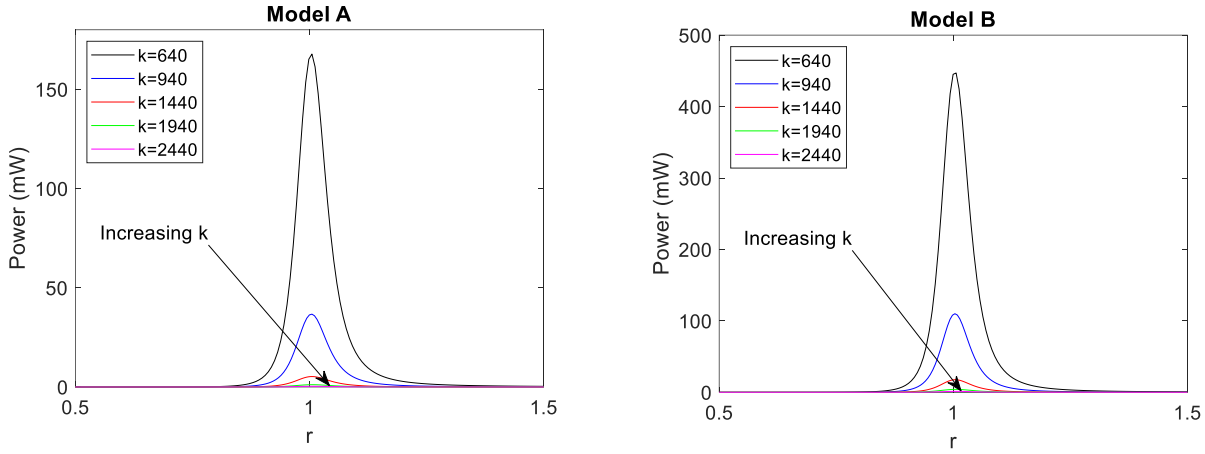

Figure 5.20 Harvested power at different k on model A (left) and model B (right) (top)

The power performance parameters of models A and B at different k is summarized in Table 5.6. Although, models A and B could be used for efficient simultaneous vibration isolation and energy harvesting especially at small static load bearing stiffness, analysis shows that as the *k* further reduces, the responses B becomes quite unstable and unbounded especially at larger excitation due to absence of the guiderails, therefore, A becomes the best option for simultaneous harvester-isolation operation.

Table 5.6 Summary of hybrid energy harvesting performance on strategies A and B at different k

Model	k (Nm^{-1})	f_n(Hz)	V_{Out} (V)	P_{Out} (mW)
A	640	9.964	2.896	167.768
B	640	10.418	4.739	449.343
A	940	14.564	1.355	36.701
B	940	15.227	2.345	110.021
A	1440	18.026	0.512	5.251
B	1440	18.847	0.940	17.682
A	1940	20.923	0.239	1.145
B	1940	21.876	0.454	4.138
A	2440	23.465	0.132	0.346
B	2440	24.533	0.256	1.315

To further characterize the suitability of A for simultaneous harvester-isolation performances at smaller k, the combined transmissibility- harvesting-isolation performance is shown in Fig. 5.21 at k = 640 Nm^{-1} (left) and k = 940 Nm^{-1} (right) of models A (top) and B (bottom).

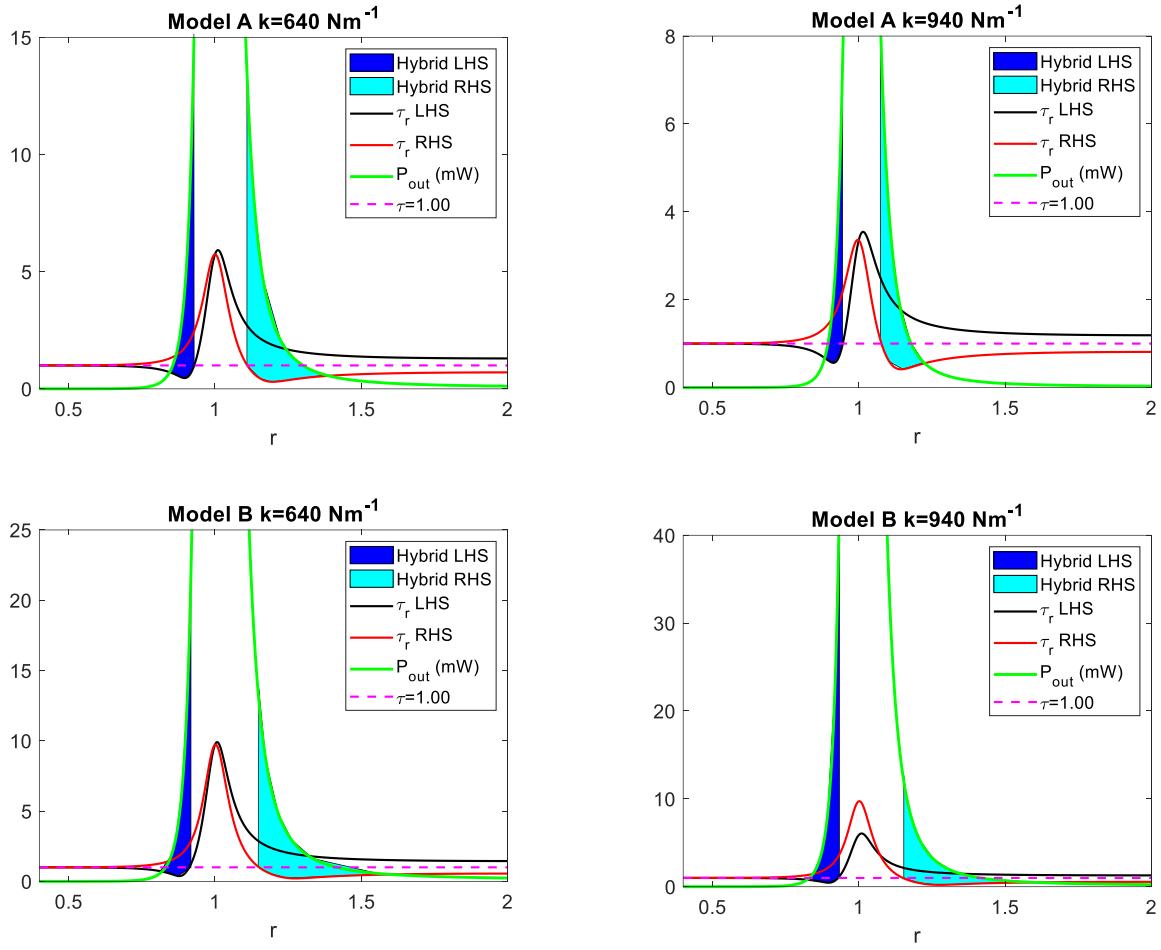

Figure 5.21 Hybrid plot of τ and power against r at k=640 Nm^{-1} (left) and k=940 Nm^{-1}(right) of model A (top) and B (bottom)

Considering the τ, maximum harvested power (P_{max}) and the identified isolation band of Fig. 5.21, it is obvious that model B attained the highest P_{max} with a compromise on the isolation depth and band relative to model A. A consideration on the practical application of the design for simultaneous isolation harvesting performances showed that as the power harvested is further enhanced by reducing *k* the isolation-harvesting capacity of B is compromised because the system will become unstable thus introducing unwanted

damage to the payload especially with larger preloads, therefore A becomes handing for simultaneous isolation-harvesting at smaller *k* and larger excitations.

5.8.2 Different load resistance (R_l)

This part characterizes the isolation-harvester of the LEDAR-SS system over different load resistance as shown in Fig. 5.22.

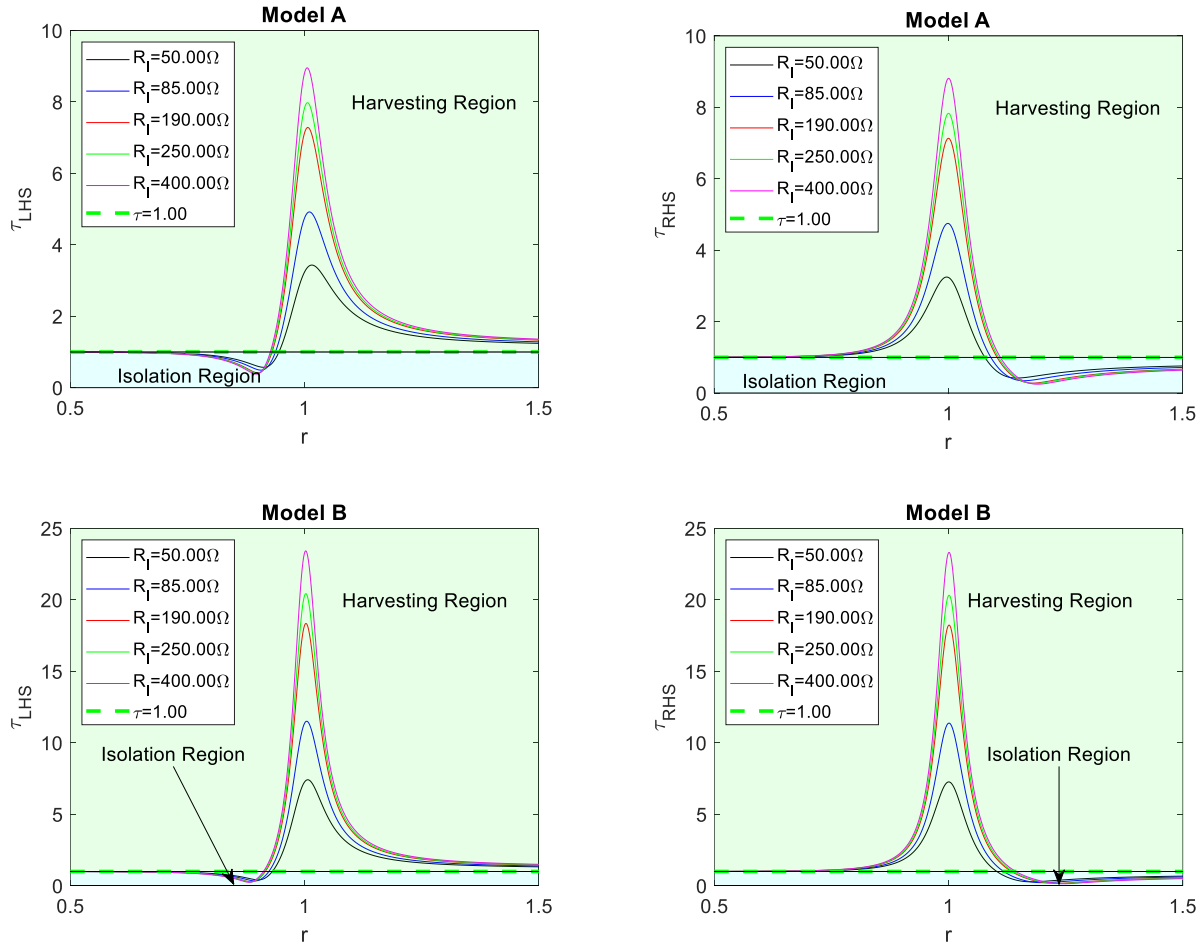

Figure 5.22 Variation of transmissibility with different load resistance, model A (top) and model B (bottom), LHS (left) and RHS (right)

The transmissibility plot of Fig. 5.22 shows that while the isolation band on A and B shows a linear variation with the load resistance, the depth of isolation is inversely related to the load resistance. Also, B attained larger resonant peaks in energy harvesting regions relative to A, hence, it is most suitable for vibration energy harvesting.

However, it is important to note that the above observation may be too generic. Therefore, to understand the specific performance preferences of A and B with the external load resistances, their isolation-harvester performances will be characterized at respective optimums as follows.

Expression for determining the optimum load of the model was obtained using the maximum power transfer theorem which asserts that $\frac{\delta P_{Out}}{\delta R_l} = 0$ when $R_c = R_l$. The derivative gives an expression for the optimum load resistance (R_l^{opt}) as shown in Eq. (5.46) where $c_i$the mechanical damping coefficient.

$$R_l^{opt} = \frac{16K^2 {l_c}^2}{c_i} + R_c \tag{5.46}$$

To identify R_l^{opt}, a plot of variation of the harvested voltages and power with R_l is shown in Fig. 5.23 at *k* is 940 Nm^{-2}. The optimum on each design strategy was identified at $R_l^{opt} = 161.50\ \Omega$ and $R_l^{opt} = 192.00\ \Omega$ corresponding to optimum power harvested at 3.32 V and 68.12 mW and 6.69 V and 370.56 mW on models A and B, respectively at 1.00 g acceleration.

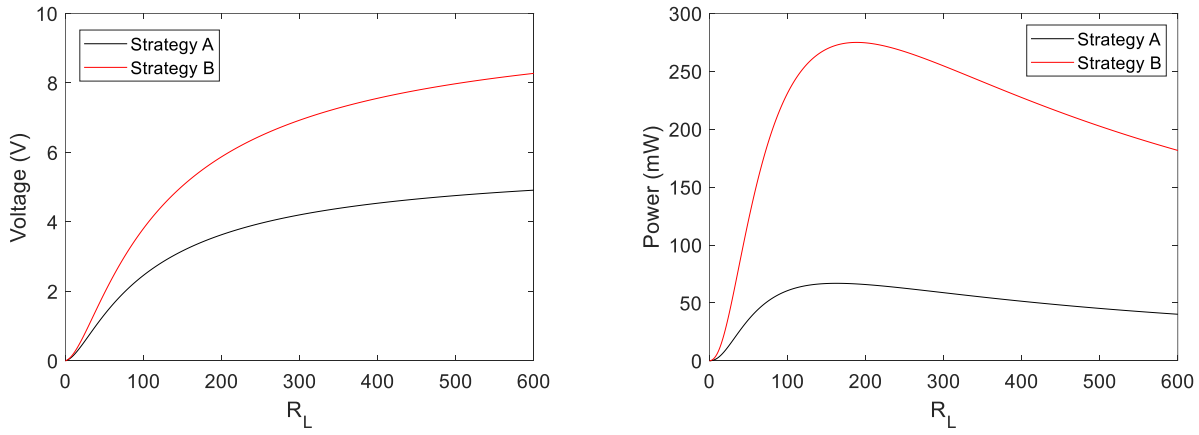

Figure 5.23 Variation of harvested voltage (left) and power (right) with different load resistance

To set a clear preference for the isolation-harvester usage, Fig. 5.24 shows the superimposed plots of transmissibility and power at optimums for A and B. The maximum power within the zone of isolation at respective optimum loads ranges from 1.00 mW to 4.25 mW and 1.00 mW to 5.87 mW, of models B and A respectively.

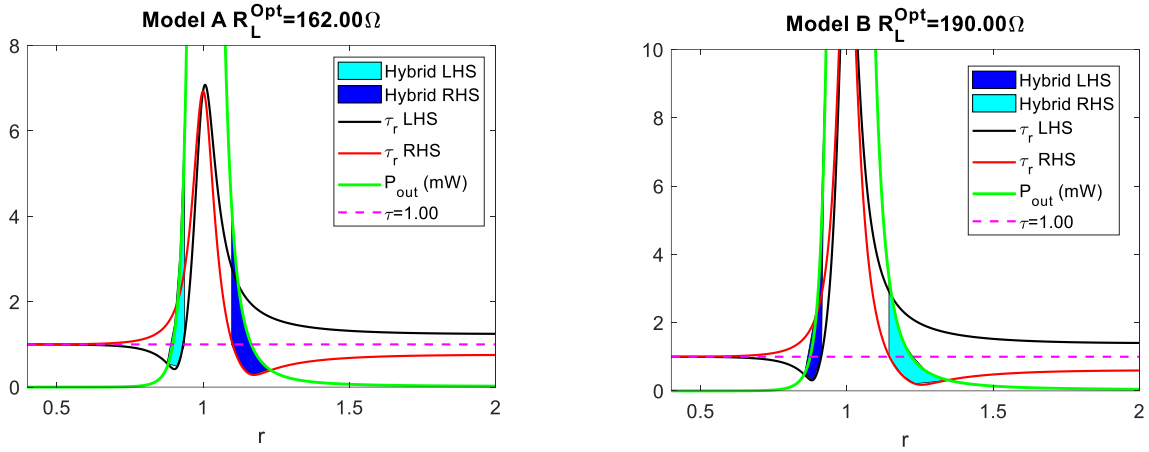

Figure 5.24 Hybrid plot of τ and power against r at respective optimums of models A and B

Fig. 5.24 shows that although the maximum resonance power is harvested in model B at R_l^{opt}, it is however compromised for simultaneous isolation-harvester operation at optimum since it only harvested about 4.25 mW while undertaking near resonance applications with a compromise on the depth of isolation. However, model A harvested about 5.87 mW of power with a better depth and band of isolation with a characterized than stability than B due to the effect of Coulomb damping from the guiderails.

Therefore, while model A generally attained better simultaneous harvester isolation performance at optimum resistances R_l^{opt} and smaller spring stiffness *k*, model B is good for simultaneous harvester-isolation application at higher spring stiffness *k* because smaller *k* will initiate stochastic and unstable responses in B.

5.9 Parametric Analysis as a function of L_b, ϵ, and M_{Tip}.

In this section, a parametric analysis on how the modification of different design parameters lever length (L_b), lever ratio (ϵ), and tip coil mass (M_{Tip}) affected the potential; thus, enhancing or compromising the isolation performance due to different level of the preloads in the springs. To gain a rich insight to the parametric analysis, a differential approach on strategies A and B was undertaken by differentiating strategy A into strategies A (having both vertical and horizontal rail), B (having only vertical rail) and C (not having any of the guiderails).

5.9.1 Effect effective lever length (L_b).

This section is focused to illustrate how different effective L_b affected the isolation performances of the lever configurations. Using the fitted values of ζ_m, $F_{r_{b1}}$, $F_{r_{b2}}$, and F_{r_s} from the fitted values reported in Chapter 5.6.1 and setting $\epsilon = 0.853$, $X_f = 0.00$ mm six different choices of L_b =150.00 mm to 400 mm at 50 mm length interval, isolation variation of the lever design with L_b was obtained as shown in Fig. 5.25, noting that the resonant for each L_b configurations was tuned to $f_n \cong 17.11$ Hz for effective comparison by addition of masses to the clamps. The effect of such additional clamp tip masses on the isolation capacity of the levered device shall be investigated in the last section of this parametric analysis.

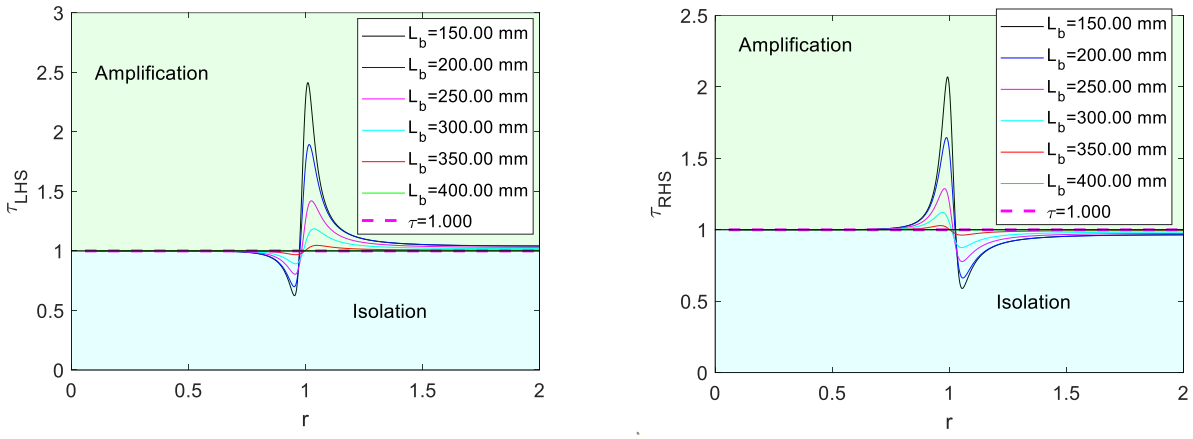

Figure 5.25 *Transmissibility versus frequency ratio at different beam length when $X_f = 0.00$ mm LHS (left) and RHS (right) when $\epsilon = 0.853$*

Fig. 5.25 shows that for a given configuration, increasing L_b resulted in a corresponding increase in the isolation depth and band by approximated 10.00 % for every 50.00 % increase in beam length because the L_b the static inertia and masses are altered as a direct relation. This observation in Fig. 5.25 also consistent with the analysis in Figs. 5.7 and 5.8 where increasing L_b requires additional masses on the LHS clamp to achieve static equilibrium hence a preload compression in the spring which obviously favored isolation.

5.9.2 Effect of lever ratio ϵ.

To further quantify the isolation preferences of the levered isolation model because of the differential potential in the respective strategies, their isolation performances defined in terms of the model transmissibility was considered over different values of ϵ as shown in Fig. 5.26.

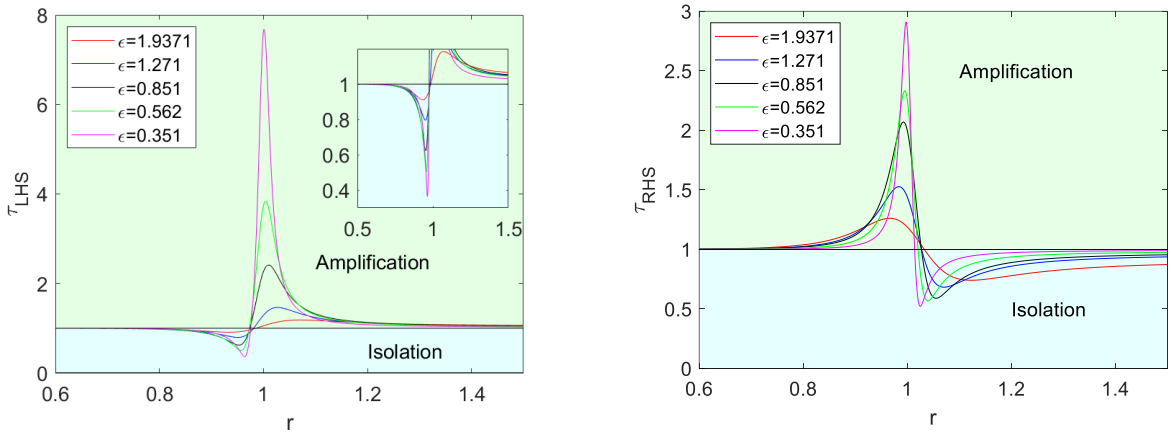

Figure 5.26 Transmissibility versus frequency ratio on the LHS (left) and RHS (right) at different values of ϵ when $X_f = 0.00$ mm

Recalling on the definition of ϵ from Eq. (5.3), a comparison of the plots in Fig 5.25 shows the variation of τ over different ϵ for a fixed beam length $L_b = 150.00$ mm. With a consideration to the design geometry, Eq. (5.3), $\epsilon > 1$ implies that $X_L > X_R$ while ϵ <1 is $X_L < X_R$, hence a preload compression and tension respectively in the springs in the static mode. Fig. 5.26 shows that at $\epsilon \cong 1$, the isolation band, isolation depth, amplification and isolation onset is a median of the inequalities $\epsilon > 1$ and $\epsilon < 1$. Generally, $\epsilon < 1$ resulted increased isolation depth with a compromise on the isolation bands because as ϵ becomes considerably lesser than unity, most of the inertia mass of the lever geometry is concentrated to the LHS, hence much larger compression in the spring in the static mode and vice versa for $\epsilon > 1$. The physical implication of such compressive spring preloads is that during excitation, most of the initial excitation energy are consumed to overcome the potential threshold such that $\delta V = \frac{\partial V}{\partial y_{off}} \rightarrow 0.00$ is observed, however, as the preload becomes tensile, δV changes considerably and the isolation performances are severely compromised.

5.9.3 Effect added mass (m_0)

As identified earlier, the size of the tip mass/clamps are quite significant to determine or tune the operational resonant and isolation band/depth. Fig. 5.27 shows the plot of the potential energy vs absolute response amplitude when m_o is added to the LHS and RHS clamps to initiate different level of offset in the potential profile and the implication of such offsets on the isolations were considered.

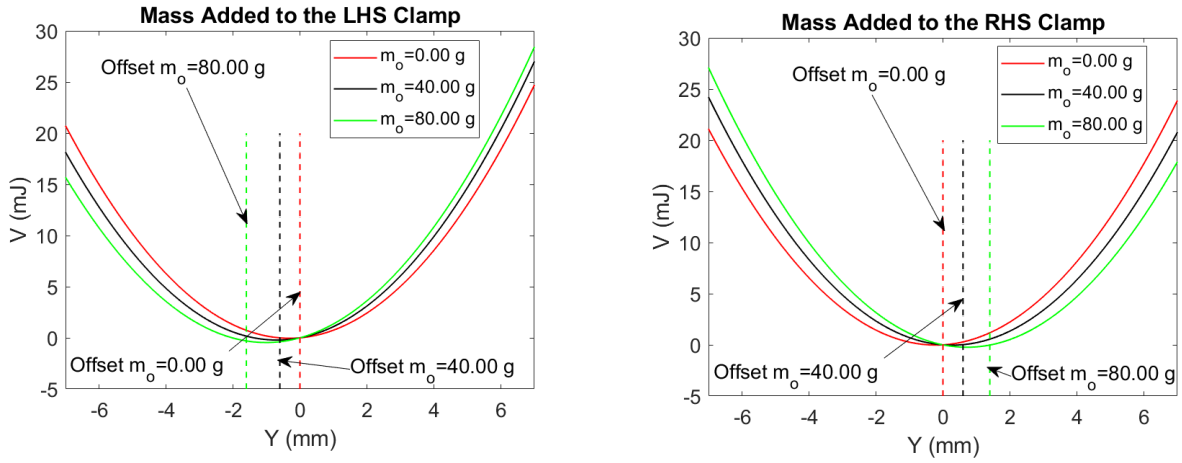

Figure 5.27 Potential energy vs absolute response amplitude offset m_o added to the LHS clamp (left) and m_o added to the RHS clamp (right)

Fig. 5.27 shows that adding masses to the clamps on either side of the lever could effectively activate different level of offset bias in the model. As shown in Fig. 5.27, adding masses to either side indicated a symmetric offset about the default $m_0 = 0.00$ g and $\epsilon \cong 1.00$ configurations. Fig. 5.27 shows that when the position of added mass m_0 is shifted from the LHS clamp to the RHS clamp or vice versa, the offset is adjusted from negative to positive or vice versa. The reversed order in the potential as highlighted above is a direct consequence of the fact that as the masses are continually added to the RHS, the preload becomes tensile (i.e., positive offset) thus shifting the potential to higher values such that δV is maximum thus compromising isolation and vice versa for mass addition to the LHS to attain a compressive preload and a minimized δV for improved isolation. The implication of such trend reversal on the isolation characteristics of the levered configuration are considered as shown in Fig. 5.27 for mass additions on the LHS and RHS.

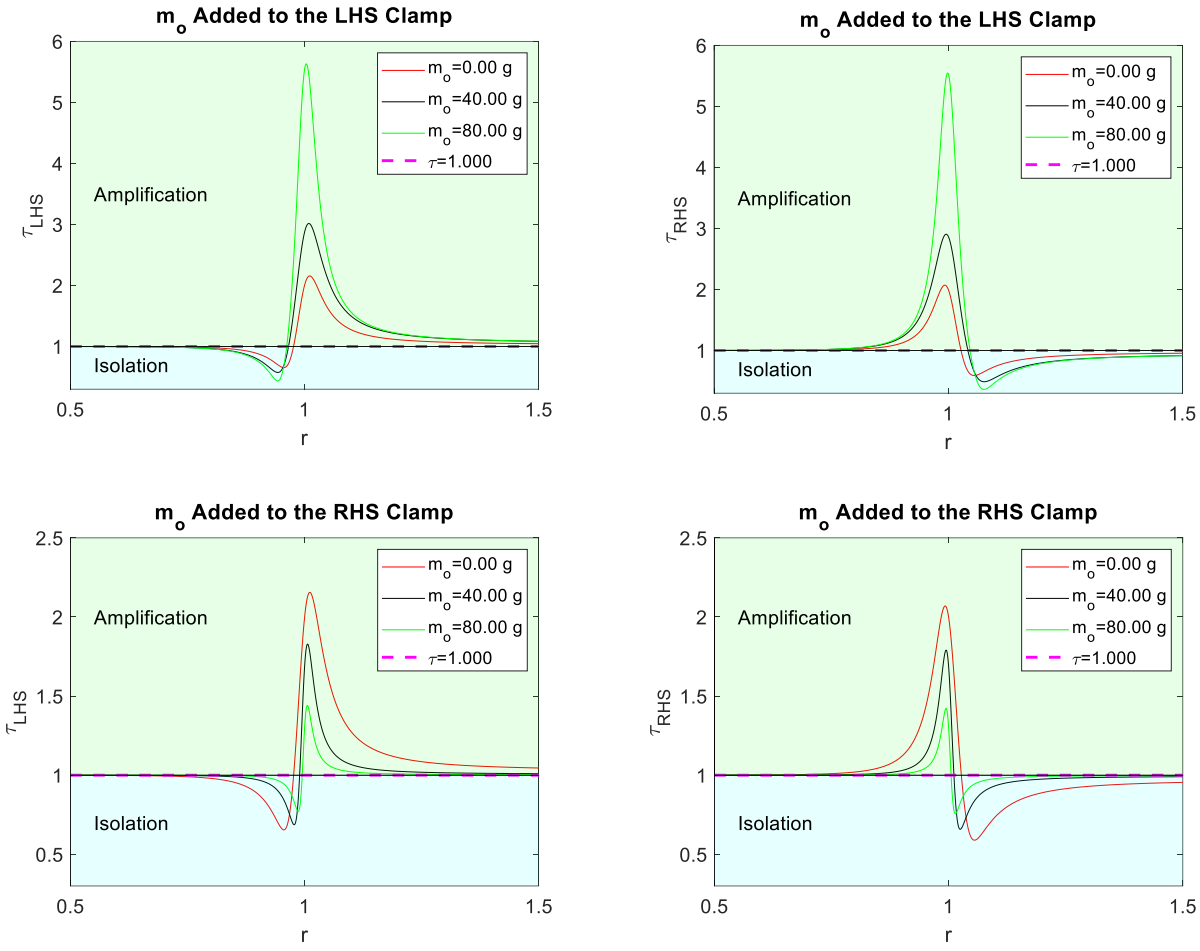

Figure 5.28 Transmissibility versus frequency ratio when m_o is added to the LHS clamp (top) and m_o added to the RHS clamp (bottom) for τ_{LHS} (left) and τ_{RHS} (right)

A plot of the transmissibility variation of Fig. 5.27 for different mass addition is shown in Fig. 5.28. It shows that a better isolation depth with an earlier onset/larger band isolation of isolation is achieved when larger m_0 is attached to the LHS clamp and vice versa when smaller m_0 is on the RHS because the preloads become compressive (i.e., negative offset) and tensile (i.e., positive offset) in both situations respectively. This trend is consistent with the potential analysis in Fig. 5.28, where adding m_0 to the LHS clamp further increased the negative offset (i.e., a preload compression in the spring) hence a much more excitation input is needed to drive/excite the spring or shift the inertia, therefore an improved isolation in the specified range and vice versa when m_0 is added to the RHS of the lever.

In summary, Fig. 5.28 shows that adding masses to the LHS clamps further increases the negative offsets (i.e., preload compression in the spring) and vice versa (i.e., preload tension in the spring) for adding masses to the RHS clamps.

5.10 Powering LED in the vibration energy harvesting mode

This section highlighted the vibration energy harvesting capacity of each design model by describing their respective performances over a rectifier in an approach different from those reported in Chapter 5.3. The performance testing with LED over a full-bridge IN4148 diode rectifier, were independently undertaken at an external load of 50.00 Ω as shown in Fig. 5.29.

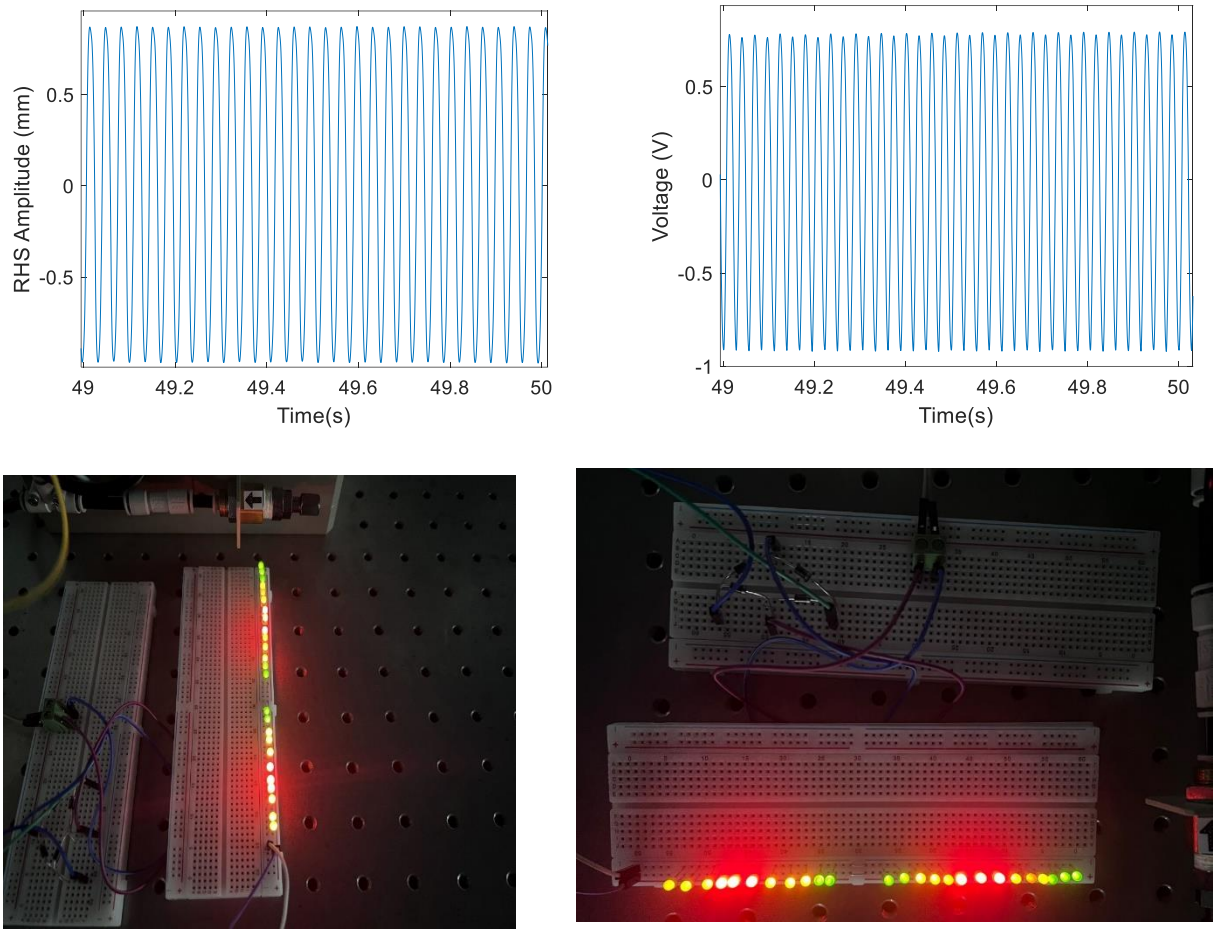

Figure 5.29 Lightening up 25 LED to full intensity, harvested voltage-time plot (top) and LED lightening (bottom); strategy A, f =14.60 Hz at 1.5g (left) and strategy B, f = 18.01 Hz at 0.5g (right)

Fig. 5.29 shows that model B conveniently powered 25 parallel connected LEDs to full intensity at 0.50 g acceleration. On the contrary, model A powered the 25 LEDs to full

intensity at acceleration of 1.50 g. This observation further confirms the harvesting preference on model B over A. This behavior is a direct consequence of the effect of higher Coulomb damping in A which allows for rapid decay of the potential and earlier onset of isolation.

5.11 Generalized condition for stick-stick slip-continuous responses per force-friction ratio.

In relativeness to the design, the motion of Coulomb damped systems are characterized as either continuous, stick or stick-slip [109 110]. Each identified response types consistently typifies regions of tensile preloads, compressive preloads on the boundary of transition from one preload to another such that stick slip is hypothesized to occur in the response profile when the preload attains large negative or positive offset such that when the spring is almost 100 % compressed, the motion is full stick. While a fairly zero static offset in the spring relative to the force ratio in the system often typifies continuous motion and to larges a tensile preload is stick-slip responses. To quantify how this variation occurs in the system, a performance parameter β which is the ratio of the Coulomb forces in the system to excitation forces is defined.

According to the Newtonian mechanics, the sign of the frictions could assume any value between +1 and -1 by the Coulomb friction model [109]. To fully characterize whether $\mathrm{sgn}(\dot{Y})$ 1 or -1, adopted convention reported the nature of the responses in Coulomb damped model as either continuous, stick or stick-slip [109]. Following the idea highlighted and taking the derivative of the response in the interval $0 \leq t \leq \frac{\pi}{\omega}$ over a half cycle set the desired condition for stick situation as $\dot{Y} = 0$ and using relevant boundary conditions therefore shows that.

$$Y \geq \left[Y_m + \frac{\mu}{\omega_n^2 \mathrm{M}_f} F_r + \frac{1}{\omega_n^2} g\right](\gamma - \varphi\beta) + \big((\omega - \varphi)\omega\cos(\delta) - (\gamma - \varphi\beta)\sin(\delta)\big)F_0 r^2 Q \qquad (5.47)$$

Using the definitions of $\sin\delta$ and $\cos\delta$ from Eq. (5.27) and Eq. (5.28) as well as the minimum condition to realize $\dot{Y} \leq 0$ stick condition is that the relative response $Y_m = 0$. Using this condition in Eq. (5.47) gives

$$Y \geq \left(\left(w(\omega-\varphi)+n(\gamma-\varphi\beta)\right)\frac{\omega}{R}+(\gamma-\varphi\beta)\right)\left(\frac{\mu}{\omega_n^2 \mathrm{M}_f}F_r+\frac{g}{\omega_n^2}\right) \tag{5.48}$$

$$\frac{\mu F_r}{\omega_n^2 \mathrm{M}_f Y} \leq \frac{1}{\left(\left(w(\omega-\varphi)+n(\gamma-\varphi\beta)\right)\frac{\omega}{R}+(\gamma-\varphi\beta)\right)}-\frac{g}{\omega_n^2} \tag{5.49}$$

where $n, w,$ and R are defined as shown in Eqs. (5.50) – (5.52)

$$n=\left[\left(\left(\frac{\gamma}{\beta}+\varphi\right)\sin(\tau)+e^{-\lambda}\right)e^{-\lambda}-1\right] \tag{5.50}$$

$$w=[2(2\varphi\gamma-\varphi^2\beta+\beta)\sin(\tau)\cos(\tau)-2(\gamma-\varphi\beta)\cos^2(\tau)-2(\varphi^2\gamma+\varphi\beta)\sin^2(\tau)] \tag{5.51}$$

$$R=\omega\left[\frac{2\gamma}{\beta}\sin(\tau)\cos(\tau)-1+\left(\left(\varphi-\frac{\gamma}{\beta}\right)\sin(\tau)-2\cos(\tau)-\omega e^{-\lambda}\right)e^{-\lambda}\right] \tag{5.52}$$

Eq. (52) defines the limit of the force ratio before the system enters the stick regime, such that when the force ratio $\beta=\frac{\nu F_r}{\omega_n^2 \mathrm{M}_f Y} \leq \beta_{lim}$, the response is always in the continuous or stick-slip region. However, beyond such friction limits, the response system is full stick with zero response. From Eq. (5.49), the limit of friction force was obtained as shown in Eq. (5.53).

$$\beta_{lim} \leq \frac{1}{\left(\left(w(\omega-\varphi)+n(\gamma-\varphi\beta)\right)\frac{\omega}{R}+(\gamma-\varphi\beta)\right)}-\frac{g}{\omega_n^2} \tag{5.53}$$

Fig. 5.29 shows the variation plot of the response regime over the three design strategies as a function of the force ratio limit when $X_f = 0.00$ mm. Three regions of responses were identified as continuous, stick-slip and stick were observed to exists independently or simultaneous in the response profile as a function of the magnitude of excitations and the force ratio components.

Subject to the nature of preloads in the spring, this section classifies the motion of the systems as either continuous, stick or stick-slip as shown in Fig. 5.29. Each identified response types consistently typifies regions of tensile preloads, compressive preloads and the boundary of transition from one preload to another such that stick slip motion is hypothesized to occur when the preload attains sufficient negative or positive offset. However, when the spring is almost 100 % compressed, the motion is full stick.

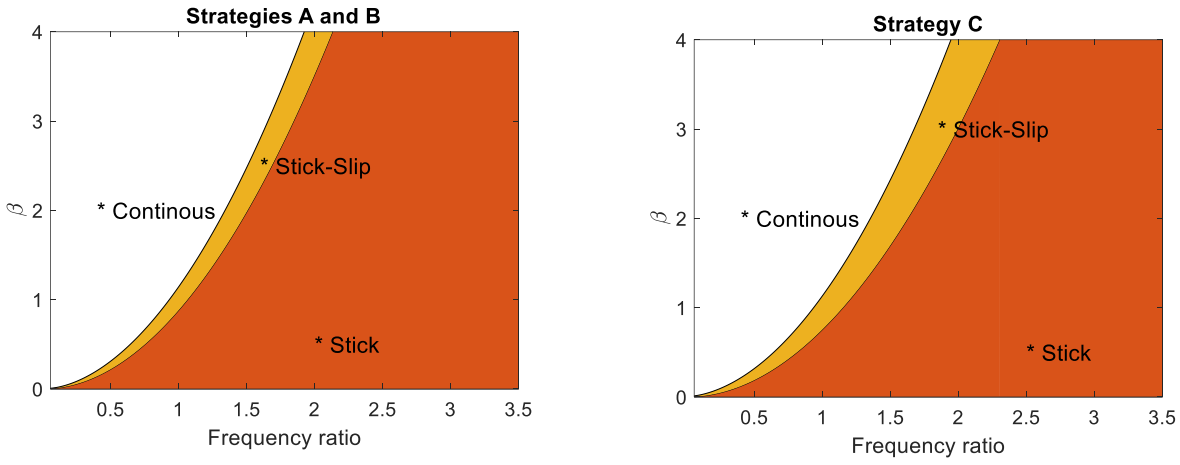

Figure 5.30 Force ratio contour line for strategies A and B (left) and strategy C (right) at $\mathrm{X_f} = 0.00$ *mm*

Also, when $y_{off} \cong 0.00$ continuous motion exists at all range of excitation because the force ratio $\left(\beta = \frac{F_r}{kY}\right) \leq$ limit of the force ratio (β_{lim}). According to the Newtonian mechanics, the sign of the frictions could assume value between +1 and -1 by the Coulomb friction model. To fully characterize wither the response nature subject to the force ratio and offsets, taking the derivative of the response in the interval $0 \leq t \leq \frac{\pi}{\omega}$ over a half cycle set the desired condition for stick situation as $\dot{Y} = 0$ for which $\beta = \frac{\nu F_r}{\omega_n^2 \mathrm{M}_f Y} \leq$ β_{lim}, in the continuous region. Expression for β_{lim} is shown in the Appendix A.

Fig. 5.29 shows the variation plot of the response regime over the three design strategies as a function of the force ratio limit when $X_f = 0.00$ mm. As earlier identified, full stick corresponds to $\beta > \beta_{lim}$ i.e., $y_{0ff} \cong 23.50$ mm compressive (i.e., when the linear spring is totally compressed) while continuous response is characterized such that the conditions $\beta < \beta_{lim}$ for which $y_{0ff} \cong 0.00$ mm while for stick-slip $\beta \cong \beta_{lim}$. Above observations thus implies that larger compressions i.e. $\beta \geq \beta_{lim}$ is desirable for enhanced isolation.

5.12 Summary

In this work, an approach that efficiently characterizes the standalone and hybrid isolation-energy harvesting capacities of a LEDAR-SS mechanism for small payload applications was analytically and experimentally investigated. Relative to simple design

perspectives, simple principle of geometry is not sufficient to characterize the standalone or hybrid harvester-isolation performance in a levered mechanism over different lever ratio as shown in various stages of analytical and experimental analysis. The models governing equations are formulated based on the Lagrange's principles and the subsequent analytical solution according to the relevant initial conditions were obtained. The models were experimentally tested and the analytical solutions were consistent with the experimental data as shown in Chapter 5.4. Stability requirements and autonomous power generation for precision payloads are becoming more stringent. This work presents a novel design for simultaneous near resonant vibration harvesting-isolation for small precision payload application such as gyroscopes and microelectromechanical sensors. The design characteristically activate isolation about resonance and simultaneously provide power for payloads as a double-banded isolation-harvesting function at $r = 1 \mp 0.099$ on the left- and right-hand sides of the lever compared to the conventional SDOF design with isolation onset at $r \geq \sqrt{2}$; r is the frequency ratio. The lever ratio was identified to initiate spring preloads offset as either compression or tensile such that lever ratio greater than and less than unity independently favors energy harvesting and isolation performances respectively while lager Coulomb damping in the design enhanced the bandwidth and degree of isolation while addition of energy harvesting coil further improve the isolation by about 2.90 %. The simultaneous harvester-isolation function showed that larger friction via the response constraining guiderails enhances for simultaneous harvester isolation at optimum resistance of $R_l^{opt} = 161.50\ \Omega$ and at lower spring stiffness, while no guiderails is best for standalone energy harvesting $R_l^{opt} = 192.00\ \Omega$ and $P_{max} = 370.53$ mW at larger stiffness. No guiderails situation obviously compromised the simultaneous isolation-harvesting because it initiates a stochastic response in the design.

Results and parametric analysis highlighted the following

1) Double band near resonant vibration isolation and energy harvesting is possible in a standalone or simultaneous approach on the lever design depending on usage.
2) The design could be decoupled into standalone vibration energy harvesting or isolation applications. In such situation, configurations with lesser friction is

suitable for energy harvesting while those with larger friction encourages early onset of isolation at a compromise on the maximum harvested power.

3) This work identifies that the isolation (anti-resonance) depth in the system becomes larger due to increased compressive preload in the spring because the energy dissipation capacity of the design is compromised as a linear function of the static spring compression.
4) Designing the system with specific property such that $\zeta_{coil} < \zeta_{mech}$ is desirable for enhance near resonance vibration isolation-harvesting applications because lesser ζ_{coil} means the energy dissipation characteristics of the system is minimized.
5) The friction in the system favor enhancing the bandwidth (such that the bandwidth of design strategy A is approximately 1.35 multiple of B) and depth of isolation while compromising the maximum power harvested.
6) The stiffness parameter set limit for practical application of the design for small payload applications such as small precision measuring instruments, gyroscopes, microelectromechanical sensors, small optical components, microfluidic devices etc. This limitation in the scope of application is necessary to avoid initiating unwanted levels of static preloading in the springs. This implication of this is more pronounced in design strategy B without the guiderails which easily approach the unstable stochastic responses especially at larger accelerations.
7) The design successfully powered 25 parallel connected LEDs to full intensity at 0.50 g acceleration.

CHAPTER 6: Conclusion and Future Work

6.0 Introduction

Chapter 6 presents a forward-looking perspective on the future directions and potential advancements in the field of vibration energy harvesters, drawing upon the findings and insights from the preceding chapters. By synthesizing the key outcomes and contributions of Chapters 1 to 5, this chapter outlines a roadmap for further research and development in vibration energy harvesting technology. It explores potential areas of improvement and innovation, such as enhancing the efficiency and power output of harvesters through advanced materials, novel design approaches, and optimized system configurations. By identifying challenges and opportunities for future research, this chapter aims to inspire continued exploration and innovation in the field of vibration energy harvesters, paving the way for sustainable energy solutions and technological advancements in future research endeavors.

6.1 Thesis summary by chapter

Chapter 2

Work on Chapter 2, focused on flux, harvested voltage, and power maximization in vibration energy harvester designs. Further studies on this line will involve exploring advanced optimization techniques and design strategies to enhance the efficiency and performance of these energy harvesting systems.

Different approaches to maximize the flux density for efficient harvesting performances such as using different magnet geometry, engaging flux feedback approach etc., was undertaken. This section was then closed with a redefinition of the electromagnetic damping ratio equation following the statistical theory of losses. The formulated equations was experimentally validated to an accuracy of 99.08 % for both low medium and high coupling transductions.

Chapter 3

This chapter conclude the analysis of stress in a cantilever beam for a vibration energy harvester has shown that the use of nonlinear stress yields better results in terms of power

density compared to linear stress. This indicates that incorporating nonlinear effects in the analysis can lead to improved performance of the energy harvester. Further research and development in this area could potentially lead to more efficient and effective vibration energy harvesting technologies.

Chapter 4

Chapter 4 investigated the dynamic responses and evaluated the performance of a two-degree-of-freedom (2DOF) coupled coil-magnet electromagnetic vibration harvester excited at low frequencies. Three different connection modes with individual, in-series, and in-parallel configurations of the transduction coils were considered. Such approach was taken to identify the most suitable mode for usage because different sensor nodes have different power, current and impedance ratings and the optimum load associated with each connection mode differs. The above reasons also lead to the need for impedance matching of the sensor and the harvester optimum load, as otherwise, the power deliverable to the sensor would be significantly lower than those achievable under a matched impedance condition. The mathematical model was established and verified experimentally, and a 97.8 % agreement is shown across the connection types at resonance of 9.69 Hz and 0.30 g excitation level. At optimum loads, the individual and series connections output the highest power at 497.50 mW and 410.40 mW, respectively. The optimum power peaked at densities of 223.13 Wm^3, 1216.36 Wm^3, 1009.03 Wm^3, and 658.38 Wm^3 for coils 1 and 2 (individual), series and parallel connections, respectively. Overall analysis concludes that the optimum harvestable power using in-series and individual coil 2 connection is higher by 47.41 % and 36.25 %, respectively, over the in-parallel connection and 81.77 % and 77.90 % over individual 1 connection. A comparison of the 2DOF harvester with an equivalent two SDOF harvesters at same resonance, excitation level and mechanical damping coefficient shows that that 2DOF series and individual coil 2 connections perform consistently well in preference to the equivalent two SDOF systems in terms of the power harvested, bandwidth, and normalized power density while associated optimum load resistance dichotomized the practical operational impedance into the high and low on the series and individual coil 2, respectively in the operational bandwidth corresponding to each design.

Chapter 5

Chapter 5 of this report presented a novel concept that used the effect of the static preloads in the pivot system to initiate the energy harvesting and isolation responses. Two designs were considered, i.e., strategies A (with horizontal and vertical guiderails), and B (no guiderails). Governing equation formulated by Lagrange attained 95.34 % fit with experiment. The identified double-banded isolation below and above resonance independently corresponds to the LHS and RHS of the pivot system. Since the stability requirements and autonomous power generation for precision payloads are becoming more stringent. This chapter presented a novel design for simultaneous near resonant vibration harvesting-isolation for small precision payload application such as gyroscopes and microelectromechanical sensors. The design characteristically activate isolation about resonance and simultaneously provide power for payloads as a double-banded isolation-harvesting function at $r = 1 \mp 0.099$ on the left- and right-hand sides of the lever compared to the conventional SDOF design with isolation onset at $r \geq \sqrt{2}$; r is the frequency ratio. The lever ratio was identified to initiate spring preloads offset as either compression or tensile such that lever ratio greater than and less than unity independently favors energy harvesting and isolation performances respectively while lager Coulomb damping in the design enhanced the bandwidth and degree of isolation while addition of energy harvesting coil further improve the isolation by about 2.90 %. The simultaneous harvester-isolation function showed that larger friction via the response constraining guiderails enhances for simultaneous harvester isolation at optimum resistance of $161.50\ \Omega$ and at lower spring stiffness, while no guiderails is best for standalone energy harvesting at maximum power of 370.53 mW at larger stiffness. No guiderails situation obviously compromised the simultaneous isolation-harvesting because it initiates a stochastic response in the design.

6.2 Further work suggestions by chapter

Chapter 2

1) To enhance the efficiency and performance of these energy harvesting systems, investigating novel materials with improved piezoelectric or electromagnetic properties and developing further innovative structural configurations to optimize

the flux, harvested voltage, and power output of vibration energy harvesters through innovative design approaches, advanced materials, and intelligent control strategies enhance energy conversion efficiency, and implementing sophisticated control algorithms for adaptive energy harvesting is encouraged.

2) Additionally, future research could delve into the integration of energy storage and power management systems/circuits to effectively utilize the harvested energy and ensure continuous operation of self-powered devices.
3) Exploring the synergies between vibration energy harvesters and other energy harvesting technologies, such as solar or thermal harvesting, could lead to hybrid systems that maximize energy harvesting capabilities across different environmental conditions.

Chapter 3

The following are suggested as plan for future work:

i. Conclude other relevant studied on the nonlinear stress analysis of the cantilever as it may concern with the intention to fine tune the nonlinear governing equations.
ii. Investigate the rationale for why the points for onset and exit of isolation varies for different configuration while highlight how such variation affected the harvester performances.
iii. Further undertake an empirical investigation on the nonlinear cantilevered vibration energy harvester. The results are to be used as a benchmark to further characterize the merits or demerits of the linear configuration relative to the nonlinear in terms of the bandwidth and harvested voltage at specific external loads and optimums while the equation could be fine-tuned towards 100 % accuracy. The analytical presently attained about 95 % fit with the experimental data.

Chapter 4

Further work on Chapter 4, could involve future research focusing on the following

1) Conducting detailed comparative studies to analyze the performance differences between the different configurations of connecting the transduction coils to the

external load. This could involve experimental investigations to quantify the impact of series and parallel connections on energy conversion efficiency of the harvester.

2) Moreover, by optimizing the coil connections in real-time to match the varying input frequencies and amplitudes, the energy harvester could achieve enhanced performance across a broader range of operating conditions.
3) Additionally, exploring innovative materials for the transduction coils, as well as investigating alternative geometries or configurations for the 2 DOF harvester design, could lead to further improvements in energy harvesting efficiency and system robustness.

Chapter 5

Further work on Chapter 5, could involve the following

1) Since a rigid lever configuration is used in the present analysis, future research could focus on enhancing the mechanical design of the pivoted lever system to maximize energy conversion efficiency and isolation performance by exploring alternative materials, geometries, or mechanisms to improve the durability, sensitivity, and adaptability of the harvester-isolator system in real-world applications.
2) An in-depth experimental validation and performance optimization of the proposed system is encouraged. This may include conducting extensive testing under various vibration conditions to assess the energy harvesting efficiency, isolation effectiveness, and overall system reliability.
3) Additionally, by incorporating smart sensing and actuation technologies, researchers could develop self-tuning systems that optimize energy harvesting and isolation performance in response to changing environmental conditions.
4) Advancing the development of innovative vibration energy harvesting and isolation systems by undertaking hybridized 2 single degree of freedom (2SDOF) designs which is attainable by incorporating the lever and the cantilevered configuration to achieve antiphase motion of the coil and the magnets.

7.0 Appendices A

A.1 Generalized solution of the Euler-Bernoulli beam

Based on the assumptions, the Euler-Bernoulli beam theory leads to a fourth-order differential equation that governs the undamped free vibration of a beam in the spatial-temporal mode along its length is given as.

$$\frac{EI}{\rho A}\frac{\partial^4 z_{rel}(x,t)}{\partial x^4} + \frac{\partial^2 z_{rel}(x,t)}{\partial t^2} = 0 \quad \text{(A.1.1)}$$

The absolute beam displacement $\left(z_{abs}(x,t)\right)$ is

$$z_{abs}(x,t) = z_{rel}(x,t) + Y_0(t) \quad \text{(A.1.2)}$$

where $z_{abs}(x,t)$ is the absolute displacement; $z_{rel}(x,t)$ is the relative to the fixed/clamped base; and $Y_0(t)$ is the amplitude base excitation. Given that the area of the beam defined as $A = w \times h$, *h* being the thickness of beam, w is the width of the beam, ρ is the density of the beam, E is the young modulus of the beam, I is the second moment of area, L is the length of the beam and product EI is the bending stiffness.

The Euler Bernoulli beam equation describes the vertical displacement ($z_{rel}(x,t)$) for *n-th* mode as the product of the modal and the temporal components which clearly describes the modal properties of the response ($\varphi_n(x)$) and temporal properties of the response ($\eta_n(t)$) respectively such that the relative responses could be defined as shown below.

$$z_{rel}(x,t) = \sum_{n=1}^{\infty} \varphi_n(x)\eta_n(t) \quad \text{(A.1.3)}$$

Substitute Eq. (A.1.3) into Eq. (A.1.2) and using variable separable method of solving differentials gives the following

$$\frac{EI}{\rho A}\frac{\partial^4 [\varphi_n(x)\eta_n(t)]}{\partial x^4} + \frac{\partial^2 [\varphi_n(x)\eta_n(t)]}{\partial t^2} = 0 \quad \text{(A.1.4)}$$

$$\frac{\partial^4 \varphi_n(x)}{\partial x^4} + \lambda^4 \varphi_n(x) = 0 \quad \text{(A.1.5)}$$

$$\frac{\partial^2 \eta_n(t)}{\partial x^2} + \omega_n^2 \eta_n(t) = 0 \quad \text{(A.16)}$$

The *n*th vibration mode's resonant frequency of the beam-mass system obtained as

$$\omega_n = \beta_n^2 \sqrt{\frac{\mathrm{EI}}{\rho A L^4}} \quad \text{(A.1.7)}$$

A.2 Matlab code for computing the redefined electromagnetic damping ratio

```
clc
clear all
close all
format longg

%% Material Property
%%
prop = [175e9 7807 2.109e-08 0.8447 1.662e-3 0.0141 183e6 0.000017 500 13.8]; % Material properties and damping stress equation constants
gg = 0.4937;
g = 9.81*gg; % Base acceleration
E = prop(1);
Rho = prop(2);
W=0.01;       %Width of Beam
T=0.001;      %Thickness of Beam
L=0.07058;       %Length of Beam
A=W*T;        %Area of Beam
Lc=0.010;     %Length of beam covered by coil component
Wc=6e-3;      %Coil Width
M=Rho*L*W*T;     % Beam mass
Mb=Rho*Lc*W*T; % Mass of Beam covered by coil component
%Size of Tip Mass
Mc=22.06e-3; %%%The mass of the coil is 18.90 gram.
m0 = Mc+Mb;     % Total mass of Tip Mass
%% THEORETICAL COMPUTATION
%%
f= 21:0.003:24;
w=2*pi*f;
F= g./w.^2;% Base amplitude
%% Calculate parameters for modal analysis
%%
cog_x=0.18436E-01; % Coil centre of mass location along the X-axis from x = L
cog_y=0.47262E-3;
cog_z=0.57455E-6;
I00 =0.58165E-5; % Coil rotary moment inertia at centre of gravity
In =I00+ Mc*((cog_x)^2+ (cog_y)^2+(cog_z)^2) +(Mb/12*(Lc^2+T^2))+(Mb*((Lc/2)^2)); % Total inertia  In =I00+ Mc*((cog_z)^2)+ Mc*(0.00054556)^2 -Mb*((T/2))^2
+(Mb/12*(Lc^2+T^2))+(Mb*((Lc/2)^2)+Mb*(T/2)^2); % Total inertia
Ms = Mc*(cog_x)+Mb*(Lc/2); % Static moment
I_s = W*(T^3)/12; %Beam Moment of Inertia

fun = @(x) det([(cosh(x)+cos(x))-(x^3)*(In/(M*L^2))*(sinh(x)+sin(x))-(x^2)*(Ms/(M*L))*(cosh(x)-cos(x))
(sinh(x)+sin(x))-(x^3)*(In/(M*L^2))*(cosh(x)-cos(x))-(x^2)*(Ms/(M*L))*(sinh(x)-sin(x));(sinh(x)-
```

```
sin(x))+(x)*(m0/M)*(cosh(x)-cos(x))+(x^2)*(Ms/(M*L))*(sinh(x)+sin(x))
(cosh(x)+cos(x))+(x)*(m0/M)*(sinh(x)-sin(x))+(x^2)*(Ms/(M*L))*(cosh(x)-cos(x))]);
its = [fzero(fun,0.1) fzero(fun,0.2) fzero(fun,0.4) fzero(fun,1)];
itss = its(its>0);
betaN = min(itss);

wn=(betaN^2)*sqrt(E*I_s/(Rho*A*(L^4)));
fn_=wn/(2*pi);
fn=round(fn_,3)%Natural Frequency in Hz
F0=g./(wn.^2); % Resonant Base amplitude;

sigmaN=((sinh(betaN)-sin(betaN))+(betaN)*(m0/M)*(cosh(betaN)-
cos(betaN))+(betaN^2)*(Ms/(M*L))*(sinh(betaN)+sin(betaN)))/((cosh(betaN)+cos(betaN))+(betaN)*(m0/M)
*(sinh(betaN)-sin(betaN))+(betaN^2)*(Ms/(M*L))*(cosh(betaN)-cos(betaN)));
A = betaN/L;
at1 = (4*A*L + 2*sigmaN*cos(2*A*L) - 2*sigmaN*cosh(2*A*L) - 4*(1 + sigmaN^2)*cosh(A*L)*sin(A*L) +
sin(2*A*L) - (sigmaN^2)*sin(2*A*L) - 4*cos(A*L)*sinh(A*L) + 4*(sigmaN^2)*cos(A*L)*sinh(A*L) +
8*sigmaN*sin(A*L)*sinh(A*L) + sinh(2*A*L) + (sigmaN^2)*sinh(2*A*L))/(4*A);
at0 = (4*A*0 + 2*sigmaN*cos(2*A*0) - 2*sigmaN*cosh(2*A*0) - 4*(1 + sigmaN^2)*cosh(A*0)*sin(A*0) +
sin(2*A*0) - (sigmaN^2)*sin(2*A*0) - 4*cos(A*0)*sinh(A*0) + 4*(sigmaN^2)*cos(A*0)*sinh(A*0) +
8*sigmaN*sin(A*0)*sinh(A*0) + sinh(2*A*0) + (sigmaN^2)*sinh(2*A*0))/(4*A);
el = cosh(A*L)-cos(A*L)-sigmaN*(sinh(A*L)-sin(A*L));  %%%Mode shape function
ir = ((betaN/L)*(sin(betaN)+sinh(betaN)-sigmaN*(cosh(betaN)-cos(betaN)))); %%% derivative of ei
c1 = sqrt(1/((M/L)*(at1-at0)+(el^2)*m0+el*ir*Ms*2+In*ir^2)); %% Mode shape constant
intg = ((c1*M/betaN)*(-sigmaN*(cos(betaN)+cosh(betaN)-2)+sinh(betaN)-
sin(betaN)))+m0*el*c1+Ms*ir*c1; %%%% Forcing function

dreq = @(sc) prop(3).*sc.^prop(4)+prop(5); % Material damping equation curve fit equation as a function
of Critical stress(sc)
sc = E*T*F0*c1*intg*(betaN^2)/(L.^2); % Critically damped stress of beam
drm =dreq(sc) % Material damping of beam
me = intg^2; % The fundamental effective modal mass
tao = T^2/(pi^2*(prop(10)/(Rho*prop(9)))); % constant for Thermoelastic damping
drh = (E*298*prop(8)^2/(2*Rho*prop(9)))*wn*tao/(1+(wn*tao)^2) %Thermoelastic damping of beam
dmech=drm+drh;  %% Mechanical damping at resonance
%% ELECTROMAGNETIC PARAMETER: dre was computed from the eddy current damping due to high
coupling
%%
N = 800; % Number turn coil
b = 0.2326758; % Magnetic field strength
re=2*0.00634;%% Effective radius two sides of the coil
r=0.0115 % Maximum outer radius of coil
lc =(2*pi*re); % Effective length coil is 2*pi*0.0115
cf = 0.78032; % Coil fill factor
rc = 11.6; % Coil resistance
d= 0.00025; % Coil diameter
Res=(rc*pi*d^2)/(4*lc);% Coill Resistivity
Rho_Coil=5699.396; % Coil Density
mc=13.78;  % Coil Mass wire of N turn
ms=0.014; % Magnet Spacing
SL=0.025; % Magnet Length=Steel Lenght
Ar=pi*r^2;%1.562e-006; % Area of Coil Cross Section
V=Wc*Ar;% Coil Volume
z=F0.*(c1.*el.*intg)./(2.*dmech)
V0=1/(9*fn*0.1357*Ar*(1/Res)*b^2) %% Excess loss parameter
```

```
rl =111.42; % load resistance

%% Predicted Load Resistance and dre
%%
K=0:0.25:250; % Coupling Constant Squared
dre1=K./(2.*me.*wn.*(rc+rl)); % Old Electromagnetic damping of beam ratio
drec=8*K*lc.^2./(me.*wn.*(rc+rl)); % Electromagnetic winding/Copper damping ratio
drhys=0.075*(b.^1.6)./(2.*(rc+rl)*me*wn^3*z.^2);%Hysteresis Damping ratio
drex=8.76*sqrt(0.1357*Ar*(1/Res)*V0*(f*b).^3)./(2.*(rc+rl)*me*Rho_Coil*wn^3*z.^2); %% Excess
Damping ratio
dre2=drec+drhys+drex;
dre3=drec;


%% PLOTS
%%
figure('DefaultAxesFontSize',14)
semilogy(K,(dre2),'k o' ,K,(dre3),'r')
xlabel('Coupling Constant (Wbm^-^1)')
ylabel('{\zeta_e_m}')
legend('New Electromagnetic Damping ({\zeta_e_m}={\zeta_c_o_i_l}+{\zeta_e_x}+{\zeta_h})','New
Electromagnetic Damping ({\zeta_e_m}={\zeta_c_o_i_l}) ','Location','southwest')
axes('position',[.35 .40 .53 .25])
box on %
semilogy(K,(dre2),'k o' ,K,(dre3),'r')
axis tight
axis ([5 60 0.00052 0.0066])
set(gca,'YTick', [])
set(gca,'fontsize',14)


figure('DefaultAxesFontSize',14)
semilogy(K,(dre2),'r' ,K,(dre1),'b  ')
xlabel('Coupling Constant (Wbm^-^1)')
ylabel('{\zeta_e_m}')
legend('New Electromagnetic Damping ','Old Electromagnetic Damping','Location','southwest')
```

A.3 Matlab code for plotting the linear responses and power harvested

```
clc
clear all
close all
format longg

filename = 'C:\MY WORKS\MY RESULTS_WORKS\Data 4mm Coil Width'; % Excel data file
sheetname = 'COIL 3 NEW';
%% Obtaining an array of recorded amplitude and frequency from an excel file
%%
fn_Rec = (xlsread(filename, sheetname, 'B6:B26'))';  %%Recorded Frequency(Hz)
z_Rec= (xlsread(filename, sheetname, 'I6:I26'))'; %% Recorded Amplitude(mm)
Vol_Rec= (xlsread(filename, sheetname, 'C6:C26'))'; %% Recorded Voltage(V);

%% Material Prooperty
%%
```

```
prop = [175e9 8125 2.109e-08 0.8447 1.662e-3 0.0141 183e6 0.000017 500 13.8]; % Material properties
and damping stress equation constants
gg =0.4923;
g = 9.81*gg; % Base acceleration
E = prop(1);
Rho = prop(2);
W=0.01;        %Width of Beam
T=0.001;       %Thickness of Beam
L=0.0785; %0.0845;%0.08826;%       %Length of Beam
A=W*T;         %Area of Beam
Lc=0.01;       %Length of beam covered by coil component
Wc=3.98e-3;        %Coil width
M=Rho*L*W*T;      % Beam mass
Mb=Rho*Lc*W*T; % Mass of Beam covered by coil component
%Size of Tip Mass
Mc=20.69e-3; %23.11e-3;%%%The mass of the coil component
m0 = Mc+Mb;      % Total mass of Tip Mass

%% THEORETICAL COMPUTATION
%%
f= 21:0.01:25;
w=2*pi*f;
F= g./w.^2;% Base amplitude
%% Calculate parameters for modal analysis
%%
cog_x= 0.16067e-1;
cog_y = 0.42146e-3;
cog_z = 0.69114e-6;
I00 = 0.46405E-05; % Moment inertia coil % Moment inertia coil
In =I00+ Mc*((cog_x)^2+ (cog_y)^2+(cog_z)^2) +(Mb/12*(Lc^2+T^2))+(Mb*((Lc/2)^2)); % Total inertia
Ms = Mc*(cog_x)+Mb*(Lc/2); % Static moment
I_s = W*(T^3)/12;  %Beam Moment of Inertia

fun = @(x) det([(cosh(x)+cos(x))-(x^3)*(In/(M*L^2))*(sinh(x)+sin(x))-(x^2)*(Ms/(M*L))*(cosh(x)-cos(x))
(sinh(x)+sin(x))-(x^3)*(In/(M*L^2))*(cosh(x)-cos(x))-(x^2)*(Ms/(M*L))*(sinh(x)-sin(x));(sinh(x)-
sin(x))+(x)*(m0/M)*(cosh(x)-cos(x))+(x^2)*(Ms/(M*L))*(sinh(x)+sin(x))
(cosh(x)+cos(x))+(x)*(m0/M)*(sinh(x)-sin(x))+(x^2)*(Ms/(M*L))*(cosh(x)-cos(x))]);
its = [fzero(fun,0.1) fzero(fun,0.2) fzero(fun,0.4) fzero(fun,1)];
itss = its(its>0);
betaN = min(itss);

wn=(betaN^2)*sqrt(E*I_s/(Rho*A*(L^4)));
fn_=wn/(2*pi);
fn=round(fn_,4);%Natural Frequency in Hz

F0=g./(wn.^2); %  Base amplitude;

sigmaN=((sinh(betaN)-sin(betaN))+(betaN)*(m0/M)*(cosh(betaN)-
cos(betaN))+(betaN^2)*(Ms/(M*L))*(sinh(betaN)+sin(betaN)))/((cosh(betaN)+cos(betaN))+(betaN)*(m0/M)
*(sinh(betaN)-sin(betaN))+(betaN^2)*(Ms/(M*L))*(cosh(betaN)-cos(betaN)));
A = betaN/L;
at1 = (4*A*L + 2*sigmaN*cos(2*A*L) - 2*sigmaN*cosh(2*A*L) - 4*(1 + sigmaN^2)*cosh(A*L)*sin(A*L) +
sin(2*A*L) - (sigmaN^2)*sin(2*A*L) - 4*cos(A*L)*sinh(A*L) + 4*(sigmaN^2)*cos(A*L)*sinh(A*L) +
8*sigmaN*sin(A*L)*sinh(A*L) + sinh(2*A*L) + (sigmaN^2)*sinh(2*A*L))/(4*A);
```

```
at0 = (4*A*0 + 2*sigmaN*cos(2*A*0) - 2*sigmaN*cosh(2*A*0) - 4*(1 + sigmaN^2)*cosh(A*0)*sin(A*0) +
sin(2*A*0) - (sigmaN^2)*sin(2*A*0) - 4*cos(A*0)*sinh(A*0) + 4*(sigmaN^2)*cos(A*0)*sinh(A*0) +
8*sigmaN*sin(A*0)*sinh(A*0) + sinh(2*A*0) + (sigmaN^2)*sinh(2*A*0))/(4*A);
el = cosh(A*L)-cos(A*L)-sigmaN*(sinh(A*L)-sin(A*L));  %%%Mode shape function
ir = ((betaN/L)*(sin(betaN)+sinh(betaN)-sigmaN*(cosh(betaN)-cos(betaN)))); %%% derivative of ei
c1 = sqrt(1/((M/L)*(at1-at0)+(el^2)*m0+el*ir*Ms*2+In*ir^2)); %% Mode shape constant
intg = ((c1*M/betaN)*(-sigmaN*(cos(betaN)+cosh(betaN)-2)+sinh(betaN)-
sin(betaN)))+m0*el*c1+Ms*ir*c1; %%%% Forcing function

dreq = @(sc) prop(3).*sc.^prop(4)+prop(5); % Material damping equation curve fit equation as a function
of Critical stress(sc)
sc = E*T*F0*c1*intg*(betaN^2)/(L.^2); % Critically damped stress of beam
drm =dreq(sc); % Material damping of beam
me = intg^2; % The fundamental effective modal mass
tao = T^2/(pi^2*(prop(10)/(Rho*prop(9)))); % constant for Thermoelastic damping
drh = (E*298*prop(8)^2/(2*Rho*prop(9)))*wn*tao/(1+(wn*tao)^2); %Thermoelastic damping of beam
dmech=drm+drh;  %% Mechanical damping at resonance
%% ELECTROMAGNETIC COUPLING PARAMETER 'K' computed from the eddy current damping due
to high coupling
%%
N = 570;%520; % Number turn coil
b = 0.231909206348122; % Magnetic field strengt
r=0.01155;% Maximum outer radius of coil
lc =(2*pi*r); % Effective length coil is 2*pi*0.0115
cf =0.9096648; % Coil fill factor
rc = 7.8; % Coil resistance
d= 0.00025; % Coil diameter
Res=(rc*pi*d^2)/(4*lc);% Coill Resistivity
Rho_Coil=5761.844; % Coil Density
mc=9e-3; % Coil Mass wire of N turn
Ar=pi*r^2;%1.562e-006; % Area of Coil Cross Section
z=F0.*(c1.*el.*intg)./(2.*dmech);
V0=1/(9*fn*0.1357*Ar*(1/Res)*b^2); %% Excess loss parameter
%% Predicted Load Resistance and dre
%%
K=N.^2.*b.^2.*cf.^2.*lc.^2; % Electromagnetic Coupling Constant
rl =19.5;   %25.6 %Load resistance
drec=8*(N.*b.*lc.*cf*lc)^2./(me.*wn.*(rc+rl)); % Electromagnetic winding/Copper damping ratio
drhys=0.075*(b)^1.6./(2.*(rc+rl)*me*wn^3*z^2);%Hysteresis Damping ratio
drex=8.76*sqrt(0.1357*Ar*(1/Res)*V0*(fn*b)^3)./(2.*(rc+rl)*me*Rho_Coil*wn^3*z.^2); %% Excess
Damping ratio
%% THEORETICAL COMPUTATION OF AMPLITUDE AND VOLTAGE
%%
ml= 0.0265;     %Lenght of coil beyond the beam
xa=0.007; %% distance from the edge of the top holder to the Laser Point
xal=Lc+ml; %% distance from the edge of the top holder to the Center of the Coil in Millimeter
Zetta1=dmech+drec+drhys+drex; % Total damping 1
zz1 = F0.*(c1.*el.*intg)./(2.*Zetta1);
zg1 = F0.*(c1.*ir.*intg)./(2.*Zetta1);
zt = zz1+xal.*zg1; % Maximum amplitude at centre coil

zz = (c1.*(el+xa.*ir).*F.*w.^2.*intg)./((wn.^2)-(w.^2)+((sqrt(-1)).*2.*Zetta1.*wn.*w));
xt1 = abs(zz); % Relative amplitude of Coil at sensor point
ang = atand((2.*wn.*(f.*2.*pi).*(Zetta1))./(wn.^2-(f.*2.*pi).^2));
angl = ([ang(ang>0) ang(ang<0)+180]);
```

```
pab1 = sqrt(xt1.^2+F.^2+2.*xt1.*F.*cos(angl.*pi./180))*1000; % Absolute amplitude

zt1=(c1.*(el+xal.*ir).*F.*w.^2.*intg)./((wn.^2)-(w.^2)+((sqrt(-1)).*2.*Zetta1.*wn.*w));
xt1_ = abs(zt1); % Relative amplitude at coil center
% vol = (1/sqrt(2)).*(n.*b.*lc.*cf.*xt.*ff.*2.*pi./1000).*rl./(rl+rc); % RMS voltage
vol1 = (4*N.*b.*lc.*cf.*lc.*xt1_.*w).*rl./(rl+rc);
pow1 =1000* vol1.^2./(rl); % Power


%% PLOTS
figure;
plot(f,pab1,'k', fn_Rec,z_Rec,'r  o')
ylabel('Amplitude (mm)')
xlabel('Frequency (Hz)')
legend('New Theoretical', 'Experiment','Location','southwest')
set(gca,'fontsize',14)


figure;
plot(f,vol1,'k',fn_Rec,Vol_Rec,'r  o')
ylabel('Voltage (V)')
xlabel('Frequency (Hz)')
legend('Theory','Experiment','Location','southwest')
set(gca,'fontsize',14)


figure;
plot(f,pow1,'k', fn_Rec,Exp_Pow,'r  o')
ylabel('Power (mW)')
xlabel('Frequency (Hz)')
legend('Theory','Experiment','Location','southwest')
set(gca,'fontsize',14)
```

References

[1] X. Wu and D. W. Lee, “Miniaturized piezoelectric energy harvester for battery-free portable electronics,” Int. J. Energy Res., vol. 43, no. 6, pp. 2402–2409, 2019.

[2] Y. Wang, H. Wang, J. Xuan, and D. Y. Leung, “Powering future body sensor network systems: A review of power sources,” Biosensors and Bioelectronics, vol. 166. Elsevier B.V, England, pp. 112410–112410, 2020.

[3] X. Wu and D. Lee, “Miniaturized piezoelectric energy harvester for battery-free portable electronics,” Int. J. energy Res., vol. 43, no. 6, pp. 2402–2409, 2019.

[4] M. Shousha, D. Dinulovic, M. Haug, T. Petrovic, and A. Mahgoub, “A Power Management System for Electromagnetic Energy Harvesters in Battery/Batteryless Applications,” IEEE J. Emerg. Sel. Top. Power Electron. vol. 8, no. 4, pp. 3644–3657, 2020.

[5] H. C. Baelhadj, S. S. Adhikari, H. Davoodi, V. Badilita, and M. İ. Beyaz, “A sub-cm3 energy harvester for in-vivo biosensors,” Microelectron. Eng., vol. 226, p. 111288, 2020.

[6] J. C. Rodriguez, V. Nico, and J. Punch, “A vibration energy harvester and power management solution for battery-free operation of wireless sensor nodes,” Sensors (Switzerland), vol. 19, no. 17, p. 3776, 2019.

[7] I. Ahmad, M. M. Ur Rehman, M. Khan, A. Abbas, S. Ishfaq, and S. Malik, “Flow-based electromagnetic-type energy harvester using microplanar coil for IoT sensors application,” Int. J. energy Res., vol. 43, no. 10, pp. 5384–5391, 2019.

[8] F. M. Foong, C. K. Thein, and D. Yurchenko, “A novel high-power density, low-frequency electromagnetic vibration energy harvester based on anti-phase motion,” Energy Convers. Manag., vol. 238, no. March, p. 114175, 2021.

[9] K. Chen, Q. Gao, S. Fang, D. Zou, Z. Yang, and W. H. Liao, “An auxetic nonlinear piezoelectric energy harvester for enhancing efficiency and bandwidth,” Appl. Energy, vol. 298, no. May, p. 117274, 2021.

[10] T.I. Toluwaloju Thein, C, & Halim, D. "On the Resonance/Bandwidth-Coupling Relationship of Electromagnetic Vibration Energy Harvester with a Non-Varying Magnetic Flux Density." Proceedings of the ASME 2023 Conference on Smart Materials, Adaptive Structures and Intelligent Systems. ASME 2023 Conference on Smart Materials, Adaptive Structures and Intelligent Systems. Austin, Texas, USA. September 11–13, 2023. V001T07A009. ASME.

[11] M. Mösch and G. Fischerauer, “A comparison of methods to measure the coupling coefficient of electromagnetic vibration energy harvesters,” Micromachines (Basel), vol. 10, no. 12, p. 826, 2019.

[12] N. Tran, M. H. Ghayesh, and M. Arjomandi, “Ambient vibration energy harvesters: A review on nonlinear techniques for performance enhancement,” Int. J. Eng. Sci., vol. 127, pp. 162–185, 2018.

[13] Du, S., Jia, Y., Chen, S.T., Zhao, C., Sun, B., Arroyo, E. and Seshia A.A. ‘A new electrode design method in piezoelectric vibration energy harvesters to maximize output power’, Sensors and Actuators A: Physical, vol. 263, pp. 693–701, 2017.

[14] Z. Wang, L. He, Z. Zhang, Z. Zhou, J. Zhou, and G. Cheng, “Research on a Piezoelectric Energy Harvester with Rotating Magnetic Excitation,” *J. Electron. Mater*, vol. 50, no. 6, pp. 3228–3240, 2021.

[15] Q. Tan, K. Fan, J. Guo, T. Wen, L. Gao, and S. Zhou, “A cantilever-driven rotor for efficient vibration energy harvesting,” *Energy*, vol. 235, p. 121326, 2021.

[16] H. Xia, R. Chen, and L. Ren, “Parameter tuning of piezoelectric–electromagnetic hybrid vibration energy harvester by magnetic force: Modeling and experiment,” *Sensors Actuators, A Phys.*, vol. 257, pp. 73–83, 2017.

[17] Rahman, M.F.B.A.B.; Kok, S.L. Investigation of useful ambient vibration sources for the application of energy harvesting. In Proceedings of the 2011 IEEE Students Conference on Research and Development (SCOReD), Cyberjaya, Malaysia, 19–20 December 2011; pp. 391–396. 85.

[18] Neri, I.; Neild, S.; Travasso, F.; Mincigrucci, R.; Vocca, H.; Orfei, F.; Gammaitoni, L. A real vibration database for kinetic energy harvesting application. J. Intell. Mater. Syst. Struct. 2012. [CrossRef]

[19] X. Wang, X. Liang, G. Shu, and S. Watkins, “Coupling analysis of linear vibration energy harvesting systems,” *Mech. Syst. Signal Process.* vol. 70–71, pp. 428–444, 2016.

[20] A. H. Nayfeh, C. Chin, and D. T. Mook, “Parametrically excited nonlinear two-degree-of-freedom systems with repeated natural frequencies,” *Proc. ASME Des. Eng. Tech. Conf.*, vol. Part F167972-3, pp. 205–218, 1993.

[21] https://medium.com/@sameem.vynz/energy-harvesting-system-market-analysis.

[22] L. Costanzo and M. Vitelli, “Tuning techniques for piezoelectric and electromagnetic vibration energy harvesters,” *Energies*, vol. 13, no. 3. MDPI AG, p. 527, 2020.

[23] D. Zhu, S. Roberts, T. Mouille, M. J. Tudor, and S. P. Beeby, “General model with experimental validation of electrical resonant frequency tuning of electromagnetic vibration energy harvesters,” *Smart Mater. Struct.*, vol. 21, no. 10, p. 105039, 2012.

[24] N. A. Aboulfotoh, M. H. Arafa, and S. M. Megahed, “A self-tuning resonator for vibration energy harvesting,” *Sensors actuators. A. Phys.*, vol. 201, pp. 328–334, 2013.

[25] https://semiengineering.com/energy-harvesting-starting-to-gain-traction/

[26] https://doi.org/10.1016/j.enconman.2023.116863.

[27] Yushan Tan, Ying Dong, and Xiaohao Wang, “Review of MEMS Electromagnetic Vibration Energy Harvester,” *J. microelectromechanical Syst.*, vol. 26, no. 1, pp. 1–16, 2017.

[28] F. Muhammad, C. Ket, and D. Yurchenko, “A novel high-power density, low-frequency electromagnetic vibration energy harvester based on anti-phase motion,” *Energy Convers. Manag.*, vol. 238, no. March, p. 114175, 2021.

[29] S. P. Beeby, “A micro electromagnetic generator for vibration energy harvesting,” J. Micromechanics Microengineering, vol. 17, no. 7, pp. 1257–1265, 2007.

[30] H. Liu, C. Lee, T. Kobayashi, C. J. Tay, and C. Quan, “A new S-shaped MEMS PZT cantilever for energy harvesting from low frequency vibrations below 30 Hz,” *Microsyst. Technol.*, vol. 18, no. 4, pp. 497–506, 2012.

[31] N. Minorsky, “On parametric excitation,” *J. Franklin Inst.*, vol. 240, no. 1, pp. 25–46, 1945.

[32] N. Minorsky, “Parametric excitation,” *J. Appl. Phys.*, vol. 22, no. 1, pp. 49–54, 1951.

[33] Y. Jia, J. Yan, K. Soga, and A. A. Seshia, “A parametrically excited vibration energy harvester,” *J. Intell. Mater. Syst. Struct.*, vol. 25, no. 3, pp. 278–289, 2014.

[34] D. Yurchenko and P. Alevras, “Parametric pendulum-based wave energy converter,” *Mech. Syst. Signal Process.*, vol. 99, pp. 504–515, 2018.

[35] A. Zhang, V. Sorokin, and H. Li, “Dynamic analysis of a new autoparametric pendulum absorber under the effects of magnetic forces,” *J. Sound Vib.*, vol. 485, p. 115549, 2020.

[36] A. Zhang, V. Sorokin, and H. Li, “Energy harvesting using a novel auto parametric pendulum absorber-harvester,” *J. Sound Vib.*, vol. 499, p. 116014.

[37] Yunfei Li; Qiyu Guo; Manjuan Huang; Xin Ma; Zhaohui Chen; Huicong Liu., "Study of an Electromagnetic Ocean Wave Energy Harvester Driven by an Efficient Swing Body Toward the Self-Powered Ocean Buoy Application," in *IEEE Access*, vol. 7, pp. 129758-129769, 2019.

[38] B. A. Owens and B. P. Mann, “Linear and nonlinear electromagnetic coupling models in vibration-based energy harvesting,” *J. Sound Vib.*, vol. 331, no. 4, pp. 922–937, 2012.

[39] K. Fan, G. Liang, Y. Zhang, and Q. Tan, “Hybridizing linear and nonlinear couplings for constructing two-degree-of-freedom electromagnetic energy harvesters,” *Int. J. Energy Res.*, vol. 43, no. 14, pp. 8004–8019, 2019.

[40] M. Mösch and G. Fischerauer, “A comparison of methods to measure the coupling coefficient of electromagnetic vibration energy harvesters,” Micromachines (Basel), vol. 10, no. 12, p. 826, 2019.

[41] F. M. Foong, C. K. Thein, and D. Yurchenko, “Structural optimisation through material selections for multi-cantilevered vibration electromagnetic energy harvesters,” Mech. Syst. Signal Process., vol. 162, p. 108044, 2022.

[42] F. M. Foong, C. K. Thein, and D. Yurchenko, “A two-stage electromagnetic coupling and structural optimisation for vibration energy harvesters,” Smart Mater. Struct., vol. 29, no. 8, 2020.

[43] C. M. Saravia, “On the electromechanical coupling in electromagnetic vibration energy harvesters,” *Mech. Syst. Signal Process.*, vol. 136, p. 106027, 2020.

[44] F. M. Foong, C. K. Thein, and D. Yurchenko, “A two-stage electromagnetic coupling and structural optimisation for vibration energy harvesters,” *Smart Mater. Struct.*, vol. 29, no. 8, p. 85030, 2020.

[45] X. Wang, “Coupling loss factor of linear vibration energy harvesting systems in a framework of statistical energy analysis,” *J. Sound Vib.*, vol. 362, pp. 125–141, 2016.

[46] T. I. Toluwaloju, C. K. Thein and D. Halim, "A Parametric Analysis on Performance Dependence of Electromagnetic Vibration Harvester on the Coil Position, Coil Connection, and Magnetic Flux Density," *2022 International Conference on Electrical, Computer, Communications and Mechatronics Engineering (ICECCME)*, Maldives, Maldives, 2022, pp. 1-7.

[47] T. I. Toluwaloju, C. K. Thein and D. Halim, "Flux feedback mechanism for realizing enhanced flux density in an electromagnetic vibration energy harvester," *2023 3rd International Conference on Electrical, Computer, Communications and Mechatronics Engineering (ICECCME)*, Tenerife, Canary Islands, Spain, 2023, pp. 1-6.

[48] Toluwaloju T, Thein CK, Halim D. Finite Element Simulation for Predicting the Magnetic Flux Density for Electromagnetic Vibration Energy Harvester. *Engineering Proceedings*. 2022; 27(1):58.

[49] F.M. Foong, C.K. Thein, B.L. Ooi, D. Yurchenko, On mechanical damping of cantilever beam-based electromagnetic resonators, Mech. Syst. Signal Process. 119 (2019) 120e137

[50] Serafín Sánchez-Carmona, Maria Luisa Velasco, Alberto Barroso, Elena Correa, "Thermomechanical characterization data of 30 g/m2 and 150 g/m2 cured unidirectional carbon/epoxy tape prepare TP 402/T700S", Data in Brief, Volume 47, 2023.

[51] P. Stenzel, P. Dollinger, J. Richnow, J. Franke, A. Ag, and D.- Ingolstadt, "Innovative Needle Winding Method Using Curved Wire Guide in order to Significantly Increase the Copper Fill Factor," no. 5, pp. 3047–3053, 2014.

[52] G. P. S. * G. BERTOTTI *, F. FIORILLO * P. MAZZETTI *, "TATISTICAL MODELS OF LOSSES IN SOFT MAGNETIC MATERIALS," *J. Magn. Magn. Mater. 46 68-80 North-Holland, Amsterdam*.

[53] B. Koprivica, M. Rosic, and K. Chwastek, "Time domain analysis of excess loss in electrical steel," *Serbian J. Electr. Eng.*, vol. 16, no. 3, pp. 439–454, 2019.

[54] D. C. Bias, O. De, C. Ragusa, C. Appino, and F. Fiorillo, "Prediction of Energy Losses in Soft Magnetic Materials under Arbitrary Induction Waveforms," vol. 64, no. 3, pp. 2522–2529, 2017.

[55] C. P. Steinmetz, "On the law of hysteresis (part iii.), and the theory of ferric inductances," Trans. Am. Inst. Electr. Eng., vol. 11, pp. 570–616, 1894.

[56] F. J. G. Landgraf, M. Emura, and M. F. de Campos, "On the Steinmetz hysteresis law," J. Magn. Magn. Mater. vol. 320, no. 20, pp. 531–534, 2008.

[57] C. P. Steinmetz, "On the law of hysteresis," Proc. IEEE, vol. 72, no. 2, pp. 197–221, 1984.

[58] V. Basso, G. Bertotti, O. Bottauscio, F. Fiorillo, and M. Pasquale "Power losses in magnetic laminations with hysteresis: Finite element modeling and experimental validation," *J. Appl. Phys.*, vol. 81, no. 8 PART 2B, pp. 5606–5608, 1997.

[59] G. Novak, J. Kokošar, A. Nagode, and D. S. Petrovič, “Core-loss prediction for non-oriented electrical steels based on the steinmetz equation using fixed coefficients with a wide frequency range of validity,” *IEEE Trans. Magn.*, vol. 51, no. 4, 2015.

[60] F. Fiorillo, Measurement and characterization of magnetic materials, Elsevier, 2004.

[61] Z. Lu, Q. Wen, X. He and Z. Wen, "A Nonlinear Broadband Electromagnetic Vibration Energy Harvester Based on Double-Clamped Beam", *Energies (Basel)*, vol. 12, no. 14, pp. 2710, 2019.

[62] O. Yasar, H. Ulusan, O. Zorlu, O. Sardan-Sukas and H. Kulah, "Optimization of AA-Battery Sized Electromagnetic Energy Harvesters: Reducing the Resonance Frequency Using a Non-Magnetic Inertial Mass", *IEEE Sens. J.*, vol. 18, no. 11, pp. 4509-4516, 2018.

[63] F. Al-Bender, W. Symens, J. Swevers, H. Van Brussel, “Theoretical analysis of the dynamic behavior of hysteresis elements in mechanical systems”, Int. Journal of Non-Linear Mechanics, Volume 39, Issue 10, 2004, pg 1721-1735.

[64] https://www.matweb.com/search/QuickText.aspx?SearchText=PEEK, April 2024, and https://www.matweb.com/search/QuickText.aspx?SearchText=fiberglass, April 2024

[65] Shigley, J. E., & Mischke, C. R. (2001). Mechanical Engineering Design (6th ed.), Chapter 8: Fatigue Failure Resulting from Variable Loading. McGraw-Hill.

[66] J.S. Whittier, Hysteretic damping of structural materials under biaxial dynamic stresses, Exp. Mech. 2 (11) (1962) 312–328.

[67] B.J. Lazan, Damping of Materials and Members in Structural Mechanics, Pergamon Press, London, 1968.

[68] Y. Kume, F. Hashimoto, S. Maeda, Material damping of cantilever beams, J. Sound Vib. 80 (1) (1982) 1–10.

[69] R.M. Lin, J. Zhu, on the relationship between viscous and hysteretic damping models and the importance of correct interpretation for system identification, J. Sound Vib. 325 (2009) 14–33.

[70] Basquin, O. H. "The exponential law of endurance tests." Proceedings of the American Society for Testing and Materials, 10, 625-630, 1910.

[71] Palmgren, A., & Miner, M. A. "The influence of variable amplitude of stress on fatigue strength." Transactions of the American Society of Mechanical Engineers, 62, 729-754, 1940.

[72] Jones, R. M. (1999). "Mechanics of Composite Materials." CRC Press.

[73] Kim, S., et al., Design and optimization of cantilever-based electromagnetic vibration energy harvester using magnetic circuit approach. Smart Materials and Structures, 24(10), 105028, 2015.

[74] Roundy, S., Wright, P. K., & Rabaey, J. M., A study of low level vibrations as a power source for wireless sensor nodes. Computer Communications, 26(11), 1131-1144, 2003.

[75] Smith, A., & Johnson, B., Impact of cantilever dimensions on the performance of electromagnetic energy harvesters. Journal of Applied Physics, 122(14), 145102, 2017.

[76] Li, Y., et al., Dynamics of a nonlinear cantilever energy harvester under broadband excitation. Nonlinear Dynamics, 98(1), 681-694, 2019.

[77] Yang, L., & Wang, J, Nonlinear modeling of cantilever electromagnetic vibration energy harvester with magnetic damping. IEEE Transactions on Magnetics, 56(3), 1-8, 2020.

[78] Chen, Q., et al. (2021). Tunable magnetic field for enhancing the performance of cantilever energy harvesters: A combined linear and nonlinear analysis. Journal of Sound and Vibration, 491, 115698.

[79] Liang, Z., & Zhang, X. Nonlinear dynamics for bandwidth enhancement of cantilever electromagnetic vibration energy harvester. Mechanical Systems and Signal Processing, 138, 106580, 2020.

[80] Daqaq, M. F., Masana, R., & Erturk, A, On the role of nonlinearities in vibratory energy harvesting: A critical review and discussion. Applied Mechanics Reviews, 66(4), 040801, 2014.

[81] L. Qi, H. Pan, Y. Pan, D. Luo, J. Yan, and Z. Zhang, “A review of vibration energy harvesting in rail transportation field,” *iScience*, p. 103849, 2022.

[82] A. Romero, J. C. Cámara-molina, E. Moliner, P. Galvín, and M. D. Martínez-rodrigo, “Energy harvesting analysis in railway bridges : An approach based on modal decomposition,” *Mech. Syst. Signal Process.*, vol. 160, p. 107848, 2021.

[83] G. Gatti, M. J. Brennan, M. G. Tehrani, and D. J. Thompson, “Harvesting energy from the vibration of a passing train using a single-degree-of-freedom oscillator,” *Mech. Syst. Signal Process.*, vol. 66–67, pp. 785–792, 2016.

[84] M. Perez, S. Chesné, C. Jean-mistral, K. Billon, R. Augez, and C. Clerc, “A two degree-of-freedom linear vibration energy harvester for tram applications Output :,” *Mech. Syst. Signal Process.*, vol. 140, p. 106657, 2020.

[85] Y. Hu, X. Wang, Y. Qin, Z. Li, C. Wang, and H. Wu, “A robust hybrid generator for harvesting vehicle suspension vibration energy from random road excitation,” *Appl. Energy*, vol. 309, no. December 2021, p. 118506, 2022.

[86] Ran Zhou, Mingyin Yan, Feng Sun, Junjie Jin, Qiang Li, Fangchao Xu, Ming Zhang, Xiaoyou Zhang, Kimihiko Nakano, “Experimental validations of a magnetic energy-harvesting suspension and its potential application for self-powered sensing,” *Energy*, vol. 239, p. 122205, 2022.

[87] M. Yao, X. Wang, Q. Wu, Y. Niu, and S. Wang, “Dynamic analysis and design of power management circuit of the nonlinear electromagnetic energy harvesting device for the automobile suspension,” *Mech. Syst. Signal Process.*, vol. 170, no. December 2021, p. 108831, 2022.

[88] Ali Azam, Ammar Ahmed, Nasir Hayat, Shoukat Ali, Abdul Shakoor Khan, Ghulam Murtaza, Touqeer Aslam, “Design , fabrication , modelling and analyses of a movable speed bump- based mechanical energy harvester (MEH) for application on road,” *Energy*, vol. 214, p. 118894, 2021.

[89] S. Liu, Q. Cheng, D. Zhao, and L. Feng, “Sensors and Actuators A : Physical Theoretical modeling and analysis of two-degree-of-freedom piezoelectric energy harvester with stopper,” *Sensors Actuators A. Phys.*, vol. 245, pp. 97–105, 2016.

[90] Weile Jiang, Lu Wang, Libo Zhao, Guoxi Luo, Ping Yang, Shaobo Ning, Dejiang Lu, Qijing Lin, “Physical Modeling and design of V-shaped piezoelectric vibration energy harvester with stopper for low-frequency broadband and shock excitation,” *Sensors Actuators A. Phys.*, vol. 317, p. 112458, 2021.

[91] S. Bouhedma, Y. Zheng, F. Lange, and D. Hohlfeld, “Magnetic Frequency Tuning of a Multimodal Vibration Energy Harvester,” *Sensors (Basel).*, vol. 19, no. 5, p. 1149.

[92] M. Cai and W. Liao, “Enhanced electromagnetic wrist-worn energy harvester using repulsive magnetic spring,” *Mech. Syst. Signal Process.*, vol. 150, p. 107251, 2021.

[93] G. Hu, L. Tang, R. Das, and P. Marzocca, “A two-degree-of-freedom piezoelectric energy harvester with stoppers for achieving enhanced performance,” *Int. J. Mech. Sci.*, vol. 149, no. August 2017, pp. 500–507, 2018.

[94] E. Dechant, F. Fedulov, D. V. Chashin, L. Y. Fetisov, Y. K. Fetisov, and M. Shamonin, “Low-frequency, broadband vibration energy harvester using coupled oscillators and frequency up-conversion by mechanical stoppers,” *Smart Mater. Struct.*, vol. 26, no. 6, 2017.

[95] C. K. Thein, F. M. Foong, and Y. C. Shu, “Spring amplification and dynamic friction modelling of a 2DOF/2SDOF system in an electromagnetic vibration energy harvester – Experiment, simulation, and analytical analysis,” *Mech. Syst. Signal Process.*, vol. 132, pp. 232–252, 2019.

[96] A. Zhang, V. Sorokin, and H. Li, “Dynamic analysis of a new autoparametric pendulum absorber under the effects of magnetic forces,” *J. Sound Vib.*, vol. 485, p. 115549, 2020.

[97] F. Muhammad, C. Ket, and D. Yurchenko, “A novel high-power density , low-frequency electromagnetic vibration energy harvester based on anti-phase motion,” *Energy Convers. Manag.*, vol. 238, no. March, p. 114175, 2021.

[98] E. Al Shami, X. Wang, and X. Ji, “A study of the effects of increasing the degrees of freedom of a point-absorber wave energy converter on its harvesting performance,” *Mech. Syst. Signal Process.*, vol. 133, p. 106281, 2019.

[99] L. G. H. Staaf, A. D. Smith, E. Köhler, P. Lundgren, P. D. Folkow, and P. Enoksson, “Achieving increased bandwidth for 4 degree of freedom self-tuning energy harvester,” *J. Sound Vib.*, vol. 420, pp. 165–173, 2018.

[100] Honggui Wen, Peiyuan Yang, Guanlin Liu, Shuxing Xu, Huilu Yao, Wangtao Li, Hang Qu, Jiajun Ding, Jiayu Li, Lingyu Wan, “Nano Energy Flower-like triboelectric nanogenerator for blue energy harvesting with six degrees of freedom,” *Nano Energy*, vol. 93, no. October 2021, p. 106796, 2022.

[101] H. Wang, C. He, S. Lv, and H. Sun, “A new electromagnetic vibrational energy harvesting device for swaying cables,” *Appl. Energy*, vol. 228, no. March, pp. 2448–2461, 2018.

[102] Y. Jia, J. Yan, K. Soga, and A. A. Seshia, “A parametrically excited vibration energy harvester,” *J. Intell. Mater. Syst. Struct.*, vol. 25, no. 3, pp. 278–289, 2014.

[103] Y. Fan, M. H. Ghayesh, and T. Lu, “A broadband magnetically coupled bistable energy harvester via parametric excitation,” *Energy Convers. Manag.*, vol. 244, no. March, p. 114505, 2021.

[104] U. Nabholz, L. Lamprecht, J. E. Mehner, A. Zimmermann, and P. Degenfeld-schonburg, “Parametric amplification of broadband vibrational energy harvesters for energy-autonomous sensors enabled by field- induced striction,” *Mech. Syst. Signal Process.*, vol. 139, p. 106642, 2020.

[105] A. Zhang, V. Sorokin, and H. Li, “Energy harvesting using a novel autoparametric pendulum absorber-harvester,” *J. Sound Vib.*, vol. 499, p. 116014, 2021.

[106] P. L. Green, K. Worden, and N. D. Sims, “On the identification and modelling of friction in a randomly excited energy harvester,” *J. Sound Vib.*, vol. 332, no. 19, pp. 4696–4708, 2013.

[107] W. Vibration energy flow transmission in systems with Coulomb frictionDai, J. Yang, and M. Wiercigroch, “Vibration energy flow transmission in systems with Coulomb friction,” *Int. J. Mech. Sci.*, vol. 214, no. July 2021, p. 106932, 2022.

[108] J. P. Den Hartog, “Forced vibrations with combined Coulomb and viscous friction,” *Trans. ASME*, vol. 53, no. 15, pp. 107–115, 1931.

[109] L. Marino and A. Cicirello, “Experimental investigation of a single-degree-of-freedom system with Coulomb friction,” *Nonlinear Dyn.*, vol. 99, no. 3, pp. 1781–1799, 2020.

[110] L. Marino, A. Cicirello, and D. A. Hills, “Displacement transmissibility of a Coulomb friction oscillator subject to joined base-wall motion,” *Nonlinear Dyn.*, vol. 98, no. 4, pp. 2595–2612, 2019.

[111] T. Information, “Linear Guideway.”

[112] H. K. Hong and C. S. Liu, “Non-sticking oscillation formulae for Coulomb friction under harmonic loading,” *J. Sound Vib.*, vol. 244, no. 5, pp. 883–898, 2001.

[113] T. I. Toluwaloju, C. Thein, and D. Halim, “A novel redefined electromagnetic damping equation for vibration energy harvester,” in *International Conference on Electrical, Computer, Communications and Mechatronics Engineering, ICECCME 2021*, 2021, no. October, pp. 7–8.

[114] T. I. Toluwaloju, C. K. Thein, and D. Halim, “An Effect of Coupling Factor on the Power Output for Electromagnetic Vibration Energy Harvester,” *Eng. Proc.*, vol. 10, no. 1, p. 5, 2021.

[115] H. Zou, M. Li, L. Zhao, Q. Gao, and K. Wei, “A magnetically coupled bistable piezoelectric harvester for underwater energy harvesting,” *Energy*, vol. 217, p. 119429, 2021.

[116] B. Liao, R. Zhao, K. Yu, C. Liu, Y. Lian, and S. Liu, “Theoretical and experimental investigation of a bi-stable piezoelectric energy harvester incorporating fluid-induced vibration,” *Energy Convers. Manag.*, vol. 255, no. October 2021, p. 115307, 2022.

[117] F. M. Foong, C. K. Thein, and D. Yurchenko, “Important considerations in optimising the structural aspect of a SDOF electromagnetic vibration energy harvester,” *J. Sound Vib.*, vol. 482, p. 115470, 2020.

[118] M. Mösch and G. Fischerauer, “A comparison of methods to measure the coupling coefficient of electromagnetic vibration energy harvesters,” *Micromachines (Basel)*, vol. 10, no. 12, p. 826, 2019.

[119] Yili Hu, Zhiran Yi, Xiaoxue Dong, Fangxiao Mou, Yingwei Tian, Qinghai Yang, Bin Yang, Jingquan Liu, “High power density energy harvester with non-uniform cantilever structure due to high average strain distribution,” *Energy (Oxford)*, vol. 169, pp. 294–304, 2019.

[120] A. Ibrahim, A. Ramini, and S. Towfighian, “Triboelectric energy harvester with large bandwidth under harmonic and random excitations,” *Energy Reports*, vol. 6, pp. 2490–2502, 2020.

[121] M. Iqbal and F. Ullah, “Hybrid vibration and wind energy harvesting using combined piezoelectric and electromagnetic conversion for bridge health monitoring applications,” *Energy Convers. Manag.*, vol. 172, no. April, pp. 611–618, 2018.

[122] M. Hasani and M. Irani, “The optimization of an electromagnetic vibration energy harvester based on developed electromagnetic damping models,” *Energy Convers. Manag.*, vol. 254, no. October 2021, p. 115271, 2022.

[123] W. Sun, F. Guo, and J. Seok, “Development of a novel vibro-wind galloping energy harvester with high power density incorporated with a nested blu ff -body structure,” *Energy Convers. Manag.*, vol. 197, no. August, p. 111880, 2019.

[124] Y. Shen and K. Lu, “Scavenging power from ultra-low frequency and large amplitude vibration source through a new non-resonant electromagnetic energy harvester,” *Energy Convers. Manag.*, vol. 222, no. July, p. 113233, 2020.

[125] O. Yasar, H. Ulusan, O. Zorlu, O. Sardan-Sukas, and H. Kulah, “Optimization of AA-Battery Sized Electromagnetic Energy Harvesters: Reducing the Resonance Frequency Using a Non-Magnetic Inertial Mass,” *IEEE Sens. J.*, vol. 18, no. 11, pp. 4509–4516, 2018.

[126] Liu, C., Zhang, W., Yu, K., Liu, T., & Zheng, Y. (2024). Quasi-zero-stiffness vibration isolation : Designs , improvements and applications. *Engineering Structures*, *301*(November 2023).

[127] Liang, Q., Luo, W., Zhou, Y., Lu, Z., Li, J., & He, Z. (2024). Vibration filtering effect of a novel three-dimensional isolation bearing on metro vibration isolation. *Engineering Structures*, *301*(November 2023), 117304.

[128] Kim, K., Cho, J. Y., Jabbar, H., Ahn, J. H., Hong, S. Do, & Woo, S. B. (2018). Optimized composite piezoelectric energy harvesting floor tile for smart home energy management. *Energy Conversion and Management*, *171*(May), 31–37.

[129] Alavi, A. H., Jiao, P., Buttlar, W. G., & Lajnef, N. (2018). Internet of Things-enabled smart cities : State-of-the-art and future trends. *Measurement*, *129*(June), 589–606.

[130] Maharjan, P., Cho, H., & Park, J. Y. (2018). An indoor power line based magnetic field energy harvester

for self-powered wireless sensors in smart home applications. *Applied Energy*, *232*(October), 398–408.

[131] Wang, C., Lai, S. K., Wang, J. M., Feng, J. J., & Ni, Y. Q. (2021). An ultra-low-frequency, broadband and multi-

stable tri-hybrid energy harvester for enabling the next-generation sustainable power. *Applied Energy*,

291(March), 116825.

[132] Wang, X. C., Huang, B., Wang, R. L., Mo, J. L., & Ouyang, H. (2020). Friction-induced stick-slip vibration and its

experimental validation. *Mechanical Systems and Signal Processing*, *142*.

[133] Donmez, A., & Cigeroglu, E. (2020). An improved quasi-zero stiffness vibration isolation system utilizing dry

friction damping. *Nonlinear Dynamics*, *101*(1), 107–121.

[134] Sun, R., Wong, W., & Cheng, L. (2022). A tunable hybrid damper with Coulomb friction and electromagnetic shunt

damping. *Journal of Sound and Vibration*, *524*(January), 116778.

[135] Hartog, J. P. Den. (1931). Forced vibrations with combined Coulomb and viscous friction. *Trans. ASME*, *53*(15),

107–115.

[136] Marino, L., & Cicirello, A. (2020). Experimental investigation of a single-degree-of-freedom system with Coulomb

friction [Article]. *Nonlinear Dynamics*, *99*(3), 1781–1799.

[137] Zhang, X., Pan, H., Qi, L., Zhang, Z., Yuan, Y., & Liu, Y. (2017). A renewable energy harvesting system using a mechanical vibration rectifier (MVR) for railroads. *Applied Energy*, *204*, 1535–1543.

[138] Lin, T., Pan, Y., Chen, S., & Zuo, L. (2018). Modeling and field testing of an electromagnetic energy harvester for rail tracks with anchorless mounting. *Applied Energy*, *213*(January), 219–226.

[139] Hosseinkhani, A., Younesian, D., Eghbali, P., Moayedizadeh, A., & Fassih, A. (2021). Sound and vibration energy harvesting for railway applications: A review on linear and nonlinear techniques. *Energy Reports*, Vol. 7, pp. 852–874.

[140] Liu, H., Huang, X., Jiang, Z., Li, S., & Rong, Z. (2024). Reliability-based design optimization scheme of isolation capacity of nonlinear vibration isolators. *Engineering Structures*, *300*(November 2023), 117220.

[141] Xie, X. D., Carpinteri, A., & Wang, Q. (2017). A theoretical model for a piezoelectric

energy harvester with a tapered shape. *Engineering Structures*, *144*, 19–25.

[142] Adonijah, S., Chamith, S., Patnam, H., Manchi, P., Lee, J., & Su, J. (2021). *Nano Energy Harsh environment – tolerant and robust triboelectric nanogenerators for mechanical-energy harvesting , sensing , and energy storage in a smart home*. *80*.

[143] Woude, C. Van Der, & Narasimhan, S. (2014). A study on vibration isolation for wind turbine structures. *Engineering Structures*, *60*, 223–234.

[144] Toluwaloju, T. I., Thein, C. K., Halim, D., & Yang, J. (2023). Dynamic responses of the 2DOF electromagnetic vibration energy harvester through different electrical coil connections. *Mechanical Systems and Signal Processing*, *184*(July 2022), 109709.

[145] Liu, G., Fang, Z., Zhang, Z., Tan, X., Dai, C., Wu, X., … Li, D. (2022). A vibration energy harvester for freight train track self-powered application. *IScience*.

[146] Yong, J., Youn, J., Woo, S., Hwan, J., Seop, W., Hee, H., & Hyun, T. (2017). Physical Design of hydro electromagnetic and piezoelectric energy harvesters for a smart water meter system. *Sensors & Actuators: A. Physical*, *261*, 261–267.

[147] Toluwaloju, T. I., Thein, C., & Halim, D. (2021). A novel redefined electromagnetic damping equation for vibration energy harvester. *International Conference on Electrical, Computer, Communications and Mechatronics Engineering, ICECCME 2021*, (October), 7–8.

[148] Wan, S., Lu, P., Yin, D., Guan, X., & Ni, W. (2023). A compact hybrid solar and electromagnetic energy harvester at 2 . 45 GHz microstrip rectenna. *International Journal of Electronics and Communications*, *172*(July).

[149] Kim, S., Shin, J., Kim, H., Lee, D., Park, J., Min, J., … Hur, S. (2023). A synergetic effect of piezoelectric energy harvester to enhance thermoelectric Power : An effective hybrid energy harvesting method. *Energy Conversion and Management*, *298*(October), 117774.

[150] Ra, Y., Kim, Y., Yang, S., Kang, N., Oh, G., Cho, C., … Choi, D. (2024). Portable triboelectric-electromagnetic hybrid biomechanical energy harvester for driving various functional light-emitting diodes with a wide range of wavelengths. *Nano Energy*, *119*(November 2023), 109052.

[151] Zhuo, J., Zheng, Z., Ma, R., Zhang, X., Wang, Y., Yang, P., … Yi, F. (2023). A

breathable and woven hybrid energy harvester with optimized power management for sustainably powering electronics. *Nano Energy*, *112*(February), 108436.

[152] Yang, X., Wang, C., & Lai, S. K. (2020). A magnetic levitation-based tristable hybrid energy harvester for scavenging energy from low-frequency structural vibration. *Engineering Structures*, *221*(March), 110789.

[153] Lu, Z., Zhao, L., Ding, H., & Chen, L. (2021). A dual-functional metamaterial for integrated vibration isolation and energy harvesting. *Journal of Sound and Vibration*, *509*(March).

[154] Xu, L., & Xiang, Z. (2022). Compliant quasi-zero stiffness device for vibration energy harvesting and isolation. *Sensors and Actuators: A. Physical Journal*, *347*(September).

[155] Liu, C., Zhao, R., Yu, K., Lee, H. P., & Liao, B. (2021). Simultaneous energy harvesting and vibration isolation via quasi-zero-stiffness support and radially distributed piezoelectric cantilever beams. *Applied Mathematical Modelling*, *100*(92), 152–169.

[156] Yan, B., Wang, X., Wang, Z., Wu, C., & Zhang, W. (2022). Enhanced lever-type vibration isolator via electromagnetic shunt damping. *International Journal of Mechanical Sciences*, *218*(January).

[157] Wang, X., Yu, N., Wu, C., Zhang, W., & Yan, B. (2022). Lever-type high-static-low-dynamic-stiffness vibration isolator with electromagnetic shunt damping. *International Journal of Non-Linear Mechanics*, *146*(June), 104128.

[158] Toluwaloju, T. I., Yadav, D., Thein, C. K., & Halim, D. (2022). Investigation on the Effect of Magnetic Coupling and Power Harvested in an Electromagnetic Vibration Energy Harvester. *Proceedings of the IEEE International Conference on Industrial Technology*, *2022-Augus*.

[159] Wang, L., Lian, C., Shu, D., Yan, Z., & Nie, X. (2023). Analytical solution and optimal design for the output performance of Galfenol cantilever energy harvester considering electromechanical coupling effect. *Scientific Reports*, 1–14.

[160] Hiwin, “Linear Guideway,” *Hiwin Linear Guid. Technol. Corp*, p. 211.html [accessed 10 Dec 2023]

[161] SMB bearing, https://www.smbbearings.com/technical/bearing-frictional-torque.html [accessed 1 July 2024.